Weighted Dynamic Aggregation Approach for Modular Large-scale Power Systems Modeling and Analysis

by

Navid Shabanikia

A thesis submitted in partial fulfillment of the requirements for the degree of

Doctor of Philosophy

in

Energy Systems

Electrical and Computer Engineering Department

University of Alberta

Abstract

Regardless of the power level, many recent power systems are designed with modular and distributed units forming complex systems. Such large-scale systems normally consist of several units with similar hardware and control configurations, which can be connected to the rest of the system at a Point of Common Coupling (PCC). The higher number of units improves reliability, system efficiency, and energy harvesting, however, it makes the system response analysis and control system design challenging. Interactions between a large number of units and the rest of the system connected to the PCC can lead to unpredictable system behaviors such as oscillations, instability, and undesirable transient responses, which can limit the flexibility and scaling of the system. Therefore, power system studies such as power planning, steady-state, and stability analyses should be continuously conducted to ensure a desirable system performance, which requires an accurate and computationally efficient model for modular large-scale systems.

This thesis proposes Weighted Dynamic aggregation (WD agg) approach to model large-scale modular systems with an equivalent unit that has a similar order and structure to an individual unit of the large-scale system. For example, the WD agg model of a PV farm becomes an equivalent single PV array, single inverter, and a controller with weighted average parameters, which hugely reduces the computational burden of the system studies. The parameter weights of each unit are obtained based on the contribution of that unit in the overall dynamic behavior of the system. The proposed approach is applied to find the WD agg model of n parallel DC-DC buck converter to facilitate the sensitivity analyses and control design of the system. Moreover, an equivalent inverter and a controller is found for n grid-forming inverters in an islanded microgrid with droop control power sharing by the proposed WD agg

method. Furthermore, the proposed approach is applied to find the WD agg model of n grid-following inverters in large-scale PV farms considering non-linearity of the PV sources. Additionally, the proposed WD agg approach is used to aggregate n induction machine-based Wind Turbine Generators (WTGs) in a large-scale wind farm considering the mechanical and electric machine dynamics. The performance of the proposed method is evaluated by simulations and experiments of small and large-scale DC microgrids, grid-forming inverter-based islanded microgrids, PV farms, and induction machine-based wind farms with equal or unequal parameters with various inputs and stability conditions under harsh power system events such as line-to-line faults and voltage sags for a comprehensive study.

The simulation and experiment results show that compared with the existing full-order models, simplified models, equivalent circuits, and conventional full, semi, and cluster/zone agg models, the proposed WD agg model can provide an accurate and computationally efficient single equivalent unit for a large number of units with different operating points and parameters, which can be readily used in the steady-state, transient, and stability analyses with superior accuracy. It also can be used to design the large-scale system controller and unit parameters to ensure a desirable system performance.

Preface

This thesis is an original work by Navid Shabanikia. Chapter 2 is published as A. A. Nia, N. Shabanikia, and S. A. Khajehoddin, "Droop-Based DC Microgrids Analysis and Control Design Using a Weighted Dynamic Aggregation Modeling Approach," in *IEEE Transactions on Industrial Electronics*, vol. 70, no. 12, pp. 12299-12310, Dec. 2023, and A. A. Nia, N. Shabanikia, and S. A. Khajehoddin, "Weighted Dynamic Aggregation Modeling of DC Microgrid Converters with Droop Control," in *2021 IEEE Energy Conversion Congress and Exposition (ECCE)*. I was responsible for developing the initial idea and assisting with model derivations and the implementation of the experimental setup. Aida Afshar Nia was responsible for simulation results and experimental measurements. Dr. S. Ali Khajehoddin was the supervisory author and was involved in concept formation and manuscript composition.

Chapter 3 is accepted to be published as N. Shabanikia and S. A. Khajehoddin, "Analysis and Design of Droop-Controlled Grid-Forming Inverters Using Novel WD Agg Approach," in *IEEE Transactions on Industrial Electronics*, accepted on Oct. 2023. I was responsible for developing the initial idea, deriving the proposed model, building simulation files, implementing the experimental setup, and measuring the results. Dr. S. Ali Khajehoddin was the supervisory author and was involved in concept formation and manuscript composition.

Chapter 4 is published as N. Shabanikia and S. A. Khajehoddin, "Weighted Dynamic Aggregation Modeling of Grid-Following Inverters to Analyze Renewable DG Integrated Microgrids," in *IEEE Transactions on Industrial Electronics*, vol. 71, no. 1, pp. 583-594, Jan. 2024, and N. Shabanikia and S. A. Khajehoddin, "Single Equivalent PV Inverter Model for PV Farms with Substantial Parameter Disparities Using

WD agg Approach," *25th European Conference on Power Electronics and Applications (EPE ECCE)*, Aalborg, Denmark, 2023. I was responsible for developing the initial idea, deriving the proposed model, building simulation files, implementing the experimental setup, and measuring the results. Dr. S. Ali Khajehoddin was the supervisory author and was involved in concept formation and manuscript composition.

Chapter 5 is published as N. Shabanikia, A. A. Nia, A. Tabesh and S. A. Khajehoddin, "Weighted Dynamic Aggregation Modeling of Induction Machine-Based Wind Farms," in *IEEE Transactions on Sustainable Energy*, vol. 12, no. 3, pp. 1604-1614, July 2021, and S. A. Khajehoddin, A. Tabesh, and N. Shabanikia, "Aggregated model of large-scale wind farms for power system simulation software tools," Dec. 24 2020. US Patent App. 16/904,959. I was responsible for developing the initial idea, deriving the proposed model, building simulation files, implementing the experimental setup, and measuring the results. Aida Afshar Nia was responsible for assisting in Doubly-Fed Induction Generator (DFIG) controller development in simulation models. Dr. S. Ali Khajehoddin and Dr. Ahmadreza Tabesh were the supervisory authors and were involved in concept formation and manuscript composition.

Acknowledgments

I would like to express my deepest gratitude to my esteemed mentor and supervisor, Prof. S. Ali Khajehoddin, for his remarkable expertise and invaluable insights that have been instrumental throughout the journey of my Ph.D. studies. His gentle demeanor, unwavering passion, and rigorous commitment to research have transformed the past couple of years into an exceptionally constructive and rewarding chapter in my academic pursuit.

My appreciation is extended to Prof. Ryan (Yunwei) Li, Prof. Gregory Kish, and other members of my committee for their constructive comments and feedbacks.

I am deeply indebted to the scholarly discussions with Prof. Ahmadreza Tabesh and Dr. Mohammad Ebrahimi, which have consistently fueled my intellectual growth. I would also like to acknowledge the insightful contributions of Dr. Nima Amouzegar Ashtiani, Dr. Rouzbeh Reza Ahrabi, and Amin Khakparvar Yazdi, whose wisdom and guidance have left an indelible mark on my academic journey. Special appreciation goes to Aida Afshar Nia for our fruitful collaboration, which has not only advanced our shared research goals but also enriched the professional aspects of this pursuit.

I extend my heartfelt gratitude to the vibrant community of graduate students in the uAPEL lab, particularly Mehdi Pourmohammad, Manouchehr Fathi, Afshin Amoorezaei, Mohammad Shahabbasi, Morteza Mahdavifard, Ali Sheykhi, Morteza Esteki, and Neda Mazloum, with whom I have engaged in numerous enriching discussions over the years.

Last but certainly not least, I extend my heartfelt appreciation to my parents and sister, whose unwavering encouragement and support have been my pillars of strength. Their love and guidance have propelled me forward during the research and writing phases of this thesis, and for that, I am truly grateful.

Dwellers of this porch, these objects abide,
Carriages of the wise, in intellect they ride.
Navigate wisdom's thread with care, don't sway,
Wise minds may wander, in thought's vast array.

-inspired by Ommar Khayyam.

To my family

Contents

List of Tables

List of Figures

Chapter 1

Introduction

Due to the high demand for clean energy, modern power systems are continuously expanding with modular large-scale systems such as wind farms, photovoltaic (PV) solar farms, battery banks, etc. [1]-[5]. These modular large-scale systems typically consist of n units with similar configurations, which are connected to the rest of the system at a Point of Common Coupling (PCC) [6, 7]. For example, a PV farm consists of numerous PV arrays connected to the grid via a multitude of paralleled inverters with similar output filters and controller structures [8]. However, the input irradiation, control parameters, output filters, and collector lines can have varying values. Islanded microgrids can also be considered as large-scale systems. Many paralleled converters are deployed to meet the increasing energy demand and improve the efficiency and reliability of the islanded microgrids [9]. Another example of large-scale systems is wind farms, which consist of a large number of wind turbines providing mechanical inputs to electrical machines known as Wind Turbine Generators (WTGs). A large-scale wind farm may comprise different types of WTGs, including fixed-speed Induction Generators (IG), Doubly-Fed Induction Generators (DFIG), and Permanent Magnet Synchronous Generators (PMSG) [10, 11]. WTGs of the same type can also have varying wind speed inputs, inverter and control parameters, and collector line values.

Increasing the number of units in a modular large-scale system can enhance the system's reliability and energy harvesting capabilities. However, integrating a large number of paralleled units into the power system can lead to unpredictable behaviors, such as oscillations, instability, and undesirable transient responses in the output, etc. [12]-[17]. For instance, connecting a substantial number of paralleled inverters to a weak grid can introduce stability issues to the system [18, 19]. Even more challenging is the task of designing the parameters of the large-scale system to ensure stabil-

ity [20]-[22] and desirable system performance across various input profiles [23], [24], especially during harsh and unpredictable power system events such as line-to-line faults, voltage sags, etc. [25]. Furthermore, a failure to establish proper load sharing and voltage regulation can result in circulating currents, potentially overloading the converters and undermining system performance [26]-[28]. Therefore, various power system studies, such as power planing, steady-state, and stability analyses should continuously be investigated to ensure the desirable system performance, which requires an accurate and computationally efficient model for the analysis and design of modular large-scale systems.

1.1 Existing Large-scale Systems Modeling Methods

Numerous methods have been proposed for modeling modular large-scale systems. Typically, existing modeling approaches exhibit a trade-off between accuracy and complexity. Those that can precisely predict stability and dynamic responses tend to be of higher order and greater complexity. The models for modular large-scale systems can be categorized into the following five groups:

1.1.1 Full-order models

A comprehensive state-space model that takes into account all states of a large-scale system can effectively capture its behavior, making it useful for power studies [29, 30]. For instance, in [31], a full-order state-space model of an inverter-based microgrid is developed, considering 13 states for each inverter. Another example involves [32], where a full-order state-space model is derived for inverter-based islanded microgrids, tailored for power system studies. Additionally, [33] presents a detailed state-space model for a DFIG-based wind farm, facilitating the analysis of electrical oscillations within wind farms. In [34], comprehensive state-space models for fixed-speed IG-based, DFIG-based, and synchronous generator-based wind farms are proposed, intended for power system transient and small-signal analyses. Notwithstanding the accuracy these models offer, fully representing large-scale systems with numerous units can pose challenges, leading to high-order and intricate models. As a consequence, power system studies become demanding and time-consuming.

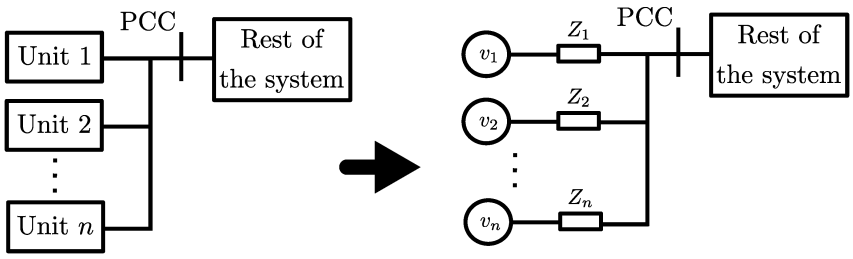

Figure 1.1: The equivalent Thevenin circuit modeling of the large-scale system.

1.1.2 Equivalent circuit models

An approach to modeling large-scale systems involves utilizing an equivalent voltage/current source and an equivalent impedance [35]-[41] as depicted in Figure 1.1. For instance, an equivalent voltage/current source and impedance are derived in [42] for grid-connected PV farms, designed for small-signal studies. However, simplifying a complex large-scale system to a single voltage/current source and impedance can result in the loss of vital frequency modes and significant dynamic system behavior. It's also worth noting that calculating the equivalent circuit of a complex large-scale system can pose challenges. To aid in obtaining equivalent circuits for large-scale systems, various models are suggested, involving the omission of certain aspects of the system during model derivation [43], [44]. For instance, an equivalent circuit is derived in [45] for an islanded microgrid with numerous grid-forming inverters, disregarding filter capacitors and controller dynamics in the equivalent model derivation. Similarly, an approach is proposed in [46] to establish an equivalent circuit for an inverter-based microgrid, neglecting droop control power sharing during model derivation. To address the challenges of determining an equivalent circuit for a large-scale system while considering the entire system, a curve fitting approach is employed to derive an equivalent circuit for DFIG-based wind farms [47]-[52]. While the resulting model can achieve accuracy, incorporating all state-space equations of a large-scale wind farm into a repetitive optimization solution incurs a substantial computational burden and contradicts the primary goal of reduced-order representation. Therefore, it's evident that calculating the equivalent circuit of a complex large-scale system can become intricate, imprecise, and time-consuming. Moreover, the equivalent circuit lacks crucial features and characteristics of the large-scale system, such as PV curves and shading events in solar and wind farms.

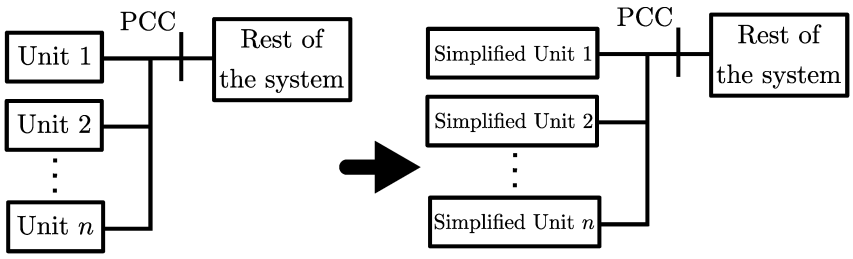

Figure 1.2: The simplified reduced-order modeling of the large-scale system.

1.1.3 Simplified reduced-order models

In order to streamline the system's complexity, it's possible to reduce the order of units within large-scale systems through simplifying assumptions as shown in Figure 1.2. For instance, one can diminish the order of a single inverter PV model by assuming fast controller responses [53], [54]. However, as the number of inverters increases, the model's order and complexity grow significantly. In [55], a reduced-order state-space model is introduced for an inverter-based islanded microgrid, concentrating solely on low oscillation modes. While this approach reduces model complexity by considering only 3 states for each inverter, its simplicity comes at the expense of accuracy, as it disregards other frequency modes. To enhance the precision of reduced-order models for specific studies, more states can be incorporated in the modeling process of large-scale systems, resulting in more intricate models [56], [57]. Nonetheless, these models still fall short of the accuracy achieved by full-order models [58]. For instance, in [59]-[61], a simplified reduced-order model is developed for a large-scale inverter-based islanded microgrid, omitting the power filter dynamics from the model derivations. It's also important to note that, similar to full-order models, the order and complexity of reduced-order models considerably increase as the number of units rises.

1.1.4 Scaled models

A large-scale system, composed of several smaller units, can be effectively modeled using a scaled unit system that shares a similar structure with those smaller units [62], [63]. This modeling approach hinges on the fundamental assumption of uniformity, implying identical machines, controllers, inverters, collector lines, etc., all with similar inputs [64, 65]. This simplifying assumption generally holds well for stability analyses and power planning studies in intricate systems, where the potential impact of varying parameters isn't a central concern. However, it's important to recognize that assuming identical parameters and inputs for all units may not align with the practical complexities and nuances of realistic large-scale systems.

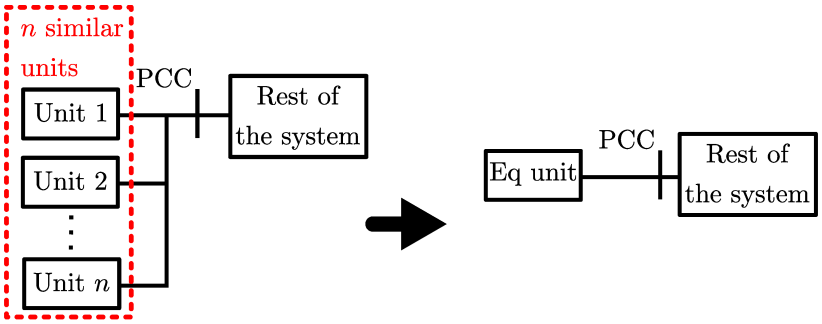

Figure 1.3: Full aggregation modeling of the large-scale system.

1.1.5 Aggregated models

To enhance model accuracy while reducing complexity, various methods have been proposed for aggregating large-scale power systems [66], [67]. An aggregated model typically comprises a single or a small number of equivalent units, mimicking the configuration of the larger-scale system units. The existing aggregation approaches can be classified into the following three groups:

Full Aggregated Models:

This approach involves modeling the large-scale system with a single equivalent unit that shares a similar configuration, as depicted in Figure 1.3 [68]. The normalized parameters of this equivalent unit are obtained by averaging the corresponding normalized parameters from the larger-scale system. Additionally, the equivalent rated power is determined by summing up the rated powers of the individual units within the large-scale configuration. The underlying assumption in this approach is that the system exhibits uniform normalized inputs and parameters across all units, with all units operating at their rated power [69]. For instance, a single aggregated unit is introduced in [70] to represent n similar paralleled grid-following inverters for use in power system studies. However, it's important to note that assuming identical parameters for all units can be restrictive, and the accuracy of Full agg models is significantly compromised when units have dissimilar inputs and/or parameters [71, 72].

Semi Aggregated Models:

To enhance the Full agg approach in situations involving unequal inputs within large-scale systems, Semi agg methods offer an alternative by aggregating a portion of the system, similar to the Full agg approach, while generally preserving the individual inputs, as depicted in Figure 1.4 [73]. In this method, the equivalent input signal is determined by summing the inputs of the larger-scale system. For instance, in [74]

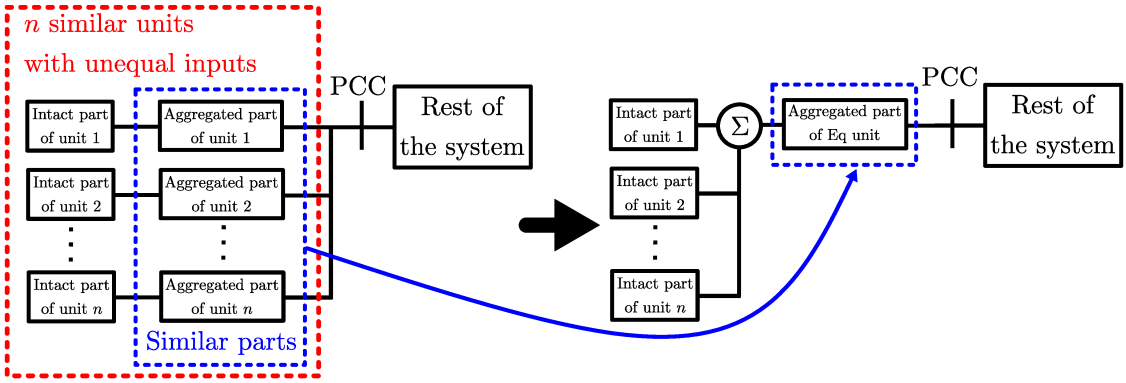

Figure 1.4: Semi aggregation modeling of the large-scale system.

and [75], a single equivalent generator and converter are proposed for a DFIG-based wind farm, while retaining the mechanical components of the WTGs. While the Semi agg method provides an accurate model, it's worth noting that it can be inefficient in large-scale systems, since it necessitates modeling the preserved portion of the system in detail.

Cluster/Zone Aggregated Models:

To enhance the Full agg method for large-scale systems with varying parameters and operational conditions, the Cluster/Zone agg approach can be employed. This approach involves dividing the large-scale system into smaller clusters or zones, based on unit similarities, and subsequently aggregating each cluster or zone, similar to the Full agg approach, as depicted in Figure 1.5 [76]. For instance, in [77]-[79], the Cluster/Zone agg approach is applied to derive a reduced-order model for large-scale wind farms, intended for use in power system studies. A similar strategy is proposed in [80] to cluster and aggregate photovoltaic grid-tied inverters based on their collector lines, without considering droop control power sharing. While this approach achieves improved accuracy, the overall system model lacks a simple single-unit representation. Furthermore, increasing differences in unit parameters will lead to a greater number of clusters and subsequently increase the complexity of the proposed model. Additionally, it's important to note that identifying suitable clusters or zones is a challenging task; a failure to accurately cluster the large-scale system can significantly undermine the accuracy of the resulting model [81], [82].

Table 1.1 provides a summary and comparison of the existing methods for modeling large-scale systems, categorized according to their model complexity, derivation time, accuracy, sensitivity to unequal inputs, and sensitivity to unequal parameters across

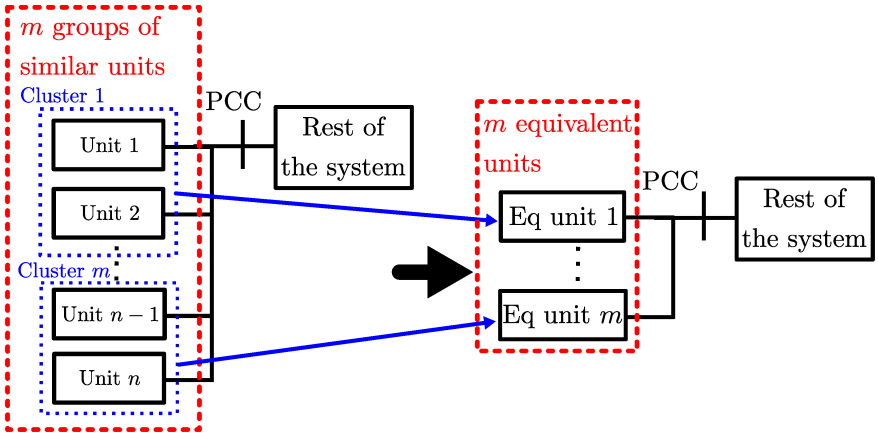

Figure 1.5: Cluster/Zone aggregation modeling of the large-scale system.

various power system studies. As indicated in Table 1.1, a trade-off typically exists between model complexity, derivation time, accuracy, and sensitivity. It's evident that no single model stands out as superior in all aspects.

Table 1.1: The existing methods and the proposed WD agg approach comparison, where 1 indicates the best performance and 7 is the lowest.

Model	Complexity	Model Derivation	Error	Sensitivity to unequal inputs	Sensitivity to unequal params	Rank
Full-order models	7	7	1	1	1	2
Scaled models	2	1	7	7	7	7
Equivalent Circuits	1	6	6	6	2	6
Full agg	2	2	5	5	6	3
Semi agg	6	5	3	1	5	3
Cluster/Zone agg	5	4	3	4	4	3
WD agg	2	3	2	1	2	1

1.2 The Proposed Weighted Dynamic Aggregation Method

To overcome the existing challenges in modeling large-scale modular systems, an innovative Weighted Dynamic Aggregation (WD agg) approach is introduced. This method aims to effectively model the detailed large-scale system as depicted in Figure 1.6, accounting for variations in inputs, parameters, and operational conditions. The structure and order of the WD agg model closely resemble that of a single unit within the large-scale system, as illustrated in Figure 1.6. For instance, in the case of a PV farm comprising numerous PV arrays connected via paralleled grid-following inverters, the WD agg model simplifies to an equivalent single PV array, a single inverter, and a controller, featuring weighted average parameters. This reduction

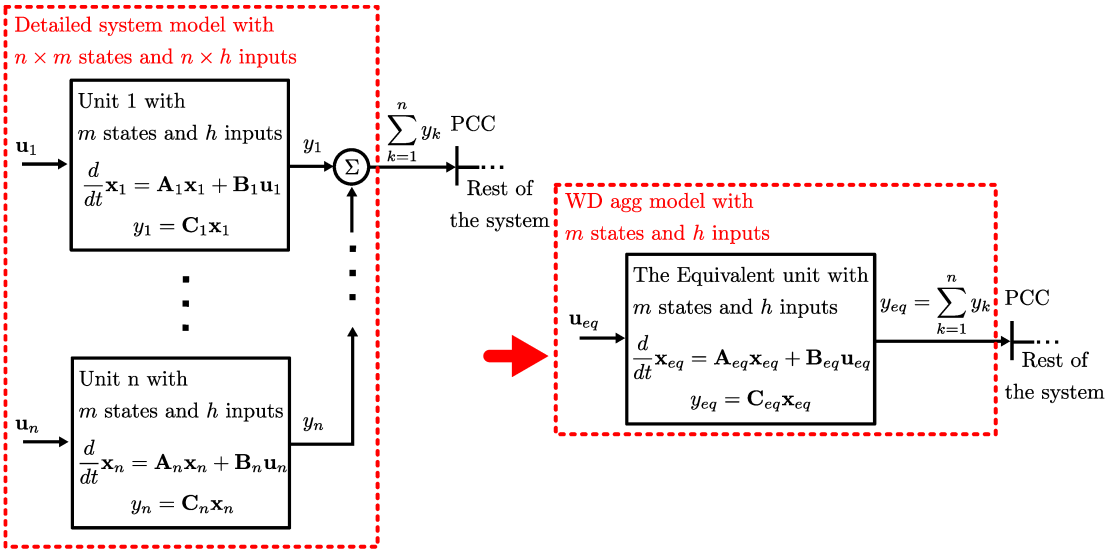

Figure 1.6: The proposed WD aggregation modeling of the large-scale system.

significantly streamlines system order in a manner akin to Full agg models. The parameter weights assigned to each unit are determined based on their contributions to the overall dynamic behavior of the desired system output. This approach lends itself to utilization in steady-state, transient, and stability studies, exhibiting high accuracy that surpasses Semi agg models and comes close to Full-order models. Furthermore, the proposed model can facilitate the design of unit parameters, considering their respective controllers, to ensure desirable performance for the entire large-scale system. For a comprehensive perspective, Table 1.1 compares the existing large-scale modeling approaches with the newly proposed WD agg method. The comparison assesses aspects such as model complexity, derivation time, accuracy, sensitivity to unequal inputs, and sensitivity to unequal parameters, across a range of power system studies.

The main objectives of this report is to derive, show and verify the accuracy and applications of the proposed WD agg method for modular large-scale systems with:

(i) Modeling and design of DC-DC buck converter integrated microgrids with high parameter disparities and considering a non-linear load such as Constant Power Load (CPL).

(ii) Modeling and analysis of three-phase grid-forming droop controlled Distributed Generations (DGs) in islanded microgrids.

(iii) Modeling of three-phase grid-following PV farms with double-stage power conversion considering source non-linearity and control system dynamics.

(iv) Modeling and analysis of grid-connected wind farms considering the mechanical and electric machine dynamics.

The rest of the report is outlined as follows:
In Chapter 2, the WD agg approach is introduced and utilized to model and design n parallel droop-controlled DC-DC buck converters and collector lines using an equivalent single droop-controlled DC-DC buck converter and collector line. Moreover, a comprehensive investigation of the proposed WD aggregation model is provided to support its accuracy and applicability in designing and analyzing the stability of vendors' models in large-scale DC microgrids. The study encompasses various stability analyses and experiments to validate the effectiveness of the WD aggregation approach in this context.
In Chapter 3, the concept of WD agg is applied to model n parallel three-phase grid-forming inverters, control systems, and collector lines, employing an equivalent single grid-forming inverter, control system, and collector line. Furthermore, the proposed WD agg model is used to design four grid-forming paralleled inverters connected to a resistive load to achieve desirable system performance. The controller parameters for the large-scale system units are then calculated using the designed WD agg model. Various stability analyses and experiments are provided to support the accuracy and applicability of the proposed WD agg model in designing and conducting stability analyses of large-scale microgrids.
In Chapter 4, the concept of WD agg is applied to model n parallel grid-following inverters, their PV arrays, control systems, and collector lines, resulting in an equivalent single grid-following inverter, single PV array, control system, and collector line. The application of the proposed model in power system planning, steady-state analysis, and evaluation of system performance under different stability conditions is demonstrated, considering the control system dynamics and PV source non-linearity. Additionally, it is illustrated that the proposed model retains important features and characteristics of a PV farm, including PV curves, shading, and input irradiance, for use in solar farm studies.
In Chapter 5, the concept of WD agg is applied to model induction machine-based wind farms. Moreover, an equivalent mechanical turbine is proposed for the wind turbines of a wind farm, providing a simpler model and better insight into the mechanical system behavior, an aspect that has not been clearly addressed in existing literature.
Finally, Chapter 6 summarizes the contributions of the report and outlines potential areas for future work.

Chapter 2

Weighted Dynamic Aggregation Concept and Application in DC Microgrids

This chapter introduces the concept of WD aggregation and demonstrates its application to a microgrid comprising a parallel arrangement of n DC-DC buck converters. The objective is to establish a step-by-step modeling process. WD aggregation models n parallel dynamic units with similar configurations with an equivalent single unit with the same configuration. The model parameters for the proposed approach are determined through the weighted aggregation of corresponding unit parameters. The weighting factor for each unit's state is determined based on its contribution to the average of the corresponding states. To validate the WD aggregation approach, a comparison is made between the detailed model's dynamic behavior and the proposed model's behavior in various case studies. Moreover, it is shown that the proposed model can be employed to effectively design the control parameters of the detailed system.

- A. A. Nia, N. Shabanikia, and S. A. Khajehoddin, "Droop-Based DC Microgrids Analysis and Control Design Using a Weighted Dynamic Aggregation Modeling Approach," in *IEEE Transactions on Industrial Electronics*, vol. 70, no. 12, pp. 12299-12310, Dec. 2023 [83].
- A. A. Nia, N. Shabanikia, and S. A. Khajehoddin, "Weighted Dynamic Aggregation Modeling of DC Microgrid Converters with Droop Control," in *2021 IEEE Energy Conversion Congress and Exposition (ECCE)*, Vancouver, BC, Canada, 2021, pp. 700-706 [84].

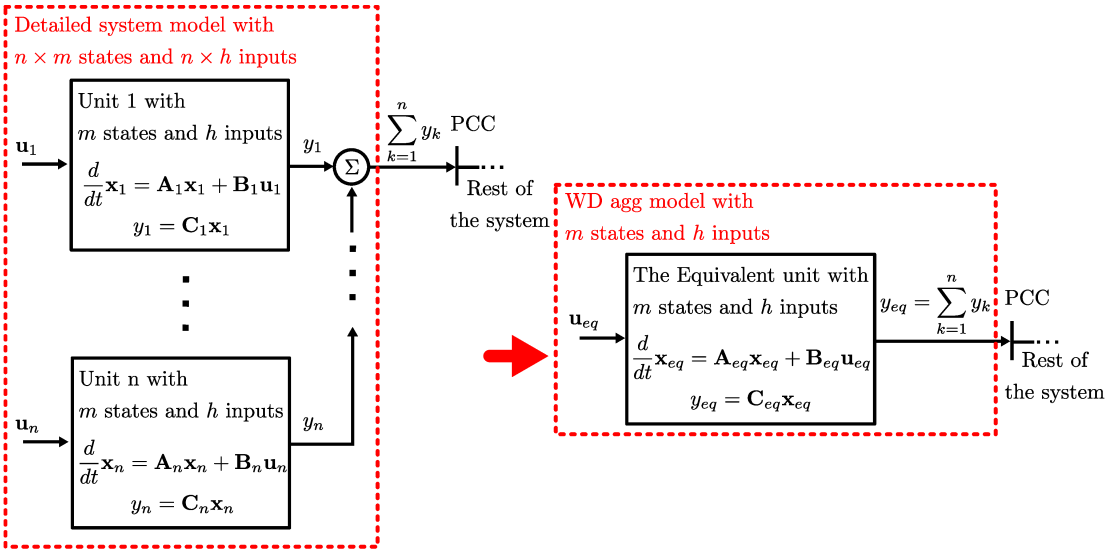

Figure 2.1: The proposed WD aggregation modeling of the large-scale system.

2.1 Basic Concept of the Weighted Dynamic Aggregation

This section introduces the basic concept of the WD agg approach. Consider n number of dynamic systems, as depicted in Figure 2.1, with the state-space representation of:

$$\begin{aligned} \frac{d}{dt}\mathbf{x}_k &= \mathbf{A}_k\mathbf{x}_k + \mathbf{B}_k\mathbf{u}_k, \\ y &= \mathbf{C}_k\mathbf{x}_k. \end{aligned} \tag{2.1}$$

The contribution of each converter to the average of corresponding states and input can be defined as two $\mathbf{M}_k$ and $\mathbf{W}_k$ matrices, which:

$$\mathbf{x}_k = \mathbf{M}_k \sum_{j=1}^{n} \mathbf{x}_j/n, \;\; \mathbf{u}_k = \mathbf{W}_k \sum_{j=1}^{n} \mathbf{u}_j/n. \tag{2.2}$$

It is worth noting that $\mathbf{M}_k$ and $\mathbf{W}_k$ can be estimated as $\mathbf{M}_k \simeq n\mathbf{X_k}/\left(\sum_{j=1}^{n}\mathbf{X}_j\right)$ and $\mathbf{W}_k \simeq n\mathbf{U_k}/\left(\sum_{j=1}^{n}\mathbf{U}_j\right)$, respectively, where $\mathbf{X}$ and $\mathbf{U}$ can be found by solving the detailed system for the steady-state operating point. Now let's define the scaling matrices $\mathbf{P_x}$ and $\mathbf{P_u}$ to find the scale of the equivalent corresponding states and inputs compare with the average of corresponding states and inputs, respectively, as:

$$\mathbf{P_x}\mathbf{x}_{eq} = \sum_{j=1}^{n} \mathbf{x}_j/n, \;\; \mathbf{P_u}\mathbf{u}_{eq} = \sum_{j=1}^{n} \mathbf{u}_j/n. \tag{2.3}$$

For example, for parallel configuration systems, the equivalent voltages can be define as the average of the corresponding voltages and the equivalent currents should be

the summation of corresponding currents. Now by substituting (2.2) into (2.1), each converter dynamic equations can be derived in terms of the equivalent states and input as:

$$\begin{aligned} \frac{d}{dt}\mathbf{M}_k\mathbf{P}_\mathbf{x}\mathbf{x}_{eq} &= \mathbf{A}_k\mathbf{M}_k\mathbf{P}_\mathbf{x}\mathbf{x}_{eq} + \mathbf{B}_k\mathbf{W}_k\mathbf{P}_\mathbf{u}\mathbf{u}_{eq}, \\ y_k &= \mathbf{C}_k\mathbf{M}_k\mathbf{P}_\mathbf{x}\mathbf{x}_{c_{eq}}. \end{aligned} \tag{2.4}$$

Now by summing n equations of (2.4), the equivalent aggregated dynamic system is obtained as:

$$\begin{aligned} \sum_{k=1}^{n}\mathbf{M}_k\mathbf{P}_\mathbf{x}\frac{d}{dt}\mathbf{x}_{eq} &= \sum_{k=1}^{n}\mathbf{A}_k\mathbf{M}_k\mathbf{P}_\mathbf{x}\mathbf{x}_{eq} + \sum_{k=1}^{n}\mathbf{B}_k\mathbf{W}_k\mathbf{P}_\mathbf{u}\mathbf{u}_{eq}, \\ y_{eq} &= \sum_{k=1}^{n}\mathbf{C}_k\mathbf{M}_k\mathbf{P}_\mathbf{x}\mathbf{x}_{c_{eq}}. \end{aligned} \tag{2.5}$$

By rewriting (2.5) in the state-space form the equivalent system model can be derived as:

$$\begin{aligned} \frac{d}{dt}\mathbf{x}_{eq} &= \mathbf{A}_{eq}\mathbf{x}_{eq} + \mathbf{B}_{eq}\mathbf{u}_{eq}, \\ y_{eq} &= \mathbf{C}_{c_{eq}}\mathbf{x}_{c_{eq}}, \end{aligned} \tag{2.6}$$

where:

$$\begin{aligned} \mathbf{A}_{eq} = \left(\sum_{k=1}^{n}\mathbf{M}_k\mathbf{P}_\mathbf{x}\right)^{-1}\sum_{k=1}^{n}\mathbf{A}_k\mathbf{M}_k\mathbf{P}_\mathbf{x},\ \mathbf{B}_{eq} = \left(\sum_{k=1}^{n}\mathbf{M}_k\mathbf{P}_\mathbf{x}\right)^{-1}\sum_{k=1}^{n}\mathbf{B}_{eq}\mathbf{W}_k\mathbf{P}_\mathbf{u}, \\ \mathbf{C}_{c_{eq}} = \left(\sum_{k=1}^{n}\mathbf{M}_k\mathbf{P}_\mathbf{x}\right)^{-1}\sum_{k=1}^{n}\mathbf{C}_k\mathbf{M}_k\mathbf{P}_\mathbf{x}, \end{aligned} \tag{2.7}$$

and $y_{eq} = \sum_{i=1}^{n} y_j$.

In the Appendix, an expansion of the mathematical proof for the WD aggregation approach presented in this section yields a demonstration of the stability-preserving characteristic of WD aggregation. Furthermore, the controlability requirement for the WD aggregation model is successfully met, ensuring that the aggregated system remains controllable and capable of achieving the desired control objectives.

2.1.1 The proposed WD agg walkthrough with a simple example

To gain a better and more detailed insight into the proposed approach explained in the previous section, the WD aggregation method is applied to an illustrative example

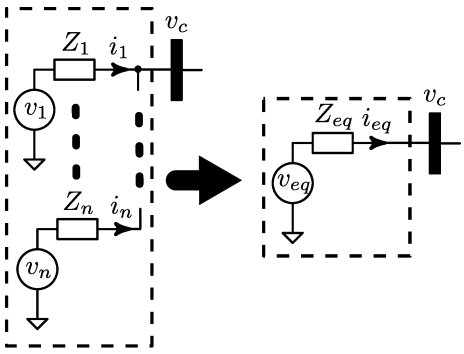

Figure 2.2: n number of paralleled voltage sources with an impedance Z and the equivalent circuit.

involving n parallel voltage sources and impedance Z, as depicted in Figure 2.2. Deriving the dynamic equations of the system yields:

$$\begin{cases} v_1 - v_c = Z_1 i_1, \\ v_2 - v_c = Z_2 i_2, \\ \vdots \\ v_n - v_c = Z_n i_n. \end{cases} \tag{2.8}$$

Now, let's define two voltage and current weights as:

$$\mu_k = \frac{n i_k}{\sum_{j=1}^{n} i_j}, \ \nu_k = \frac{n v_k}{\sum_{j=1}^{n} v_j}. \tag{2.9}$$

These weights represent the contribution of each unit's voltage/current dynamics to the average of corresponding voltage/current dynamics. Subsituting (2.9) to (2.8) results in:

$$\begin{cases} \nu_1 \dfrac{\sum_{j=1}^{n} v_j}{n} - v_c = Z_1 \mu_1 \dfrac{\sum_{j=1}^{n} i_j}{n}, \\ \nu_2 \dfrac{\sum_{j=1}^{n} v_j}{n} - v_c = Z_2 \mu_2 \dfrac{\sum_{j=1}^{n} i_j}{n}, \\ \vdots \\ \nu_n \dfrac{\sum_{j=1}^{n} v_j}{n} - v_c = Z_n \mu_n \dfrac{\sum_{j=1}^{n} i_j}{n}. \end{cases} \tag{2.10}$$

Now let's find a single equivalent circuit as demonstrated in Figure 2.2 with the following dynamic equation:

$$v_{eq} - v_c = Z_{eq} i_{eq}, \tag{2.11}$$

that mimics the dynamic behavior of the detailed system shown in Figure 2.2 from the v_c bus point of view. In order to fulfill this goal the equivalent output voltage of

should be v_c and the output current should be the summation of the output currents as:

$$i_{eq} = \sum_{j=1}^{n} i_j. \tag{2.12}$$

Substituting (2.12) to (2.10) yields:

$$\begin{cases} \nu_1 \dfrac{\sum_{j=1}^{n} v_j}{n} - v_c = Z_1 \mu_1 \dfrac{i_{eq}}{n}, \\ \nu_2 \dfrac{\sum_{j=1}^{n} v_j}{n} - v_c = Z_2 \mu_2 \dfrac{i_{eq}}{n}, \\ \vdots \\ \nu_n \dfrac{\sum_{j=1}^{n} v_j}{n} - v_c = Z_n \mu_n \dfrac{i_{eq}}{n}. \end{cases} \tag{2.13}$$

Now summing n equations of (2.13) results in:

$$\sum_{k=1}^{n} \nu_k \frac{\sum_{j=1}^{n} v_j}{n} - n v_c = \sum_{k=1}^{n} Z_k \mu_k \frac{i_{eq}}{n}. \tag{2.14}$$

Dividing (2.14) by n and rewriting it by considering $\nu_k = \frac{n v_k}{\sum_{j=1}^{n} v_j}$ yields:

$$\sum_{k=1}^{n} \frac{v_k}{n} - v_c = \sum_{k=1}^{n} \frac{Z_k \mu_k}{n^2} i_{eq}. \tag{2.15}$$

By comparing (2.11) and (2.15), the equivalent circuit parameters can be found as:

$$v_{eq} = \sum_{k=1}^{n} \frac{v_k}{n}, \;\; Z_{eq} = \sum_{k=1}^{n} \frac{Z_k \mu_k}{n^2}. \tag{2.16}$$

Considering $\mu_k = n(I_k + \tilde{i}_k) / \left(\sum_{j=1}^{n} (I_j + \tilde{i}_j) \right)$ and $\nu_k = n(V_k + \tilde{v}_k) / \left(\sum_{j=1}^{n} (V_j + \tilde{v}_j) \right)$, where I, V and $\tilde{i}$, $\tilde{v}$ represents the steady-state and the small-signal values, respectively, the weights can be estimated as:

$$\mu_k = \frac{n I_k}{\sum_{j=1}^{n} I_j}, \;\; \nu_k = \frac{n V_k}{\sum_{j=1}^{n} V_j}. \tag{2.17}$$

Therefore, the equivalent circuit is found as (2.11) with the parameters obtained as (2.16) and estimated weights as (2.17). It is worth noting that the weights obtained using (2.17) are constant values and specific to the system's operating point. If the system has multiple steady-states or variable operating points, the aggregated system can be divided into different time intervals, and the equivalent model can be updated based on the final operating point of each time interval.

It is important to emphasize that the proposed WD agg modeling approach is based on the following assumptions:

- The proposed modeling approach is applicable to systems with similar structures, regardless of differences in their parameters and sizes.
- The proposed approach aggregates units connected at a common bus with the aim of efficiently and accurately predicting the dynamic behavior of the detailed system from the common bus's point of view.
- The proposed modeling approach is developed for white-box systems, where the specifics of the detailed system are known.

This approach is particularly beneficial for vendors seeking to effectively model, analyze, and optimize their products within large-scale systems. For black-box systems, commonly encountered in utility applications, the proposed modeling approach can still be applied. In such cases, system parameter estimation can be carried out by leveraging various measurements at the Point of Common Coupling (PCC) bus. Subsequently, the proposed model can be employed using the estimated parameters derived from the detailed system. Next section applies the WD agg approach to find an equivalent DC-DC buck converter for n paralleled DC-DC buck converters as an example.

2.2 WD agg Model of n Paralleled DC-DC Buck Converters without Controller

In this section, the WD aggregation approach is employed to identify an equivalent DC-DC buck converter for a configuration consisting of n paralleled DC-DC buck converters, as depicted in Figure 2.3a. Each individual converter provides an output voltage $v_o = dV_{in}$ based directly on a reference signal d as the input. To determine the equivalent buck converter, the dynamics equations of the detailed system are initially derived. Subsequently, weights for the states and inputs are determined. The dynamic equations of each converter are then expressed in terms of the equivalent converter states. Ultimately, the dynamic equations of the n converters are aggregated to obtain the dynamic equation of the equivalent converter. By comparing the achieved dynamic equations of the equivalent converter with those of a single converter, the parameters of the equivalent converters can be determined. This process allows for the effective characterization of the parallel system as a single equivalent converter.

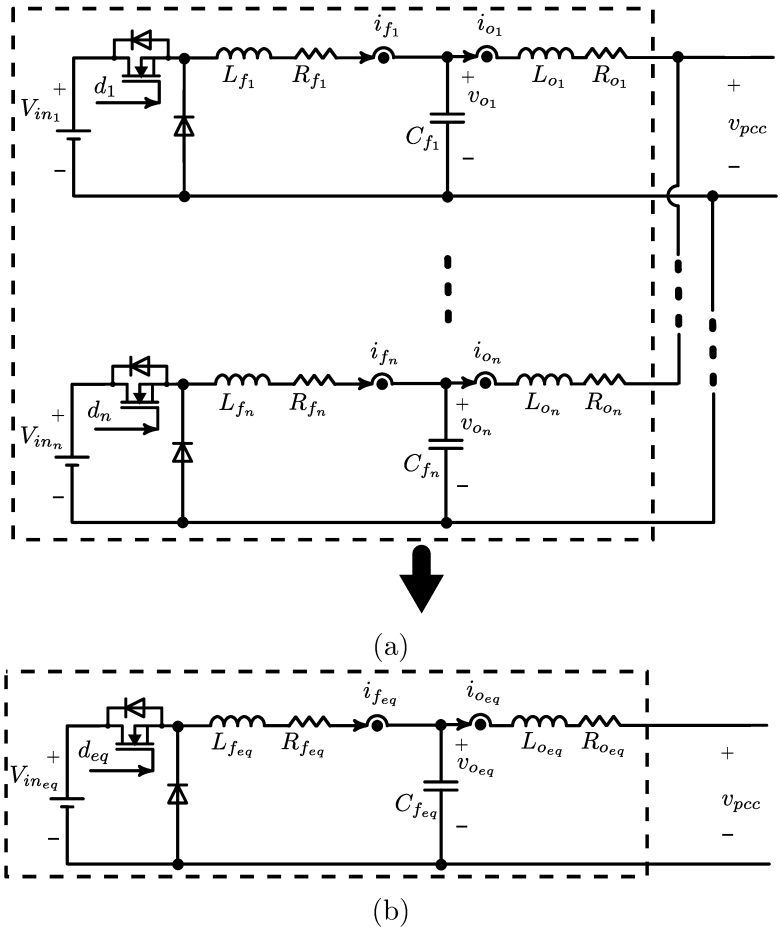

Figure 2.3: a) n paralleled DC-DC buck converters, b) The equivalent single DC-DC buck converter.

2.2.1 The equivalent model derivation

The kth converter dynamic equations can be derived as:

$$\begin{cases} d_k V_{in_k} - v_{o_k} = (\dfrac{d}{dt} L_{f_k} + R_{f_k}) i_{f_k}, \\ i_{f_k} - i_{o_k} = C_{f_k} \dfrac{d}{dt} v_{o_k}, \\ v_{o_k} - v_{pcc} = (\dfrac{d}{dt} L_{o_k} + R_{o_k}) i_{o_k}. \end{cases} \tag{2.18}$$

Now lets determine the state and input weights as:

$$\mu_{i_{f_k}} = \frac{n i_{f_k}}{\sum_{j=1}^{n} i_{f_j}},\ \mu_{v_{o_k}} = \frac{n v_{o_k}}{\sum_{j=1}^{n} v_{o_j}},\ \mu_{i_{o_k}} = \frac{n i_{o_k}}{\sum_{j=1}^{n} i_{o_j}},\ \nu_{d_k} = \frac{n d_k}{\sum_{j=1}^{n} d_j}. \tag{2.19}$$

Substituting (2.19) to (2.18) yields:

$$\begin{cases} \dfrac{\sum_{j=1}^{n} d_j}{n}\nu_{d_k}V_{in_k} - \dfrac{\sum_{j=1}^{n} v_{o_j}}{n}\mu_{v_{o_k}} = \left(\dfrac{d}{dt}L_{f_k} + R_{f_k}\right)\dfrac{\sum_{j=1}^{n} i_{f_j}}{n}\mu_{i_{f_k}}, \\ \dfrac{\sum_{j=1}^{n} i_{f_j}}{n}\mu_{i_{f_k}} - \dfrac{\sum_{j=1}^{n} i_{o_j}}{n}\mu_{i_{o_k}} = C_{f_k}\dfrac{d}{dt}\dfrac{\sum_{j=1}^{n} v_{o_j}}{n}\mu_{v_{o_k}}, \\ \dfrac{\sum_{j=1}^{n} v_{o_j}}{n}\mu_{v_{o_k}} - v_{pcc} = \left(\dfrac{d}{dt}L_{o_k} + R_{o_k}\right)\dfrac{\sum_{j=1}^{n} i_{o_j}}{n}\mu_{i_{o_k}}. \end{cases} \tag{2.20}$$

Now let's find the equivalent converter as shown in Figure 2.3b with the following dynamic equations:

$$\begin{cases} d_{eq}V_{in_{eq}} - v_{o_{eq}} = (\dfrac{d}{dt}L_{f_{eq}} + R_{f_{eq}})i_{f_{eq}}, \\ i_{f_{eq}} - i_{o_{eq}} = C_{f_{eq}}\dfrac{d}{dt}v_{o_{eq}}, \\ v_{o_{eq}} - v_{pcc} = (\dfrac{d}{dt}L_{o_{eq}} + R_{o_{eq}})i_{o_{eq}}, \end{cases} \tag{2.21}$$

where the equivalent PCC bus voltage is v_g and the output current mimics the overall system dynamic behavior, hence $i_{o_{eq}} = \sum_{k=1}^{n} i_{o_k}$. Therefore, (2.20) can be derived in terms of i_{eq} as:

$$\begin{cases} \dfrac{\sum_{j=1}^{n} d_j}{n}\nu_{d_k}V_{in_k} - \dfrac{\sum_{j=1}^{n} v_{o_j}}{n}\mu_{v_{o_k}} = \left(\dfrac{d}{dt}L_{f_k} + R_{f_k}\right)\dfrac{\sum_{j=1}^{n} i_{f_j}}{n}\mu_{i_{f_k}}, \\ \dfrac{\sum_{j=1}^{n} i_{f_j}}{n}\mu_{i_{f_k}} - \dfrac{\sum_{j=1}^{n} i_{o_j}}{n}\mu_{i_{o_k}} = C_{f_k}\dfrac{d}{dt}\dfrac{\sum_{j=1}^{n} v_{o_j}}{n}\mu_{v_{o_k}}, \\ \dfrac{\sum_{j=1}^{n} v_{o_j}}{n}\mu_{v_{o_k}} - v_{pcc} = \left(\dfrac{d}{dt}L_{o_k} + R_{o_k}\right)\dfrac{i_{o_{eq}}}{n}\mu_{i_{o_k}}. \end{cases} \tag{2.22}$$

Now summing n set of dynamic equations of (2.22) results in:

$$\begin{cases} \sum_{k=1}^{n}\left(\dfrac{\sum_{j=1}^{n} d_j}{n}\nu_{d_k}V_{in_k} - \dfrac{\sum_{j=1}^{n} v_{o_j}}{n}\mu_{v_{o_k}}\right) = \sum_{k=1}^{n}\left(\left(\dfrac{d}{dt}L_{f_k} + R_{f_k}\right)\mu_{i_{f_k}}\right)\dfrac{\sum_{j=1}^{n} i_{f_j}}{n}, \\ \sum_{k=1}^{n}\left(\dfrac{\sum_{j=1}^{n} i_{f_j}}{n}\mu_{i_{f_k}} - \dfrac{\sum_{j=1}^{n} i_{o_j}}{n}\mu_{i_{o_k}}\right) = \sum_{k=1}^{n} C_{f_k}\dfrac{d}{dt}\mu_{v_{o_k}}\dfrac{\sum_{j=1}^{n} v_{o_j}}{n}, \\ \dfrac{\sum_{j=1}^{n} v_{o_j}}{n}\sum_{k=1}^{n}\mu_{v_{o_k}} - nv_{pcc} = \sum_{k=1}^{n}\left(\left(\dfrac{d}{dt}L_{o_k} + R_{o_k}\right)\mu_{i_{o_k}}\right)\dfrac{i_{o_{eq}}}{n}. \end{cases} \tag{2.23}$$

Considering that $\sum_{k=1}^{n}\mu_{v_{o_k}}\sum_{j=1}^{n}v_{o_j}/n=\sum_{k=1}^{n}v_{o_k}$, $\sum_{k=1}^{n}\mu_{i_{f_k}}\sum_{j=1}^{n}i_{f_j}/n=\sum_{k=1}^{n}i_{f_k}$, and $\sum_{k=1}^{n}\mu_{i_{o_k}}\sum_{j=1}^{n}i_{o_j}/n=\sum_{k=1}^{n}i_{o_k}$, thus (2.23) can be rewritten as:

$$\begin{cases}\sum_{j=1}^{n}\frac{d_j}{n}\sum_{k=1}^{n}\nu_{d_k}V_{in_k}-\sum_{k=1}^{n}v_{o_k}=\sum_{k=1}^{n}\left(\left(\frac{d}{dt}L_{f_k}+R_{f_k}\right)\mu_{i_{f_k}}\right)\frac{\sum_{j=1}^{n}i_{f_j}}{n},\\ \sum_{j=1}^{n}i_{f_j}-\sum_{j=1}^{n}i_{o_j}=\sum_{k=1}^{n}\left(C_{f_k}\mu_{v_{o_k}}\right)\frac{d}{dt}\frac{\sum_{j=1}^{n}v_{o_j}}{n},\\ \sum_{j=1}^{n}v_{o_j}-nv_{pcc}=\sum_{k=1}^{n}\left(\left(\frac{d}{dt}L_{o_k}+R_{o_k}\right)\mu_{i_{o_k}}\right)\frac{i_{o_{eq}}}{n}.\end{cases}\tag{2.24}$$

Considering that:

$$\begin{aligned}\mu_{i_{f_k}}&=\frac{n\left(I_{f_k}+\tilde{i}_{f_k}\right)}{\sum_{j=1}^{n}\left(I_{f_j}+\tilde{i}_{f_j}\right)},\ \mu_{v_{o_k}}=\frac{n\left(V_{o_k}+\tilde{v}_{o_k}\right)}{\sum_{j=1}^{n}\left(V_{o_j}+\tilde{v}_{o_j}\right)},\\ \mu_{i_{o_k}}&=\frac{n\left(I_{o_k}+\tilde{i}_{o_k}\right)}{\sum_{j=1}^{n}\left(I_{o_j}+\tilde{i}_{o_j}\right)},\ \nu_{d_k}=\frac{n\left(D_k+\tilde{d}_k\right)}{\sum_{j=1}^{n}\left(D_j+\tilde{d}_j\right)},\end{aligned}\tag{2.25}$$

thus, the weights can be estimated by their steady-state values as:

$$\mu_{i_{f_k}}=\frac{nI_{f_k}}{\sum_{j=1}^{n}I_{f_j}},\ \mu_{v_{o_k}}=\frac{nV_{o_k}}{\sum_{j=1}^{n}V_{o_j}},\ \mu_{i_{o_k}}=\frac{nI_{o_k}}{\sum_{j=1}^{n}I_{o_j}},\ \nu_{d_k}=\frac{nD_k}{\sum_{j=1}^{n}D_j}.\tag{2.26}$$

Substituting (2.26) into (2.24) and dividing the first and third equation of (2.24) by n yields:

$$\begin{cases}\sum_{j=1}^{n}\frac{d_j}{n}\sum_{k=1}^{n}\frac{\nu_{d_k}V_{in_k}}{n}-\sum_{k=1}^{n}\frac{v_{o_k}}{n}=\sum_{k=1}^{n}\left(\left(\frac{d}{dt}L_{f_k}+R_{f_k}\right)\mu_{i_{f_k}}/n^2\right)\sum_{j=1}^{n}i_{f_j},\\ \sum_{j=1}^{n}i_{f_j}-\sum_{j=1}^{n}i_{o_j}=\sum_{k=1}^{n}\left(C_{f_k}\mu_{v_{o_k}}\right)\frac{d}{dt}\frac{\sum_{j=1}^{n}v_{o_j}}{n},\\ \sum_{j=1}^{n}\frac{v_{o_j}}{n}-v_{pcc}=\sum_{k=1}^{n}\left(\left(\frac{d}{dt}L_{o_k}+R_{o_k}\right)\mu_{i_{o_k}}/n^2\right)i_{o_{eq}}.\end{cases}\tag{2.27}$$

Now by comparing the (2.21) and (2.27), the equivalent buck converter parameters can be found as:

$$\begin{aligned}V_{in_{eq}}&=\sum_{k=1}^{n}\nu_{d_k}V_{in_k}/n,\ L_{f_{eq}}=\sum_{k=1}^{n}L_{f_k}\mu_{i_{f_k}}/n^2,\ R_{f_{eq}}=\sum_{k=1}^{n}R_{f_k}\mu_{i_{f_k}}/n^2,\\ C_{f_{eq}}&=\sum_{k=1}^{n}C_{f_k}\mu_{v_{o_k}},\ L_{o_{eq}}=\sum_{k=1}^{n}L_{o_k}\mu_{i_{o_k}}/n^2,\ R_{o_{eq}}=\sum_{k=1}^{n}R_{o_k}\mu_{i_{o_k}}/n^2,\\ \text{where: }d_{eq}&=\sum_{j=1}^{n}\frac{d_j}{n},\ i_{f_{eq}}=\sum_{j=1}^{n}i_{f_j},\ i_{o_{eq}}=\sum_{j=1}^{n}i_{o_j},\ v_{o_{eq}}=\sum_{j=1}^{n}\frac{v_{o_j}}{n}.\end{aligned}\tag{2.28}$$

Table 2.1: Converters parameters depicted in Figure 2.3b.

Parameters	Conv. 1	Conv. 2	Conv. 3	Conv. eq	Units
V_{in}	120	110	100	110	$[V]$
d	0.4250	0.4681	0.5300	0.4743	$[-]$
L_f	150	200	250	63.97	$[\mu H]$
R_f	0.6	0.4	0.2	0.0915	$[\Omega]$
C_f	1.5	2.0	1.0	3.4516	$[\mu F]$
L_o	2.0	3.0	1.0	0.5433	$[mH]$
R_o	0.1	0.4	0.2	0.0916	$[\Omega]$

$$v_{pcc} = 50\ [V]$$

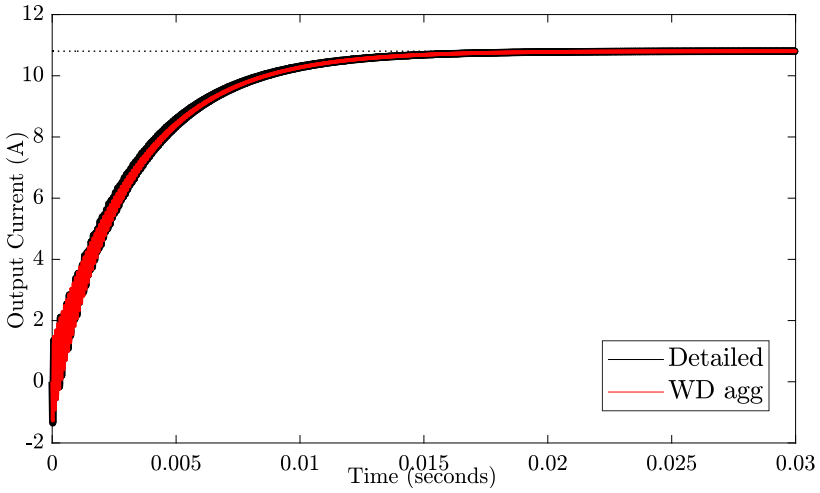

Figure 2.4: The output current comparison.

To validate the proposed WD agg approach a microgrid with three DC-DC buck converter as shown in Figure 2.3 and Table 2.1 parameters is modeled in details and aggregated with WD agg approach. The obtained parameters of the equivalent converter are listed in Table 2.1 and the output current comparison is presented in Figure 2.4. As Figure 2.4 demonstrates, the proposed WD agg model accurately mimics the dynamic behavior of the system form the PCC bus point of view.

2.3 WD agg Model of n Paralleled DC-DC Buck Converters with Controller

In this section, we utilize the WD aggregation approach to find an equivalent DC-DC buck converter for a setup comprising of n parallel DC-DC buck converters, as illustrated in Figure 2.7. Each individual converter generates an output voltage v_o, which

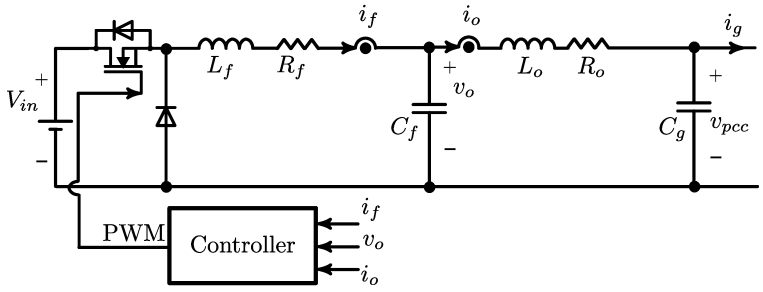

Figure 2.5: A single DC-DC buck converter with controller configuration.

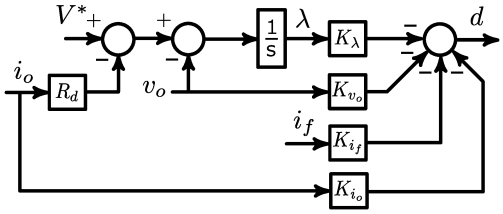

Figure 2.6: The control diagram of a DC-DC buck converter.

is regulated using the state-feedback controller depicted in Figure 2.6. To establish the equivalent buck converter, similar to the previous section, we begin by deriving the dynamic equations of the detailed system. Afterward, we ascertain appropriate weights for the states and inputs. The dynamic equations of each converter are then rephrased to describe the equivalent converter states. Finally, the dynamic equations of all n converters are consolidated, leading to the dynamic equation of the equivalent converter. Through a comparison between the resultant dynamic equations of the equivalent converter and those of a solitary converter, we can deduce the parameters of the equivalent converters. This procedure enables a proficient characterization of the parallel system as a singular equivalent converter.

2.3.1 Closed-loop model of a single converter

A single DC-DC buck converter with controller is demonstrated in Figure 2.5. As shown in Figure 2.5, the converter can be modeled similar to (2.18) as:

$$\begin{aligned} \frac{d}{dt}\mathbf{x}_{p_k} &= \mathbf{A}_{p_k}\mathbf{x}_{p_k} + \mathbf{B}_{p_k}\mathbf{u}_k + \mathbf{E}_{p_k}\mathbf{w}_k, \\ y_k &= \mathbf{C}_{p_k}\mathbf{x}_{p_k}, \end{aligned} \tag{2.29}$$

where:

$$\mathbf{x}_p = [\mathbf{x}_{LCL}^T,\ v_{pcc}]^T,\ \mathbf{x}_{LCL} = [i_f,\ v_o,\ i_o]^T,\ \mathbf{u} = [d],\ \mathbf{w} = [i_g],$$

$$\mathbf{A}_p = \begin{bmatrix} \mathbf{A}_{LCL} & \mathbf{A}_{pcc} \\ \mathbf{A}_o & 0 \end{bmatrix},\ \mathbf{A}_{LCL} = \begin{bmatrix} -\frac{R_f}{L_f} & -\frac{1}{L_f} & 0 \\ \frac{1}{C_f} & 0 & -\frac{1}{C_f} \\ 0 & \frac{1}{L_o} & \frac{R_o}{L_o} \end{bmatrix},$$

$$\mathbf{A}_{pcc} = \begin{bmatrix} 0 \\ 0 \\ -\frac{1}{L_o} \end{bmatrix},\ \mathbf{A}_o = \begin{bmatrix} 0 & 0 & \frac{1}{C_g} \end{bmatrix},$$
$$\mathbf{B}_p = \begin{bmatrix} \mathbf{B}_{LCL} \\ 0 \end{bmatrix}, \mathbf{B}_{LCL} = \begin{bmatrix} \frac{V_{in}}{L_f} \\ 0 \\ 0 \end{bmatrix},\ \mathbf{E}_p = \begin{bmatrix} O_{3\times1} \\ -\frac{1}{C_g} \end{bmatrix},\ \mathbf{C}_p = [0\ 1\ 0\ 0]. \tag{2.30}$$

To add a controller with an integral compensator as shown in Figure 2.6 to the derived plant model $(\mathbf{A}_p, \mathbf{B}_p, \mathbf{C}_p)$, the open-loop system can be derived as:

$$\frac{d}{dt}\begin{bmatrix} \mathbf{x}_{p_k} \\ \lambda_k \end{bmatrix} = \mathbf{A}_{c_k}\begin{bmatrix} \mathbf{x}_{p_k} \\ \lambda_k \end{bmatrix} + \mathbf{B}_{c_k}\begin{bmatrix} \mathbf{u}_k \\ 0 \end{bmatrix} + \mathbf{E}_{c_k}\begin{bmatrix} \mathbf{w} \\ 0 \end{bmatrix} + \begin{bmatrix} O_{4\times1} \\ 1 \end{bmatrix} V_k^*,$$
$$y_k = \mathbf{C}_{c_k}\begin{bmatrix} \mathbf{x}_{p_k} \\ \lambda_k \end{bmatrix}, \tag{2.31}$$

where:

$$\mathbf{A}_c = \begin{bmatrix} & \mathbf{A}_p & & O_{4\times1} \\ 0 & -1 & -R_d & 0 & 0 \end{bmatrix},\ \mathbf{B}_c = \begin{bmatrix} \mathbf{B}_p \\ 0 \end{bmatrix},\ \mathbf{E}_c = \begin{bmatrix} \mathbf{E}_p \\ 0 \end{bmatrix},\ \mathbf{C}_c = [\mathbf{C}_p\ 0]. \tag{2.32}$$

By solving the optimum equations for (name of the equation) equations with `lqr(ss(A_c,B_c,C_c,0),Q,1,0)` in MATLAB, the state-feedback gains can be found as $\mathbf{K}_b$ [85]. Hence, the closed-loop model can be derived as:

$$\frac{d}{dt}\begin{bmatrix} \mathbf{x}_{p_k} \\ \lambda_k \end{bmatrix} = (\mathbf{A}_{c_k} - \mathbf{B}_{c_k}\mathbf{K}_{b_k})\begin{bmatrix} \mathbf{x}_{p_k} \\ \lambda_k \end{bmatrix} + \mathbf{E}_{c_k}\begin{bmatrix} \mathbf{w} \\ 0 \end{bmatrix} + \begin{bmatrix} O_{4\times1} \\ 1 \end{bmatrix} V_k^*,$$
$$y_k = \mathbf{C}_{c_k}\begin{bmatrix} \mathbf{x}_{p_k} \\ \lambda_k \end{bmatrix}, \tag{2.33}$$

where:

$$\mathbf{K_b} = \begin{bmatrix} K_{i_f} & K_{v_o} & K_{i_o} & K_{v_{pcc}} & K_\lambda \end{bmatrix}. \tag{2.34}$$

2.3.2 Closed-loop detailed model of n paralleled converters

A system compromising n paralleled DC-DC buck converters with state-feedback controllers is demonstrated in Figure 2.7. As shown in Figure 2.7, each converter can be modeled as:

$$\frac{d}{dt}\mathbf{x}_{det} = (\mathbf{A}_{det} - \mathbf{B}_{det}\mathbf{K}_{det})\,\mathbf{x}_{det} + \mathbf{E}_{det}\mathbf{w} + \mathbf{T}_{det}\mathbf{r},$$
$$\mathbf{y} = \mathbf{C}_{det}\mathbf{x}_{det}, \tag{2.35}$$

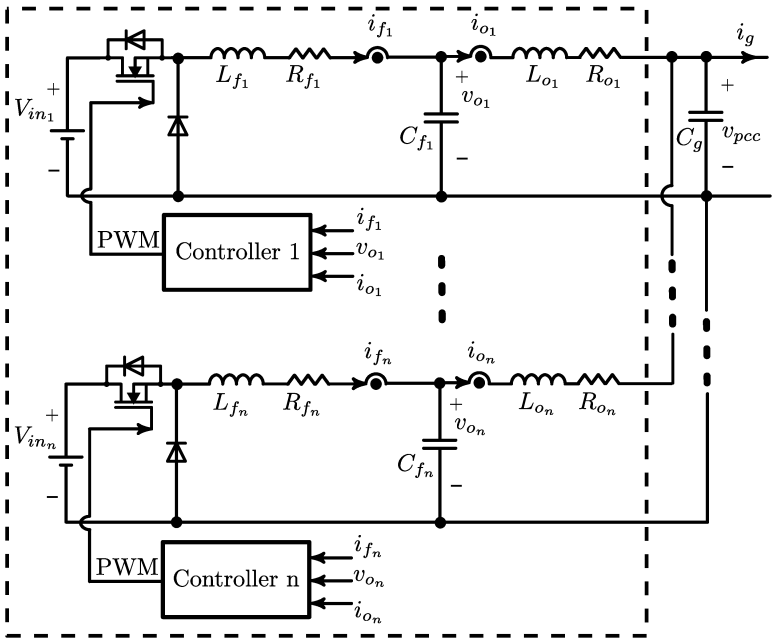

Figure 2.7: n paralleled DC-DC buck converters with state-feedback controllers.

where:

$$\mathbf{x}_{det} = \begin{bmatrix}\begin{bmatrix}\mathbf{x}_{LCL_1}^T & \lambda_1\end{bmatrix} & \cdots & \begin{bmatrix}\mathbf{x}_{LCL_n}^T & \lambda_n\end{bmatrix} & v_{pcc}\end{bmatrix}^T,\ \mathbf{w} = i_g,\ \mathbf{r} = \begin{bmatrix}V_1^* & \cdots & V_n^*\end{bmatrix}^T,$$

$$\mathbf{A}_{det} = \begin{bmatrix} \mathbf{A}_{cl_1} & \cdots & O_{4\times 4} & \begin{bmatrix}\mathbf{A}_{pcc_1}\\ 0\end{bmatrix} \\ \vdots & \ddots & & \vdots \\ O_{4\times 4} & \cdots & \mathbf{A}_{cl_n} & \begin{bmatrix}\mathbf{A}_{pcc_n}\\ 0\end{bmatrix} \\ \begin{bmatrix}\mathbf{A}_o & 0\end{bmatrix} & \cdots & \begin{bmatrix}\mathbf{A}_o & 0\end{bmatrix} & 0 \end{bmatrix},\ \mathbf{A}_{cl} = \begin{bmatrix} & \mathbf{A}_{LCL} & & 0 \\ & & & 0 \\ & & & 0 \\ 0 & -1 & -R_d & 0 \end{bmatrix},$$

$$\mathbf{B}_{det} = \begin{bmatrix} \begin{bmatrix}\mathbf{B}_{LCL_1}\\ 0\end{bmatrix} & \cdots & O_{4\times 1} \\ \vdots & \ddots & \vdots \\ O_{4\times 1} & \cdots & \begin{bmatrix}\mathbf{B}_{LCL_n}\\ 0\end{bmatrix} \\ & O_{3\times n} & \end{bmatrix},\ \mathbf{T}_{det} = \begin{bmatrix} \mathbf{T}_{cl} & \cdots & O_{4\times 1} \\ \vdots & \ddots & \vdots \\ O_{4\times 1} & \cdots & \mathbf{T}_{cl} \end{bmatrix},\ \mathbf{T}_{cl} = \begin{bmatrix}0\\0\\0\\1\end{bmatrix},$$

$$\mathbf{C}_{det} = \begin{bmatrix} \mathbf{C}_{cl} & \cdots & O_{1\times 4} & \\ \vdots & \ddots & \vdots & O_{n\times 1} \\ O_{1\times 4} & \cdots & \mathbf{C}_{cl} & \end{bmatrix},\ \mathbf{C}_{cl} = \begin{bmatrix}0 & 1 & 0 & 0\end{bmatrix},$$

$$\mathbf{K}_{det} = \begin{bmatrix} \mathbf{K}_{cl_1} & \cdots & O_{4\times 1} & \mathbf{K}_{Ig_1} \\ \vdots & \ddots & \vdots & \vdots \\ O_{4\times 1} & \cdots & \mathbf{K}_{cl_n} & \mathbf{K}_{Ig_n} \end{bmatrix},\ \begin{matrix}\mathbf{K}_{cl} = [K_{i_f}\ K_{v_o}\ K_{i_o}\ K_\lambda], \\ \mathbf{K}_{Ig} = [K_{i_g}].\end{matrix} \tag{2.36}$$

To find the steady-state parameters of the system which are being used as the weights in WD agg model derivation, $\frac{d}{dt}\mathbf{x}_{det} = 0$ yields:

$$\mathbf{X}_{det} = -(\mathbf{A}_{det} - \mathbf{B}_{det}\mathbf{K}_{det})^{-1}(\mathbf{E}_{det}\mathbf{w} + \mathbf{T}_{det}\mathbf{r}). \tag{2.37}$$

2.3.3 WD agg model of n paralleled converters

Consider n number of buck converters with dynamic state-space representation of (2.33). The contribution of each converter to the average of corresponding states and input can be defined as two $\mathbf{M}_k$ and $\mathbf{W}_k$ matrices, which:

$$\mathbf{x}_{c_k} = \mathbf{M}_k \sum_{j=1}^{n} \mathbf{x}_{c_j}/n,\ V_k^* = \mathbf{W}_k \sum_{j=1}^{n} V_j^*/n,\ \text{where: } \mathbf{x}_{c_k} = \begin{bmatrix} \mathbf{x}_p \\ \lambda \end{bmatrix}. \tag{2.38}$$

It is worth noting that $\mathbf{M}_k$ can be estimated as $\mathbf{M}_k \simeq n\mathbf{X}_{\mathbf{c_k}} / \left(\sum_{j=1}^{n} \mathbf{X}_{c_j}\right)$, where $\mathbf{X}_c$ can be found by (2.37). Now let's define the scaling matrix $\mathbf{P}_\mathbf{x}$ to find the scale of the equivalent corresponding states compare with the average of corresponding states as:

$$\mathbf{P}_\mathbf{x}\mathbf{x}_{c_{eq}} = \sum_{j=1}^{n} \mathbf{x}_{c_j}/n. \tag{2.39}$$

Based on the insight found in 2.1 derivations, the equivalent voltages can be define as the average of the corresponding voltages and the equivalent currents should be the summation of corresponding currents, i.e.:

$$\mathbf{P}_\mathbf{x} = \begin{bmatrix} 1/n & 0 & 0 & 0 & 0 \\ 0 & 1 & 0 & 0 & 0 \\ 0 & 0 & 1/n & 0 & 0 \\ 0 & 0 & 0 & 1 & 0 \\ 0 & 0 & 0 & 0 & 1 \end{bmatrix},\ V_{eq}^* = \sum_{i=1}^{n} V_j^*/n. \tag{2.40}$$

Now by substituting (2.40) into (2.33), each converter dynamic equations can be derived in terms of the equivalent states and input as:

$$\begin{gathered} \frac{d}{dt}\mathbf{M}_k\mathbf{P}_\mathbf{x}\mathbf{x}_{c_{eq}} = (\mathbf{A}_{c_k} - \mathbf{B}_{c_k}\mathbf{K}_{b_k})\,\mathbf{M}_k\mathbf{P}_\mathbf{x}\mathbf{x}_{c_{eq}} + \mathbf{E}_{c_k}\begin{bmatrix} \mathbf{w} \\ 0 \end{bmatrix} + \begin{bmatrix} O_{4\times 1} \\ 1 \end{bmatrix}\mathbf{W}_k V_{eq}^*, \\ y_k = \mathbf{C}_{c_k}\mathbf{M}_k\mathbf{P}_\mathbf{x}\mathbf{x}_{c_{eq}}. \end{gathered} \tag{2.41}$$

Now by summing n equations of (2.41), the equivalent aggregated dynamic system is obtained as:

$$\begin{aligned}\sum_{k=1}^{n}\mathbf{M}_k\mathbf{P}_{\mathbf{x}}\frac{d}{dt}\mathbf{x}_{c_{eq}} &= \sum_{k=1}^{n}\left(\mathbf{A}_{c_k}-\mathbf{B}_{c_k}\mathbf{K}_{b_k}\right)\mathbf{M}_k\mathbf{P}_{\mathbf{x}}\mathbf{x}_{c_{eq}}+\cdots\\ &\cdots+\sum_{k=1}^{n}\mathbf{E}_{c_k}\begin{bmatrix}\mathbf{w}\\0\end{bmatrix}+\begin{bmatrix}O_{4\times1}\\1\end{bmatrix}\sum_{k=1}^{n}\mathbf{W}_kV_{eq}^{*},\\ y_{eq} &= \sum_{k=1}^{n}\mathbf{C}_{c_k}\mathbf{M}_k\mathbf{P}_{\mathbf{x}}\mathbf{x}_{c_{eq}}.\end{aligned} \tag{2.42}$$

By rewriting (2.42) in the state-space form the equivalent system model can be derived as:

$$\begin{aligned}\frac{d}{dt}\mathbf{x}_{c_{eq}} &= \left(\mathbf{A}_{c_{eq}}-\mathbf{B}_{c_{eq}}\mathbf{K}_{b_{eq}}\right)\mathbf{x}_{c_{eq}}+\mathbf{E}_{c_{eq}}\begin{bmatrix}\mathbf{w}\\0\end{bmatrix}+\begin{bmatrix}O_{4\times1}\\1\end{bmatrix}V_{eq}^{*},\\ y_{eq} &= \mathbf{C}_{c_{eq}}\mathbf{x}_{c_{eq}},\end{aligned} \tag{2.43}$$

where:

$$\begin{aligned}\mathbf{A}_{c_{eq}}-\mathbf{B}_{c_{eq}}\mathbf{K}_{b_{eq}} &= \left(\sum_{k=1}^{n}\mathbf{M}_k\mathbf{P}_{\mathbf{x}}\right)^{-1}\sum_{k=1}^{n}\left(\mathbf{A}_{c_k}-\mathbf{B}_{c_k}\mathbf{K}_{b_k}\right)\mathbf{M}_k\mathbf{P}_{\mathbf{x}},\\ \mathbf{E}_{c_{eq}} = \left(\sum_{k=1}^{n}\mathbf{M}_k\mathbf{P}_{\mathbf{x}}\right)^{-1}\sum_{k=1}^{n}\mathbf{E}_{c_k},\ \mathbf{C}_{c_{eq}} &= \left(\sum_{k=1}^{n}\mathbf{M}_k\mathbf{P}_{\mathbf{x}}\right)^{-1}\sum_{k=1}^{n}\mathbf{C}_{c_k}\mathbf{M}_k\mathbf{P}_{\mathbf{x}}.\end{aligned} \tag{2.44}$$

2.4 Application of WD agg model in designing control parameters of n paralleled DC-DC buck converters

In this section, the WD aggregation model is utilized, consisting of n parallel DC-DC buck converters linked to a resistive load through a PI transmission line. The aim is to achieve the optimal control parameters for each converter within the intricate system. To accomplish this objective, the approach involves initial design of the WD aggregation model using LQR parameter designing technique, followed by the determination of control parameters for the detailed system. This determination takes into account the specific contribution of each unit to the overall system performance.

2.4.1 Detailed model of the microgrid

A system compromising n paralleled DC-DC buck converters with state-feedback controllers connected to resistive load via a PI transmission line is demonstrated in

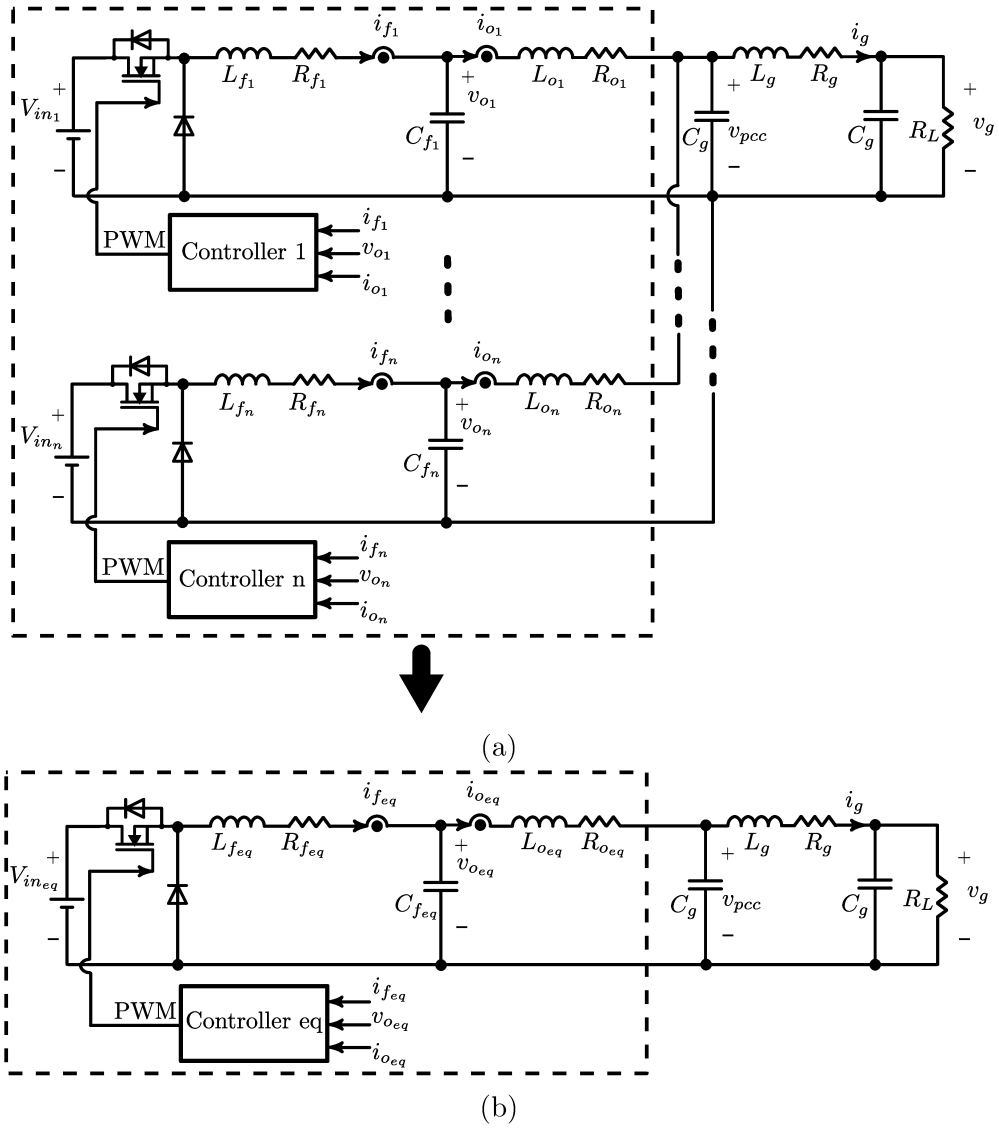

Figure 2.8: a) n paralleled DC-DC buck converters connected to a resistive load via a PI transmission line, b) The equivalent single DC-DC buck converter.

Figure 2.8a. As shown in Figure 2.8a, each converter can be modeled as:

$$\begin{aligned} \frac{d}{dt}\mathbf{x}_{det} &= \left(\mathbf{A}_{det} - \mathbf{B}_{det}\mathbf{K}_{det}\right)\mathbf{x}_{det} + \mathbf{T}_{det}\mathbf{r}, \\ \mathbf{y} &= \mathbf{C}_{det}\mathbf{x}_{det}, \end{aligned} \tag{2.45}$$

where:

$$\mathbf{x}_{det} = \begin{bmatrix} \begin{bmatrix}\mathbf{x}_{LCL_1}^T & \lambda_1\end{bmatrix} & \cdots & \begin{bmatrix}\mathbf{x}_{LCL_n}^T & \lambda_n\end{bmatrix} & v_{pcc} & i_g & v_g \end{bmatrix}^T, \ \mathbf{r} = \begin{bmatrix} V_1^* & \cdots & V_n^* \end{bmatrix}^T,$$

$$\mathbf{A}_{det} = \begin{bmatrix} \mathbf{A}_{cl_1} & \cdots & O_{4\times4} & \begin{bmatrix}\mathbf{A}_{pcc_1}\\ O_{1\times3}\end{bmatrix} \\ \vdots & \ddots & & \vdots \\ O_{4\times4} & \cdots & \mathbf{A}_{cl_n} & \begin{bmatrix}\mathbf{A}_{pcc_n}\\ O_{1\times3}\end{bmatrix} \\ \begin{bmatrix}\mathbf{A}_o & O_{3\times1}\end{bmatrix} & \cdots & \begin{bmatrix}\mathbf{A}_o & O_{3\times1}\end{bmatrix} & \mathbf{A}_{PI} \end{bmatrix},\ \mathbf{A}_{cl} = \begin{bmatrix} & & & 0 \\ & \mathbf{A}_{LCL} & & 0 \\ & & & 0 \\ 0 & -1 & 0 & 0 \end{bmatrix},$$

$$\mathbf{B}_{det} = \begin{bmatrix} \begin{bmatrix}\mathbf{B}_{LCL_1}\\ 0\end{bmatrix} & \cdots & O_{4\times1} \\ \vdots & \ddots & \vdots \\ O_{4\times1} & \cdots & \begin{bmatrix}\mathbf{B}_{LCL_n}\\ 0\end{bmatrix} \\ & O_{3\times n} & \end{bmatrix},\ \mathbf{T}_{det} = \begin{bmatrix} \mathbf{T}_{cl} & \cdots & O_{4\times1} \\ \vdots & \ddots & \vdots \\ O_{4\times1} & \cdots & \mathbf{T}_{cl} \\ & O_{3\times n} & \end{bmatrix},\ \mathbf{T}_{cl} = \begin{bmatrix}0\\0\\0\\1\end{bmatrix},$$

$$\mathbf{C}_{det} = \begin{bmatrix} \mathbf{C}_{cl} & \cdots & O_{1\times4} & \\ \vdots & \ddots & \vdots & O_{n\times3} \\ O_{1\times4} & \cdots & \mathbf{C}_{cl} & \end{bmatrix},\ \mathbf{C}_{cl} = \begin{bmatrix}0 & 1 & 0 & 0\end{bmatrix}, \tag{2.46}$$

$$\mathbf{K}_{det} = \begin{bmatrix} \mathbf{K}_{cl_1} & \cdots & O_{4\times1} & \mathbf{K}_{PI_1} \\ \vdots & \ddots & \vdots & \vdots \\ O_{4\times1} & \cdots & \mathbf{K}_{cl_n} & \mathbf{K}_{PI_n} \end{bmatrix},\ \begin{matrix}\mathbf{K}_{cl} = [K_{i_f}\ K_{v_o}\ K_{i_o}\ K_\lambda], \\ \mathbf{K}_{PI} = [K_{v_{pcc}}\ K_{i_g}\ K_{v_g}].\end{matrix}$$

It is worth noting that the droop coefficients are considered to be zero, i.e. $R_d = 0$, $\mathbf{A}_{PI}$ is introduced, and $\mathbf{A}_{pcc}$, $\mathbf{A}_o$ are modified as follows:

$$\mathbf{A}_{pcc} = \begin{bmatrix} 0 & 0 & 0 \\ 0 & 0 & 0 \\ -\frac{1}{L_o} & 0 & 0 \end{bmatrix},\ \mathbf{A}_o = \begin{bmatrix} 0 & 0 & \frac{1}{C_g} \\ 0 & 0 & 0 \\ 0 & 0 & 0 \end{bmatrix},\ \mathbf{A}_{PI} = \begin{bmatrix} 0 & -\frac{1}{C_g} & 0 \\ \frac{1}{L_g} & -\frac{R_g}{L_g} & -\frac{1}{L_g} \\ 0 & \frac{1}{C_g} & -\frac{1}{C_g R_L} \end{bmatrix}. \tag{2.47}$$

To find the steady-state parameters of the system which are being used as the weights in WD agg model derivation, $\frac{d}{dt}\mathbf{x}_{det} = 0$ yields:

$$\mathbf{X}_{det} = -(\mathbf{A}_{det} - \mathbf{B}_{det}\mathbf{K}_{det})^{-1}\mathbf{T}_{det}\mathbf{r}. \tag{2.48}$$

2.4.2 Design control parameters using WD agg model

To find the control parameters of the detailed system, first the equivalent controller of WD agg model should be designed. Then based on the obtained equivalent control parameters, the detailed system control parameters can be found based on units' contribution. To add a controller with an integral compensator as shown in Figure 2.6 to the equivalent WD agg model $(\mathbf{A}_{p_{eq}}, \mathbf{B}_{p_{eq}}, \mathbf{C}_{p_{eq}})$ derived in (2.27), the open-loop system can be derived as:

$$\begin{aligned} \frac{d}{dt}\begin{bmatrix}\mathbf{x}_{p_{eq}}\\ \lambda_{eq}\end{bmatrix} &= \mathbf{A}_{c_{eq}}\begin{bmatrix}\mathbf{x}_{p_{eq}}\\ \lambda_{eq}\end{bmatrix} + \mathbf{B}_{c_{eq}}\begin{bmatrix}\mathbf{u}_{eq}\\ 0\end{bmatrix} + \begin{bmatrix}O_{6\times1}\\ 1\end{bmatrix}V^*_{eq}, \\ y_{eq} &= \mathbf{C}_{c_{eq}}\begin{bmatrix}\mathbf{x}_{p_{eq}}\\ \lambda_{eq}\end{bmatrix}, \end{aligned} \tag{2.49}$$

where:

$$\mathbf{A}_{c_{eq}} = \begin{bmatrix} & \mathbf{A}_{p_{eq}} & & O_{6\times1} \\ 0 & -1 \; 0 \; 0 \; 0 \; 0 & & 0 \end{bmatrix}, \; \mathbf{B}_{c_{eq}} = \begin{bmatrix} \mathbf{B}_{p_{eq}} \\ 0 \end{bmatrix}, \; \mathbf{C}_{c_{eq}} = [\mathbf{C}_{p_{eq}} \; 0]. \tag{2.50}$$

By finding the optimum gains for the associated algebraic Riccati equation with `lqr(ss (A_ceq,B_ceq,C_ceq,0),Q,1,0)` in MATLAB, the state-feedback gains can be found as $\mathbf{K}_{eq}$, thus, the closed-loop model can be derived as:

$$\begin{gathered} \frac{d}{dt}\begin{bmatrix} \mathbf{x}_{p_{eq}} \\ \lambda_{eq} \end{bmatrix} = \left(\mathbf{A}_{c_{eq}} - \mathbf{B}_{c_{eq}}\mathbf{K}_{eq}\right)\begin{bmatrix} \mathbf{x}_{eq} \\ \lambda_{eq} \end{bmatrix} + \begin{bmatrix} O_{6\times1} \\ 1 \end{bmatrix} V_{eq}^{*}, \\ y_{eq} = \mathbf{C}_{c_{eq}}\begin{bmatrix} \mathbf{x}_{p_{eq}} \\ \lambda_{eq} \end{bmatrix}, \end{gathered} \tag{2.51}$$

where:

$$\mathbf{K}_{eq} = \begin{bmatrix} K_{i_{f_{eq}}} & K_{v_{o_{eq}}} & K_{i_{o_{eq}}} & K_{v_{pcc_{eq}}} & K_{i_{g_{eq}}} & K_{v_{g_{eq}}} & K_{\lambda_{eq}} \end{bmatrix}. \tag{2.52}$$

To find the detailed system control parameters, based on 2.44 it can be concluded that:

$$\mathbf{B}_{c_{eq}}\mathbf{K}_{eq} = \left(\sum_{k=1}^{n}\mathbf{M}_k\mathbf{P}_{\mathbf{x}}\right)^{-1}\sum_{k=1}^{n}\mathbf{B}_{c_k}\mathbf{K}_{f_k}\mathbf{M}_k\mathbf{P}_{\mathbf{x}}. \tag{2.53}$$

Given the equation (2.53), the task involves determining $7n$ unknown variables, while having only n equations at hand. As a result, there exists a possibility of infinite solutions for the control parameters. To identify the optimal solution, we resort to numerical methods and solve the subsequent equation set. The process commences with initial values of $\mathbf{K}_{b_k}$ for $k = 1 : n$, and iterates until the value of ϵ becomes lower than a predetermined target error.

$$\text{Equations Sol: } \left\{\mathbf{B}_{c_{eq}}\mathbf{K}_{eq} - \left(\sum_{k=1}^{n}\mathbf{M}_k\mathbf{P}_{\mathbf{x}}\right)^{-1}\sum_{k=1}^{n}\mathbf{B}_{c_k}\mathbf{K}_{f_k}\mathbf{M}_k\mathbf{P}_{\mathbf{x}} < \epsilon\mathbf{J}\right\}, \tag{2.54}$$

where $\mathbf{J}$ is matrix of ones. The aforementioned goal can be achieved by using `fsolve(Equations Sol,[Kb(1:n)], 'Algorithm','levenberg-marquardt')` in MATLAB.

To demonstrate the practical applications of the WD aggregation approach in the design of control parameters for complex systems, this study focuses on a setup consisting of three parallel DC-DC buck converters connected to a resistive load through a PI transmission line. This configuration is illustrated in Figure 2.8, while the specific system parameters are provided in Table 2.2. Individually, each converter is meticulously designed to achieve the desired performance, as evidenced by the results shown

Table 2.2: Converters parameters used in the designing study utilizing WD agg model.

Parameters	Conv. 1	Conv. 2	Conv. 3	Units
V_{in}	100	100	100	$[V]$
L_f	1.5	2.0	2.5	$[mH]$
R_f	0.6	0.4	0.2	$[\Omega]$
C_f	1.5	2.0	1.0	$[\mu F]$
L_o	2.0	3.0	1.0	$[mH]$
R_o	0.1	0.4	0.2	$[\Omega]$

$v_{pcc} = 50\ [V],\ R_g = 0.3\ [\Omega],\ L_g = 1.5\ [mH],\ C_g = 2.5\ [mF],\ R_L = 20\ [\Omega]$

Table 2.3: Under-designed control parameters.

Parameters	K_{i_f}	K_{v_o}	K_{i_o}	K_λ
Conv 1	9.9903	0.0592	-0.0028	-89.4427
Conv 2	9.9904	-0.0378	-0.0062	-89.4427
Conv 3	9.9988	0.02812	-0.0035	-89.4427

in Figure 2.9a and 2.10, along with the corresponding control parameters detailed in Table 2.3. However, a notable overshoot of 20% is observed in the output voltage behavior of all converters. This phenomenon is attributed to interactions between the converters that were not considered in the isolated design approach. To address this issue, a proposed WD aggregation model is compared to the responses of the systems that were individually designed. This comparison is depicted in Figure 2.9a and 2.10. Remarkably, the proposed WD aggregation model precisely and effectively replicates the undesired output voltage behavior, underscoring its efficacy in simulating the dynamic performance of the system. The proposed WD aggregation model, as defined in equation (2.49), is now employed to configure the system for achieving the intended performance, as illustrated in Figure 2.9b and 2.10. The control parameters of the detailed system are obtained through an optimization procedure detailed in section 2.4.2, and the resultant parameters are presented in Table 2.4. Figure 2.9b and 2.10 showcase the output voltage behavior of all converters, displaying the sought-after performance for each individual unit. This accomplishment can be attributed to the WD aggregation model, which considers the individual contributions of all converters with their respective weights during the design process. This approach effectively addresses the interactions among the converters and ensures the realization of the desired performance.

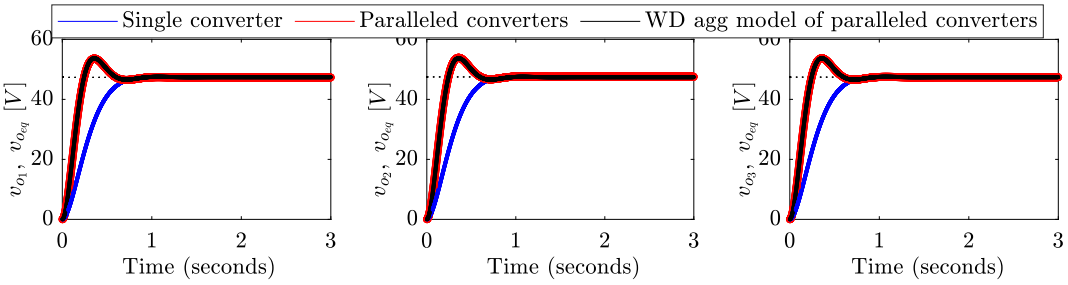

(a) Under-designed system.

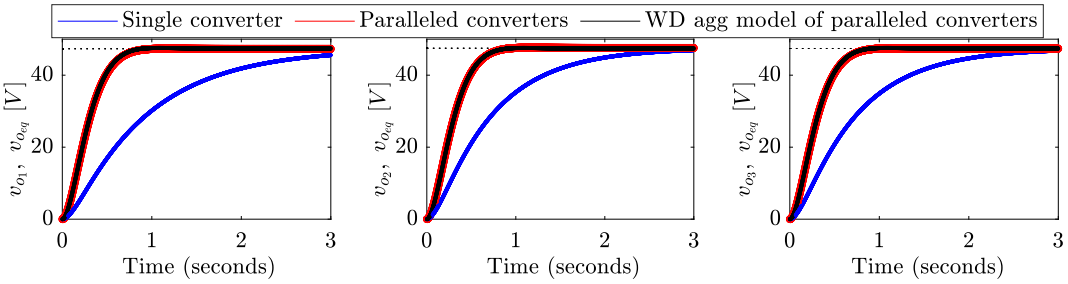

(b) Well-desigend system with the help of WD agg model.

Figure 2.9: a) Under-designed system, b) Well-desigend system with the help of WD agg model.

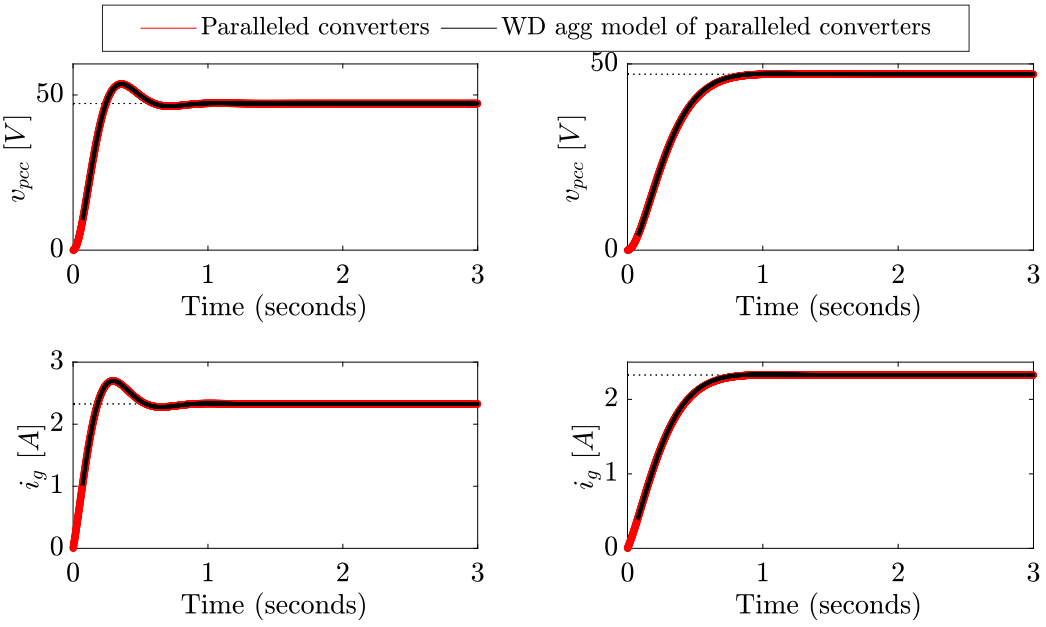

Figure 2.10: Under-designed and well-designed systems.

Table 2.4: Well-designed control parameters.

Parameters	K_{i_f}	K_{v_o}	K_{i_o}	K_λ
Conv Eq	10.0000	0.4505	-0.0008	-89.4427
Conv 1	34.6605	1.6844	-0.0010	-89.4427
Conv 2	27.2006	1.1862	-0.0050	-89.4427
Conv 3	27.4259	1.0052	-0.0022	-89.4427

2.5 Validation of WD agg Model in Dynamic Behavior and Sensitivity Analyses of DC microgrids with CPL

To validate and demonstrate the application of WD agg model found as (2.44) in the previous section a system with three paralleled DC-DC buck converters as shown in Figure 2.11a with Table 2.5 parameters is studied under various scenarios. A Constant Power Load (CPL) is chosen as the system load to make system conditions more challenging. The system detailed and WD agg models are found as explained the previous sections and compared to show the accuracy and application of the proposed approach. Furthermore, the proposed model also is compared with two other existing modeling approach as Tahim [39] and MTS [86, 87] to show the superiority of the proposed method compared to existing modeling approaches.

Figure 2.12 shows a CPL configuration, where it can be modeled by its linearized current equation for a given power P_{cpl} and voltage V_{pcc} operating point [88] as:

$$i_g = \frac{-P_{cpl}}{{V_{pcc}}^2} v_{pcc} + \frac{2P_{cpl}}{V_{pcc}}, \tag{2.55}$$

where v_{pcc} and i_g are the CPL input voltage and current, respectively . Eq. (2.55) indicates that a CPL can be modeled by a negative resistance $R_{cpl} = -{V_{pcc}}^2/P_{cpl}$ parallel with a constant current source $I_{cpl} = 2P_{cpl}/V_{pcc}$ as shown in Figure 2.11. Therefore, the dynamic equation of the CPL input capacitor C_g can be found as:

$$C_g \frac{d}{dt} v_{pcc} = \sum_{j=1}^{n} i_{o_j} - I_{cpl} - \frac{v_{pcc}}{R_{cpl}}. \tag{2.56}$$

Therefore, (2.35) can be modified accordingly to represents the system with a CPL load.

To assess the proposed method throughout different frequencies, the bode diagrams of the detailed model, WD agg model, MTS, and Tahim model are plotted in Fig-

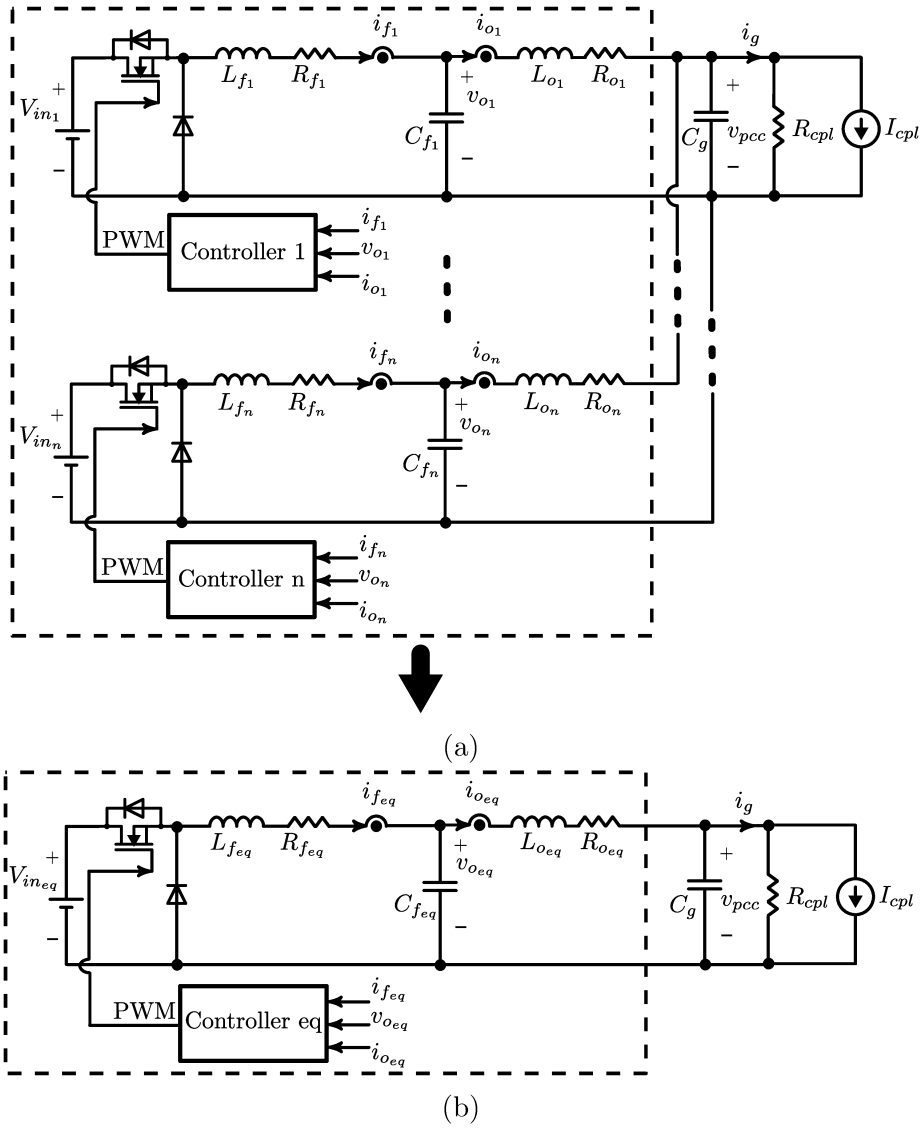

Figure 2.11: a) n paralleled DC-DC buck converters connected to a CPL, b) The equivalent single DC-DC buck converter.

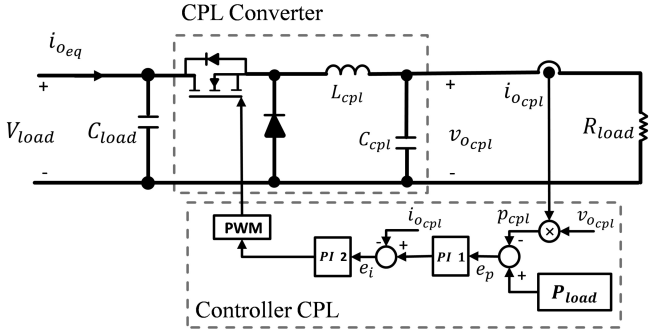

Figure 2.12: CPL converter and controller.

Table 2.5: The studied system specifications.

Parameter	Value	Parameter	Value
$V_{pcc}(V)$	80	R_{load} (Ω)	16
P_{load} (W)	200	C_{load} (μF)	390
V_{in_1}, V_{in_2}, V_{in_3} (V)	100	R_{o_1}, R_{o_2}, R_{o_3} (Ω)	0.163, 0.113, 0.118
L_{o_1}, L_{o_2}, L_{o_3} (mH)	1.2, 1, 0.9	L_{f_1}, L_{f_2}, L_{f_3} (mH)	2.2, 1.8, 1.9
C_{f_1}, C_{f_2}, C_{f_3} (μF)	2.3, 2.7, 2.5	R_{d_1}, R_{d_2}, R_{d_3}	0.6, 1.35, 0.7
k_{λ_1}, k_{λ_2}, k_{λ_3}	0.08	$k_{i_{f_1}}$, $k_{i_{f_2}}$, $k_{i_{f_3}}$	0.1478
$k_{v_{o_1}}$, $k_{v_{o_2}}$, $k_{v_{o_3}}$	0.0012	$k_{i_{o_1}}$, $k_{i_{o_2}}$, $k_{i_{o_3}}$	-0.1213
L_{cpl} (mH)	2.2	C_{cpl} (μF)	2.5
k_{PI_1}	P=0.0005, I=0.05	k_{PI_2}	P=0.1, I=1

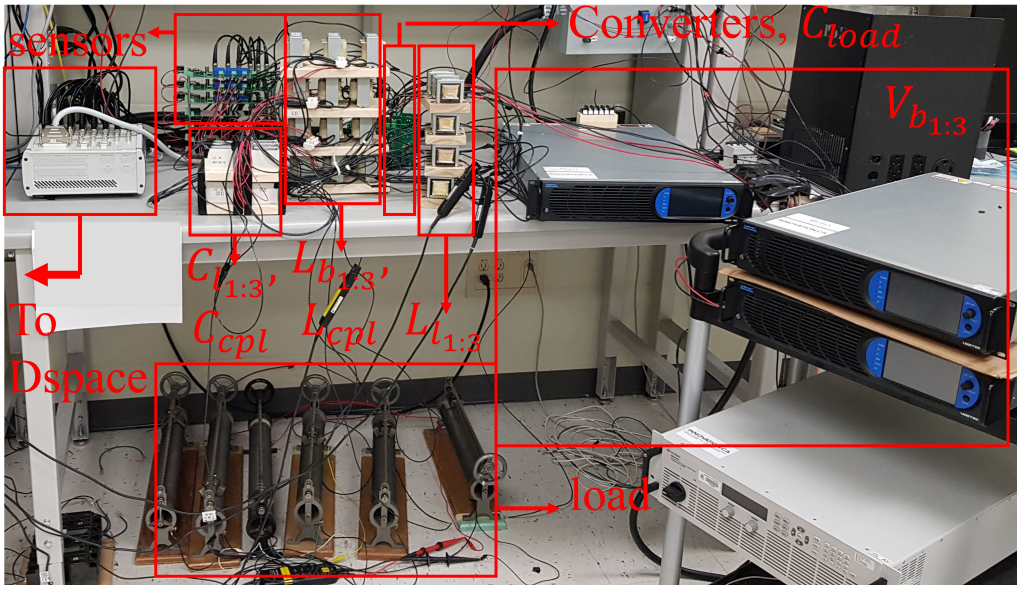

Figure 2.13: Experimental setup of the three parallel buck converters connected to a CPL.

ure 2.14 for both open-loop and closed-loop systems. Figure 2.14 only presents the closed-loop response of MTS and Tahim model because an ideal voltage source and an impedance are considered as the converter and its corresponding controller in MTS and Tahim model. Figure 2.14 demonstrates the superiority of WD agg model in mimicking the frequency response of the detailed model compared to the other existing models. The rest of the results are discussed in the following two parts separately, where they validate the proposed WD agg model in stability analyses and mimicking the dynamic behavior of the detailed system. The system parameters can be found in Table 2.5.

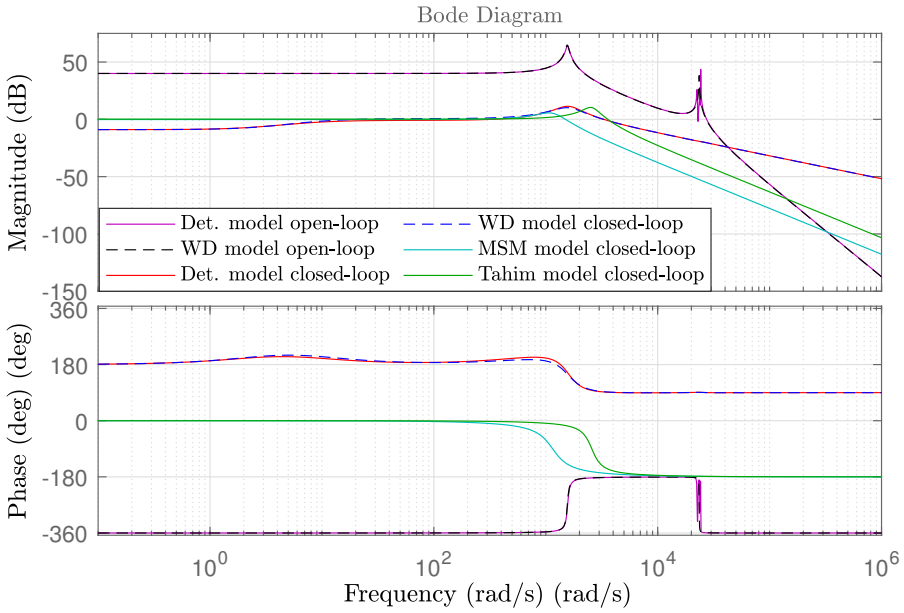

Figure 2.14: Bode diagram comparison of the Detailed model, WD agg model, MTS model, and Tahim model.

2.5.1 System stability and eigenvalue analysis

Controller parameters can significantly impact the system stability; therefore, the trajectory of the closed-loop eigenvalues of the system with variation of $k_{i_{f_j}}$ and $k_{i_{o_j}}$ values are plotted in Figure 2.15b and Figure 2.15d, respectively. Figure 2.15b shows the trajectory of the eigenvalues of the closed-loop system with $k_{i_{f_j}}$ 0.05 to 0.3, and it reveals that the system becomes stable for $k_{i_{f_j}}$ values greater than 0.123 for both the detailed model and WD agg model. Likewise, the trajectory of the closed-loop eigenvalues of the system with $k_{i_{o_j}}$ to -0.4 is plotted in Figure 2.15d. Considering both the detailed and WD agg models, Figure 2.15d shows that the system becomes unstable at $k_{i_{o_j}}$ values smaller than -0.145. Hence, the proposed aggregated model can be used to tune the gain of the converters and to achieve stable and optimal performance. Similarly, the impact of other system parameters on stability can also be explored. For instance, Figure 2.16 shows the trajectory of closed-loop eigenvalues of the system with $C_g = 1\mu F$ to $1mF$. As shown, the system moves toward instability if C_g is smaller than $37.5\mu F$. Thus, the result of Figure 2.16 can be used to develop a suitable filter for the load. The eigenvalue trajectory of WD agg model, presented in Figure 2.15, correlates with the corresponding eigenvalue trajectory of the detailed model, which validates the accuracy of WD agg model in the eigenvalue analysis.

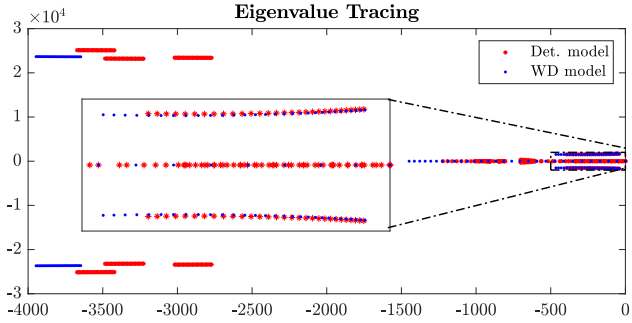

(a) $k_{i_{\lambda_j}} = 0.001$ to $k_{i_{\lambda_j}} = 15$.

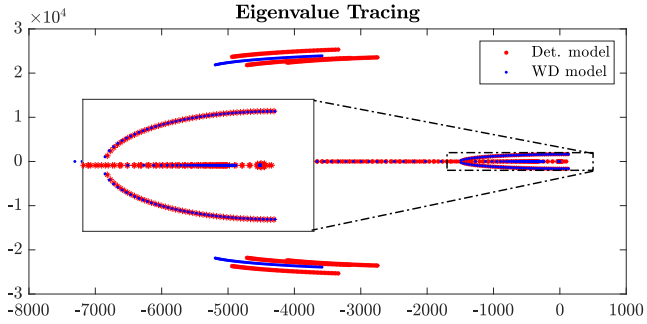

(b) $k_{i_{f_j}} = 0.11$ to $k_{i_{f_j}} = 0.3$.

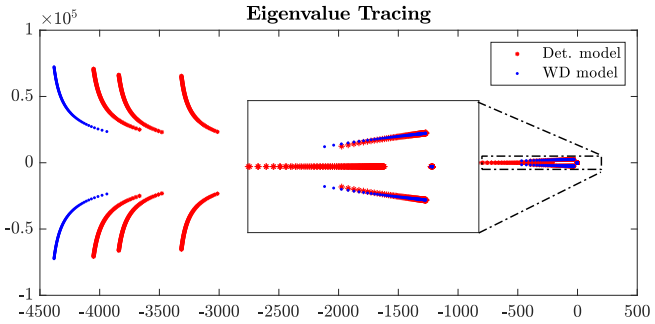

(c) $k_{v_{o_j}} = 0.001$ to $k_{v_{o_j}} = 0.2$.

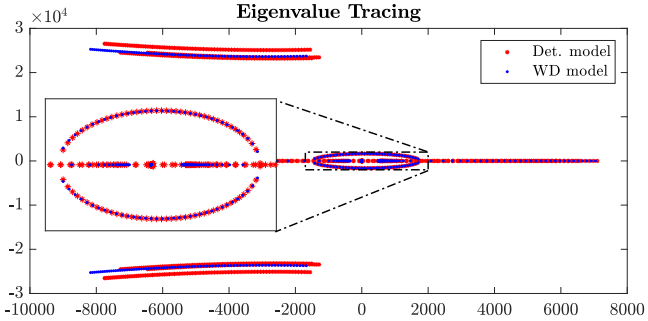

(d) $k_{i_{o_j}} = -0.001$ to $k_{i_{o_j}} = -0.4$.

Figure 2.15: Closed-loop eigenvalues comparison of the detailed and the proposed WD agg models for various control parameters.

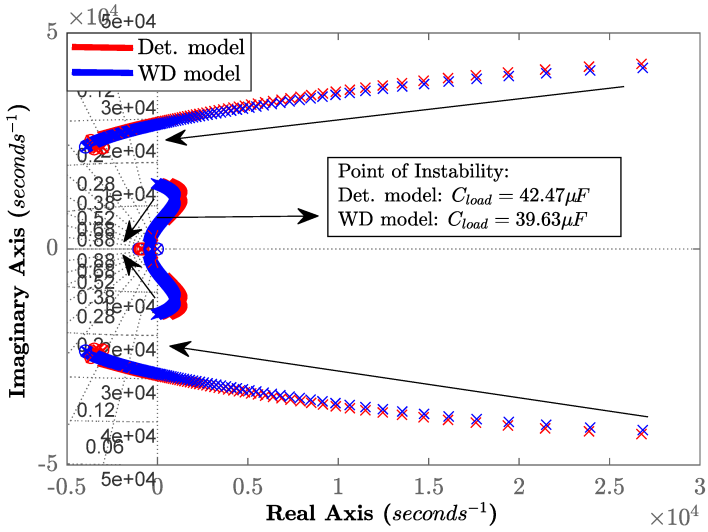

Figure 2.16: Closed-loop eigenvalues comparison of the detailed and the proposed WD agg models for $C_g = C_{load} = 1\mu F$ to $1mF$.

2.5.2 Experminetal steady-state and transient behavior comparison

To evaluate the performance of the proposed WD agg model, an islanded DC microgrid with three parallel buck converters connected to a CPL is built. System parameters are defined in Table 2.5, and the system is shown in Figure 2.13. The experimental setup part numbers can be found in Table 2.6. Experimental and simulation results of the steady-state and transient behavior of the output current and voltage of the parallel buck converters are plotted in Figure 2.17 to 2.22. Figure 2.17a demonstrates the experimental and simulation results of the output current and voltage at the start-up and load power change from 200W to 250W at t=7.8s for the detailed model and simulated WD agg model. To evaluate WD agg model performance, the aforementioned steady-state and transient behavior of the simulated detailed model and WD agg model is compared with two existing modeling approaches: MTS and Tahim models in Figure 2.17b. By considering equal power generation and collector line parameters, a Tahim model is proposed in [39] to divide the system into smaller clusters, where each cluster is modeled based on its equivalent Thevenin voltage, and impedance. Furthermore, Multi-Time Scale (MTS) model is proposed in [86, 87] to improve the model accuracy considering unequal parameters. MTS clusters converters with the same ratio of droop coefficients to the line inductance and models each cluster similar to the Thevenin-based approach. As shown, the output currents of the MTS and Tahim models are discontinuous due to modeling the converters with a

Table 2.6: Experimental part numbers and f_{sw}.

Device	Part Number
Controller	dSpace MicroLabBox
Switches	STF23N80K5
Current Sensors	TMCS1101A1UQDRQ1
Voltage Sensors	LV 25-P
DC source 1	Chroma 62050H-600S
DC source 2	Keysight N8937APV
DC source 3	Chroma 62020H-150S

$f_{sw} = 20$ [kHz]

voltage source and an impedance. Figure 2.17 indicates that WD agg model is more accurate than the MTS and Tahim models at reproducing the behavior of the detailed model in steady-state and during transients at the start-up duration and load power changes. To evaluate the behavior of WD agg model in an unstable condition, the detailed and WD agg model are simulated with $C_g = 1\mu F$ at the start-up shown in Figure 2.18. As shown in Figure 2.16, system becomes unstable for C_g values smaller than 37.5μF. Figure 2.18 shows that WD agg model resembles the steady-state and transient behavior of the detailed model in unstable conditions. To assess WD agg model with different response times through load power changes from 200W to 250W and from 250W to 300W, where Table 2.8 provides the units steady-state current sharing values and CPL voltage regulation, and the steady-state and transient results of the experimental and simulation detailed model are compared to the respective WD agg model results in Figure 2.19 for $k_{\lambda_j} = 0.04,\ 0.32$ with $j = 1,\ 2,\ 3$. The results obtained with various k_{λ_j} values indicate that higher gains lead the system toward a faster response but lower stability margin. As shown in Figure 2.17 to 2.19, the simulated WD agg model results match the detailed model experimental and simulation results at the start-up and with various k_{λ_j} and C_g parameters when the controller parameters of paralleled converters are the same.

To study the behavior of the proposed WD agg model for the system with unequal control parameters, the updated system parameters outlined in Table 2.7 are used in experiments 4 to 6. In the fourth experiment, unequal $k_{i_{f_j}}, k_{v_{o_j}}$, and $k_{i_{o_j}}$ parameters is used for the paralleled converters, and the results are shown in Figure 2.20a for the load power change from 200W to 250W at t=8.5s. As shown in Figure 2.19, k_{λ_j} affects the response behavior of the jth converter output voltage more significantly because k_{λ_j} controls the tracking error of the system. Thus, the steady-state and transient

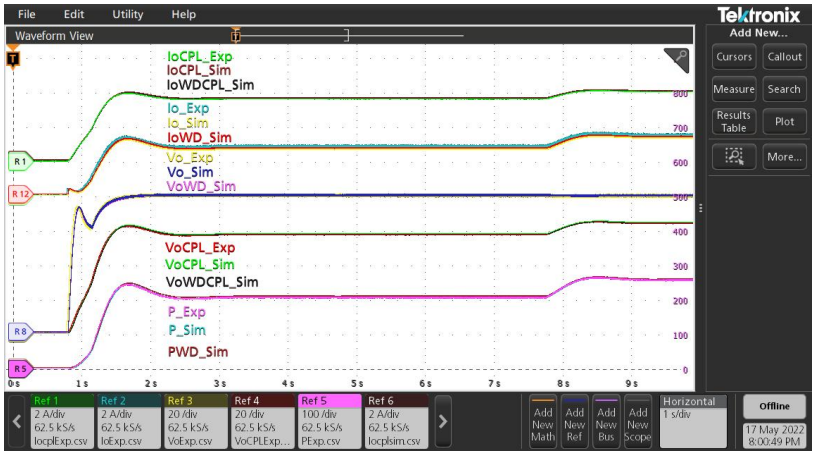

(a)

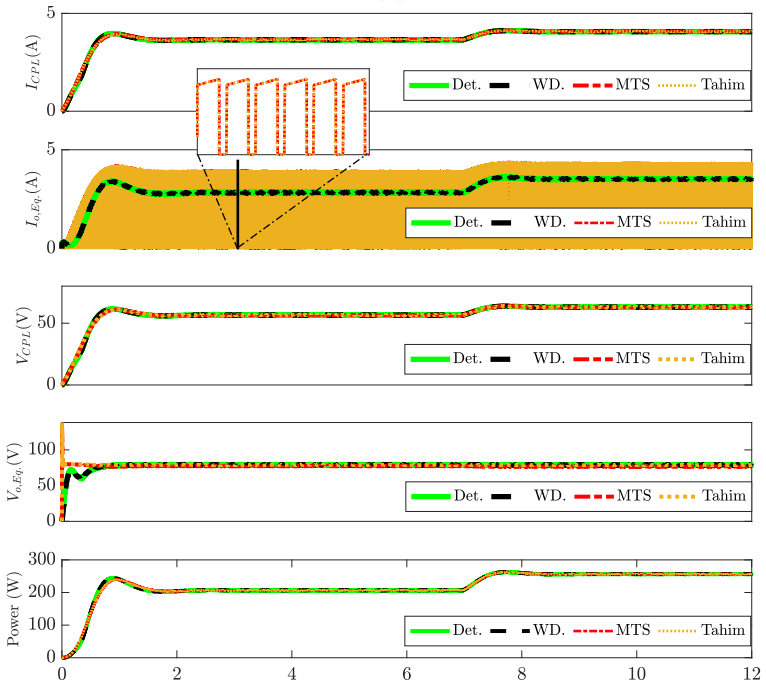

(b)

Figure 2.17: Exp. 1: Steady-state and transient behavior comparison of a) experimental and simulation detailed model and WD agg model b) simulation detailed model, WD agg model, MTS model, and Tahim model at the start-up and load power changes from 200W to 250W.

Table 2.7: Experimental parameters for Exp. 4-6.

	Exp. 4	*Exp.* 5	*Exp.* 6
$V_{in_1},\ V_{in_2},\ V_{in_3}$	100	100	120, 110, 100
$k_{\lambda_1},\ k_{\lambda_2},\ k_{\lambda_3}$	0.08	0.08, 0.12, 0.096	0.08, 0.11, 0.096
$k_{i_{f_1}},\ k_{i_{f_2}},\ k_{i_{f_3}}$	0.1692, 0.1854, 0.1525		
$k_{v_{o_1}},\ k_{v_{o_2}},\ k_{v_{o_3}}$	0.0008, 0.0012, 0.0010		
$k_{i_{o_1}},\ k_{i_{o_2}},\ k_{i_{o_3}}$	-0.1233, -0.1437, -0.1381		

Table 2.8: Voltage regulation at CPL and current sharing of each unit.

$P_{cpl}[W]$	200	250	300
$I_{o_1}[A]$	1.155	1.437	1.742
$I_{o_2}[A]$	0.976	1.211	1.448
$I_{o_3}[A]$	0.562	0.690	0.833
$V_{cpl}[V]$	78.83	78.62	78.43
VR[%]	1.48	1.75	2.00

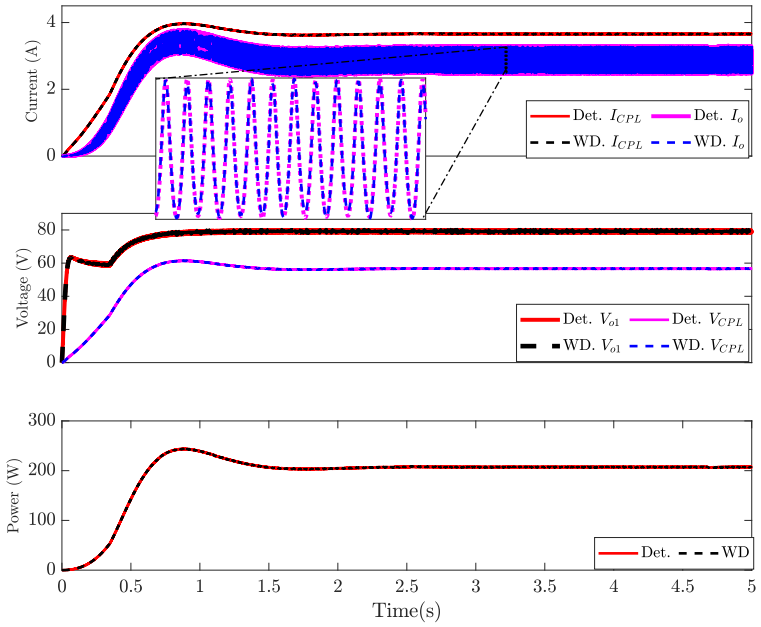

Figure 2.18: Steady-state and transient behavior of the simulation detailed and WD agg models at the start-up with $C_g = 1\mu F$.

behavior of the load voltage with unequal k_{λ_j} is plotted in Figure 2.20b. In Exp. 5, all the parallel converters' control parameters are unequal, and the results are shown for the following load power changes from 200W to 250W at t=8.5s and from 250W to 300W at t=14.5s. Figure 2.20 suggests that the steady-state and transient results

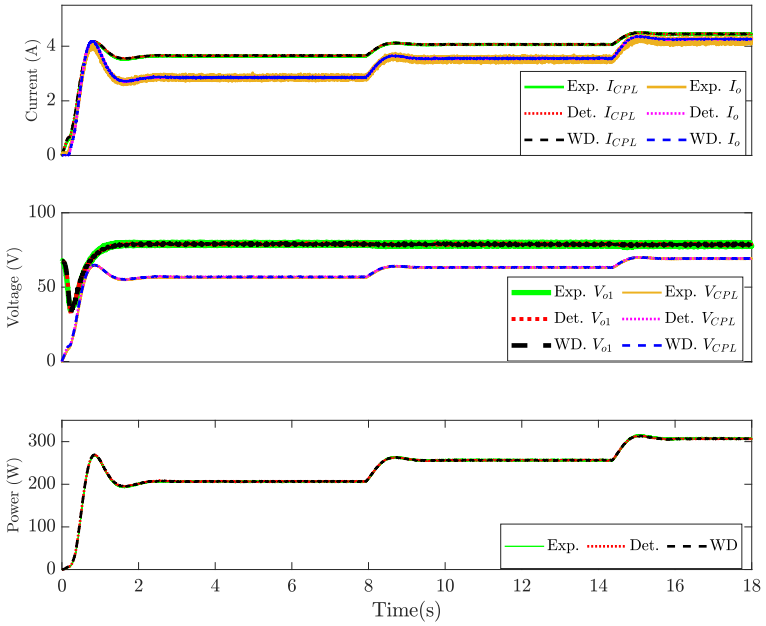

(a) $k_{\lambda_1} = k_{\lambda_2} = k_{\lambda_3} = 0.04$.

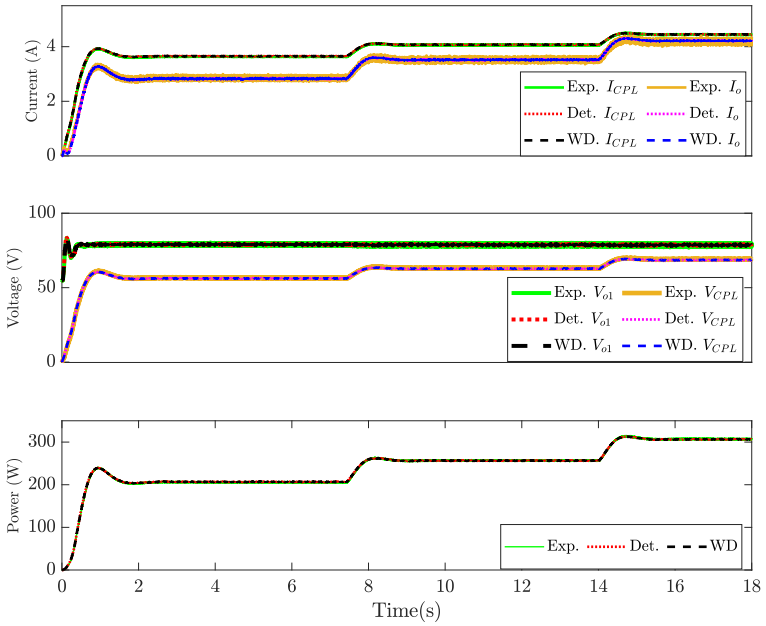

(b) $k_{\lambda_1} = k_{\lambda_2} = k_{\lambda_3} = 0.32$.

Figure 2.19: Exp. 2 and 3: Steady-state and transient results of the experimental and simulation detailed model and WD agg model with various k_{λ_j}.

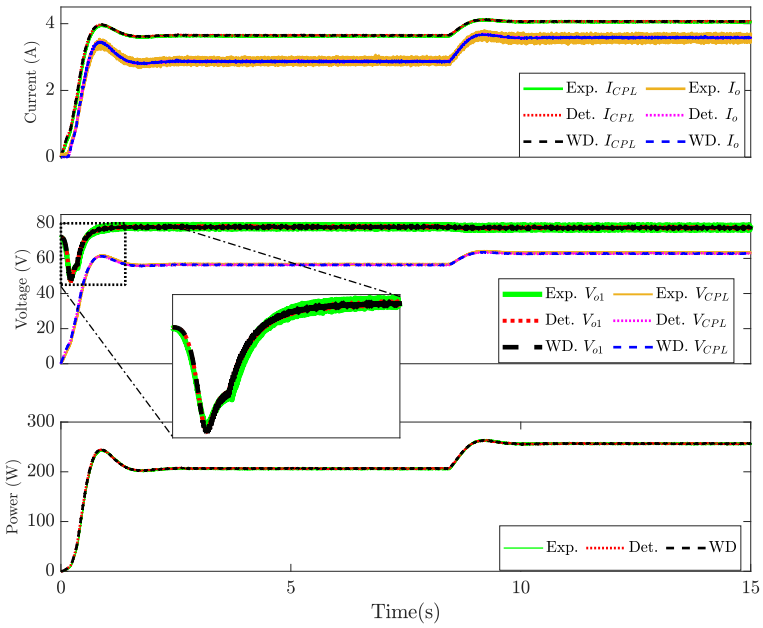

(a) $k_{\lambda_1} = k_{\lambda_2} = k_{\lambda_3} = 0.08$.

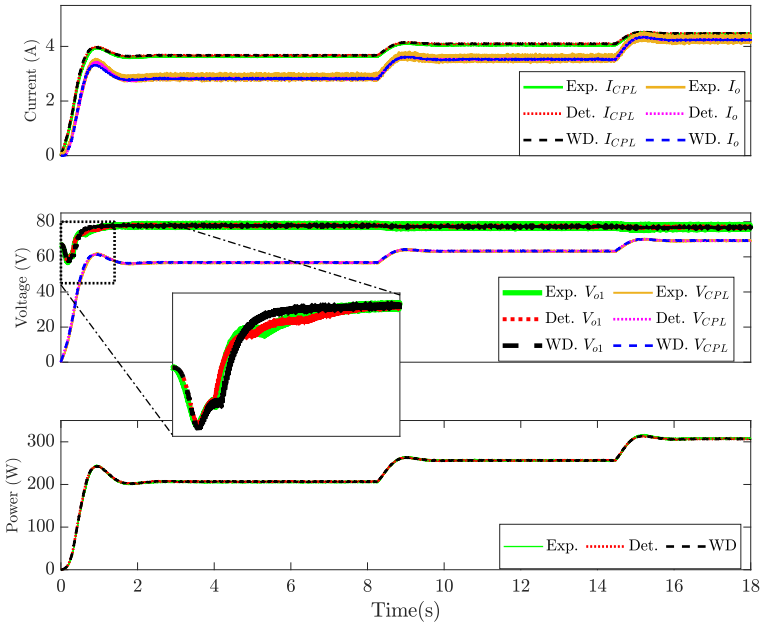

(b) $k_{\lambda_1} = 0.08,\ k_{\lambda_2} = 0.012,\ k_{\lambda_3} = 0.096$.

Figure 2.20: Exp. 4 and 5: Steady-state and transient results of the experimental and simulation detailed model and WD agg model with unequal control parameters: a) except k_{λ_j}, b) including k_{λ_j}.

Table 2.9: Experimental parameters for extreme parameters differences.

Parameters	Value	Unit
$V_{in_1},\ V_{in_2},\ V_{in_3}$	120, 110, 100	(V)
$k_{\lambda_1},\ k_{\lambda_2},\ k_{\lambda_3}$	0.08, 0.12, 0.16	-
$R_{o_1},\ R_{o_2},\ R_{o_3}$	0.163, 0.113, 0.118	(Ω)
$f_{sw_1},\ f_{sw_2},\ f_{sw_3}$	20, 25, 15	(kHz)
$L_{o_1},\ L_{o_2},\ L_{o_3}$	1.2, 1, 0.9	(mH)
$L_{f_1},\ L_{f_2},\ L_{f_3}$	2.2, 1.8, 1.9	(mH)
$C_{f_1},\ C_{f_2},\ C_{f_3}$	2.3, 2.7, 2.5	(μF)
$R_{d_1},\ R_{d_2},\ R_{d_3}$	0.6, 1.35, 0.7	(Ω)

of WD agg model mimic the behavior of the detailed model in both experimental and simulation results for the system with unequal converters and control parameters. To make the system more realistic and challenging, different input voltages are assumed for Exp. 6. Figure 2.21 shows the steady-state and transient behavior of the experimental and simulation detailed model and WD agg model with unequal input voltages $V_{in_1} = 120V,\ V_{in_2} = 110V,\ V_{in_3} = 100V$ and unequal control parameters for the load power change from 200W to 250W at t=4.5s. To validate the accuracy of proposed method in systems with extreme parameters difference, Table 2.9 detailed model is simulated and experimentally implemented and is compared with its WD model in Figure 2.22. The results shown in Figure 2.17 to 2.21 verify WD agg model performance accuracy in the steady-state and transient behavior for the system with unequal converter, controller, and input voltage parameters. Moreover, representing the detailed system with a single equivalent converter instead of three has reduced computation time by approximately threefold, all while preserving model accuracy.

2.6 Conclusion

This chapter introduced the WD aggregation approach as a powerful method for modeling a large number of paralleled units with significant parameter disparities. The application of the WD aggregation technique to a DC-DC buck converter integrated microgrid resulted in an equivalent single converter and control system, serving as a reduced-order model for a system comprising multiple droop-controlled DC-DC converters with different parameter values. The proposed model's parameters were determined through weighted averaging of corresponding detailed model parameters, with each converter's weight reflecting its contribution to the overall dynamic behavior of the system. Through a thorough evaluation, the proposed model demonstrated its effectiveness in diverse scenarios involving three paralleled buck converters con-

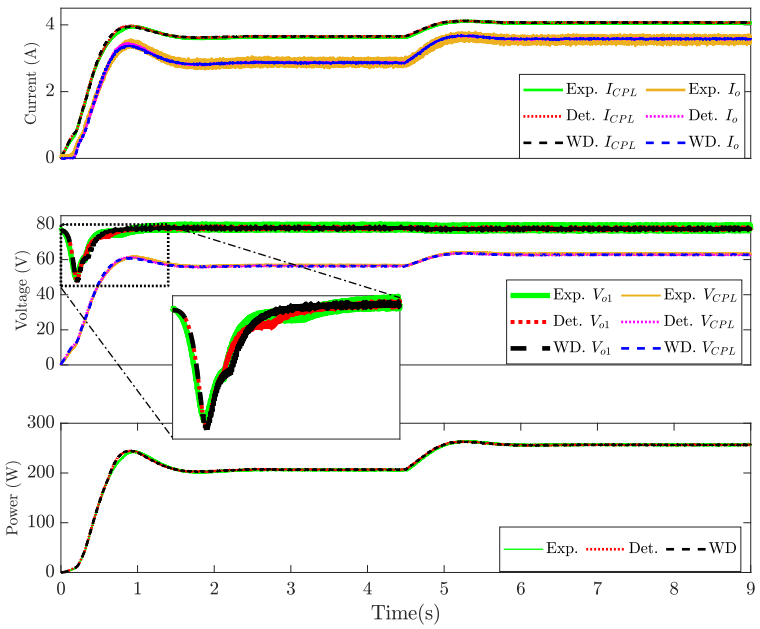

Figure 2.21: Exp. 6: Steady-state and transient results of the experimental and simulation detailed model and WD agg model with unequal control parameters including $k_{\lambda_1} = 0.08$, $k_{\lambda_2} = 0.012$, $k_{\lambda_3} = 0.096$, and unequal input voltages $V_{in_1} = 120V$, $V_{in_2} = 110V$, $V_{in_3} = 100V$.

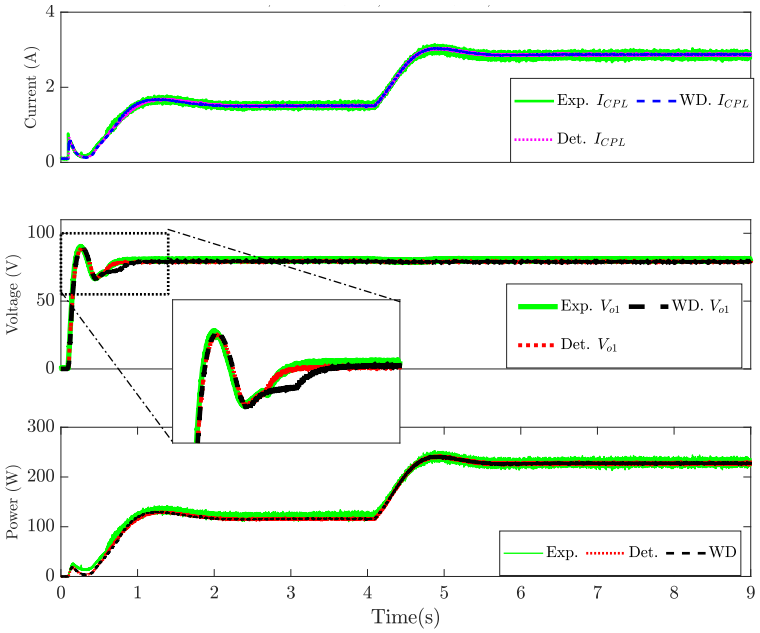

Figure 2.22: Exp. 7: Steady-state and transient results of the experimental and simulation detailed model and WD agg model with extreme parameters difference: $k_{\lambda_1} = 0.08$, $k_{\lambda_2} = 0.012$, $k_{\lambda_3} = 0.096$.

nected to a CPL. The analysis covered different control parameters, output filter capacitance, unequal converter and controller parameters, and unequal input voltages. Comparisons were made in two sections: eigenvalue analysis and steady-state and transient behavior comparison. The results obtained from bode diagrams, root locus, and eigenvalue trajectories validated the accuracy of the WD aggregation model in stability analysis, sensitivity analysis, and proper filter design for the load. Additionally, when compared with the detailed model, the WD aggregation model showed excellent agreement in steady-state and transient behavior, including start-up and CPL power steps, even with unequal converter and controller parameters and unequal input voltages. Both simulation and experimental results provided compelling evidence supporting the use of the WD aggregation model for stability analysis, sensitivity analysis, and design studies in parallel DC-DC power systems. Overall, the WD aggregation approach proves to be a valuable tool for effectively handling complex and diverse configurations in large-scale microgrids.

Chapter 3

Modeling of n Paralleled Three-phase Grid-forming Inverters based on WD agg Approach

This chapter applies the concept of WD agg to grid-forming inverters in DG integrated islanded microgrids as an example to illustrate the challenges and applications of WD agg model in modeling three-phase systems. WD agg models n parallel grid-forming inverters, control systems, and collector lines with an equivalent single grid-forming inverter, a control system, and a collector line. The contribution of each inverter in the aggregated model is quantified and factored into the equivalent model, which significantly increases the model accuracy compared to the existing single scaled and aggregated models.

The performance of the proposed method is evaluated based on time-domain simulation of a microgrid, which consists of four grid-forming parallel inverters in four scenarios that studies equal and unequal inverters parameters and operating points. Simulations results conducted under stable and unstable microgrid operating conditions demonstrate an accurate performance of the proposed model and the equivalent unit to be readily used to reduce the computational burden of the system studies. Moreover, the proposed WD agg model is used to design and calculate the large-scale system control parameters for various desirable system performances. Finally, a microgrid, which consists of four grid-forming parallel inverters is experimentally

---

- N. Shabanikia and S. A. Khajehoddin, "Analysis and Design of Droop-Controlled Grid-Forming Inverters Using Novel WD Agg Approach," in *IEEE Transactions on Industrial Electronics*, accepted on 2023.

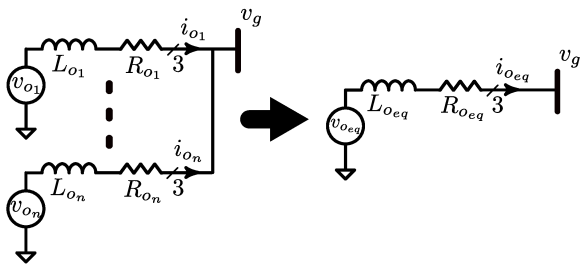

Figure 3.1: n paralleled three-phase system and the equivalent three-phase system.

implemented to evaluate the accuracy of the proposed method with various input reference signals.

3.1 WD agg Approach Derivation in Rotating Reference Frames

This section focuses on addressing the central challenge associated with applying the WD aggregation approach to three-phase systems. The scenario at hand revolves around a configuration featuring n paralleled three-phase systems, as depicted in Figure 3.1. These systems encompass a three-phase voltage source $v_{o_{abc}}$ interconnected with a grid $v_{g_{abc}}$ via a three-phase RL filter. The state-space model for each individual system can be derived in the following manner:

$$\begin{gathered}
\frac{d}{dt}\mathbf{x} = \mathbf{A}\mathbf{x} + \mathbf{B}\mathbf{u} + \mathbf{E}\mathbf{w}, \\
\text{where: } \mathbf{x} = [\mathbf{i}_o],\ \mathbf{u} = [\mathbf{v}_o],\ \mathbf{w} = [\mathbf{v_g}], \\
\mathbf{i}_o = [i_{o_a}\ i_{o_b}\ i_{o_c}]^T,\ \mathbf{v}_o = [v_{o_a}\ v_{o_b}\ v_{o_c}]^T,\ \mathbf{v}_g = [v_{g_a}\ v_{g_b}\ v_{g_c}]^T, \\
\mathbf{A} = -\begin{bmatrix} \frac{R_o}{L_o} & 0 & 0 \\ 0 & \frac{R_o}{L_o} & 0 \\ 0 & 0 & \frac{R_o}{L_o} \end{bmatrix},\ \mathbf{B} = \begin{bmatrix} \frac{1}{L_o} & 0 & 0 \\ 0 & \frac{1}{L_o} & 0 \\ 0 & 0 & \frac{1}{L_o} \end{bmatrix},\ \mathbf{E} = -\mathbf{B}.
\end{gathered} \tag{3.1}$$

Figure 3.1 three-phase system can be transform using Clarke/Park transformation to two coupled systems so-called d-axis and q-axis systems where they can be modeled as:

$$\begin{aligned}
\text{d-axis: } v_{od_k} - v_{gd} &= \left(L_{o_k}\frac{d}{dt} + R_{o_k}\right) i_{od} - \omega L_{o_k} i_{oq_k}, \\
\text{q-axis: } v_{oq_k} - v_{gq} &= \left(L_{o_k}\frac{d}{dt} + R_{o_k}\right) i_{oq} + \omega L_{o_k} i_{od_k}.
\end{aligned} \tag{3.2}$$

Now to find the equivalent inductor $L_{o_{eq}}$ and resistor $R_{o_{eq}}$, let's define the i_o state and v_o input contribution weights as:

$$\mu_{d_k} = \frac{n i_{od_k}}{\sum_{j=1}^{n} i_{od_j}},\ \mu_{q_k} = \frac{n i_{oq_k}}{\sum_{j=1}^{n} i_{oq_j}},\ \nu_{d_k} = \frac{n v_{od_k}}{\sum_{j=1}^{n} v_{od_j}},\ \nu_{q_k} = \frac{n v_{oq_k}}{\sum_{j=1}^{n} v_{oq_j}}, \tag{3.3}$$

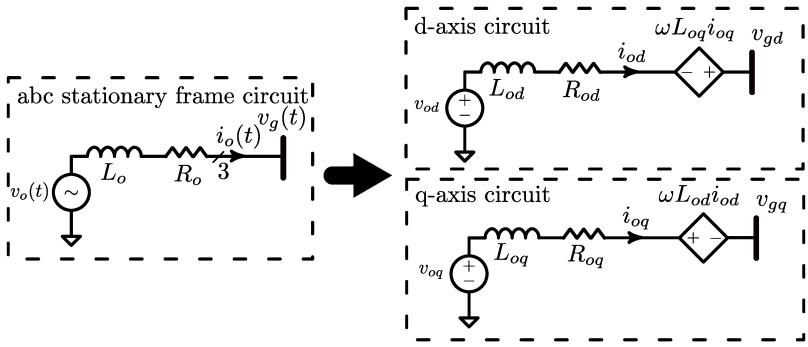

Figure 3.2: The stationary frame and dq-axis models of kth three-phase system shown Figure 3.1.

and consider that $i_{od_{eq}} = \sum_{k=1}^{n} i_{od_k}$ and $i_{oq_{eq}} = \sum_{k=1}^{n} i_{oq_k}$. Now by substituting (3.3) to (3.2), the kth dynamic equation can be derived in terms of $i_{odq_{eq}}$ as:

$$\begin{aligned} \nu_{d_k} v_{od_{eq}} - v_{gd} &= \left(L_{o_k} \frac{d}{dt} + R_{o_k} \right) \mu_{d_k} \frac{i_{od_{eq}}}{n} - \omega L_{o_k} \mu_{q_k} \frac{i_{oq_{eq}}}{n}, \\ \nu_{q_k} v_{oq_{eq}} - v_{gq} &= \left(L_{o_k} \frac{d}{dt} + R_{o_k} \right) \mu_{q_k} \frac{i_{oq_{eq}}}{n} + \omega L_{o_k} \mu_{d_k} \frac{i_{od_{eq}}}{n}. \end{aligned} \tag{3.4}$$

Averaging n equations of (3.4) yields:

$$\begin{aligned} v_{od_{eq}} - v_{gd} &= \frac{1}{n^2} \sum_{k=1}^{n} \left(L_{o_k} \frac{d}{dt} + R_{o_k} \right) \mu_{d_k} i_{od_{eq}} - \omega \frac{1}{n^2} \sum_{k=1}^{n} L_{o_k} \mu_{q_k} i_{oq_{eq}}, \\ v_{oq_{eq}} - v_{gq} &= \frac{1}{n^2} \sum_{k=1}^{n} \left(L_{o_k} \frac{d}{dt} + R_{o_k} \right) \mu_{q_k} i_{oq_{eq}} + \omega \frac{1}{n^2} \sum_{k=1}^{n} L_{o_k} \mu_{d_k} i_{od_{eq}}. \end{aligned} \tag{3.5}$$

By comparing (3.5) with the d-q circuits demonstrated in Figure 3.2, the model of equivalent d-axis and q-axis circuits can be derived as:

$$\begin{aligned} v_{od_{eq}} - v_{gd} &= \left(L_{od_{eq}} \frac{d}{dt} + R_{od_{eq}} \right) i_{od_{eq}} - \omega L_{oq_{eq}} i_{oq_{eq}}, \\ v_{oq_{eq}} - v_{gq} &= \left(L_{oq_{eq}} \frac{d}{dt} + R_{oq_{eq}} \right) i_{oq_{eq}} + \omega L_{od_{eq}} i_{od_{eq}}, \\ \text{where: } L_{od_{eq}} &= \frac{1}{n^2} \sum_{k=1}^{n} L_{o_k} \mu_{d_k}, \ R_{od_{eq}} = \frac{1}{n^2} \sum_{k=1}^{n} R_{o_k} \mu_{d_k}, \\ L_{oq_{eq}} &= \frac{1}{n^2} \sum_{k=1}^{n} L_{o_k} \mu_{q_k}, \ R_{oq_{eq}} = \frac{1}{n^2} \sum_{k=1}^{n} R_{o_k} \mu_{q_k}. \end{aligned} \tag{3.6}$$

If $\mu_{d_k} \neq \mu_{q_k}$, thus, $L_{od_{eq}} \neq L_{oq_{eq}}$ and $R_{od_{eq}} \neq R_{oq_{eq}}$, hence there is no physical realization of (3.6) model. To find an equivalent circuit that can have a physical

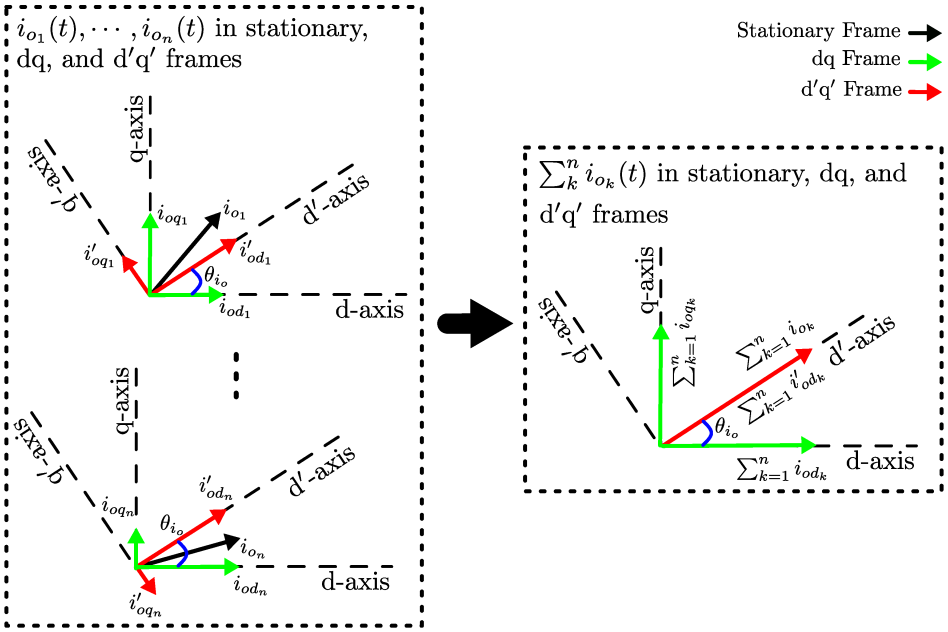

Figure 3.3: $i_{o_k}(t)$ in the stationary, dq, d′q′ reference frames.

realization let's find (3.4) in a new d′q′ reference frame to satisfy the condition of $\sum_{j=1}^n i'_{oq_j} = 0$, which can be determined as:

$$i_{odq} = i'_{odq}e^{j\theta_{i_o}},\ v_{odq} = v'_{odq}e^{j\theta_{i_o}},\ v_{gdq} = v'_{gdq}e^{j\theta_{i_o}},\ \theta_{i_o} = \arctan\left(\frac{\sum_{j=1}^n i_{oq_j}}{\sum_{j=1}^n i_{od_j}}\right). \quad (3.7)$$

This transformation will shift the dq reference frame to d′q′ as depicted in Figure 3.3. Therefore, rewriting (3.2) in d′q′ reference frame yields:

$$\begin{aligned} \text{d-axis: } v'_{od_k} - v'_{gd} &= \left(L_{o_k}\frac{d}{dt} + R_{o_k}\right) i'_{od} - \omega L_{o_k} i'_{oq_k}, \\ \text{q-axis: } v'_{oq_k} - v'_{gq} &= \left(L_{o_k}\frac{d}{dt} + R_{o_k}\right) i'_{oq} + \omega L_{o_k} i'_{od_k}. \end{aligned} \quad (3.8)$$

Following the similar steps from (3.2) to (3.5) for the new d′q′ reference frame results in:

$$\begin{aligned} v'_{od_{eq}} - v'_{gd} &= \frac{1}{n^2}\sum_{k=1}^n \left(L_{o_k}\frac{d}{dt} + R_{o_k}\right) \mu'_{d_k} i'_{od_{eq}}, \\ v'_{oq_{eq}} - v'_{gq} &= \frac{1}{n^2}\sum_{k=1}^n \omega L_{o_k} \mu'_{d_k} i'_{od_{eq}}. \end{aligned} \quad (3.9)$$

Assuming that $\mu'_{d_k} = (I'_{d_k} + \tilde{i}'_{d_k}) / \left(\sum_{j=1}^n (I'_{d_j} + \tilde{i}'_{d_j})\right)$, where I and $\tilde{i}$ are the steady-state and the small-signal values, respectively, hence, μ'_{d_k} can be estimated by their steady-state values as $\mu'_{d_k} \simeq I'_{d_k} / \left(\sum_{j=1}^n I'_{d_j}\right)$. Now by multiplying q-axis equation of

(3.9) with j and summing it with the d-axis equation the combined dynamic equation of L_o and R_o can be found as:

$$\begin{aligned}\left(v'_{od_{eq}} + jv'_{od_{eq}}\right) - \left(v'_{gd} + jv'_{gq}\right) = \frac{1}{n^2}\sum_{k=1}^{n} L_{o_k}\mu'_{d_k}(\frac{d}{dt} + j\omega)i'_{od_{eq}} + \cdots \\ \cdots + \frac{1}{n^2}\sum_{k=1}^{n} R_{o_k}\mu_{d_k}i'_{od_{eq}}.\end{aligned} \tag{3.10}$$

To return (3.10) to the stationary frame, (3.10) can be multiplied by $e^{j(\omega t+\theta_{i_o})}$, which results in:

$$\begin{aligned}\left(v'_{od_{eq}} + jv'_{od_{eq}}\right)e^{j(\omega t+\theta_{i_o})} - \left(v'_{gd} + jv'_{gq}\right)e^{j(\omega t+\theta_{i_o})} = \\ \frac{1}{n^2}\sum_{k=1}^{n} L_{o_k}\mu_{d_k}\frac{d}{dt}\left(i'_{od_{eq}}e^{j(\omega t+\theta_{i_o})}\right) + \frac{1}{n^2}\sum_{k=1}^{n} R_{o_k}\mu_{d_k}i'_{od_{eq}}e^{j(\omega t+\theta_{i_o})}.\end{aligned} \tag{3.11}$$

Considering that $v(t) = (v'_d + jv'_q)e^{j(\omega t+\theta_{i_o})}$ and $i(t) = (i'_d + ji'_q)e^{j(\omega t+\theta_{i_o})}$, therefore (3.11) can be rewritten as:

$$v_{o_{eq}}(t) - v_g(t) = \frac{1}{n^2}\sum_{k=1}^{n} L_{o_k}\mu_{d_k}\frac{d}{dt}i_{o_{eq}}(t) + \frac{1}{n^2}\sum_{k=1}^{n} R_{o_k}\mu_{d_k}i_{o_{eq}}(t). \tag{3.12}$$

Thus, the equivalent $L_{o_{eq}}$ and $R_{o_{eq}}$ are found as:

$$L_{o_{eq}} = \frac{1}{n^2}\sum_{k=1}^{n} L_{o_k}\mu'_{d_k},\ R_{o_{eq}} = \frac{1}{n^2}\sum_{k=1}^{n} R_{o_k}\mu'_{d_k}. \tag{3.13}$$

3.2 Detailed Modeling of Microgrids with Paralleled Grid-forming Inverters

A microgrid consists of n grid-forming parallel inverters with loads shown in Fig. 3.4a is studied in this section. A resistive load is chosen as the load type for simplicity. It is worth noting that the proposed model can be used for other load types without the loss of generality. Fig. 3.5a shows the grid-forming inverter control system with droop control power-sharing. As Fig. 3.5a shows, each inverter has an active power-sharing droop control loop that generates the angle reference signal of the inverter local reference frame. Furthermore, each inverter has a reactive power-sharing droop control loop that generates the output voltage reference signal. The output active and reactive powers are calculated in the power calculation block based on locally measured output voltage and current signals. Due to local measurements each inverter control system operates at its local d'q' reference frame, while the state-space model

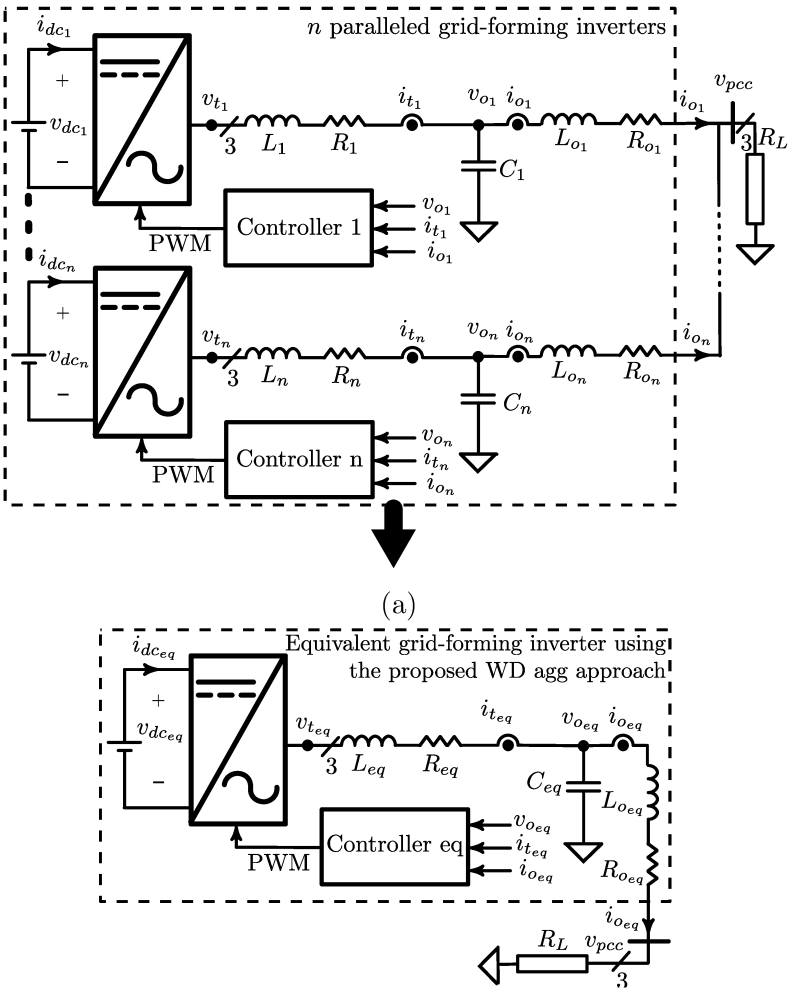

Figure 3.4: a) Islanded microgrid with grid-forming inverters, b) The proposed equivalent WD agg model.

of the whole system should be derived in a similar reference frame such as PCC dq reference frame as shown in Fig. 3.5b. Finally, as Fig. 3.5a shows the outer voltage control loop generates the inner current control loop reference signals and the inner current control loop generates the inverter gating signals.

3.2.1 Inverter #k dynamic equations

This section models #k grid-forming inverter with droop control power-sharing in the following five steps:

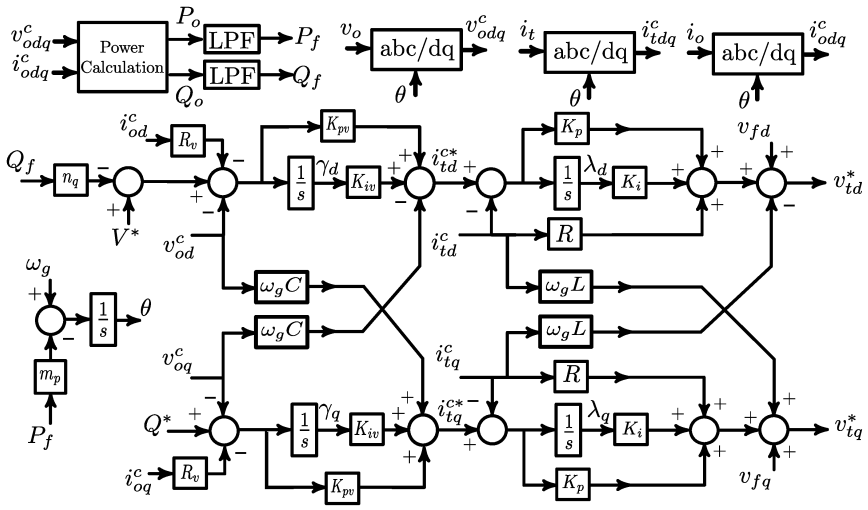

(a)

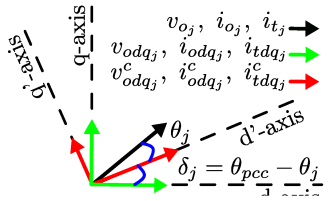

(b)

Figure 3.5: a) Grid-forming inverter control system with droop control power sharing, b) Reference frames representation.

Inverter #k LCL filter, and PCC voltage modeling:

The dynamic equation of kth inverter output LCL filter in the microgrid can be given as:

$$\begin{aligned} v_{t_k}(t) - v_{o_k}(t) &= (L_k \frac{d}{dt} + R_k) i_{t_k}(t), \\ i_{t_k}(t) - i_{o_k}(t) &= C_k \frac{d}{dt} v_{o_k}(t), \\ v_{o_k}(t) - v_g(t) = (L_{o_k} \frac{d}{dt} + R_{o_k}) i_{o_k}(t),\ & v_g(t) = v_{pcc}(t) = R_L \sum_{m=1}^{n} i_{o_m}(t), \end{aligned} \tag{3.14}$$

Deriving (3.14) in the desired dq reference frame with the angle of $(\omega t + \theta_0)$ yields:

$$\begin{aligned} v^{\theta_0}_{td_k} - v^{\theta_0}_{od_k} &= (L_k \frac{d}{dt} + R_k) i^{\theta_0}_{td_k} - \omega L_k i^{\theta_0}_{tq_k},\ i^{\theta_0}_{td_k} - i^{\theta_0}_{od_k} = C_k \frac{d}{dt} v^{\theta_0}_{od_k} - \omega C_k v^{\theta_0}_{oq_k}, \\ v^{\theta_0}_{tq_k} - v^{\theta_0}_{oq_k} &= (L_k \frac{d}{dt} + R_k) i^{\theta_0}_{tq_k} + \omega L_k i^{\theta_0}_{td_k},\ i^{\theta_0}_{tq_k} - i^{\theta_0}_{oq_k} = C_k \frac{d}{dt} v^{\theta_0}_{oq_k} + \omega C_k v^{\theta_0}_{od_k}, \\ v^{\theta_0}_{od_k} - v^{\theta_0}_{gd} &= (L_{o_k} \frac{d}{dt} + R_{o_k}) i^{\theta_0}_{od_k} - \omega L_{o_k} i^{\theta_0}_{oq_k},\ v^{\theta_0}_{gd} = R_L \sum_{m=1}^{n} i^{\theta_0}_{od_m}, \end{aligned}$$

$$v_{oq_k}^{\theta_0} - v_{gq}^{\theta_0} = (L_{o_k}\frac{d}{dt} + R_{o_k})i_{oq_k}^{\theta_0} + \omega L_{o_k} i_{od_k}^{\theta_0},\ v_{gq}^{\theta_0} = R_L \sum_{m=1}^{n} i_{oq_m}^{\theta_0}. \tag{3.15}$$

Inverter #k droop controller modeling:

The droop control low-pass filter dynamic equations of mth inverter can be given as:

$$\frac{d}{dt}P_{f_k} = \omega_c(P_{o_k} - P_{f_k}),\ \frac{d}{dt}Q_{f_k} = \omega_c(Q_{o_k} - Q_{f_k}), \tag{3.16}$$

where P_{f_k} and Q_{f_k} are filtered signals shown in Figure 3.5, and:

$$P_{o_k} = \frac{3}{2}(i_{od_k}^c v_{od_k}^c + i_{oq_k}^c v_{oq_k}^c),\ Q_{o_k} = \frac{3}{2}(i_{od_k}^c v_{oq_k}^c - i_{od_k}^c v_{oq_k}^c). \tag{3.17}$$

Also, the droop equations can be derived as:

$$\begin{aligned} v_{od_k}^{c^*} &= V^* - n_{q_k}Q_{f_k} - R_{v_k} i_{od_k}^c, \\ v_{oq_k}^{c^*} &= Q_k^* - R_{v_k} i_{oq_k}^c,\ \omega = \omega_g - m_{p_k} P_{f_k}. \end{aligned} \tag{3.18}$$

Inverter #k local reference frame controller modeling:

Each inverter is locally controlled, and the angle model required for the controller DQ transformer can be given as:

$$\frac{d}{dt}\theta_k = \omega_g - m_{p_k} P_{f_k} = \omega. \tag{3.19}$$

Inverter #k voltage controllers modeling:

Each inverter control loop works on its local d'q' reference frame, while the state-space model of the whole system should be derived in PCC dq reference frame as shown in Fig. 3.5b. For that purpose, first, each controller state-space equation is derived in its local reference frame and then each term is replaced by its PCC reference frame terms. The voltage controllers dynamic equations of kth inverter in the microgrid can be given as:

$$\begin{aligned} i_{td_k}^{c^*} &= (K_{pv_k}\frac{d}{dt} + K_{iv_k})\gamma_{d_k} - C_k\omega_g v_{oq_k}^c,\ \gamma_{d_k} = v_{od}^{c^*} - v_{od}^c, \\ i_{tq_k}^{c^*} &= (K_{pv_k}\frac{d}{dt} + K_{iv_k})\gamma_{q_k} + C_k\omega_g v_{od_k}^c,\ \gamma_{q_k} = v_{oq}^{c^*} - v_{oq}^c, \end{aligned} \tag{3.20}$$

and $v_{odq}^{c^*}$ can be found by (3.18).

Inverter #k current controller modeling:

The current controllers dynamic equations of kth inverter in the microgrid can be given as:

$$\begin{aligned} v_{td_k}^{c^*} &= (K_{p_k}\frac{d}{dt} + K_{i_k})\lambda_{d_k} - L_k\omega_g i_{tq_k}^c - Ri_{td_k}^c + v_{fd}, \\ v_{tq_k}^{c^*} &= (K_{p_k}\frac{d}{dt} + K_{i_k})\lambda_{q_k} + L_k\omega_g i_{td_k}^c - Ri_{tq_k}^c + v_{fq}, \\ \lambda_{d_k} &= i_{td_k}^{c^*} - i_{td_k}^c,\ \lambda_{q_k} = i_{tq_k}^{c^*} - i_{tq_k}^c,\ v_{fd} = V_o^*,\ v_{fq} = 0. \end{aligned} \tag{3.21}$$

Inverter #k overall state-space model:

Augmenting n controller equations derived in (3.16)-(3.21) results in the detailed controllers state-space models, where $\mathbf{x_c} = [\boldsymbol{\lambda}_{dq}\ \boldsymbol{\gamma}_{dq}\ \boldsymbol{\theta}\ \mathbf{P}_f\ \mathbf{Q}_f]$, $\mathbf{u_c} = [\mathbf{i}_{odq}\ \mathbf{v}_{odq}\ \mathbf{i}_{tdq}\ V^*\ \omega_g]$, and each array of $\mathbf{x_c}$ includes all corresponding states of all controllers, e.g. $\boldsymbol{\lambda}_{dq} = [\boldsymbol{\lambda}_d\ \boldsymbol{\lambda}_q]$, where $\boldsymbol{\lambda}_d = [\lambda_{d_1},\ \ldots,\ \lambda_{d_n}]$, and $\boldsymbol{\lambda}_q = [\lambda_{q_1},\ \ldots,\ \lambda_{q_n}]$. Moreover, as shown in Figure 3.5a, the kth controller output is the inverter output voltage signal as $v_{out_k} = \sqrt{(v_{td_k}^*)^2 + (v_{tq_k}^*)^2}\ \sin\Big(\theta_k + \arctan(v_{tq_k}^*/v_{td_k}^*)\Big)$. Furthermore, solving the obtained dynamic equations for $d/dt = 0$ yields the stead-states of the system. Deriving the Jacobian matrix of the achieved equations and applying the initial states found in the previous part will lead to the linerized kth controller model of $\dot{\mathbf{x}}_\mathbf{c} = \mathbf{A_c}\mathbf{x_c} + \mathbf{B_c}\mathbf{u_c}$, $v_{out_k} = \mathbf{C_{c}}_k\mathbf{x_c} + \mathbf{D_{c}}_k\mathbf{u_c}$, and $\mathbf{A_c}$, $\mathbf{B_c}$, $\mathbf{C_{c}}_k$, $\mathbf{D_{c}}_k$ matrices can be found as:

$$\mathbf{A_c} = \frac{\partial f_c}{\partial x_c},\ \mathbf{B_c} = \frac{\partial f_c}{\partial u_c},\ \mathbf{C_{c}}_k = \frac{\partial v_{out_k}}{\partial x_c},\ \mathbf{D_{c}}_k = \frac{\partial v_{out_k}}{\partial u_c}, \tag{3.22}$$

where, f_c is $\dot{x}_c$ in terms of $\mathbf{x_c}$ and $\mathbf{u_c}$, x_c is the system states, and u_c is the system inputs. The controller state-space model can be used in the controller design using open-loop and closed-loop frequency response analyses. Furthermore, the obtained controller model can be used to design a desirable feedback gain with root-loci analyses.

3.2.2 Linearization and detailed system state-space model

Augmenting n inverter equations derived in (3.15)-(3.21) results in the detailed system state-space model where $\mathbf{x} = [\mathbf{i}_{odq}\ \mathbf{v}_{odq}\ \mathbf{i}_{tdq}\ \boldsymbol{\lambda}_{dq}\ \boldsymbol{\gamma}_{dq}\ \boldsymbol{\theta}\ \mathbf{P}_f\ \mathbf{Q}_f]$, $\mathbf{u} = [V^*\ \omega_g]$, and each array of $\mathbf{x}$ includes all corresponding states of inverters, e.g. $\mathbf{i}_{odq} = [\mathbf{i}_{od}\ \mathbf{i}_{oq}]$, where $\mathbf{i}_{od} = [i_{od_1},\ \ldots,\ i_{od_n}]$, and $\mathbf{i}_{oq} = [i_{oq_1},\ \ldots,\ i_{oq_n}]$. Solving the obtained dynamic equations for $d/dt = 0$ yields the stead-states of the system. Moreover, deriving the Jacobian matrix of the achieved dynamic equations and applying the initial states found in the previous part will lead to the linerized system $\dot{\mathbf{x}} = \mathbf{A}\mathbf{x} + \mathbf{B}\mathbf{u}$, and $\mathbf{A}$ and $\mathbf{B}$ matrices can be found as:

$$\mathbf{A} = \frac{\partial f}{\partial x},\ \mathbf{B} = \frac{\partial f}{\partial u}, \tag{3.23}$$

where, f is $\frac{d}{dt}x$ in terms of $\mathbf{x}$ and $\mathbf{u}$, x is the system states, and u is the system inputs. The system $\mathbf{A}$ matrix will be a $13n \times 13n$ because each inverter has 13 states. The $13n$ eigenvalues of $\mathbf{A}$ matrix can predict the stability of the system.

3.3 WD agg Model of Microgrids with Paralleled Grid-forming Inverters

The main goal of WD agg method is to find an equivalent set of dynamic equations with a similar structure of a single droop-controlled inverter for n grid-forming inverters shown in Figure. 3.4a. To achieve this goal, first, the dynamic equations of n inverters in the detailed system is derived and then a weight of contribution for each unit is defined. Finally, the weighted average of n inverter dynamic equations is derived and compared with the individual inverter equations to find the equivalent set of equations. The achieved equivalent set of equations represent the detailed system with a single equivalent inverter and an equivalent controller as shown in Figure 3.4b. It is shown that the equivalent inverter and controller parameters are found by the weighted average of the corresponding parameters. The mathematical proof of the equivalent model shown in Figure 3.4b is provided in the three following steps:

3.3.1 Equivalent LCL

This section finds the equivalent LCL in three separate parts as follows:

Equivalent L_{eq} and R_{eq}:

Consider L_k dynamic equation of (3.14) derived in the desired reference frame with $(\omega t + \theta_0 + \delta_{i_t})$ angle, where:

$$\begin{aligned} v_{td_k}^{\delta_{i_t}} - v_{od_k}^{\delta_{i_t}} &= (L_k \frac{d}{dt} + R_k) i_{td_k}^{\delta_{i_t}} - \omega L_k i_{tq_k}^{\delta_{i_t}}, \\ v_{tq_k}^{\delta_{i_t}} - v_{oq_k}^{\delta_{i_t}} &= (L_k \frac{d}{dt} + R_k) i_{tq_k}^{\delta_{i_t}} + \omega L_k i_{td_k}^{\delta_{i_t}}, \\ \text{and: } \tan \delta_{i_t} &= \left(\sum_{j=1}^{n} i_{tq_j}^{\theta_0} \right) \Big/ \left(\sum_{j=1}^{n} i_{td_k}^{\theta_0} \right), \end{aligned} \tag{3.24}$$

which results in $\sum_{j=1}^{n} i_{tq_j}^{\delta_{i_t}} = 0$. The weight of each inverter in the equivalent corresponding i_t state can be determined as:

$$\mu_{i_{td_k}} = \frac{n i_{td_k}^{\delta_{i_t}}}{i_{td_{eq}}^{\delta_{i_t}}}, \ \mu_{i_{tq_k}} = \frac{n i_{tq_k}^{\delta_{i_t}}}{i_{tq_{eq}}^{\delta_{i_t}}}, \tag{3.25}$$

where $i_{td_{eq}}^{\delta_{i_t}} = \sum_{j=1}^{n} i_{td_j}^{\delta_{i_t}}$ and $i_{tq_{eq}}^{\delta_{i_t}} = \sum_{j=1}^{n} i_{tq_j}^{\delta_{i_t}}$. Rewriting (3.24) in terms of the equivalent voltages and currents yields:

$$\begin{aligned} v_{td_k}^{\delta_{i_t}} - v_{od_k}^{\delta_{i_t}} &= (L_k \frac{d}{dt} + R_k)\frac{\mu_{i_{td_k}}}{n} i_{td_{eq}}^{\delta_{i_t}} - \omega L_k \frac{\mu_{i_{tq_k}}}{n} i_{tq_{eq}}^{\delta_{i_t}}, \\ v_{tq_k}^{\delta_{i_t}} - v_{oq_k}^{\delta_{i_t}} &= (L_k \frac{d}{dt} + R_k)\frac{\mu_{i_{tq_k}}}{n} i_{tq_{eq}}^{\delta_{i_t}} + \omega L_k \frac{\mu_{i_{td_k}}}{n} i_{td_{eq}}^{\delta_{i_t}}. \end{aligned} \tag{3.26}$$

Now by considering $i_{tq_{eq}}^{\delta_{i_t}} = \sum_{j=1}^{n} i_{tq_j}^{\delta_{i_t}} = 0$ and averaging n equation of (3.26) results in:

$$\begin{aligned} \frac{1}{n}\sum_{k=1}^{n}\left(v_{td_k}^{\delta_{i_t}} - v_{od_k}^{\delta_{i_t}}\right) &= \sum_{k=1}^{n}\left((L_k \frac{d}{dt} + R_k)\frac{\mu_{i_{td_k}}}{n^2}\right) i_{td_{eq}}^{\delta_{i_t}}, \\ \frac{1}{n}\sum_{k=1}^{n}\left(v_{tq_k}^{\delta_{i_t}} - v_{oq_k}^{\delta_{i_t}}\right) &= \omega \sum_{k=1}^{n}\left(L_k \frac{\mu_{i_{td_k}}}{n^2}\right) i_{td_{eq}}^{\delta_{i_t}}. \end{aligned} \tag{3.27}$$

Considering $\mu_{i_{td_k}} = n i_{td_k}^{\delta_{i_t}} / i_{td_{eq}}^{\delta_{i_t}}$ and $i_{td}^{\delta_{i_t}} = I_{td}^{\delta_{i_t}} + \tilde{i}_{td}^{\delta_{i_t}}$, where I and $\tilde{i}$ are the steady-state and small-signal values, respectively, and $I >> \tilde{i}$, thus, the weights can be estimated as $\mu_{i_{td_k}} \simeq n I_{td_k}^{\delta_{i_t}} / I_{td_{eq}}^{\delta_{i_t}}$. Multiplying the (3.27) q-axis equation with j and adding it to the d-axis equation yields:

$$\begin{aligned} &\left(v_{td_{eq}}^{\delta_{i_t}} + j v_{tq_{eq}}^{\delta_{i_t}}\right) - \left(v_{od_{eq}}^{\delta_{i_t}} + j v_{oq_{eq}}^{\delta_{i_t}}\right) = \\ &\sum_{k=1}^{n}\left(L_k \frac{\mu_{i_{td_k}}}{n^2}\frac{d}{dt} + R_k \frac{\mu_{i_{td_k}}}{n^2}\right) i_{td_{eq}}^{\delta_{i_t}} + j\omega \sum_{k=1}^{n}\left(L_k \frac{\mu_{i_{td_k}}}{n^2}\right) i_{td_{eq}}^{\delta_{i_t}}, \\ &\text{where: } v_{td_{eq}}^{\delta_{i_t}} = \frac{1}{n}\sum_{k=1}^{n} v_{td_k}^{\delta_{i_t}},\ v_{tq_{eq}}^{\delta_{i_t}} = \frac{1}{n}\sum_{k=1}^{n} v_{tq_k}^{\delta_{i_t}}, \\ &v_{od_{eq}}^{\delta_{i_t}} = \frac{1}{n}\sum_{k=1}^{n} v_{od_k}^{\delta_{i_t}},\ v_{oq_{eq}}^{\delta_{i_t}} = \frac{1}{n}\sum_{k=1}^{n} v_{oq_k}^{\delta_{i_t}}. \end{aligned} \tag{3.28}$$

Transforming (3.28) to the *abc* stationary frame by multiplying (3.28) with $e^{j(\omega t + \theta_0 + \delta_{i_t})}$ yields:

$$v_{t_{eq}}(t) - v_{o_{eq}}(t) = \sum_{k=1}^{n}\left(L_k \frac{\mu_{i_{td_k}}}{n^2}\frac{d}{dt} + R_k \frac{\mu_{i_{td_k}}}{n^2}\right) i_{t_{eq}}(t). \tag{3.29}$$

By comparing (3.29) with a single unit dynamic equation shown in (3.14), the equivalent L_{eq} and R_{eq} can be achieved as:

$$L_{eq} = \sum_{k=1}^{n} L_k \frac{\mu_{i_{td_k}}}{n^2},\ R_{eq} = \sum_{k=1}^{n} R_k \frac{\mu_{i_{td_k}}}{n^2}. \tag{3.30}$$

Equivalent C_{eq}:

Consider C_k dynamic equation of (3.14) derived in the desired reference frame with $(\omega t + \theta_0 + \delta_{i_t})$ angle, where:

$$\begin{aligned} i_{td_k}^{\delta_{v_o}} - i_{od_k}^{\delta_{v_o}} &= C_k \frac{d}{dt} v_{td_k}^{\delta_{v_o}} - \omega C_k i_{tq_k}^{\delta_{v_o}}, \\ i_{tq_k}^{\delta_{v_o}} - i_{oq_k}^{\delta_{v_o}} &= C_k \frac{d}{dt} v_{tq_k}^{\delta_{v_o}} + \omega C_k v_{td_k}^{\delta_{v_o}}, \\ \text{and: } \tan \delta_{v_o} &= \left(\sum_{j=1}^{n} v_{tq_j}^{\theta_0} \right) \Big/ \left(\sum_{j=1}^{n} v_{td_k}^{\theta_0} \right), \end{aligned} \tag{3.31}$$

which results in $\sum_{j=1}^{n} v_{tq_j}^{\delta_{v_o}} = 0$. The weight of each inverter in the equivalent corresponding v_t state can be determined as:

$$\mu_{v_{od_k}} = \frac{n v_{td_k}^{\delta_{v_o}}}{v_{td_{eq}}^{\delta_{v_o}}}, \ \mu_{v_{oq_k}} = \frac{n v_{tq_k}^{\delta_{v_o}}}{v_{tq_{eq}}^{\delta_{v_o}}}, \tag{3.32}$$

where $v_{td_{eq}}^{\delta_{v_o}} = \sum_{j=1}^{n} v_{td_j}^{\delta_{v_o}}/n$ and $v_{tq_{eq}}^{\delta_{v_o}} = \sum_{j=1}^{n} v_{tq_j}^{\delta_{v_o}}/n$. Following a similar steps to the previous parts the final dynamic equation of filter capacitor in the *abc* stationary can be obtained as:

$$i_{t_{eq}}(t) - i_{o_{eq}}(t) = \sum_{k=1}^{n} C_k \mu_{v_{od_k}} \frac{d}{dt} v_{o_{eq}}(t). \tag{3.33}$$

By comparing (3.33) with a single unit dynamic equation shown in (3.14), the equivalent C_{eq} can be achieved as:

$$C_{eq} = \sum_{k=1}^{n} C_k \mu_{v_{od_k}}. \tag{3.34}$$

Equivalent $L_{o_{eq}}$ and $R_{o_{eq}}$:

Consider L_{o_k} dynamic equation of (3.14) derived in the desired reference frame with $(\omega t + \theta_0 + \delta_{i_o})$ angle, where:

$$\begin{aligned} v_{od_k}^{\delta_{i_o}} - v_{gd_k}^{\delta_{i_o}} &= (L_{o_k} \frac{d}{dt} + R_{o_k}) i_{od_k}^{\delta_{i_o}} - \omega L_{o_k} i_{oq_k}^{\delta_{i_o}}, \\ v_{oq_k}^{\delta_{i_o}} - v_{gq_k}^{\delta_{i_o}} &= (L_{o_k} \frac{d}{dt} + R_{o_k}) i_{oq_k}^{\delta_{i_o}} + \omega L_{o_k} i_{od_k}^{\delta_{i_o}}, \\ \text{and: } \tan \delta_{i_o} &= \left(\sum_{j=1}^{n} i_{oq_j}^{\theta_0} \right) \Big/ \left(\sum_{j=1}^{n} i_{od_k}^{\theta_0} \right), \end{aligned} \tag{3.35}$$

which results in $\sum_{j=1}^{n} i_{oq_j}^{\delta_{i_o}} = 0$. The weight of each inverter in the equivalent corresponding i_o state can be determined as:

$$\mu_{i_{od_k}} = \frac{n i_{od_k}^{\delta_{i_o}}}{i_{od_{eq}}^{\delta_{i_o}}}, \ \mu_{i_{oq_k}} = \frac{n i_{oq_k}^{\delta_{i_o}}}{i_{oq_{eq}}^{\delta_{i_o}}}, \tag{3.36}$$

where $i^{\delta_{io}}_{od_{eq}} = \sum_{j=1}^{n} i^{\delta_{io}}_{od_j}$ and $i^{\delta_{io}}_{oq_{eq}} = \sum_{j=1}^{n} i^{\delta_{io}}_{oq_j}$. Following a similar steps to the two previous parts the final dynamic equation of filter capacitor in the *abc* stationary can be obtained as:

$$v_{o_{eq}}(t) - v_g(t) = \sum_{k=1}^{n} \left(L_{o_k} \frac{\mu_{i_{od_k}}}{n^2} \frac{d}{dt} + R_{o_k} \frac{\mu_{i_{od_k}}}{n^2} \right) i_{o_{eq}}(t). \tag{3.37}$$

By comparing (3.37) with a single unit dynamic equation shown in (3.14), the equivalent $L_{o_{eq}}$ and $R_{o_{eq}}$ can be achieved as:

$$L_{o_{eq}} = \sum_{k=1}^{n} L_{o_k} \frac{\mu_{i_{od_k}}}{n^2}, \;\; R_{o_{eq}} = \sum_{k=1}^{n} R_{o_k} \frac{\mu_{i_{od_k}}}{n^2}. \tag{3.38}$$

To summarize, the equivalent LCL parameters can be found as:

$$\begin{gathered} L_{o_{eq}} = \sum_{m=1}^{n} \frac{\mu_{i_{od_m}}}{n^2} L_{o_m}, \;\; R_{o_{eq}} = \sum_{m=1}^{n} \frac{\mu_{i_{od_m}}}{n^2} R_{o_m}, \;\; L_{eq} = \sum_{m=1}^{n} \frac{\mu_{i_{td_m}}}{n^2} L_m, \\ R_{eq} = \sum_{m=1}^{n} \frac{\mu_{i_{td_m}}}{n^2} R_m, \quad C_{eq} = \sum_{m=1}^{n} \mu_{v_{od_m}} C_m. \end{gathered} \tag{3.39}$$

3.3.2 Equivalent voltage and current controllers

Similar to the previous section, the equivalent current controller for the proposed WD agg model can be found by, first, deriving n current controller dynamic equations, and then determining the controller state contributions. Finally, the weighted average of n controller dynamic equations is derived and compared with the individual controller equations to find the equivalent set of equations. The equivalent controller parameters are found in two following parts separately.

Equivalent current controller:

The kth inverter current controller model in the Laplace form and the desired reference frame with $(\omega t + \theta_c)$ angle can be given as:

$$\begin{aligned} v^c_{td_k} =& (K_{p_k} + K_{i_k}/s)\lambda^c_{d_k} + R_k i^c_{td_k} - \omega_g L_k i^c_{tq_k} + V^*, \\ v^c_{tq_k} =& (K_{p_k} + K_{i_k}/s)\lambda^c_{q_k} + R_k i^c_{tq_k} + \omega_g L_k i^c_{td_k}. \end{aligned} \tag{3.40}$$

A single dynamic equation can be written for the kth controller by multiplying q-axis of (3.40) with j and summing it to the d-axis equation as follows:

$$\begin{aligned} v^c_{td_k} + j v^c_{tq_k} =& (K_{p_k} + K_{i_k}/s)\left(\lambda^c_{d_k} + j\lambda^c_{q_k}\right) + \cdots \\ & \cdots + R_k \left(i^c_{td_k} + j i^c_{tq_k}\right) + j\omega_g L_k \left(i^c_{td_k} + j i^c_{tq_k}\right) + V^*. \end{aligned} \tag{3.41}$$

It is worth noting each converter has (3.41) dynamic equation in its own θ_c local reference frame. To derive all controllers dynamic equations in a common rotating

frame, let's define $z^c_{td_k} + jz^c_{tq_k} = \left(z^{\theta_0}_{td_k} + jz^{\theta_0}_{tq_k}\right) e^{j\Delta_c}$, where $z = i,\ v,\ \lambda$. Therefore, (3.41) can be rewritten in the common rotating frame as:

$$\begin{aligned} v^{\theta_0}_{td_k} + jv^{\theta_0}_{tq_k} =& (K_{p_k} + K_{i_k}/s)\left(\lambda^{\theta_0}_{d_k} + j\lambda^{\theta_0}_{q_k}\right) + \cdots \\ & \cdots + R_k\left(i^{\theta_0}_{td_k} + ji^{\theta_0}_{tq_k}\right) + j\omega_g L_k\left(i^{\theta_0}_{td_k} + ji^{\theta_0}_{tq_k}\right) + V^{\theta_0 *}. \end{aligned} \tag{3.42}$$

Deriving (3.42) in the desired reference frame with $(\omega t + \theta_0 + \delta_\lambda)$ angle, where:

$$\begin{aligned} v^{\delta_\lambda}_{td_k} &= (K_{p_k} + K_{i_k}/s)\lambda^{\delta_\lambda}_{d_k} + R_k i^{\delta_\lambda}_{td_k} - \omega_g L_k i^{\delta_\lambda}_{tq_k} + V_d^{\delta_\lambda *}, \\ v^{\delta_\lambda}_{tq_k} &= (K_{p_k} + K_{i_k}/s)\lambda^{\delta_\lambda}_{q_k} + R_k i^{\delta_\lambda}_{tq_k} + \omega_g L_k i^{\delta_\lambda}_{td_k}, \\ \text{and: } \tan\delta_\lambda &= \left(\sum_{j=1}^{n}\lambda^{\theta_0}_{q_j}\right) \Big/ \left(\sum_{j=1}^{n}\lambda^{\theta_0}_{d_k}\right), \end{aligned} \tag{3.43}$$

which results in $\sum_{j=1}^{n}\lambda^{\delta_\lambda}_{q_j} = 0$. Moreover, consider the phase difference between $\vec{i}^{\delta_\lambda}_{tdq_k}$ and $\vec{i}^{\delta_{i_t}}_{tdq_k}$ as $\delta_{\Delta\lambda}$, where:

$$(i^{\delta_\lambda}_{td_k} + ji^{\delta_\lambda}_{tq_k}) = \left(i^{\delta_{i_t}}_{td_k} + ji^{\delta_{i_t}}_{tq_k}\right) e^{j\delta_{\Delta\lambda}}. \tag{3.44}$$

Substituting (3.44) in(3.43) results in:

$$\begin{aligned} v^{\delta_\lambda}_{td_k} &= (K_{p_k} + K_{i_k}/s)\lambda^{\delta_\lambda}_{d_k} + R_k i^{\delta_{i_t}}_{td_k} e^{j\delta_{\Delta\lambda}} - \omega_g L_k i^{\delta_{i_t}}_{tq_k} e^{j\delta_{\Delta\lambda}} + V_d^{\delta_\lambda *}, \\ v^{\delta_\lambda}_{tq_k} &= (K_{p_k} + K_{i_k}/s)\lambda^{\delta_\lambda}_{q_k} + R_k i^{\delta_{i_t}}_{tq_k} e^{j\delta_{\Delta\lambda}} + \omega_g L_k i^{\delta_{i_t}}_{td_k} e^{j\delta_{\Delta\lambda}}. \end{aligned} \tag{3.45}$$

Now the weight of each inverter in the equivalent corresponding λ state can be determined as:

$$\mu_{\lambda_{d_k}} = \frac{n\lambda^{\delta_\lambda}_{d_k}}{\lambda^{\delta_\lambda}_{d_{eq}}},\ \mu_{\lambda_{q_k}} = \frac{n\lambda^{\delta_\lambda}_{q_k}}{\lambda^{\delta_\lambda}_{q_{eq}}}, \tag{3.46}$$

where $\lambda^{\delta_\lambda}_{d_{eq}} = \sum_{j=1}^{n}\lambda^{\delta_\lambda}_{d_j}$ and $\lambda^{\delta_\lambda}_{q_{eq}} = \sum_{j=1}^{n}\lambda^{\delta_\lambda}_{q_j}$. Rewriting (3.45) in terms of the equivalent states yields:

$$\begin{aligned} v^{\delta_\lambda}_{td_k} &= (K_{p_k} + K_{i_k}/s)\frac{\mu_{\lambda_{d_k}}}{n}\lambda^{\delta_\lambda}_{d_{eq}} + R_k\frac{\mu_{i_{td_k}}}{n} i^{\delta_{i_t}}_{td_{eq}} e^{j\delta_{\Delta\lambda}} - \omega_g L_k\frac{\mu_{i_{tq_k}}}{n} i^{\delta_{i_t}}_{tq_{eq}} e^{j\delta_{\Delta\lambda}} + V_d^{\delta_\lambda *}, \\ v^{\delta_\lambda}_{tq_k} &= (K_{p_k} + K_{i_k}/s)\frac{\mu_{\lambda_{q_k}}}{n}\lambda^{\delta_\lambda}_{q_{eq}} + R_k\frac{\mu_{i_{tq_k}}}{n} i^{\delta_{i_t}}_{tq_{eq}} e^{j\delta_{\Delta\lambda}} + \omega_g L_k\frac{\mu_{i_{td_k}}}{n} i^{\delta_{i_t}}_{td_{eq}} e^{j\delta_{\Delta\lambda}}. \end{aligned} \tag{3.47}$$

Now by considering $\lambda^{\delta_\lambda}_{tq_{eq}} = \sum_{j=1}^{n}\lambda^{\delta_\lambda}_{tq_j} = 0$ and $i^{\delta_{i_t}}_{tq_{eq}} = \sum_{j=1}^{n} i^{\delta_{i_t}}_{tq_j} = 0$ averaging n equation of (3.47) results in:

$$\begin{aligned} \frac{1}{n}\sum_{k=1}^{n} v^{\delta_\lambda}_{td_k} &= \sum_{k=1}^{n}\left((K_{p_k} + K_{i_k}/s)\frac{\mu_{\lambda_{d_k}}}{n^2}\right)\lambda^{\delta_\lambda}_{d_{eq}} + \sum_{k=1}^{n}\left(R_k\frac{\mu_{i_{td_k}}}{n^2}\right) i^{\delta_{i_t}}_{td_{eq}} e^{j\delta_{\Delta\lambda}} + V_d^{\delta_\lambda *}, \\ \frac{1}{n}\sum_{k=1}^{n} v^{\delta_\lambda}_{tq_k} &= \omega_g\sum_{k=1}^{n}\left(L_k\frac{\mu_{i_{td_k}}}{n^2}\right) i^{\delta_{i_t}}_{td_{eq}} e^{j\delta_{\Delta\lambda}}. \end{aligned} \tag{3.48}$$

Considering $\mu_{\lambda_{d_k}} = n\lambda_{d_k}^{\delta_\lambda}/\lambda_{d_{eq}}^{\delta_\lambda}$, where Λ and $\tilde{\lambda}$ are the steady-state and small-signal values, respectively, and $\Lambda >> \tilde{\lambda}$, thus, the weights can be estimated as $\mu_{\lambda_{d_k}} \simeq n\Lambda_{d_k}^{\delta_\lambda}/\Lambda_{d_{eq}}^{\delta_\lambda}$. Multiplying the (3.48) q-axis equation with j and adding it to the d-axis equation while considering (3.44) yields:

$$\begin{aligned} v_{td_{eq}}^{\delta_\lambda} + jv_{tq_{eq}}^{\delta_\lambda} = &\sum_{k=1}^{n}\left((K_{p_k} + K_{i_k}/s)\frac{\mu_{\lambda_{d_k}}}{n^2}\right)\left(\lambda_{d_{eq}}^{\delta_\lambda} + j\lambda_{q_{eq}}^{\delta_\lambda}\right) + \cdots \\ &\cdots + R_{eq}i_{td_{eq}}^{\delta_\lambda} + j\omega_g L_{eq}i_{td_{eq}}^{\delta_\lambda} + V_d^{\delta_\lambda *}, \\ \text{where: } v_{td_{eq}}^{\delta_\lambda} = \frac{1}{n}\sum_{k=1}^{n} v_{td_k}^{\delta_\lambda},\ v_{tq_{eq}}^{\delta_\lambda} = &\frac{1}{n}\sum_{k=1}^{n} v_{tq_k}^{\delta_\lambda}. \end{aligned} \tag{3.49}$$

Returning (3.49) to the reference frame with $(\omega t + \theta_c)$ angle by a δ_λ phase shift yields:

$$\begin{aligned} v_{td_{eq}}^{c} + jv_{tq_{eq}}^{c} = &\sum_{k=1}^{n}\left((K_{p_k} + K_{i_k}/s)\frac{\mu_{\lambda_{d_k}}}{n^2}\right)\left(\lambda_{d_{eq}}^{c} + j\lambda_{q_{eq}}^{c}\right) + \cdots \\ &\cdots + R_{eq}i_{td_{eq}}^{c} + j\omega_g L_{eq}i_{td_{eq}}^{c} + V^*. \end{aligned} \tag{3.50}$$

By comparing (3.50) with (3.41), the equivalent current controller parameters can be found as:

$$K_{p_{eq}} = \sum_{k=1}^{n}\frac{\mu_{\lambda_{d_k}}}{n^2}K_{p_k},\ K_{i_{eq}} = \sum_{k=1}^{n}\frac{\mu_{\lambda_{d_k}}}{n^2}K_{i_k}. \tag{3.51}$$

Equivalent voltage controller:

The kth inverter voltage controller model in the Laplace form and the desired reference frame with $(\omega t + \theta_c)$ angle can be given as:

$$\begin{aligned} i_{td_k}^{c^*} =&(K_{pv_k} + K_{iv_k}/s)\gamma_{d_k}^{c} - C_k\omega_g v_{oq_k}^{c}, \\ i_{tq_k}^{c^*} =&(K_{pv_k} + K_{iv_k}/s)\gamma_{q_k}^{c} + C_k\omega_g v_{od_k}^{c}. \end{aligned} \tag{3.52}$$

A single dynamic equation can be written for the kth controller by multiplying q-axis of (3.52) with j and summing it to the d-axis equation as follows:

$$i_{td_k}^{c^*} + ji_{tq_k}^{c^*} =(K_{pv_k} + K_{iv_k}/s)\left(\gamma_{d_k}^{c} + j\gamma_{q_k}^{c}\right) + j\omega_g C_k\left(v_{od_k}^{c} + jv_{oq_k}^{c}\right). \tag{3.53}$$

Similar to the previous part, (3.53) can be rewritten in the common rotating frame as:

$$i_{td_k}^{\theta_0^*} + ji_{tq_k}^{\theta_0^*} =(K_{pv_k} + K_{iv_k}/s)\left(\gamma_{d_k}^{\theta_0} + j\gamma_{q_k}^{\theta_0}\right) + j\omega_g C_k\left(v_{od_k}^{\theta_0} + jv_{oq_k}^{\theta_0}\right). \tag{3.54}$$

Deriving (3.54) in the desired reference frame with $(\omega t + \theta_c + \delta_\gamma)$ angle, where:

$$\begin{aligned} i_{td_k}^{\delta_\gamma^*} &= (K_{pv_k} + K_{iv_k}/s)\gamma_{d_k}^{\delta_\gamma} - C_k\omega_g v_{oq_k}^{\delta_\gamma}, \\ i_{tq_k}^{\delta_\gamma^*} &= (K_{pv_k} + K_{iv_k}/s)\gamma_{q_k}^{\delta_\gamma} + C_k\omega_g v_{od_k}^{\delta_\gamma}, \\ \text{and: } \tan\delta_\gamma &= \left(\sum_{j=1}^{n}\gamma_{q_j}^{\theta_0}\right) \Big/ \left(\sum_{j=1}^{n}\gamma_{d_k}^{\theta_0}\right), \end{aligned} \tag{3.55}$$

which results in $\sum_{j=1}^{n} \gamma_{q_j}^{\delta_\gamma} = 0$. Moreover, consider the phase difference between $\vec{v}_{odq_k}^{\delta_\gamma}$ and $\vec{v}_{odq_k}^{\delta_{v_o}}$ as $\delta_{\Delta\gamma}$, where:

$$(v_{od_k}^{\delta_\gamma} + jv_{oq_k}^{\delta_\gamma}) = \left(v_{od_k}^{\delta_{v_o}} + jv_{oq_k}^{\delta_{v_o}}\right) e^{j\delta_{\Delta\gamma}}. \tag{3.56}$$

Substituting (3.56) in(3.55) results in:

$$\begin{aligned} i_{td_k}^{\delta_\gamma^*} &= (K_{pv_k} + K_{iv_k}/s)\gamma_{d_k}^{\delta_\gamma} - C_k\omega_g v_{oq_k}^{\delta_{v_o}} e^{j\delta_{\Delta\gamma}}, \\ i_{tq_k}^{\delta_\gamma^*} &= (K_{pv_k} + K_{iv_k}/s)\gamma_{q_k}^{\delta_\gamma} + C_k\omega_g v_{od_k}^{\delta_{v_o}} e^{j\delta_{\Delta\gamma}}. \end{aligned} \tag{3.57}$$

Now the weight of each inverter in the equivalent corresponding γ state can be determined as:

$$\mu_{\gamma_{d_k}} = \frac{n\gamma_{d_k}^{\delta_\gamma}}{\gamma_{d_{eq}}^{\delta_\gamma}},\ \mu_{\gamma_{q_k}} = \frac{n\gamma_{q_k}^{\delta_\gamma}}{\gamma_{q_{eq}}^{\delta_\gamma}}, \tag{3.58}$$

where $\gamma_{d_{eq}}^{\delta_\gamma} = \sum_{j=1}^{n} \gamma_{d_j}^{\delta_\gamma}/n$ and $\gamma_{q_{eq}}^{\delta_\gamma} = \sum_{j=1}^{n} \gamma_{q_j}^{\delta_\gamma}/n$. Following a similar steps of (3.47) to (3.49) yields:

$$i_{td_{eq}}^{c^*} + ji_{tq_{eq}}^{c^*} = \sum_{k=1}^{n} \left((K_{pv_k} + K_{iv_k}/s)\mu_{\gamma_{d_k}}\right) \left(\gamma_{d_{eq}}^{c} + j\gamma_{q_{eq}}^{c}\right) + j\omega_g C_{eq} v_{od_{eq}}^{c}. \tag{3.59}$$

By comparing (3.59) with (3.53), the equivalent current controller parameters can be found as:

$$K_{pv_{eq}} = \sum_{k=1}^{n} \mu_{\gamma_{d_k}} K_{pv_k},\ K_{iv_{eq}} = \sum_{k=1}^{n} \mu_{\gamma_{d_k}} K_{iv_k}. \tag{3.60}$$

3.3.3 Equivalent droop controller

The equivalent system $\omega_{0_{eq}} = \omega_0 = \omega_g - m_{p_m} P_{o_m}$, therefore, $m_{p_{eq}} P_{o_{eq}} = m_{p_m} P_{o_m}$, thus:

$$\sum_{k=1}^{n} \frac{m_{p_{eq}}}{m_{p_k}} P_{o_{eq}} = \sum_{k=1}^{n} P_{o_k} \Rightarrow\ m_{p_{eq}} = 1/\sum_{k=1}^{n} \frac{1}{m_{p_k}}. \tag{3.61}$$

As $Q_{o_{eq}} = \sum_{k=1}^{n} Q_{o_k}$, and to have a proper reactive power sharing:

$$n_{q_1} Q_{o_1} \simeq \cdots \simeq n_{q_n} Q_{o_n} \simeq n_{q_{eq}} Q_{o_{eq}} \Rightarrow\ n_{q_{eq}} = 1/\sum_{k=1}^{n} \frac{1}{n_{q_k}}. \tag{3.62}$$

Finally, the equivalent $R_{v_{eq}}$ can be found similar to $R_{o_{eq}}$ as $R_{v_{eq}} = \sum_{k=1}^{n} \mu_{i_{od_k}} R_{v_k}/n^2$, because the physical realization of R_v is in series with R_o.

Table 3.1: The studied microgrids common parameters.

Parameter	Inv 1 to 4	Unit	Parameter	Inv 1 to 4	Unit
V_{DC}	200	$[V]$	R	10	$[m\Omega]$
V^*	$60.1\sqrt{2}$	$[V]$	C	2.5	$[\mu F]$
ω_g	$60\times 2\pi$	$[rad/s]$	L_o	1.0	$[mH]$
f_{sw}	20	$[kHz]$	R_o	1	$[\Omega]$
L	2.5	$[mH]$			

3.4 Simulation Results

To demonstrate the effectiveness of the suggested WD agg model, a microgrid with three grid-form inverters and a resistive load is modeled using the proposed WD agg approach in Fig. 3.4b for different conditions with similar and dissimilar parameters as shown in Fig. 3.4a. Then a fourth inverter with a similar structure to the microgrid inverters is added to the system at the PCC bus. Overall desirable performance of the system is obtained with various case studies by using a combination of stability, designing, and analysis tools, such as eigenvalue trajectory, frequency response, root-loci, and time-domain performance, that are provided in the following three subsections. Moreover, the results of the detailed and reduced-order systems are compared to validate the applicability and accuracy of the proposed model. Furthermore, the proposed model applications are compared with the existing Full aggregation and impedance models. Two recent models, the aggregation approach from [81] and the impedance model from [89], are chosen as conventional aggregated and impedance models for comparisons. To quantify the models accuracy, an error function is defined as Error $= |(P_d - P_m)|/P_d \times 100$, where P_d and P_m are the output active power of the detailed and the reduced-order models, respectively.

3.4.1 Eigenvalue trajectory and stability analyses

Case 1: The detailed and aggregated models of Figure 3.4aa system are evaluated under two stability conditions while providing power to a $R_L = 12.12$ [Ω] resistive load, with parameters identified in Table 3.1 and 3.2. Figure 3.6a shows the system output active, reactive power, and eigenvalue analysis of the detailed and the aggregated models while Figure 3.7 shows the aggregated models active power error with $R_{v_4} = 4$. As Figure 3.6a and 3.7 show, the detailed, the proposed WD agg and the conventional models are all stable while the proposed model has at least three times superior accuracy at all times. Figure 3.6a verifies that all models are stable while the proposed WD agg model predict the the dominant eigenvalues of the detailed system more accurately.
Now by decreasing the virtual resistance value to $R_{v_4} = 2$ both of the detailed and the proposed WD agg models move towards instability while the conventional model is still stable as shown in Figure 3.6b.

Table 3.2: Case 1 and 2 specifications.

Parameter	Inv 1	Inv 2	Inv 3	Inv 4	Unit
K_p	6	6	6	6	-
K_i	400	400	400	400	-
K_{pv}	0.004	0.006	0.004	0.006	-
K_{iv}	12	8	12	8	-
R_v	16	12	8	4	$[\Omega]$
m_p	6π	4π	2π	2π	$[rad/(s.kW)]$
n_q	0.6	0.4	0.2	0.1	$[V/VAr]$

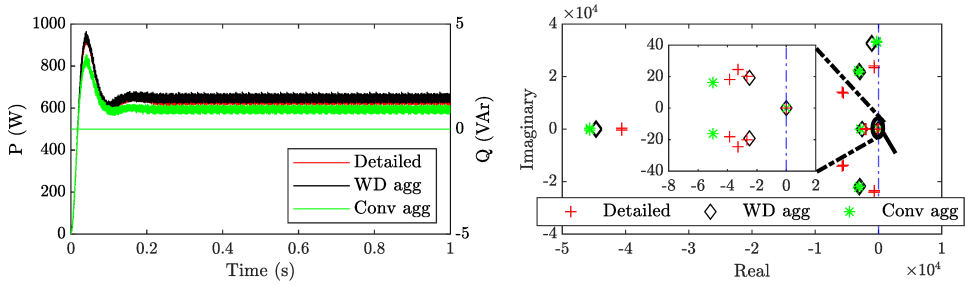

(a) $R_{v_4} = 4$.

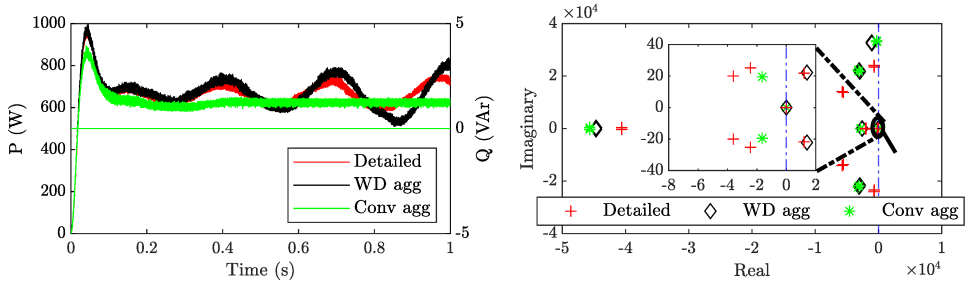

(b) $R_{v_4} = 2$.

Figure 3.6: Case 1: The system output active P, reactive power Q, and the corresponding eigenvalues map for: a) $R_{v_4} = 4$, b) $R_{v_4} = 2$.

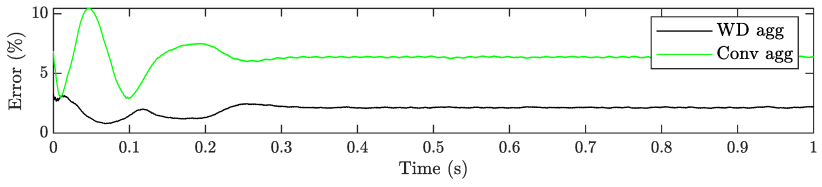

Figure 3.7: Case 1: The aggregated models active power error in Figure 3.6a.

Case 2: Figure 3.8a shows the eigenvalue trajectory of the detailed, conventional, and proposed WD agg models when K_{iv_4} is increased from 1 to 5, and $K_{p_1} = K_{p_2} = K_{p_3} = K_{p_4} = 0.6$. Figure 3.8b also shows the eigenvalue trajectory of the detailed,

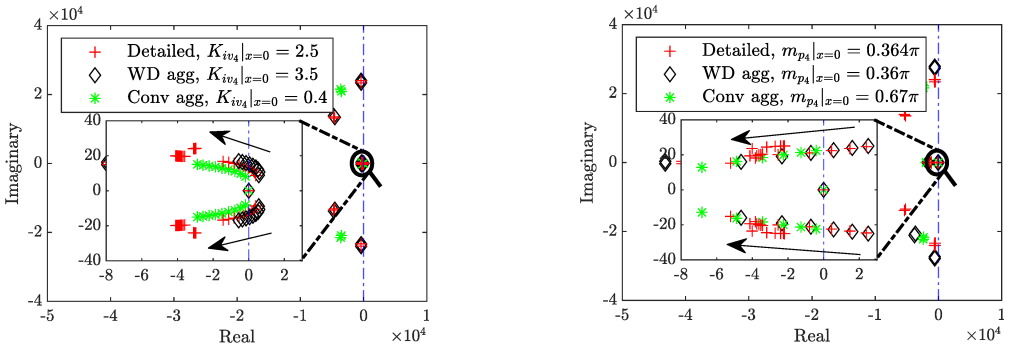

(a) $K_{iv_4} = 1$ to 5. (b) $m_{p_4} = 6\pi[\frac{rad}{skW}]$ to $1\pi[\frac{rad}{skW}]$.

Figure 3.8: Case 2: The eigenvalue trajectory of the detailed, the conventional and the proposed WD agg models for changes in K_{iv_4} and m_{p_4}.

conventional, and proposed WD agg models when m_{p_4} decreased from 6π $[\frac{rad}{skW}]$ to 1π $[\frac{rad}{skW}]$, $K_{p_1} = K_{p_3} = 5$, and $K_{p_2} = K_{p_4} = 3$. The rest of the system parameters can be found in Table 3.1 and 3.2. As Figure 3.8a and 3.8b illustrate all models move towards stability by increasing K_{iv_4} and/or decreasing m_{p_4}, while the proposed WD agg model more accurately predicts the corresponding parameter for a marginally stable system.

Case 3: A stability analysis of a microgrid with parameters from Table 3.3, and various droop coefficients n_q is conducted using both WD agg eigenvalue analyses and characteristic loci analyses as proposed in [89]. Figure 3.9 demonstrates that both of the impedance and proposed WD agg models predict the stability of the system when $n_{q_4} = 0.01$. The time-domain results of the detailed and WD agg models also verify the stability of the system. However, by increasing the droop coefficient value to $n_{q_4} = 0.2$, similar to detailed model, the proposed WD agg eigenvalue analyses predicts the instability of the system accurately, while the characteristic loci of the impedance model still predicts a stable system. The impedance model predicts the instability at $n_{q_4} = 0.4$.
Figure 3.10 shows the overall output admittance of the inverters with low and high droop coefficients n_{q_4}. Figure 3.10 illustrates that with higher n_{q_4} inverters output admittance decreases that results in less stable system, because $|Y_{inv}Z_{load}|$ will have higher values. Figure 3.10 also shows the accuracy of the proposed WD agg model in mimicking the system response and output admittance in different time-scales and frequencies.

3.4.2 Steady-state and dynamic performance investigations

Case 4: Figure 3.11a shows the performance of the detailed and WD agg models with $R_L = 16$ [Ω] load and various K_i values. The rest of the system parameters can be found in Table 3.1 and 3.4. As Figure 3.11a shows the transient duration decreases by increasing the controllers K_i values. Also, Figure 3.11a shows that the

Table 3.3: Case 3, 6, and 7 specifications.

Parameter	Inv 1	Inv 2	Inv 3	Inv 4	Unit
R	0.10	0.05	0.01	0.01	$[\Omega]$
L	3.5	2.0	1.5	2.5	$[mH]$
C	1.5	2.5	2.0	2.5	$[\mu F]$
L_o	1.5	1.0	0.5	1.0	$[mH]$
R_o	0.8	1.2	0.2	1.0	$[\Omega]$
K_p	8	4	2	2	-
K_i	1600	800	400	400	-
K_{pv}	0.016	0.012	0.008	0.016	-
K_{iv}	12	8	4	12	-
R_v	16	12	8	8	$[\Omega]$
m_p	4π	2π	1π	1π	$[rad/(s.kW)]$
n_q	6	4	2	1	$[V/VAr]$

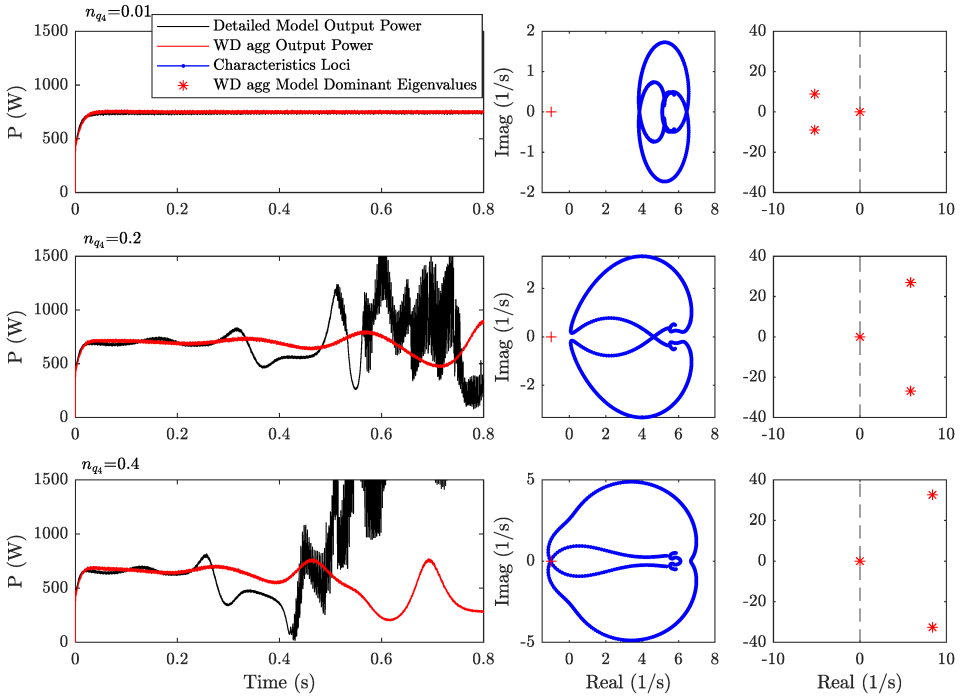

Figure 3.9: Case 3: The proposed WD agg eigenvalue analyses, characteristic loci of existing impedance models, and the system time-domain validation for stability analysis comparison.

proposed model follows the dynamic behavior of the detailed system accurately with a similar features such as damping duration, low-frequency dominant oscillation, and high-frequency sub-oscillation.

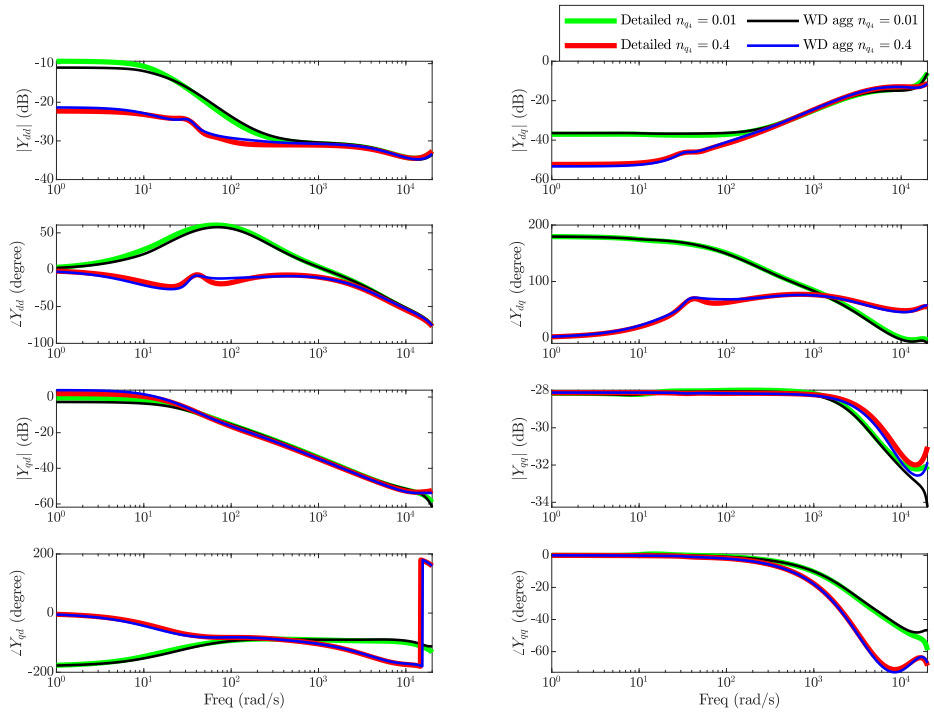

Figure 3.10: Case 3: The overall output admittance of the inverters with low and high droop coefficients n_{q_4} for the both detailed and proposed WD agg models.

Table 3.4: Case 4 specifications.

Parameter	Inv 1	Inv 2	Inv 3	Inv 4	Unit
K_p	0.1	0.1	0.1	0.1	-
K_{pv}	0.001	0.001	0.001	0.001	-
K_{iv}	8	6	8	6	-
R_v	16	12	16	12	$[\Omega]$
m_p	8π	4π	8π	4π	$[rad/(s.kW)]$
n_q	0.4	0.2	0.4	0.2	$[V/VAr]$

Table 3.5: Case 5 specifications.

Parameter	Inv 1	Inv 2	Inv 3	Inv 4	Unit
K_i	400	400	400	400	-
K_{pv}	0.004	0.006	0.004	0.006	-
K_{iv}	12	8	12	8	-
R_v	16	12	8	4	$[\Omega]$
m_p	6π	4π	2π	2π	$[rad/(s.kW)]$
n_q	0.6	0.4	0.2	0.1	$[V/VAr]$

Case 5: Figure 3.11b shows the performance of the detailed and WD agg model with $R_L = 12$ $[\Omega]$ load and various K_p values. A load increase to $R_L = 6$ $[\Omega]$ is applied

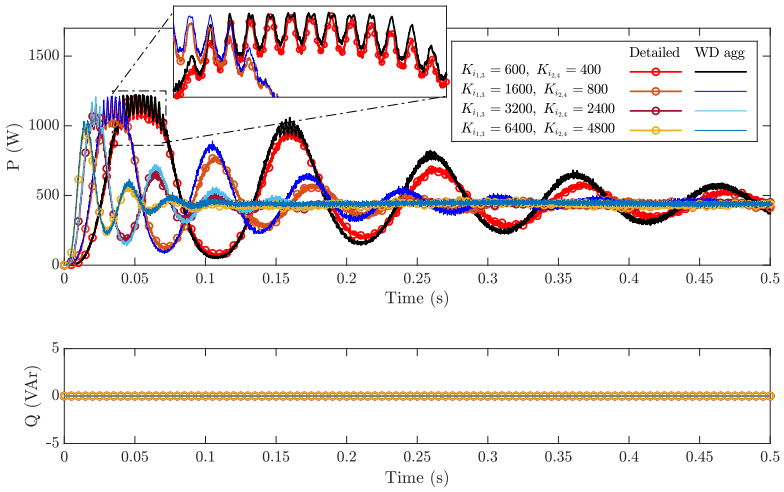

(a) Case 4: Various K_i values.

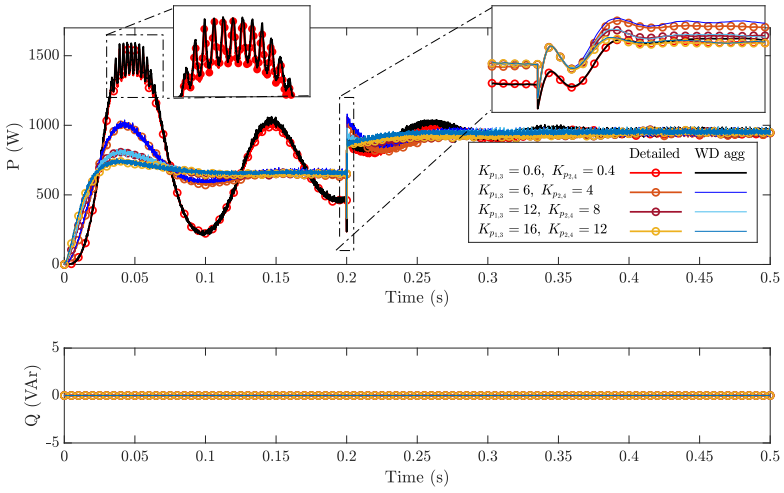

(b) Case 5: Various K_p values.

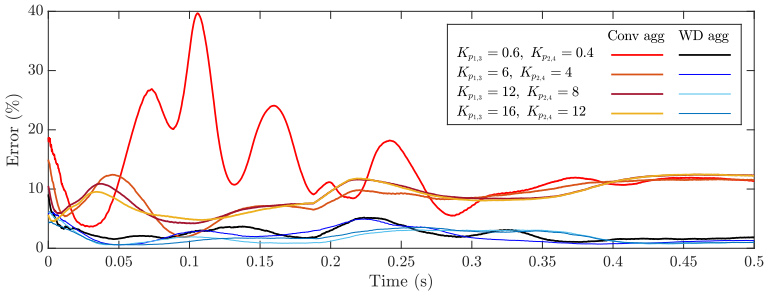

(c) Active power error for Figure 3.11b.

Figure 3.11: Case 4 & 5: The output power performance of the detailed, the proposed WD agg, and the Conv agg models for various K_i and K_p.

at t=0.2s. The rest of the system parameters can be found in Table 3.1 and 3.5. As Figure 3.11b shows the transient overshoot decreases by increasing the controllers

K_p values. Also, Figure 3.11b shows that the proposed model follows the dynamic behavior of the detailed system accurately with a similar features such as transient duration, dominant low-frequency oscillation, and high-frequency sub-oscillation. For the same circuit parameters of Figure 3.11b, Figure 3.11c shows the active power error of proposed WD agg and conventional models, verifying the accuracy of the proposed approach. Moreover, representing the first three inverters of the detailed system with a single equivalent inverter has reduced computation time by approximately twofold, all while preserving model accuracy.

3.4.3 Frequency response and root-loci analyses

Case 6 & 7: The microgrid consisting of four inverters, with the parameters given in Table 3.3, is chosen for Case 6 to study the frequency response and root-loci. Case 7 assumes Case 6 parameters, where K_p values are increased 10 times to investigate various control parameters scenarios. Figure 3.12 shows the open-loop frequency response of Inv 4 controller for output voltage signal to the input ω_g and V^* signals. As Figure 3.12 demonstrates that the proposed WD agg model provides similar gain and phase margins compared with the detailed system which makes it suitable for the controller stability analyses. Figure 3.13 verifies the accuracy of the WD agg model by studying the root-loci for Inv 4 controller output voltage signal to the input ω_g and V^* signals.

3.4.4 Large-scale microgrid application

Case 8: In order to demonstrate the practical application of the proposed WD agg approach in large-scale systems, we have utilized it to model the CIGRE MV/LV benchmark shown in Figure 3.14 for renewable energies (proposed in [90]) in islanded mode. To provide the rated 20 $[kV]$ voltage for the system, a battery bank comprising four paralleled droop-controlled three-phase inverters with the parameters specified in Table 3.6 has been added to Bus 3. To analyze the transient behavior of the system, three-phase line-to-line short circuits with an impedance of $R_g = 1$ $[m\Omega]$ was applied and cleared after 20 $[ms]$ at Bus 3 (at $t = 1$ $[s]$) and at Bus 10 (at $t = 1.5$ $[s]$).
In Figure 3.15 and 3.16, a comparison is presented between the detailed system and the WD agg model in terms of active power, reactive power, instantaneous voltage, and current, along with their respective RMS values. The results obtained from the proposed WD agg model validate its accuracy in replicating the dynamic and steady-state behavior of large-scale practical systems.
One of the main requirements of aggregation methods is that the aggregated units should have a proper coherency. However, we can utilize the coherency identification technique introduced in [91] to evaluate the coherency status among the microgrid buses across all temporal intervals. To provide additional evidence of the accuracy exhibited by the proposed WD agg model in emulating the dynamic behavior of the intricate system, a comparison is made between the coherency indices, $CC_{i,j}$, of the generating buses within the detailed system and those within the WD agg model. The results are presented in Table 3.7. Moreover, the successful incorporation of the

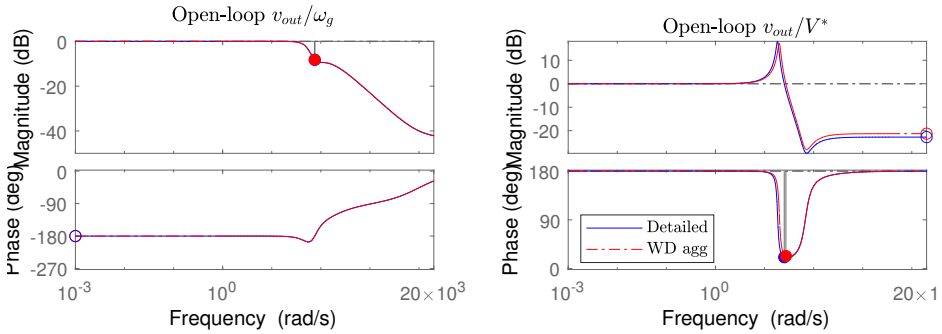

(a) Case 6.

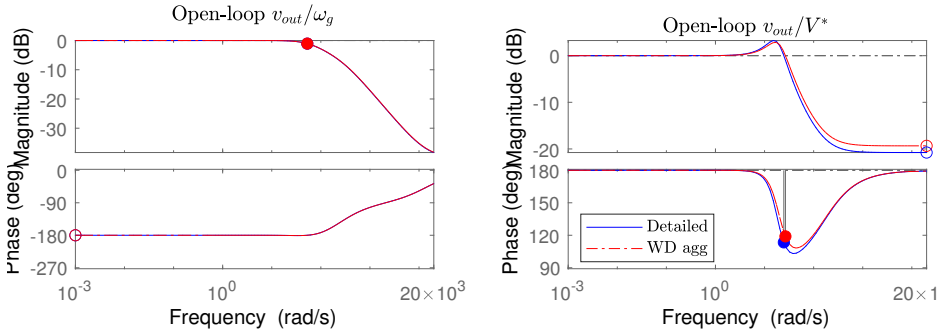

(b) Case 7.

Figure 3.12: Case 6 & 7: The open-loop frequency response of the Inv 4 controller for Case 5 and 6 output voltage to the input ω_g and V^* signals.

Table 3.6: Case CIGRE benchmark Bus 3 battery bank inverters specifications.

Parameter	Inv 1	Inv 2	Inv 3	Inv 4	Unit
V_{DC}	15	15	15	15	$[kV]$
V_o	6.9	6.9	6.9	6.9	$[kV]$
ω_g	$2\pi\times$ 60	$2\pi\times$ 60	$2\pi\times$60	$2\pi\times$60	$[rad/s]$
R	1.67	2.5	1.67	2.5	$[m\Omega]$
L	416.7	333.4	416.7	333.4	$[\mu H]$
C	15	18	15	18	$[\mu F]$
L_o	200	166.7	200	166.7	$[\mu H]$
R_o	150	166.7	150	166.7	$[m\Omega]$
K_p	6	4	6	4	-
K_i	180	120	180	120	-
K_{pv}	0.024	0.0192	0.024	0.0192	-
K_{iv}	12	8	12	8	-
R_v	2	1	2	1	$[\Omega]$
m_p	2π	π	2π	π	$[rad/(s.GW)]$
n_q	0.15	0.1	0.15	0.1	$[V/kVAr]$

WD agg model is expanded to encompass coherency zone identification for extensive

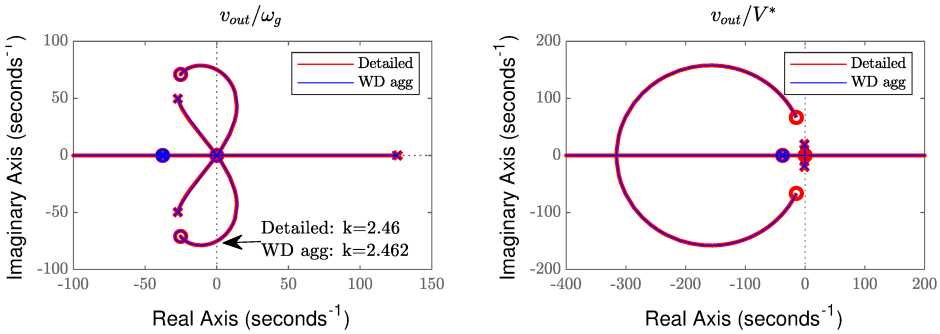

(a) Case 6.

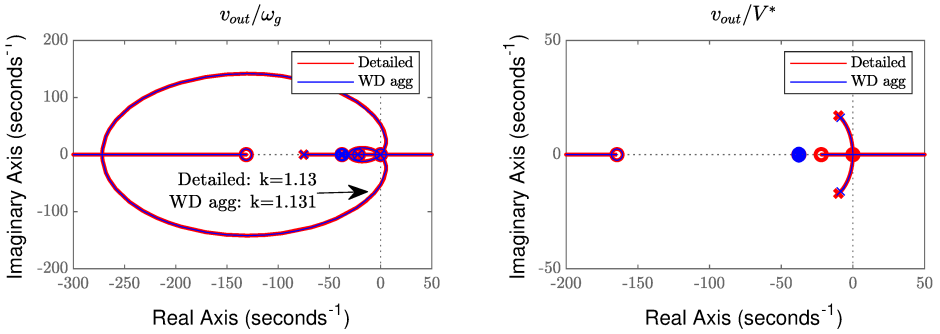

(b) Case 7.

Figure 3.13: Case 6 & 7: the root-loci for Inv 4 controller output voltage signal to the input ω_g and V^* signals.

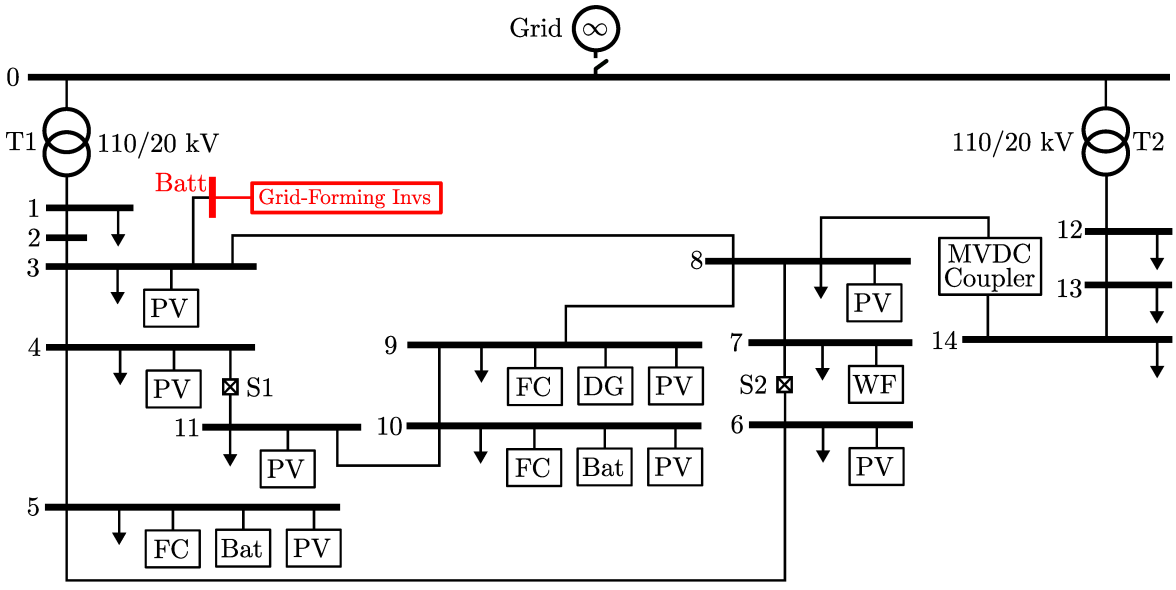

Figure 3.14: CIGRE MV/LV 14-Bus for renewable energies.

systems, exemplified by its effective application to the MV/LV CIGRE benchmark. Furthermore, the computational efficiency of the detailed model and the proposed WD agg model are compared in Table 3.8, revealing that the proposed model outperforms

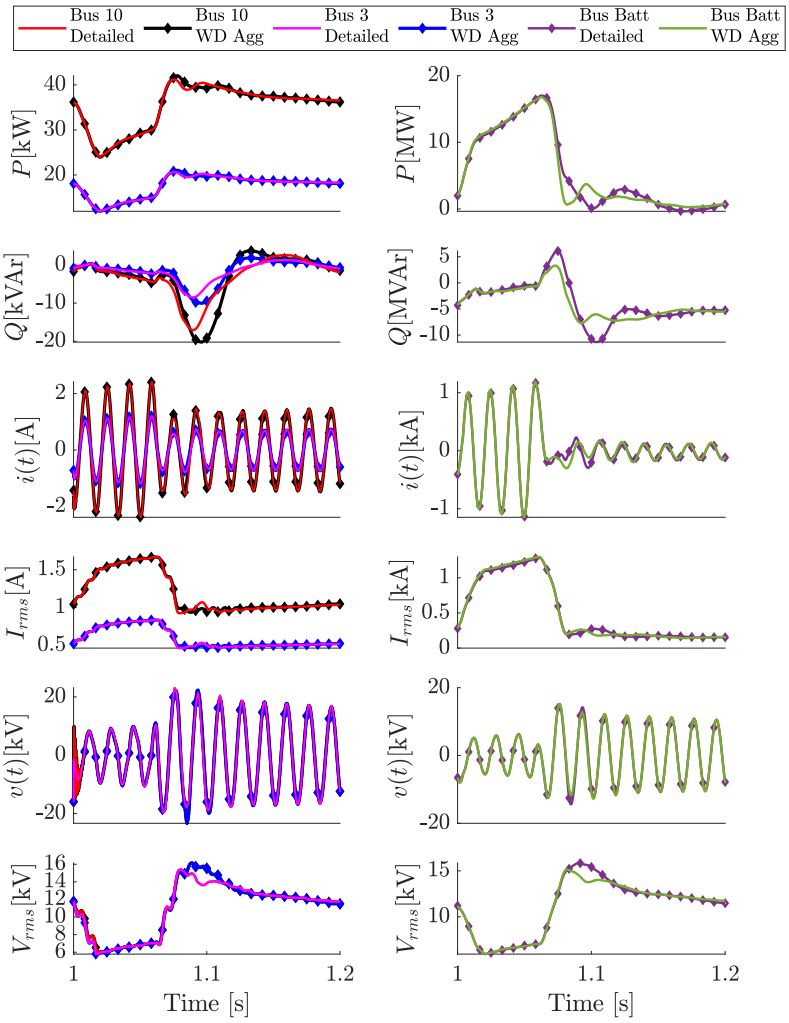

Figure 3.15: Case 8 line-to-line fault at Bus 3: P active power, Q reactive power, $i(t)$ instantaneous output current, I_{rms} output rms current, $v(t)$ instantaneous output voltage, and V_{rms} bus rms phase voltage for PV units at Bus 3, Bus 10, and Bus Batt.

the detailed model by being more than five times faster. This comparison confirms the practical applicability of the proposed method in such systems.

3.5 Experimental Results

To verify the proposed modeling approach a system with four paralleled inverters similar to Figure 3.4a is implemented experimentally as shown in Figure 3.17 and parameters of Table 3.1. The experimental part numbers can also be found in Table 3.10.

Case Exp 1: To evaluate the system performance and dynamic behavior of the experimental setup with Table 3.9 parameters, three voltage reference steps are ap-

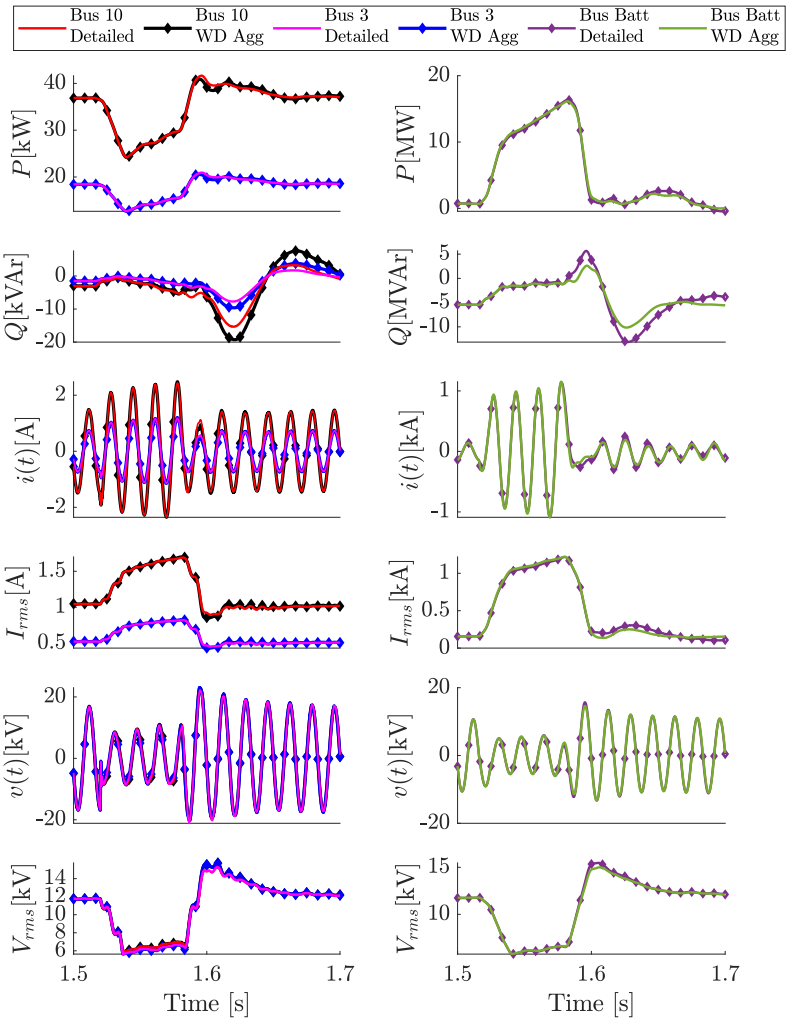

Figure 3.16: Case 8 line-to-line fault at Bus 10: P active power, Q reactive power, $i(t)$ instantaneous output current, I_{rms} output rms current, $v(t)$ instantaneous output voltage, and V_{rms} bus rms phase voltage for PV units at Bus 3, Bus 10, and Bus Batt.

plied at $t = 1$s, $t = 2$s, and $t = 3$s, respectively. Figure 3.18 shows the experimental three-phase current, voltage, active, and reactive powers. Figure 3.19a verifies the accuracy of the proposed WD agg approach by comparing the output power of the experimental system and the proposed WD agg model. Figure 3.19b validates that the proposed WD agg model accurately mimics the experimental system behavior and instantaneous wave forms such as phase voltage and output current.

Case Exp 2: The experimental setup consists of four inverters, a resistive load with a value of 34 [Ω], and the parameters specified in Table 3.11 and 3.12 are incorporated to validate the performance of the proposed WD agg model considering unequal input DC voltages and various control parameters. The implemented experimental setup allows for direct comparison between the measured results and the results obtained

Table 3.7: Distinct Coherency Zones of $\gamma = 0.99$ for Bus 3 to 11.

Zone	$CC_{i,j}$	Start-up ($t = 0$[s] to 1[s])		During Bus 3 fault ($t = 1.0$[s] to 1.06[s])	
		Detailed	WD agg	Detailed	WD agg
Zone 1	$CC_{3,4}$	0.9999	0.9999	0.9999	0.9999
	$CC_{3,5}$	0.9998	0.9998	0.9999	0.9999
	$CC_{3,6}$	0.9997	0.9996	0.9999	0.9999
	$CC_{3,7}$	0.9994	0.9992	0.9998	0.9982
	$CC_{3,8}$	0.9998	0.9998	0.9998	0.9997
	$CC_{3,9}$	0.9996	0.9996	0.9996	0.9996
	$CC_{3,10}$	0.9997	0.9997	0.9996	0.9996
	$CC_{3,11}$	0.9997	0.9997	0.9996	0.9996

Zone	$CC_{i,j}$	During Bus 10 fault ($t = 1.52$[s] to 1.58[s])	
		Detailed	WD agg
Zone 1	$CC_{3,4}$	0.9999	0.9999
	$CC_{3,5}$	0.9999	0.9999
	$CC_{3,6}$	0.9999	0.9999
Zone 2	$CC_{7,8}$	0.9930	0.9936
Zone 4	$CC_{10,11}$	0.9999	0.9999

Table 3.8: Models computational time comparison.

Model	Detailed	WD agg	Unit
Computational time	17290	3385	$[s]$

Table 3.9: Case Exp 1 setup specifications.

Parameter	Inv 1	Inv 2	Inv 3	Inv 4	Unit
K_p	6	6	6	6	-
K_i	400	400	400	400	-
K_{pv}	0.006	0.0048	0.006	0.0048	-
K_{iv}	120	80	120	80	-
R_v	16	12	16	12	$[\Omega]$
m_p	8π	4π	8π	4π	$[rad/(s.kW)]$
n_q	0.06	0.04	0.06	0.04	$[V/VAr]$

from the proposed WD agg model. This comparison serves to validate the accuracy of the proposed method in predicting the steady-state and dynamic behavior of the actual system under different control parameters. Figure 3.20 depicts the active and reactive power outputs of both the experimental system and the proposed WD agg model. The figure demonstrates that by increasing the values of K_p while keeping K_i constant, or by decreasing the values of K_i while keeping K_p constant, a more desirable performance with reduced overshoot can be achieved.

Table 3.10: Experimental part numbers.

Device	Part Number
Controller	dSpace MicroLabBox
Switches	STF23N80K5
Current Sensors	TMCS1101A1UQDRQ1
Voltage Sensors	LV 25-P
DC Source 1 & 2	California Instruments AST 3003
DC Source 3	Chroma 62050H-600S
DC Source 4	Keysight N8937APV

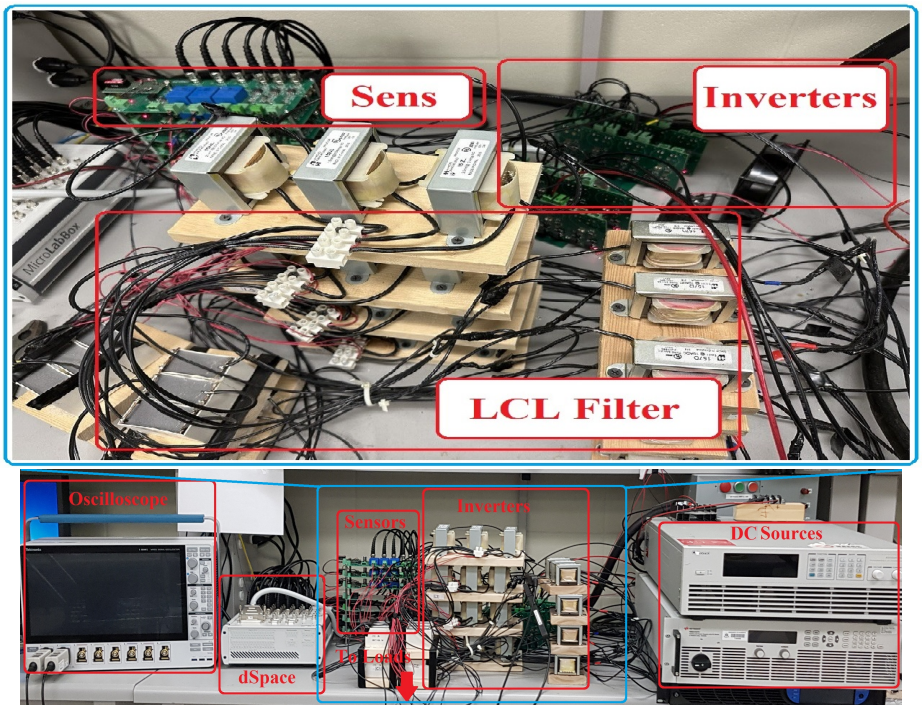

Figure 3.17: Experimental setup.

Table 3.11: Case Exp 2 & 3 common specifications.

Parameter	Inv 1	Inv 2	Inv 3	Inv 4	Unit
L	2.5	2.5	2.5	2.5	$[mH]$
R	280	280	280	280	$[m\Omega]$
C	2.5	2.5	2.5	2.5	$[\mu F]$
L_o	1.0	1.0	1.0	1.0	$[mH]$
R_o	1.0	1.0	1.0	1.0	$[\Omega]$
R_v	24	18	24	18	$[\Omega]$
m_p	8π	4π	8π	4π	$[rad/(s.kW)]$
n_q	0.6	0.4	0.6	0.4	$[V/VAr]$

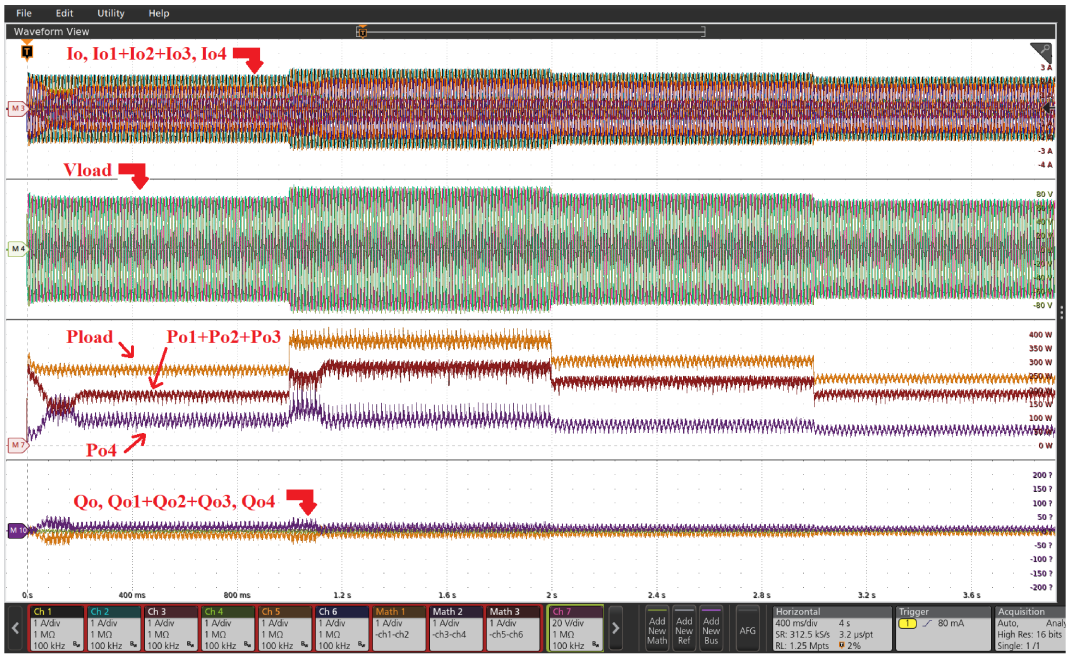

Figure 3.18: Case Exp 1: Experimental load three-phase current, voltage, active, and reactive powers for various voltage reference signals.

Table 3.12: Case Exp 2 specifications.

Parameter	Inv 1	Inv 2	Inv 3	Inv 4	Unit
V_{DC}	275	250	262.5	250	$[V]$
V_o	75	75	75	75	$[V]$
K_p (decreasing K_i)	6	4	6	4	-
K_i (increasing K_p)	60	40	60	40	-
K_{pv} (decreasing K_i)	0.006	0.0048	0.006	0.0048	-
K_{pv} (increasing K_p)	0.009	0.006	0.009	0.006	-
K_{iv}	4.8	3.2	4.8	3.2	-

Case Exp 3: Another experimental setup was implemented, also consisting of four inverters, a 34 $[\Omega]$ resistive load, and the parameters specified in Table 3.11 and 3.13 to validate the performance of the proposed WD agg in tuning control parameters discussed as Case 6. The measured results were compared with the predictions of the proposed WD agg model to further validate its accuracy in predicting the steady-state and dynamic behavior of the system under different control parameters. Figure 3.21 displays the output active and reactive power of both the experimental system and the proposed WD agg model. It is observed from Figure 3.21 that the transient duration can be decreased by increasing the K_i values.

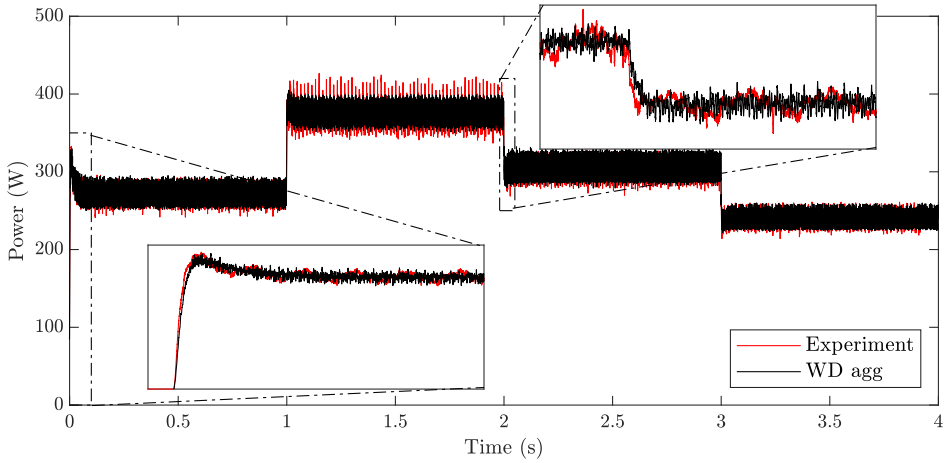

(a) Output power comparison.

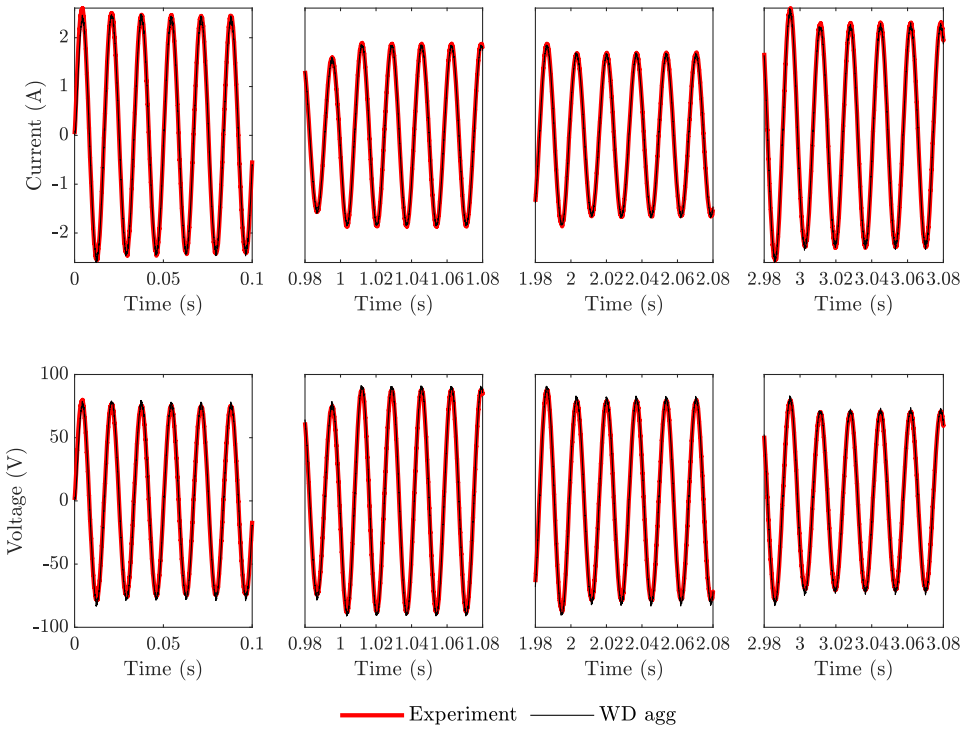

(b) Output phase current and voltage comparison.

Figure 3.19: Case Exp 1: The output power, phase current, and phase voltage comparison of experimental system and the proposed WD agg model.

3.6 Conclusion

This chapter presents a novel modeling approach for representing large networks of inverters with droop control power sharing using one equivalent inverter and a controller. The parameters of the proposed WD agg model are obtained by quantifying the contribution of each state to the corresponding equivalent state. The effectiveness

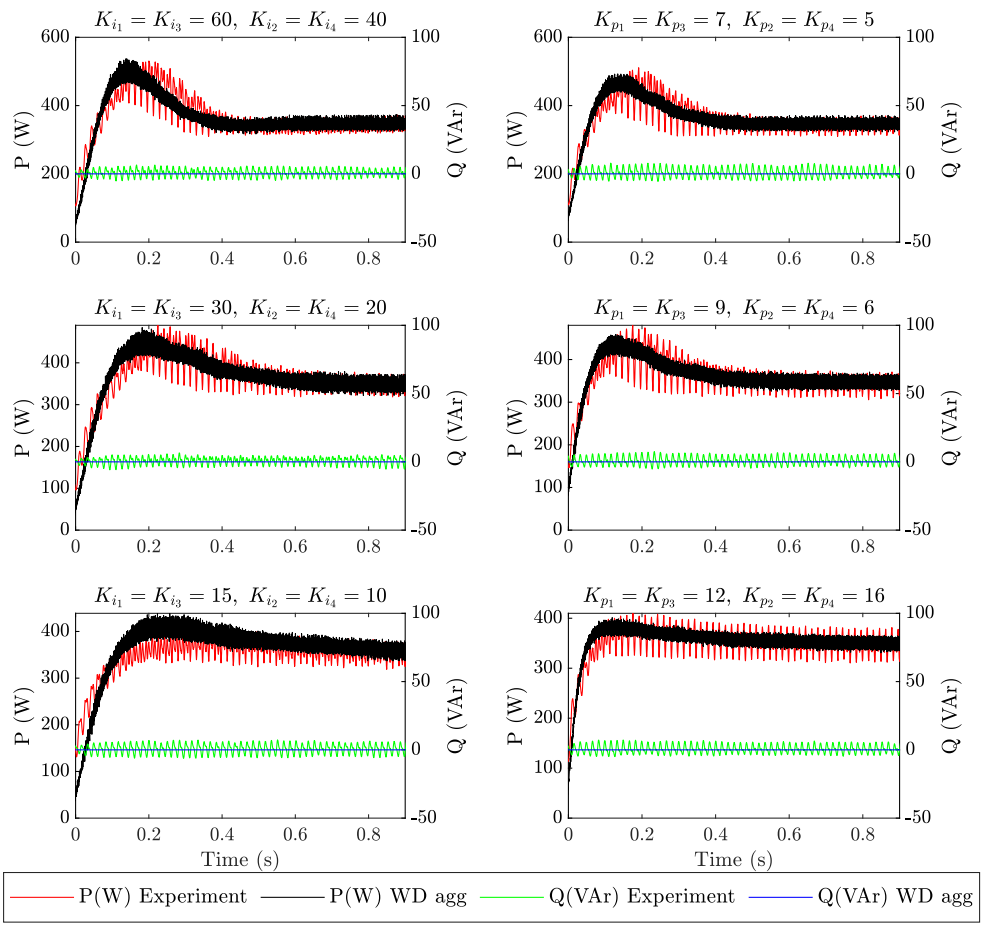

Figure 3.20: Case Exp 2: The active and reactive power performance comparison between the proposed WD agg model and experimental results for various control parameters.

Table 3.13: Case Exp 3 increasing K_i specifications.

Parameter	Inv 1	Inv 2	Inv 3	Inv 4	Unit
V_{DC}	220	200	210	200	$[V]$
V_o	60	60	60	60	$[V]$
K_p	6	4	6	4	-
K_{pv}	0.012	0.0096	0.012	0.0096	-
K_{iv}	1.2	0.8	1.2	0.8	-

of the WD agg model was determined through simulations and experiments with a microgrid composed of four grid-forming parallel inverters connected to a resistive load. The results showed that when there is a 300% difference in control parameters, the WD agg model has a maximum error of 5%, while other conventional methods may have errors up to 40%. The proposed WD agg method accurately replicates the detailed system behavior in large-scale systems, such as the CIGRE MV/LV bench-

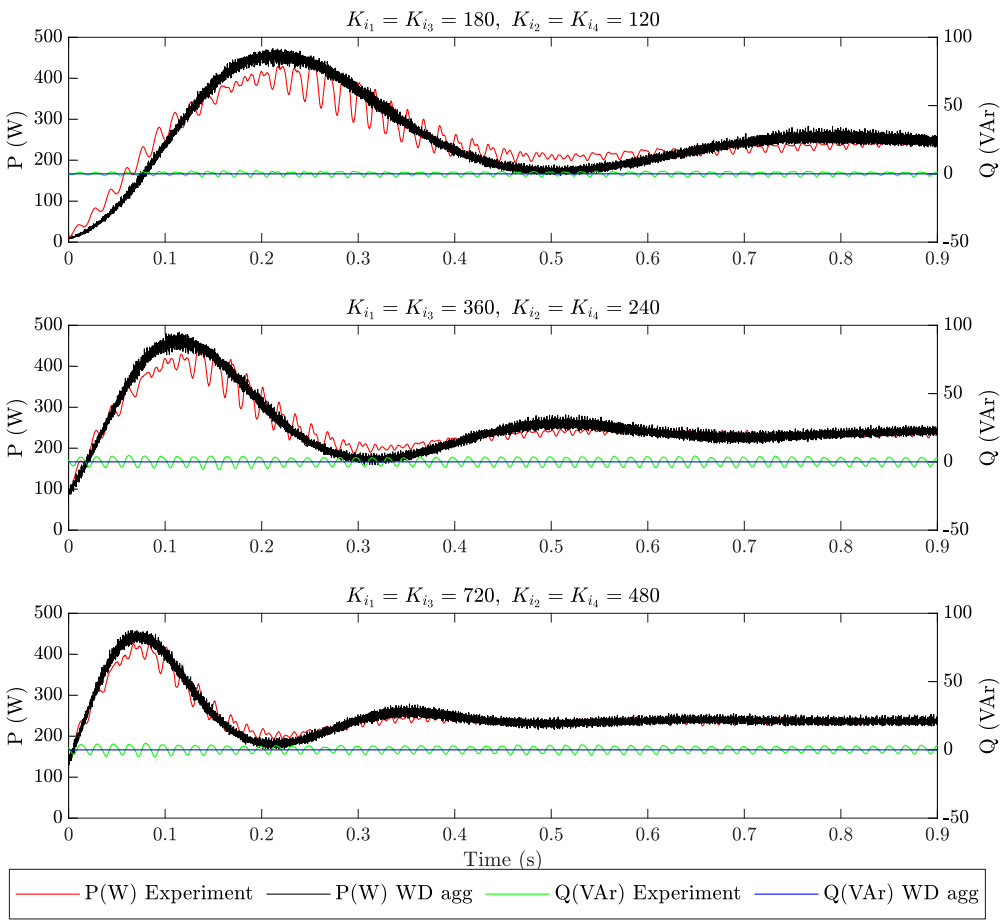

Figure 3.21: Case Exp 3: The active and reactive power performance comparison between the proposed WD agg model and experimental results for various start-up transient duration.

mark for renewable energies, with various control parameters and input changes, while reducing the computational burden by at least five times compared to detailed modeling approach. The single equivalent unit is derived through a one-time calculation, resulting in significantly less computational burden and model complexity compared to other methods such as the equivalent admittance and clustering approaches. Moreover, it is shown that the WD agg model can be effectively used for stability analysis due to superior accuracy of bode diagrams, eigenvalue trajectory and root-loci analyses.

Chapter 4

WD Aggregation Applications in DG Integrated Hybrid Microgrids with Non-linear DC Source

This chapter focuses on the application of the WD (Weighted-Dynamic) aggregation method to PV (Photovoltaic) farms equipped with grid-following inverters. The aim is to examine the accuracy and challenges of the proposed WD aggregation model for grid-following inverters with non-linear DC sources. In this study, the WD aggregation model is employed to combine multiple parallel grid-following inverters, their associated PV arrays, control systems, and collector lines into an equivalent single grid-following inverter system, single PV array, control system, and collector line. The parameters of the proposed model are determined through a weighted average of the corresponding PV unit parameters. The weighting of each inverter is based on its contribution to the desired dynamic behavior of the overall system. The application of this proposed model is demonstrated in power system planning and evaluation of system performance under various stability conditions.
Furthermore, the chapter investigates the challenges of applying the WD aggregation approach to PV units with double-stage power conversion. It is shown that the WD aggregation method effectively models photovoltaic units equipped with a maximum power point tracking (MPPT) algorithm and a boost converter for power conversion, even in the presence of significant parameter disparities. The proposed model accurately preserves crucial features of a PV farm, such as PV curves, shading effects, and input irradiance, making it highly suitable for solar farm studies. To evaluate the performance of the proposed method, extensive time-domain simulations

---

- N. Shabanikia and S. A. Khajehoddin, "Weighted Dynamic Aggregation Modeling of Grid-Following Inverters to Analyze Renewable DG Integrated Microgrids," in *IEEE Transactions on Industrial Electronics*, vol. 71, no. 1, pp. 583-594, Jan. 2024 [92].
- N. Shabanikia and S. A. Khajehoddin, "Single Equivalent PV Inverter Model for PV Farms with Substantial Parameter Disparities Using WD agg Approach," *25th European Conference on Power Electronics and Applications (EPE ECCE)*, Aalborg, Denmark, 2023.

are conducted on PV farms consisting of three paralleled PV units with substantial parameter disparities. These simulations cover various case studies involving different stability conditions and irradiation inputs. The results showcase the effectiveness and reliability of the WD aggregation model in mimicking the steady-state, transient, and dynamic behavior of PV systems when uncertainties in the system parameters are negligible. The proposed model is also applied to CIGRE HV/MV 14-bus benchmark for renewable energies to show the functionality of the proposed model in large-scale and practical systems.

4.1 PV Farm Model with Grid-Following Inverters without DC-DC Power Stage

A grid-following PV farm with n paralleled PV units shown in Figure 4.1(a). Each inverter is controlled locally using an outer DC-link voltage loop and inner current control loop, illustrated in Figure 4.2. The detailed model of the studied system can be discussed in the following five sections:

4.1.1 PV array model

Each PV array can be modeled by a variable current source, where the output current is:

$$i_{pv} = I_{sc}(1 - C_1(e^{\frac{v_{dc}}{C_2 V_{oc}}} - 1)),$$
$$C_1 = (1 - \frac{I_{mp}}{I_{sc}})e^{\frac{-V_{mp}}{C_2 V_{oc}}}, \quad C_2 = (\frac{V_{mp}}{V_{oc}} - 1)/\ln(1 - \frac{I_{mp}}{I_{sc}}), \tag{4.1}$$

where v_{dc} is the DC-link voltage, I_{sc} is the PV array short circuit current, V_{oc} is the PV array open circuit voltage, and I_{mp} and V_{mp} are the PV array maximum power operating current and voltage, respectively.

4.1.2 DC-link bus model

DC-link consists of a capacitor connecting a PV array to a 3-leg bridge inverter. The DC-link model can be shown as:

$$C_{dc}\frac{d}{dt}v_{dc} = i_{pv} - i_{dc}, \tag{4.2}$$

where C_{dc} is DC-link capacitor and $i_{dc} = p_{dc}/v_{dc}$, thus $i_{dc} = 3(v_{td}i_{td} + v_{tq}i_{tq})/2v_{dc}$, where v_{tdq} and i_{tdq} are the inverter output dq frame voltages and currents, respectively.

4.1.3 Inverter controller model

Each inverter controller has a local Phase-Lock-Loop (PLL) with the following model [93]:

$$\frac{d}{dt}\theta = K_{p_{pll}}v_{oq}^{c} + K_{i_{pll}}\phi \quad , \quad \frac{d}{dt}\phi = v_{oq}^{c},$$

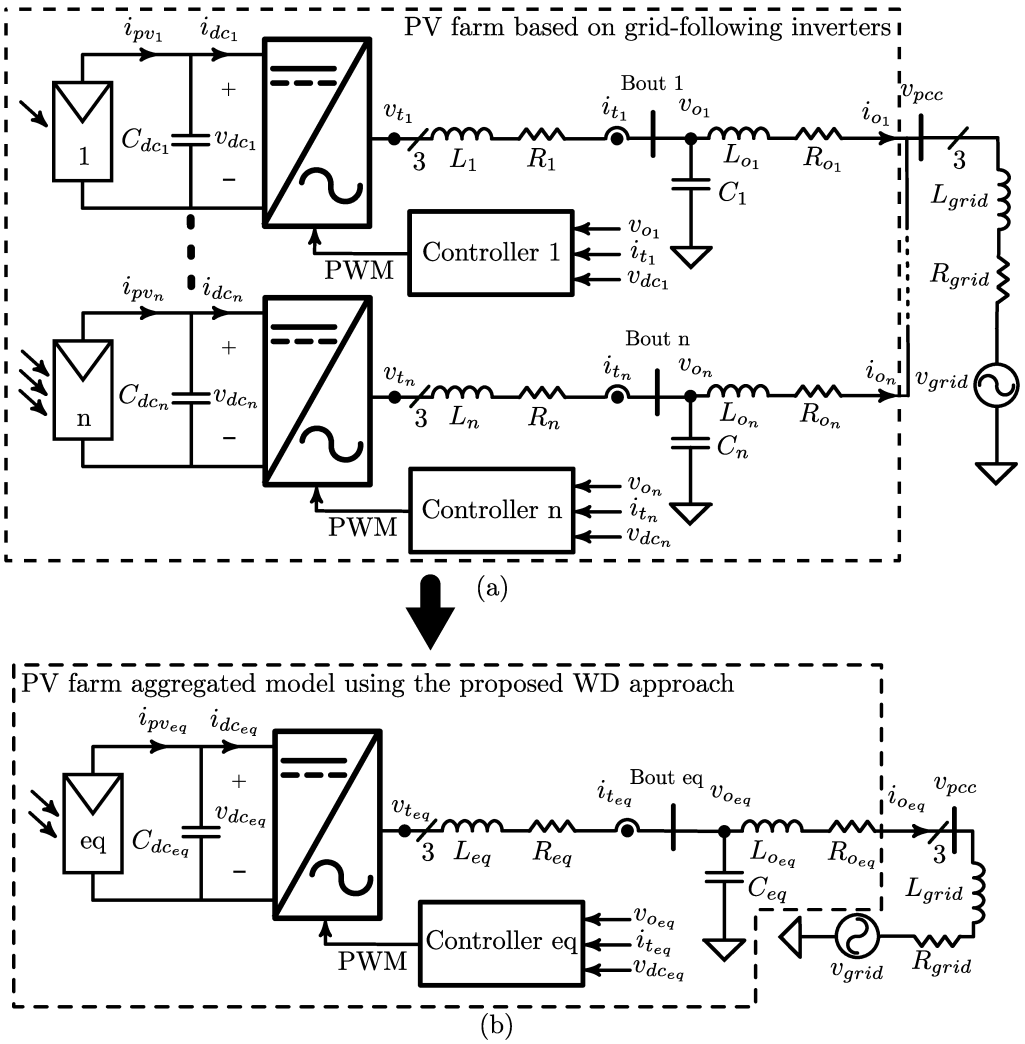

Figure 4.1: a) PV farm with grid-following inverters, b) The equivalent WD agg model.

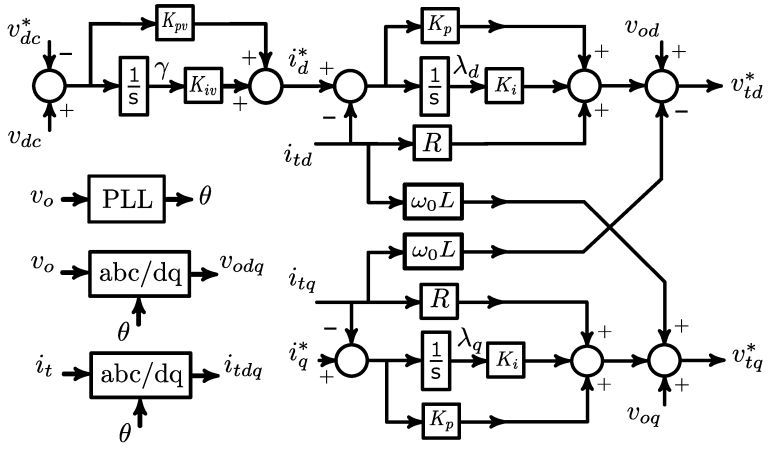

Figure 4.2: Grid-following inverter control block diagram.

$$\text{where: } v^c_{od_k} = v_{od_k}\cos\delta_k + v_{oq_k}\sin\delta_k,\ v^c_{oq_k} = v_{oq_k}\cos\delta_k - v_{od_k}\sin\delta_k, \tag{4.3}$$

$\delta_k = \theta_k - \theta_1$ for kth inverter, and v_{odq} are the output filter capacitor d-q frame voltages. As Figure 4.2 shows the DC-link voltage controller can be derived as:

$$\frac{d}{dt}\gamma = v_{dc} - v^*_{dc}, \tag{4.4}$$

where v^*_{dc} is the DC-link voltage reference signal. Finally, the inner current control loop of each inverter can be modeled as:

$$\begin{gathered}\frac{d}{dt}\lambda_d = i^*_d - i^c_{td},\ \frac{d}{dt}\lambda_q = i^*_q - i^c_{tq},\ i^*_d = K_{pv}(v_{dc} - v^*_{dc}) + K_{iv}\gamma,\ i^*_q = Q^*, \\ i^c_{td} = i_{td}\cos\theta + i_{tq}\sin\theta \quad , \quad i^c_{tq} = i_{tq}\cos\theta - i_{td}\sin\theta.\end{gathered} \tag{4.5}$$

4.1.4 LCL filter model

The inverter output filter model can be given as:

$$\begin{gathered}(L_o\frac{d}{dt} + R_o)i_{od} - \omega_0 L_o i_{oq} = v_{od} - v_{gd},\ C\frac{d}{dt}v_{od} - \omega_0 C v_{oq} = i_{td} - i_{od}, \\ (L_o\frac{d}{dt} + R_o)i_{oq} + \omega_0 L_o i_{od} = v_{oq} - v_{gq},\ C\frac{d}{dt}v_{oq} + \omega_0 C v_{od} = i_{tq} - i_{oq}, \\ (L\frac{d}{dt} + R)i_{td} - \omega_0 L i_{tq} = v_{td} - v_{od},\ (L\frac{d}{dt} + R)i_{tq} + \omega_0 L i_{td} = v_{tq} - v_{oq}.\end{gathered} \tag{4.6}$$

where, i_{odq} are the LCL filter output current and:

$$\begin{gathered}v_{td_k} = v^*_{td_k}\cos\delta_k - v^*_{tq_k}\sin\delta_k,\ v_{tq_k} = v^*_{tq_k}\cos\delta_k + v^*_{td_k}\sin\delta_k, \\ v^*_{td} = K_p(i^*_d - i_{td}) + K_i\lambda_d + v_{od} + Ri_{td} - \omega_0 L i_{tq}, \\ v^*_{tq} = K_p(i^*_q - i_{tq}) + K_i\lambda_q + v_{oq} + Ri_{tq} + \omega_0 L i_{td}.\end{gathered} \tag{4.7}$$

4.1.5 Line model

The system transmission line model can be derived as:

$$\begin{aligned}v_{gd} - v_{gridd} &= (L_{grid}\frac{d}{dt} + R_{grid})\sum_{k=1}^{n} i_{od} - \omega_0 L_{grid}\sum_{k=1}^{n} i_{oq}, \\ v_{gq} - v_{gridq} &= (L_{grid}\frac{d}{dt} + R_{grid})\sum_{k=1}^{n} i_{oq} + \omega_0 L_{grid}\sum_{k=1}^{n} i_{od}.\end{aligned} \tag{4.8}$$

Thus, considering (4.1)-(4.8) the detailed model of a PV farm with n paralleled inverters at PCC bus are obtained that is connected to the grid with a transmission line.

4.2 Weighted Dynamic Aggregation Model of Grid-Following Inverters

The WD agg method is applied to a PV farm with n grid-following inverters shown in Figure 4.1(a). The objective is to find an equivalent set of dynamic equations with a similar structure of a single PV unit to represent the PV farm as shown in Figure 4.1(b). This is first done by deriving the dynamic equations of n inverters in the detailed system and defining a weight of contribution for each unit. Then the weighted average of n inverter dynamic equations is derived to achieve the equivalent set of dynamic equations which is then compared with the individual inverter equations to find the equivalent unit parameters. The WD aggregation of output LCL filter and current controllers is similar to previous chapter and the derivations can be found in 3.3.1 and 3.3.2, respectively. The rest of this procedure is done separately for the voltage controllers, DC-link capacitors, and PV arrays as shown in the followings. The mathematical proof of the equivalent model shown in Figure 4.1(b) is provided in the three following steps:

4.2.1 Equivalent DC-link capacitor

The mth inverter delivers a power as $p_{dc_m} = v_{dc_m} i_{dc_m}$. By defining $\mu_{dc_m} = v_{dc_m}/v_{dc_{eq}}$, where $v_{dc_{eq}} = \frac{1}{n}\sum_{k=1}^{n} v_{dc_k}$, DC-link power equation can be found as:

$$p_{dc_{eq}} = v_{dc_{eq}} i_{dc_{eq}} = \sum_{k=1}^{n} \mu_{dc_k} i_{dc_k} v_{dc_{eq}} \Rightarrow i_{dc_{eq}} = \sum_{k=1}^{n} \mu_{dc_k} i_{dc_k}. \tag{4.9}$$

It is worth noting that $\mu_{dc_m} = (V_{dc_m} + \tilde{v}_{dc_m})/(V_{dc_{eq}} + \tilde{v}_{dc_{eq}}) \simeq V_{dc_m}/V_{dc_{eq}}$. The differential equation for mth DC-link capacitor can be given as:

$$C_{dc_m} \frac{d}{dt} v_{dc_m} = i_{pv_m} - i_{dc_m}. \tag{4.10}$$

Multiplying (4.10) by μ_{dc_m} and summing all n differential equations leads to:

$$\sum_{m=1}^{n} \mu_{dc_m}^2 C_{dc_m} \frac{d}{dt} v_{dc_{eq}} = \sum_{m=1}^{n} \mu_{dc_m} i_{pv_m} - \sum_{m=1}^{n} \mu_{dc_m} i_{dc_m}. \tag{4.11}$$

By comparing (4.2) and (4.11) the equivalent DC-link model can be found as:

$$C_{dc_{eq}} \frac{d}{dt} v_{dc_{eq}} = i_{pv_{eq}} - i_{dc_{eq}}, \text{ where:}$$

$$C_{dc_{eq}} = \sum_{m=1}^{n} \mu_{dc_m}^2 C_{dc_m}, \quad i_{pv_{eq}} = \sum_{m=1}^{n} \mu_{dc_m} i_{pv_m}. \tag{4.12}$$

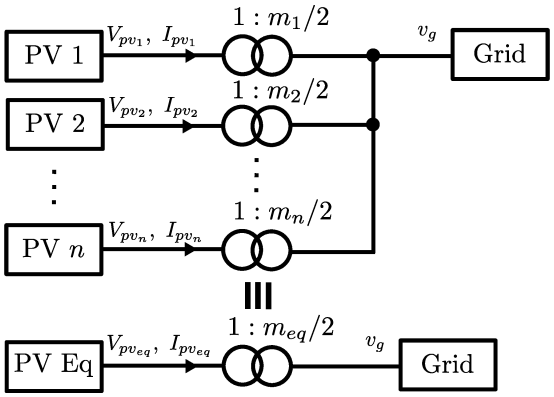

Figure 4.3: Developing an equivalent PV array for n paralleled PV units.

4.2.2 Equivalent DC-link controller

Similar to current controller modeling approach, first, n DC-link voltage controller dynamic equations are derived, and then the controller state contributions are defined to determine the parameters of the equivalent DC-link voltage controller. Deriving the model for the mth DC-link voltage controller shown in Figure 4.2 results in:

$$(k_{pv_m} + k_{iv_m}/s)(v_{dc_m} - v^*_{dc_m}) = i^*_{d_m}. \tag{4.13}$$

The equation can be rewritten by defining $\mu'_{dc_m} = v^*_{dc_m}/v^*_{dc_{eq}} = (V^*_{dc_m} + \tilde{v}^*_{dc_m})/(V^*_{dc_{eq}} + \tilde{v}^*_{dc_{eq}}) \simeq V^*_{dc_m}/V^*_{dc_{eq}}$ and assuming the controller will ensure zero steady state error, $V^*_{dc} = V_{dc}$, therefore, $\mu'_{dc_m} = \mu_{dc_m}$. Substituting μ_{dc_m} in (4.13) results in:

$$\mu_{dc_m}(k_{pv_m} + k_{iv_m}/s)(v_{dc_{eq}} - v^*_{dc_{eq}}) = i^*_{d_m}. \tag{4.14}$$

Summing the n DC-link voltage controllers differential equations of (4.14) yields:

$$\sum_{m=1}^{n} \mu_{dc_m}(k_{pv_m} + k_{iv_m}/s)(v_{dc_{eq}} - v^*_{dc_{eq}}) = \sum_{m=1}^{n} i^*_{d_m}. \tag{4.15}$$

By comparing (4.13) and (4.15), the equivalent DC-link voltage controller differential equation can be found as:

$$(k_{pv_{eq}} + k_{iv_{eq}}/s)(v_{dc_{eq}} - v^*_{dc_{eq}}) = i^*_{d_{eq}}, \text{ where:}$$

$$k_{pv_{eq}} = \sum_{m=1}^{n} \mu_{dc_m} k_{pv_m},\ k_{iv_{eq}} = \sum_{m=1}^{n} \mu_{dc_m} k_{iv_m},\ i^*_{d_{eq}} = \sum_{m=1}^{n} i^*_{d_m}. \tag{4.16}$$

4.2.3 Equivalent PV array in PV farms without DC-DC Power Stage

To find the equivalent PV array for the equivalent PV unit, $I_{sc_{eq}}$, $V_{oc_{eq}}$, $V_{mp_{eq}}$, and $I_{mp_{eq}}$ should be determined. $I_{sc_{eq}}$ can be found by $\sum_{k=1}^{n} I_{sc_k}$ because the equivalent

PV array should provide the total short circuit current of the PV farm. Figure 4.3 demonstrates that the equivalent PV array for n paralleled PV units. The equivalent PV array output current can be found by $I_{pv_{eq}} = m_{eq} \sum_{k=1}^{n} I_{pv_k}/m_k$, where m is the modulation index of inverter. The equivalent PV array also is modeled as (4.1) and the output power of the equivalent PV array should be the summation of all PV units as $V_{pv_{eq}} I_{pv_{eq}} = \sum_{k=1}^{n} V_{pv_k} I_{pv_k}$, thus the equivalent PV array $V_{oc_{eq}}$, $V_{mp_{eq}}$, and $I_{mp_{eq}}$ can be found by the following equations at the MPP operating point:

$$I_{mp_{eq}} = m_{mp_{eq}} \sum_{k=1}^{n} I_{mp_k}/m_{mp_k},\ V_{mp_{eq}} I_{mp_{eq}} = \sum_{k=1}^{n} V_{mp_k} I_{mp_k},$$

$$I_{mp_{eq}} = I_{sc_{eq}}(1 - C_{1_{eq}}(e^{\frac{V_{mp_{eq}}}{C_{2_{eq}} V_{oc_{eq}}}} - 1)),\ C_{1_{eq}} = (1 - \frac{I_{mp_{eq}}}{I_{sc_{eq}}}) e^{\frac{-V_{mp_{eq}}}{C_2 V_{oc_{eq}}}},$$

$$C_{2_{eq}} = (\frac{V_{mp_{eq}}}{V_{oc_{eq}}} - 1)/\ln(1 - \frac{I_{mp_{eq}}}{I_{sc_{eq}}}),\ m^{mp} = \frac{2V_g}{V_{mp}}. \tag{4.17}$$

The equivalent DC voltage reference signal can be found as $V^*_{pv_{eq}} I_{pv_{eq}} = \sum_{k=1}^{n} V^*_{pv_k} I_{pv_k}$, where I_{pv_h}, $h = \{1,\ 2,\ \ldots,\ n,\ eq\}$ can be found with (4.1).

4.3 PV Farm Configuration with DC-DC Power Stage

This section studies a grid-following PV farm with n-paralleled PV units shown in Figure 4.4a. Each PV unit is compromising a PV array connected to a DC link via a boost converter controlled with Incremental Conductance Method (ICM) Maximum Power Point Tracking (MPPT) algorithm discussed in [94]. As shown in Figure 4.4a, the DC link is connected to a PCC bus via a grid-following inverter and a collector line. As shown in Figure 4.2, each inverter is controlled locally using an outer DC-link voltage loop and inner current control loop. The modeling derivations of the DC-link bus and controller can be found in the previous section 4.1.2 and 4.1.3, respectively. Moreover, the inverter output filter model can be found in the previous chapter 3.2.1. However, models of the PV array, the boost converter and its controller is presented in the following two subsections for further discussions:

4.3.1 Boost converter model

A boost converter is utilized to facilitate the PV array to work at the MPP all the time. The boost converter shown in Figure 4.4a can be modeled as:

$$\begin{gathered} C_{pv}\frac{d}{dt}v_{pv} = i_{pv} - i_b,\ C_{dc}\frac{d}{dt}v_{dc} = d'i_b - i_{dc}, \\ (L_b\frac{d}{dt} + R_b)i_b = v_{pv} - d'v_{dc}, \end{gathered} \tag{4.18}$$

where the input and output capacitors of the boost converter are represented by C_{pv} and C_{dc}, respectively, while their respective voltages are denoted by v_{pv} and v_{dc}. The

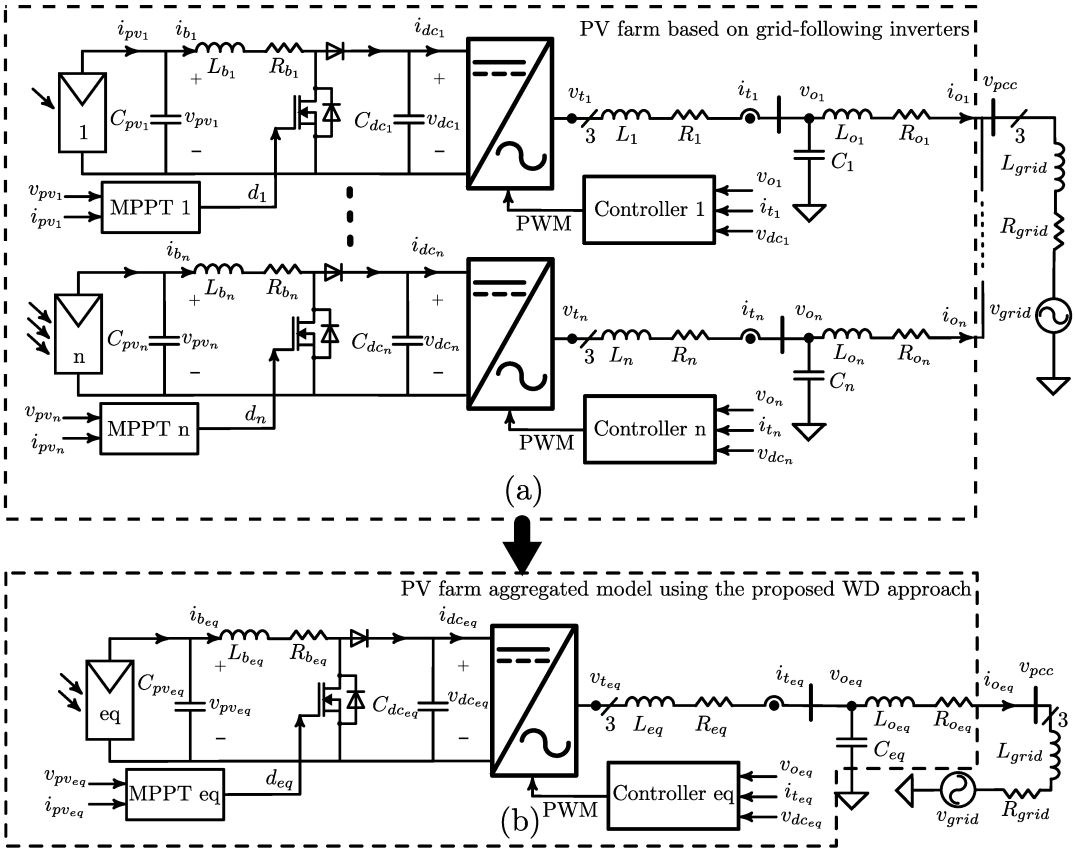

Figure 4.4: a) PV farm with grid-following inverters and MPPT action, b) The equivalent WD agg model.

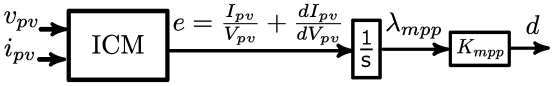

Figure 4.5: Boost converter control block diagram.

input and output currents of the boost converter are i_{pv} and i_{dc}, respectively. The converter's inductor is characterized by its inductance L_b, resistance R_b, and current i_b. Lastly, $d' = 1 - d$, where d refers to the converter's duty cycle.

4.3.2 PV array model

Each PV array can be represented by a variable current source, with the output current given as:

$$\begin{aligned} i_{pv} &= I_{sc}\left(1 - C_1(e^{\frac{v_{pv}}{C_2 V_{oc}}} - 1)\right), \\ C_1 &= \left(1 - \frac{I_{mp}}{I_{sc}}\right) e^{\frac{-V_{mp}}{C_2 V_{oc}}},\ C_2 = \left(\frac{V_{mp}}{V_{oc}} - 1\right) \Big/ \ln\left(1 - \frac{I_{mp}}{I_{sc}}\right), \end{aligned} \tag{4.19}$$

where v_{dc} is the DC-link voltage, I_{sc} is the PV array short circuit current, V_{oc} is the PV array open circuit voltage, and I_{mp} and V_{mp} are the PV array maximum power

operating current and voltage, respectively.

4.4 WD agg Model of PV Farm with DC-DC Power Stage

The WD agg method is applied to a PV farm consisting of n grid-following inverters, as shown in Figure 4.4a. The objective is to identify an equivalent set of dynamic equations that resemble a single PV unit structure to represent the PV farm, as illustrated in Figure 4.4b. This is achieved by first obtaining the dynamic equations of n PV units in the detailed system and determining a contribution weight for each unit. Next, the weighted average of the n PV units' dynamic equations is calculated to obtain the equivalent set of dynamic equations, which is then compared with the individual PV unit equations to identify the equivalent PV unit parameters. This process is conducted separately for the inverter with LCL output filters and its controllers, and the results are presented in the table of Figure 4.4b. This section provides a mathematical proof of the equivalent model for the boost converter, MPPT controller, and PV array, as shown in Figure 4.4b, through the following three steps:

4.4.1 Equivalent boost converter

mth boost converter set of dynamic equations can be given as:

$$\begin{aligned} C_{pv_m}\frac{d}{dt}v_{pv_m} &= i_{pv_m} - i_{b_m}, \\ C_{dc_m}\frac{d}{dt}v_{dc_m} &= (d'i_b)_m - i_{dc_m}, \\ (L_{b_m}\frac{d}{dt} + R_{b_m})i_{b_m} &= v_{pv_m} - (d'v_{dc})_m. \end{aligned} \tag{4.20}$$

Considering $p_{dc} = v_{dc}i_{dc}$ and the equivalent $p_{dc_{eq}} = \sum_{k=1}^{n} p_{dc_k}$. By defining $\mu_{dc} = v_{dc_m}/v_{dc_{eq}}$, where $v_{dc} = \frac{1}{n}\sum_{k=1}^{n} v_{dc_k}$, the equivalent $i_{dc_{eq}}$ can be found as:

$$p_{dc_{eq}} = \sum_{k=1}^{n} \mu_{dc_k} i_{dc_k} v_{dc_{eq}} \Rightarrow i_{dc_{eq}} = \sum_{k=1}^{n} \mu_{dc_k} i_{dc_k}. \tag{4.21}$$

It is worth noting that $\mu_{dc_k} = (V_{dc_k} + \tilde{v}_{dc_k})/(V_{dc_{eq}} + \tilde{v}_{dc_{eq}}) \simeq V_{dc_k}/V_{dc_{eq}}$. Multiplying the dynamic equation of mth output capacitor yields:

$$\mu_{dc_m} C_{dc_m}\frac{d}{dt}v_{dc_m} = \mu_{dc_m}(d'i_b)_m - \mu_{dc_m} i_{dc_m}. \tag{4.22}$$

Now summing n equations of (4.22) gives:

$$\sum_{k=1}^{n} (\mu_{dc_k})^2 C_{dc_k}\frac{d}{dt}v_{dc_{eq}} = \sum_{k=1}^{n} \mu_{dc_k}(d'i_b)_k - \sum_{k=1}^{n} \mu_{dc_k} i_{dc_k}. \tag{4.23}$$

Comparing (4.23) with (4.21) and the single output capacitor dynamic equation given in (4.18) results in:

$$C_{dc_{eq}}\frac{d}{dt}v_{dc_{eq}} = (d'i_b)_{eq} - i_{dc_{eq}},\ \text{where:}$$

$$C_{dc_{eq}} = \sum_{k=1}^{n}(\mu_{dc_k})^2\, C_{dc_k},\ (d'i_b)_{eq} = \sum_{k=1}^{n}\mu_{dc_k}(d'i_b)_k. \tag{4.24}$$

By considering n dynamic equations of converters inductors and defining $\mu_{b_m} = i_{b_m}/i_{b_{eq}}$, $\mu_{pv_m} = v_{pv_m}/v_{pv_{eq}}$, and $\mu'_{pv_m} = (d'v_{dc})_m\,/\,(d'v_{dc})_{eq}$, the kth dynamic equation can be given as:

$$(L_{b_m}\frac{d}{dt} + R_{b_m})\mu_{b_m}i_{b_{eq}} = \mu_{pv_m}v_{pv_{eq}} - \mu'_{pv_m}(d'v_{dc})_{eq}. \tag{4.25}$$

It is worth noting that:

$$\begin{aligned}\mu_{b_m} &= \frac{I_{pv_m} + \tilde{i}_{pv_m}}{I_{pv_{eq}} + \tilde{i}_{pv_{eq}}} \simeq \frac{I_{pv_m}}{I_{pv_{eq}}},\ \mu_{pv_m} = \frac{V_{pv_m} + \tilde{v}_{pv_m}}{V_{pv_{eq}} + \tilde{v}_{pv_{eq}}} \simeq \frac{V_{pv_m}}{V_{pv_{eq}}},\\ \mu'_{pv_m} &= \frac{(D'V_{dc})_m + d'\tilde{v}_{dcm}}{(D'V_{dc})_{eq} + d'\tilde{v}_{dceq}} \simeq \frac{(D'V_{dc})_m}{(D'V_{dc})_{eq}} = \frac{V_{pv_m}}{V_{pv_{eq}}} = \mu_{pv_m}.\end{aligned} \tag{4.26}$$

Therefore, (4.25) can be rewritten as:

$$\frac{\mu_{b_m}}{\mu_{pv_m}}(L_{b_m}\frac{d}{dt} + R_{b_m})i_{b_{eq}} = v_{pv_{eq}} - (d'v_{dc})_{eq}. \tag{4.27}$$

Now, averaging n dynamic equations of (4.27) yields:

$$\left(\sum_{k=1}^{n}\frac{\mu_{b_k}}{n\mu_{pv_k}}L_{b_k}\frac{d}{dt} + \sum_{k=1}^{n}\frac{\mu_{b_k}}{n\mu_{pv_k}}R_{b_k}\right)i_{b_{eq}} = v_{pv_{eq}} - (d'v_{dc})_{eq}\,. \tag{4.28}$$

Comparing (4.28) with the single dynamic equation of the inductor gives:

$$(L_{b_{eq}}\frac{d}{dt} + R_{b_{eq}})i_{b_{eq}} = v_{pv_{eq}} - (d'v_{dc})_{eq},\ \text{where:}$$

$$L_{b_{eq}} = \sum_{k=1}^{n}\frac{\mu_{b_k}}{n\mu_{pv_k}}L_{b_k},\ R_{b_{eq}} = \sum_{k=1}^{n}\frac{\mu_{b_k}}{n\mu_{pv_k}}R_{b_k}. \tag{4.29}$$

By considering n dynamic equations of input capacitor and defining $\mu'_{b_m} = i_{pv_m}/i_{pv_{eq}}$, the kth dynamic equation can be given as:

$$C_{pv_m}\frac{d}{dt}\mu_{pv_m}v_{pv_{eq}} = \mu'_{b_m}i_{pv_{eq}} - \mu_{b_m}i_{b_{eq}}. \tag{4.30}$$

It is worth noting that $\mu'_{b_m} = (I_{pv_m} + \tilde{i}_{pv_m})/(I_{pv_{eq}} + \tilde{i}_{pv_{eq}}) \simeq I_{pv_m}/I_{pv_{eq}} = I_{b_m}/I_{b_{eq}} = \mu_{b_m}$. Therefore, (4.30) can be rewritten as:

$$\frac{d}{dt}v_{pv_{eq}} = \left(i_{pv_{eq}} - i_{b_{eq}}\right) \Big/ \left(\frac{\mu_{pv_m}}{\mu_{b_m}}C_{pv_m}\right). \tag{4.31}$$

Averaging n dynamic equations of (4.31) yields:

$$\frac{d}{dt}v_{pv_{eq}} = \left(\sum_{k=1}^{n}\frac{1}{n\left(\frac{\mu_{pv_k}}{\mu_{b_k}}C_{pv_k}\right)}\right)\left(i_{pv_{eq}} - i_{b_{eq}}\right). \tag{4.32}$$

Comparing (4.32) with the single input capacitor dynamic equation given in (4.18) results in:

$$C_{pv_{eq}}\frac{d}{dt}v_{pv_{eq}} = i_{pv_{eq}} - i_{b_{eq}}, \text{ where:}$$

$$C_{pv_{eq}} = 1\Big/\left(\sum_{k=1}^{n}1\Big/\left(n\frac{\mu_{pv_k}}{\mu_{b_k}}C_{pv_k}\right)\right). \tag{4.33}$$

4.4.2 Equivalent MPPT controller

As illustrated in Figure 4.5, mth MPPT model can be given as:

$$e_m K_{mpp_m}/s = d_m, \tag{4.34}$$

where e is the MPPT error and K_{mpp} is the compensator gain. Recalling $d'_m v_{dc_m} = v_{pv_m}$, therefore, for each PV unit we have:

$$\frac{\mu_{dc_m}}{\mu_{pv_m}}d'_m v_{dc_{eq}} = v_{pv_{eq}}. \tag{4.35}$$

Averaging n equations of (4.35) results in:

$$\sum_{k=1}^{n}\frac{\mu_{dc_k}}{n\mu_{pv_k}}d'_k v_{dc_{eq}} = v_{pv_{eq}}. \tag{4.36}$$

Hence, based on (4.36) it can be concluded that:

$$d'_{eq} = \sum_{k=1}^{n}\frac{\mu_{dc_k}}{n\mu_{pv_k}}d'_k \Rightarrow D_{eq} = 1 - D'_{eq}. \tag{4.37}$$

Defining $\lambda_{mpp_m} = \frac{d}{dt}e_m$, thus, $\lambda_{mpp_m}K_{mpp_m} = d_m$. Considering that the equivalent compensator should compensate the cumulative error of the PV farm, thus, $\lambda_{mpp_{eq}} = \sum_{k=1}^{n}\lambda_{mpp_k}$, therefore:

$$\Lambda_{mpp_{eq}} = \sum_{k=1}^{n}\frac{D_k}{K_{mpp_k}}, \tag{4.38}$$

where Λ_{mpp} and D are the steady-state values. Hence, using (4.38), $K_{mpp_{eq}}$ can be found as:

$$K_{mpp_{eq}} = D_{eq}\Big/\left(\sum_{k=1}^{n}\frac{D_k}{K_{mpp_k}}\right). \tag{4.39}$$

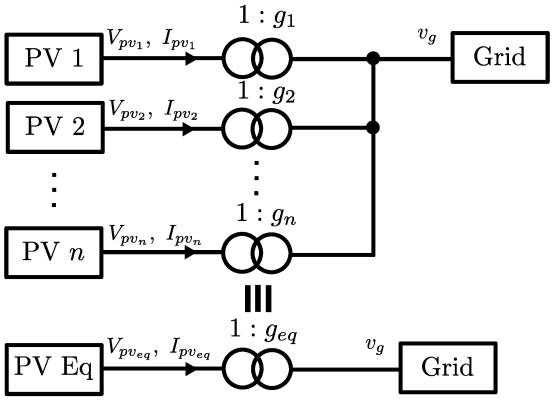

Figure 4.6: Developing an equivalent PV array for n paralleled PV units.

4.4.3 Equivalent PV array in PV farms with DC-DC Power Stage

In order to determine the equivalent PV array for a PV unit, it is necessary to determine $I_{sc_{eq}}$, $V_{oc_{eq}}$, $I_{mp_{eq}}$, and $V_{mp_{eq}}$. The total short circuit current of the PV farm can be obtained by adding up the short circuit currents of all the PV units, i.e., $\sum_{k=1}^{n} I_{sc_k}$. An illustration of a PV farm with n paralleled PV units and its equivalent PV array can be seen in Figure 4.6. Figure 4.6 demonstrates that the output current of the equivalent PV array can be calculated using the PV unit gain compromising inverter inverse modulation index $m = 2V_g/V_{dc}$ and the inverse boost gain $(1 - D)$, and the individual PV unit currents, i.e., $I_{pv_{eq}} = g_{eq} \sum_{k=1}^{n} I_{pv_k}/g_k$. Additionally, the output power of the equivalent PV array should be the sum of all PV units, which can be expressed as $V_{pv_{eq}} I_{pv_{eq}} = \sum_{k=1}^{n} V_{pv_k} I_{pv_k}$. The equations to find the equivalent PV array $V_{oc_{eq}}$, $V_{mp_{eq}}$, and $I_{mp_{eq}}$ at the MPP are given below.

$$
\begin{aligned}
I_{mp_{eq}} = g_{mp_{eq}} \sum_{k=1}^{n} I_{mp_k}/g_{mp_k},\ V_{mp_{eq}} I_{mp_{eq}} = \sum_{k=1}^{n} V_{mp_k} I_{mp_k},\\
I_{mp_{eq}} = I_{sc_{eq}}(1 - C_{1_{eq}}(e^{\frac{V_{mp_{eq}}}{C_{2_{eq}} V_{oc_{eq}}}} - 1)),\\
C_{1_{eq}} = (1 - \frac{I_{mp_{eq}}}{I_{sc_{eq}}}) e^{\frac{-V_{mp_{eq}}}{C_{2_{eq}} V_{oc_{eq}}}},\ g_{mp} = \frac{2V_g}{V_{mp}}(1 - D_{mp}),\\
C_{2_{eq}} = (\frac{V_{mp_{eq}}}{V_{oc_{eq}}} - 1)/\ln(1 - \frac{I_{mp_{eq}}}{I_{sc_{eq}}}).
\end{aligned}
\tag{4.40}
$$

4.5 Simulations Results

Two systems with various case studies are introduced in this section to evaluate the proposed model. A small-scale system, consisting three PV units as shown Figure 4.1(a) and the control system shown in Figure 4.2, is simulated to verify the accuracy of the proposed model in the system steady-state analysis and dynamic behavior under different stability conditions. Additionally, the proposed method is applied to

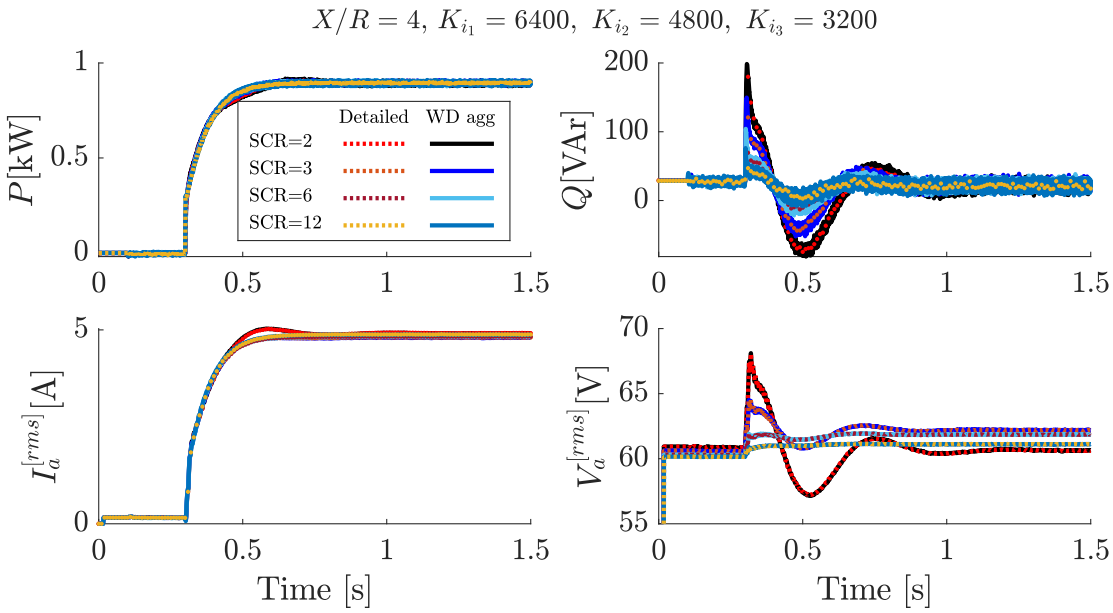

Figure 4.7: Detailed and WD agg models PCC bus output active power P, reactive power Q, phase current $I_a^{[rms]}$, and phase voltage $V_a^{[rms]}$ comparison for different grid SCR.

PV units of CIGRE MV/LV 14-bus benchmark [90] to evaluate the functionality of the proposed method in large-scale systems.

4.5.1 Three-Paralleled inverters PV farm without DC-DC power stage

To investigate the performance of the proposed WD agg model in the systems with various grid strength, the WD agg and detailed models of the system with controller parameters given in Table 4.2 and the inverters parameters given in Sc. A of Table 4.1 are obtained in various SCRs and the results are presented in Figure 4.7. Figure 4.7 illustrates, the system with low SCR (SCR=2 very weak grid, SCR=3 weak grid) has larger swings in both reactive power as well as the PCC bus voltage, as opposed to the system with higher SCR (SCR=12 strong grid) at the system start-up. It is worth noting that each inverter is locally controlled by i_t current that results in zero reactive power injection at Bout 1, 2, and 3 buses ($Q_{out}^{(1)} = Q_{out}^{(2)} = Q_{out}^{(3)} = 0$). However, the reactive power injected to the grid at PCC bus is not zero ($Q_{PCC} \neq 0$) due to the existence of collector line inductors L_{o_1}, L_{o_2}, L_{o_3} and the filter capacitors C_1, C_2, C_3. Figure 4.7 verifies that WD agg model mimics the oscillatory behavior of the detailed system accurately. A PV farm with three PV units and Sc. A parameters of Table 4.1 in Appendix is studied in nine case studies. These case studies are the combination of various unequal inverters parameters and stability conditions. The detailed and proposed aggregated model are presented for comparison.
To further investigate the functionality of the proposed system, a PV farm with three

Table 4.1: Simulation and experimental systems specifications.

Parameter	Scenario A			Scenario B		Scenario C
	Inv 1	Inv 2	Inv 3	Inv A	Inv B	Inv exp
$L[mH]$	2.5	2.0	2.5	2.5	2.0	2.5
$R[\Omega]$	0.44	0.64	0.44	0.44	0.44	0.44
$C[\mu F]$	2.5	2.5	2	2.5	3.0	2.5
$R_c[m\Omega]$	3.1	3.1	3.1	3.1	3.1	3.1
$L_o[mH]$	1	1	0.5	1	1.5	1
$R_o[\Omega]$	0.38	0.38	0.38	0.38	0.38	0.38
K_p	12	12	12	12	16	12
K_i	160	120	80	100	200	100
K_{pv}	0.0060	0.0072	0.0036	0.012	0.016	0.01
K_{iv}	24	20	16	72	84	160
$C_{DC}[\mu F]$	390	390	390	390	390	390

$v_{g_{LL}} = 104\ [V],\ f = 60\ [Hz],\ L_{grid} = 150\ [\mu H],\ R_{grid} = 13\ [m\Omega]$

Table 4.2: Inverters control parameters for weak-grid studies.

Parameter	Inv 1	Inv 2	Inv 3
K_p	24	24	24
K_i	6400	4800	3200
K_{pv}	0.240	0.288	0.144
K_{iv}	9.6	8.0	6.4

PV units and unequal parameters as Table 4.1 Inv 1, 2, and 3 is presented. Figure 4.8 illustrates the PV farm output active power P with various control parameters for both detailed and WD agg models. As Figure 4.8 shows, the system approach instability by increasing K_{iv} values to $K_{iv_1} = 1440,\ K_{iv_2} = 1200,\ K_{iv_3} = 960$, and the proposed method mimics the system oscillatory behavior with a close oscillation frequency. By increasing K_{pv} values to $K_{pv_1} = 0.120,\ K_{pv_2} = 0.144,\ K_{pv_3} = 0.072$, and $K_{pv_1} = 0.360,\ K_{pv_2} = 0.432,\ K_{pv_3} = 0.216$, the system can reach a stable state with low, medium, and fast response times, respectively, while the proposed WD agg model has a close behavior compared to the detailed system. Figure 4.8 illustrates that the proposed model has significantly reduced the order of the system model while still predicting the instability of the system and its dominant oscillation frequency with a very small error, which are necessary for dynamic behavior studies and controller design of the system. The small error between the detailed and the proposed models' oscillation frequency generates a cumulative phase error, which is not as important as the dominant oscillation frequency in the system studies. To quantify the error of the proposed model, the error function is defined as $(\int_{t_0}^{t_{\text{end}}} |S_d - S_{eq}|dt)/(\int_{t_0}^{t_{\text{end}}} |S_d|dt)$, where S_d and S_{eq} can be any corresponding signals of the detailed and the proposed models, respectively. The calculated error for the active power during the first oscillation cycles of Figure 4.8 shows that the proposed has less than 4% error. Also, the

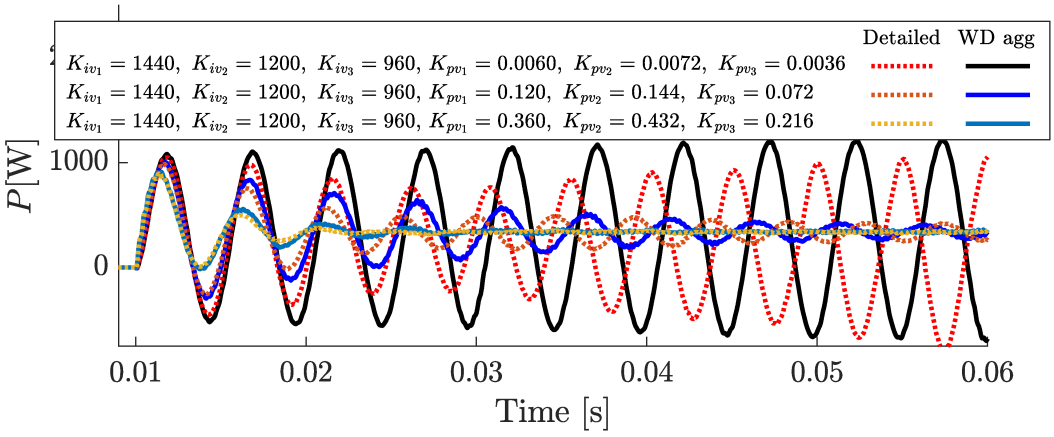

Figure 4.8: PV units with unequal parameters: PV farm output active power $P = P_1 + P_2 + P_3$ for various control parameters.

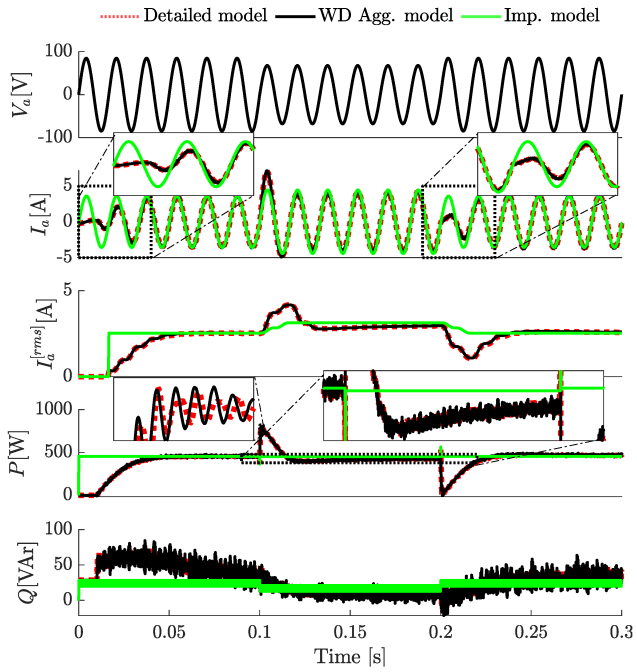

Figure 4.9: Grid voltage sag in critically and well damped system: Detailed, WD agg, and impedance models comparison.

proposed model has less than 2% error in predicting the oscillation frequencies.
To highlight the advantages of the proposed model compared with the impedance model, the detailed, the impedance, and the proposed WD agg models of a PV farm with three units and Table I Sc. A parameters are derived and the results are shown in Figure 4.9 to 4.11. An 0.2 pu voltage sag is applied at $t = 0.1$s and is cleared at $t = 0.2$s to investigate the dynamic behavior of the system. As demonstrated in Figure 4.9 the method accuracy and performance is superior compared to a single source

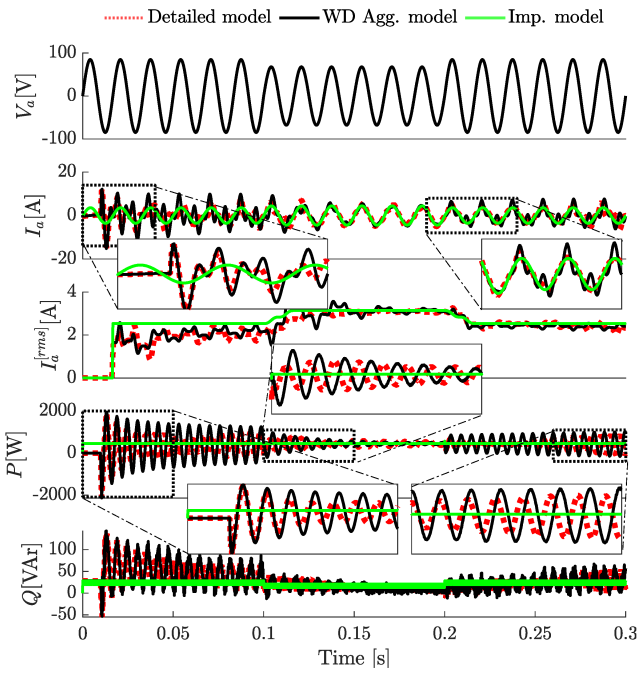

Figure 4.10: Grid voltage sag in marginally stable and under-damped system: Detailed, WD agg, and impedance models comparison.

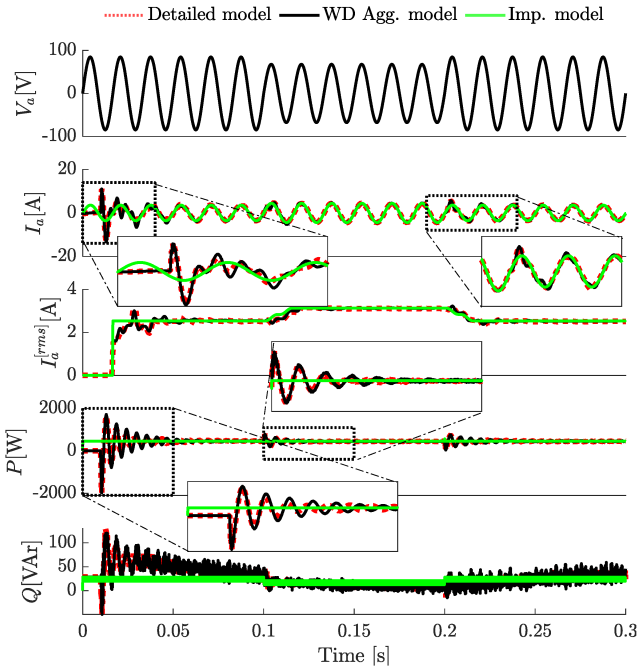

Figure 4.11: Grid voltage sag in under-damped system: Detailed, WD agg, and impedance models comparison.

and impedance. By increasing K_{iv} values to $K_{iv_1} = 1008$, $K_{iv_2} = 840$, $K_{iv_3} = 672$, Figure 4.10 shows that the system has an oscillatory behavior while the impedance model is unable to predict the oscillations, the proposed WD agg model can. Fig-

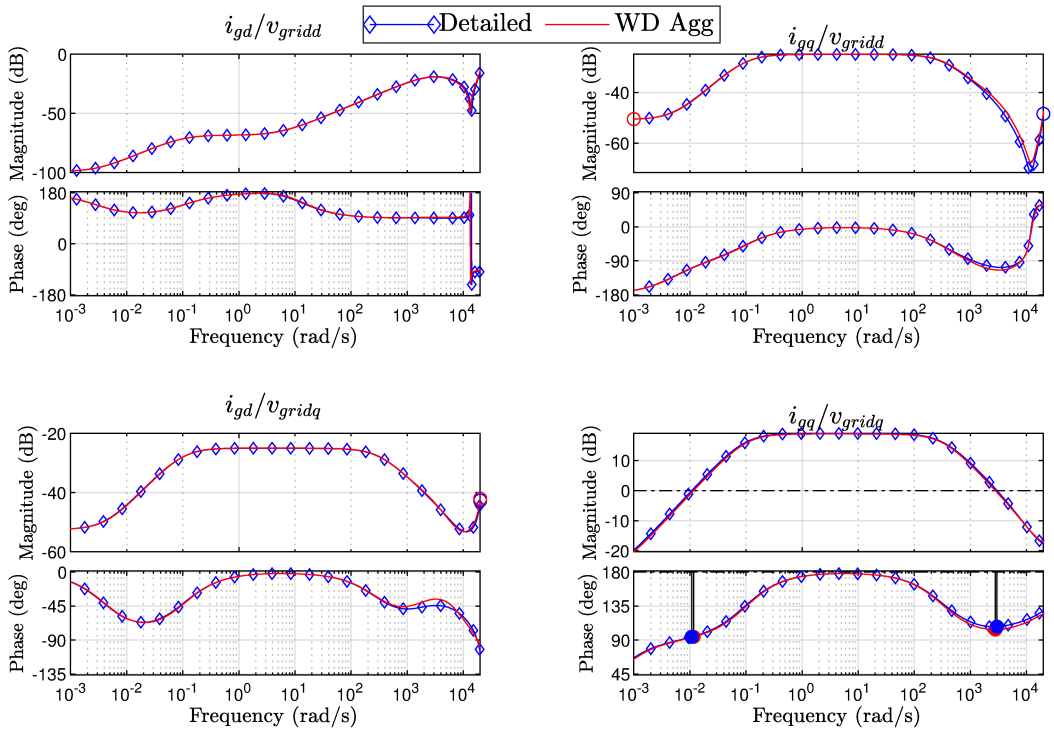

Figure 4.12: The frequency response of the detailed and WD agg models.

ure 4.10 also demonstrates that both detailed and the proposed WD agg models leans towards stability during the voltage sag. Now by increasing K_{pv} values to $K_{pv_1} = 0.12$, $K_{pv_2} = 0.144$, $K_{pv_3} = 0.072$, the oscillations of the system can be damped as shown in Figure 4.11. Figure 4.11 verifies the accuracy of the proposed WD agg model in predicting the dominant oscillation frequencies and the stability condition of the system while the impedance model can only predict a steady-state. Figure 4.12 shows and compares the frequency response of the detailed and WD agg models. As demonstrated in Figure 4.12, the frequency response of the WD agg model matches with the detailed model and it has a very similar phase and gain margins to the detailed model.

4.5.2 CIGRE MV/LV 14-Bus benchmark for renewable energies

To assess the accuracy and functionality of the proposed model in large-scale systems, the proposed method is used to aggregate the PV units that are connected to a similar bus in CIGRE MV/LV 14-bus benchmark for renewable energies, shown in Fig. 4.13. The detailed model of CIGRE MV/LV 14-bus benchmark is also simulated to compare with the aggregated model. To have a comprehensive evaluation of the proposed method, the system with two sets of parameters are presented. The first system has similar 10KW paralleled PV units with parameters of Inv type A given in Scenario B of Table 4.1, while in the second system half of the paralleled PV units

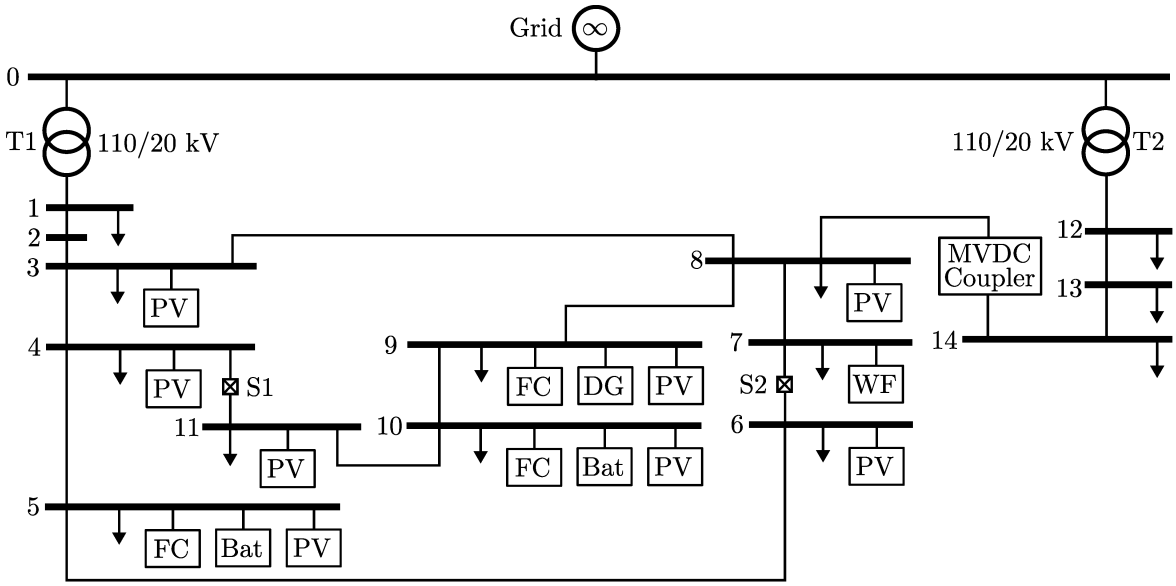

Figure 4.13: CIGRE MV/LV 14-Bus for renewable energies.

are Inv type A and the rest are Inv type B. It is worth noting that the overall power rating of aggregated PV farms in the benchmark is 210 kW.

Figure 4.14 shows the system start-up transient behavior of active power P, reactive power Q, output rms current I_{rms}, and the bus rms phase voltage V_{rms} for PV units at Bus 3 and Bus 10 in system 1 and 2. As Figure 4.14 shows the reduced-order model completely matches the detailed system and shows that the proposed model has a high accuracy in large-signal events such as plug-ins and plug-outs.

A line-to-line short-circuit fault is applied at Bus 10 on $t = 2.02$s and is cleared after 3 full cycles on $t = 2.08$s ($\Delta t = 60$ms). Figure 4.15 show the system dynamic behavior of active power P, reactive power Q, output rms current I_{rms}, and the bus rms phase voltage V_{rms} for PV units at Bus 3 and Bus 10 in system 1 and 2. As Figure 4.15 shows, a line-to-line short-circuit fault at Bus 10 results in extremer swings in Bus 10 transient behaviors compared to Bus 3, due to the presence of a 1500 kW wind farm at Bus 7. The wind farm machines' inertia impacts the angle stability of Bus 10 more compared to Bus 3 because Bus 7 has a smaller electrical distance to Bus 10 than Bus 3. Figure 4.15 shows that PV farms with unequal parameters intensify the post-fault clearing oscillations.

A line-to-line short-circuit fault is applied at Bus 3 on $t = 2.3$s and is cleared after 3 full cycles on $t = 2.36$s ($\Delta t = 60$ms). Figure 4.16 show the system dynamic behavior of active power P, reactive power Q, output rms current I_{rms}, and the bus rms phase voltage V_{rms} for PV farms at Bus 3 and Bus 10 in system 1 and 2, respectively. As Figure 4.16 shows, locating the line-to-line short-circuit fault at Bus 3 deteriorates the overall dynamic behavior of the system compared to Bus 10 shown in Figure 4.15, due to the dominant location of Bus 3 over Bus 7 and Bus 10. Also, Figure 4.15 and 4.16 show that the proposed model completely matches the detailed model and predicts the dynamic behavior of the system accurately.

A 0.2pu voltage sag is applied to the infinite bus voltage to study the proposed

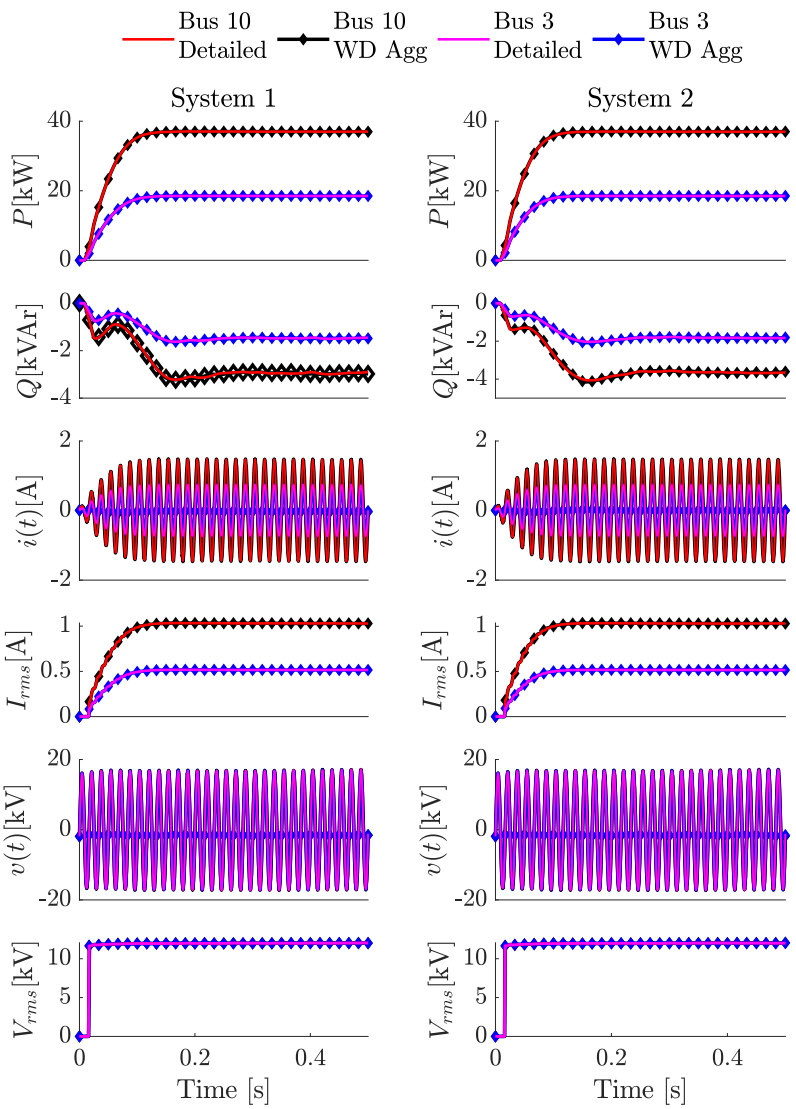

Figure 4.14: System 1 & 2 start-up: P active power, Q reactive power, $i(t)$ instantaneous output current, I_{rms} output rms current, $v(t)$ instantaneous output voltage, and V_{rms} bus rms phase voltage for PV units at Bus 3 and Bus 10.

model when the system operates in a critical condition. Figure 4.17 shows the system trend of active power P, reactive power Q, output rms current I_{rms}, and the bus rms phase voltage V_{rms} for PV farms at Bus 3 and Bus 10 in system 1 and 2. As Figure 4.17 shows the proposed model mimics the effect of wind farm inertia in the active and reactive powers while it predicts the high-frequency mode oscillations in reactive power output current during the transient window.

It is worth noting that the calculated cumulative error for active and reactive power during all events are 0.1% and 2.2%, respectively. Moreover, in this case study, the proposed model only took 19% of the detailed model simulation time to be simulated on a similar simulator system. Therefore, it significantly reduced the computational

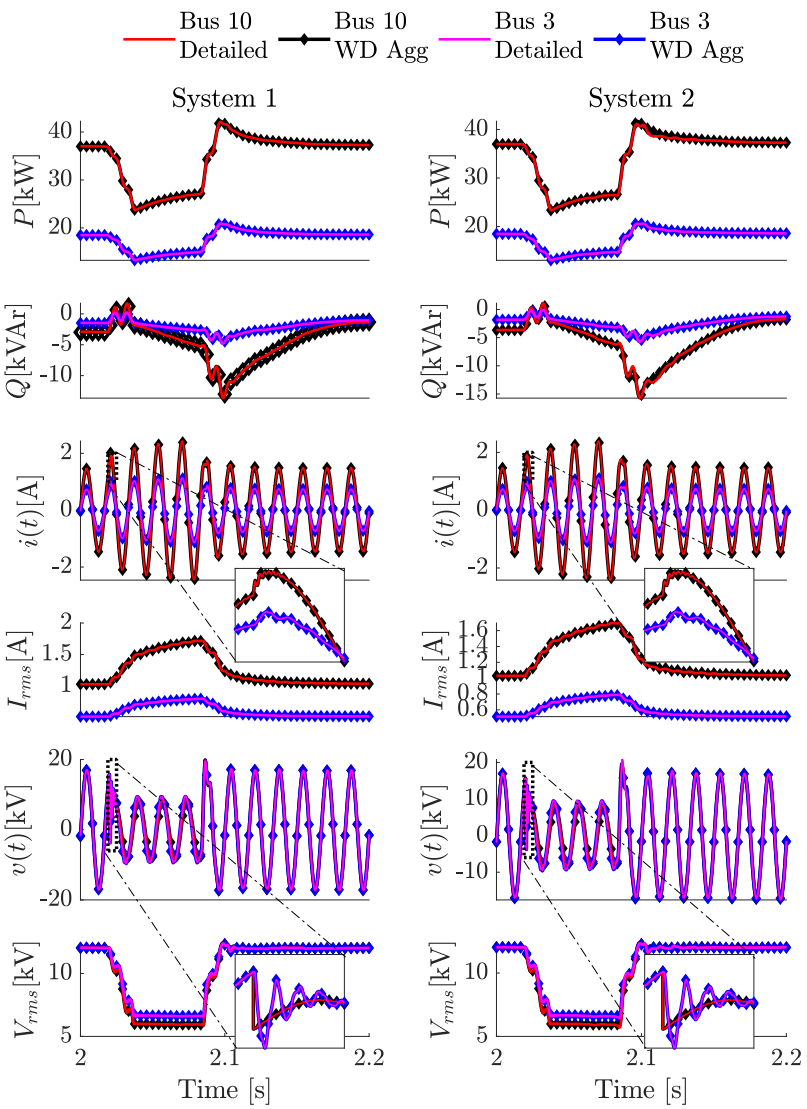

Figure 4.15: System 1 & 2, line-to-line fault at Bus 10: P active power, Q reactive power, $i(t)$ instantaneous output current, I_{rms} output rms current, $v(t)$ instantaneous output voltage, and V_{rms} bus rms phase voltage for PV units at Bus 3 and Bus 10.

burden of the system.

4.5.3 Three-Paralleled inverters PV farm with DC-DC power stage

The study analyzed a PV farm consisting of three PV units with the parameters provided in Table 4.3. To demonstrate the proposed model's accuracy in mimicking the dynamic behavior of the system, a voltage sag of 0.2 pu is applied at $t = 0.2$ [s], and it is cleared at $t = 0.4$ [s], and the results are presented for strong and weak grid conditions as Case 1 and 2. To assess the functionality of the proposed model during

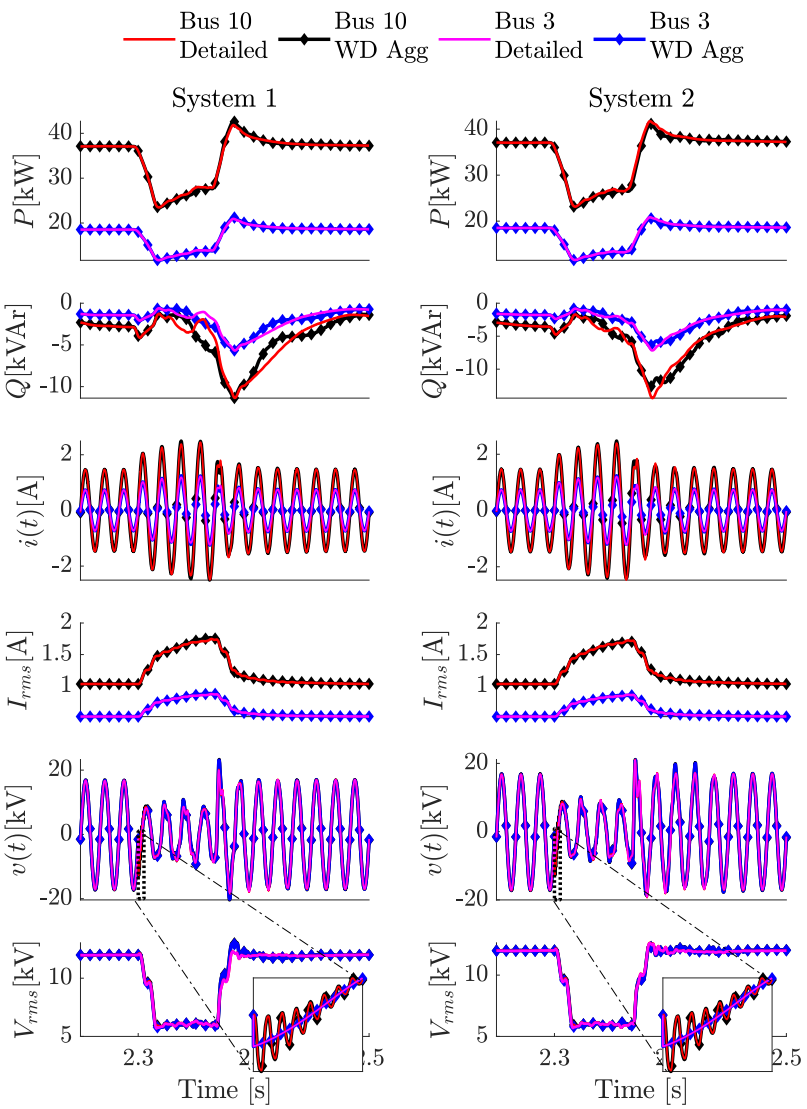

Figure 4.16: System 1 & 2, line-to-line fault at Bus 3: P active power, Q reactive power, $i(t)$ instantaneous output current, I_{rms} output rms current, $v(t)$ instantaneous output voltage, and V_{rms} bus rms phase voltage for PV units at Bus 3 and Bus 10.

partial shaded of PV farm, the same PV farm with the Table 4.3 given PV array characteristics is studied while PV 1 is partially shaded to $V_{oc} = 220$ $[V]$, $V_{mp} = 215$ $[V]$, $I_{sc} = 1.2$ $[A]$, and $I_{mp} = 1.1$ $[A]$. The partially shading is cleared at at $t = 0.4$ [s] and results are represented for strong and weak grid conditions as Case 3 and 4, respectively. Finally to validate the application of the proposed WD agg model in small-signal and large-signal analyses, the behavior of the detailed system and the proposed model is studied during small grid voltage steps and symmetrical line-to-line short-circuit faults, specifically under extreme weak grid condition as Case 5 and 6.

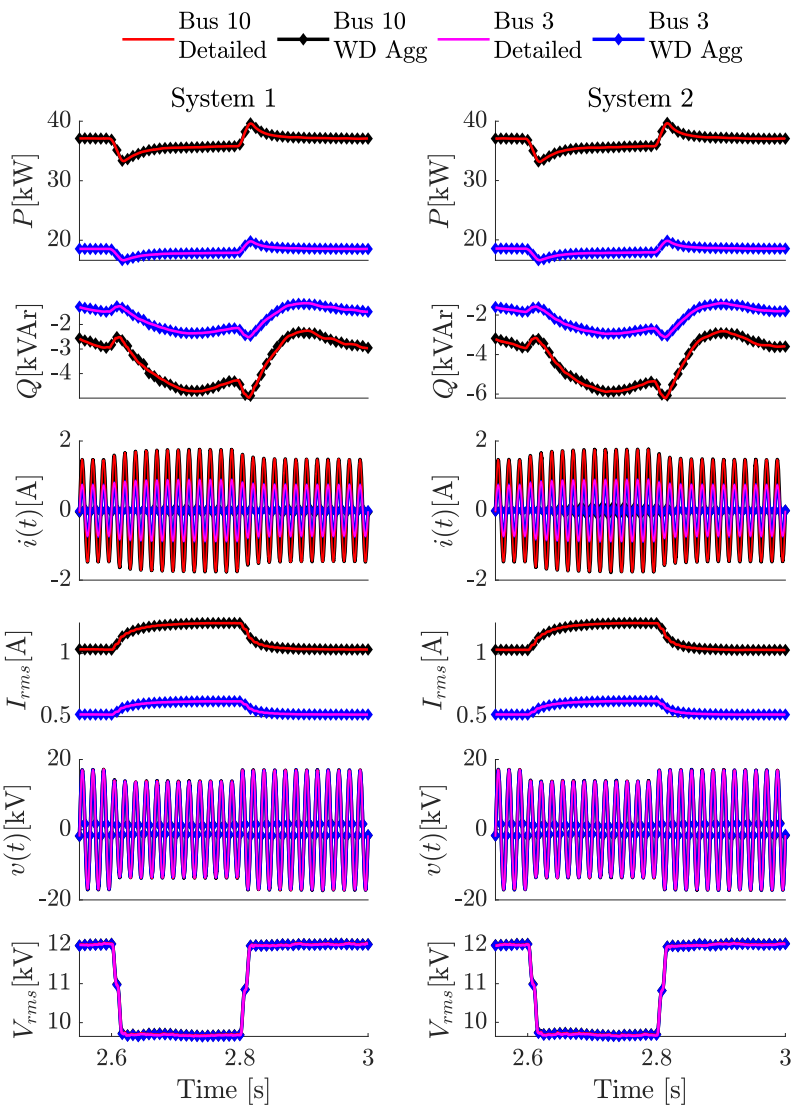

Figure 4.17: System 1 & 2, 0.2pu voltage sag at infinite bus: P active power, Q reactive power, $i(t)$ instantaneous output current, I_{rms} output rms current, $v(t)$ instantaneous output voltage, and V_{rms} bus rms phase voltage for PV units at Bus 3 and Bus 10.

Grid voltage sag dynamic performance:

Figure 4.18a shows the PV farm output active power (P), reactive power (Q), phase instantaneous ($i_a(t)$) and RMS ($I_a^{[rms]}$) current, and PCC bus instantaneous ($v_a(t)$) and RMS $V_a^{[rms]}$ voltage for both detailed and the proposed aggregated models in a strong grid with $SCR = 11.5$ and $X/R = 4$ as Case 1. As Figure 4.18a illustrates the system will reach the MPP with the minimal oscillations. It is worth noting that during the grid voltage sag the PV farm output current is increased to deliver the MPP active power to the grid. Furthermore, Figure 4.18a verifies the accuracy of the

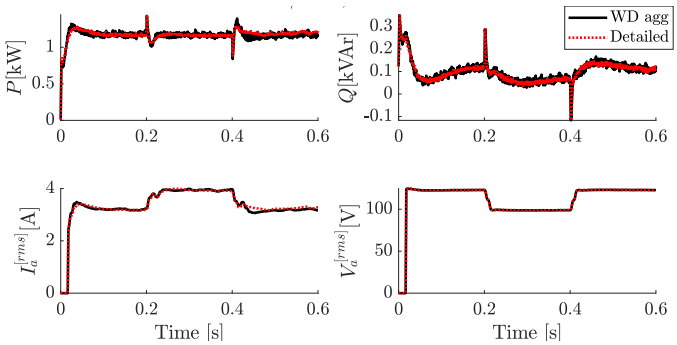

(a) Strong grid: $X/R = 4,\ SCR = 11.5$.

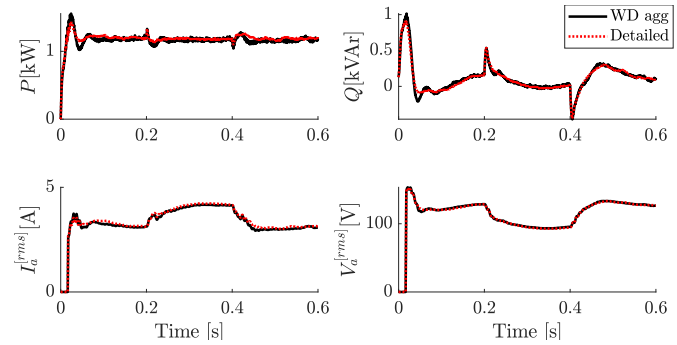

(b) Weak grid: $X/R = 4,\ SCR = 2.75$.

Figure 4.18: Case 1 & 2 (Grid Voltage Sag): The PV farm output active power (P), reactive power (Q), phase RMS ($I_a^{[rms]}$) current, and PCC bus RMS $V_a^{[rms]}$ voltage for both detailed and the proposed aggregated models in: a) Strong grid, b) Weak grid.

proposed model in predicting the overshoot and undershoots of the measured signals and the overall dynamic behavior of the system.
Case 2 compares the PV farm output active power (P), reactive power (Q), phase instantaneous current ($i_a(t)$) and RMS current ($I_a^{[rms]}$), and PCC bus instantaneous voltage ($v_a(t)$) and RMS voltage ($V_a^{[rms]}$) between the detailed and proposed aggregated models in a weak grid with $SCR = 2.75$ and $X/R = 4$, and the results are shown in Figure 4.18b. Figure 4.18b indicates that the system can reach the MPP with higher oscillations compared to the strong grid. It should be noted that similar to the strong grid, during grid voltage sags, the PV farm output current increases to deliver the MPP active power to the grid. Additionally, Figure 4.18b demonstrates the accuracy of the proposed model in predicting overshoots, undershoots, and the dominant osculations of the system.

Partially shaded PV farm:

To validates the performance of the proposed model in systems with shaded PV units, the PV farm is considered to have the initial characteristics shown in Figure 4.19a. Then, PV array 1 is partially shaded at $t = 0.2$ [s] as shown in the Figure 4.19b.

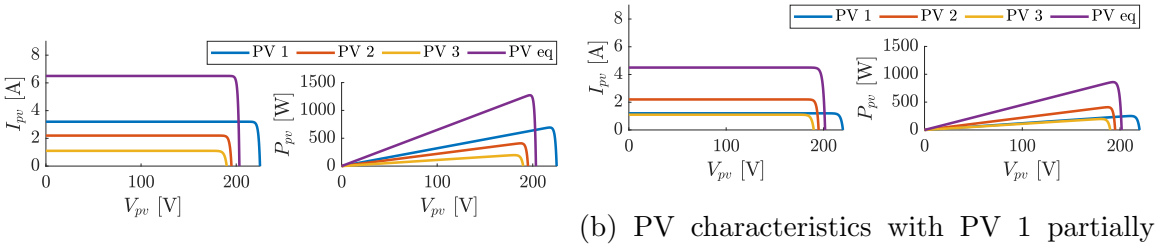

(a) PV characteristics with no shading.

(b) PV characteristics with PV 1 partially shaded.

Figure 4.19: The phase voltage and output current of the experimental and the WD agg model at each voltage reference signal step of.

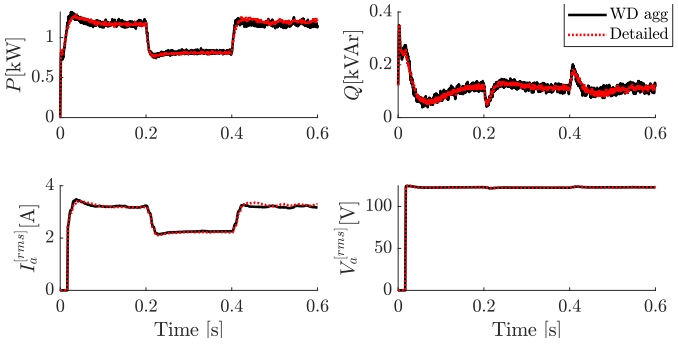

(a) Strong grid: $X/R = 4,\ SCR = 11.5$.

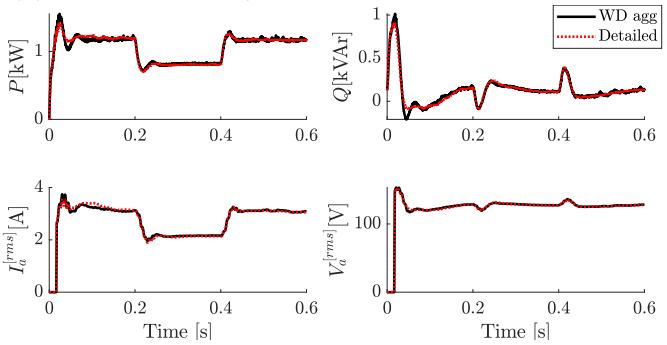

(b) Weak grid: $X/R = 4,\ SCR = 2.75$.

Figure 4.20: Case 3 & 4 (Partially shaded PV farm): The PV farm output active power (P), reactive power (Q), phase RMS ($I_a^{[rms]}$) current, and PCC bus RMS $V_a^{[rms]}$ voltage for both detailed and the proposed aggregated models in: a) Strong grid, b) Weak grid.

Furthermore, the system returns to its full generating power at $t = 0.4$ [s]. The PV farm output active power (P), reactive power (Q), phase instantaneous ($i_a(t)$) and RMS ($I_a^{[rms]}$) current, and PCC bus instantaneous ($v_a(t)$) and RMS $V_a^{[rms]}$ voltage for both detailed and the proposed aggregated models are shown in Figure 4.20a and 4.20b for a strong grid with $SCR = 11.5$ and $X/R = 4$ as Case 3 and a weak grid with $SCR = 2.75$ and $X/R = 4$ as Case 4. Both cases show a reduction in the PV farm output power during the shaded window, however the transient duration windows

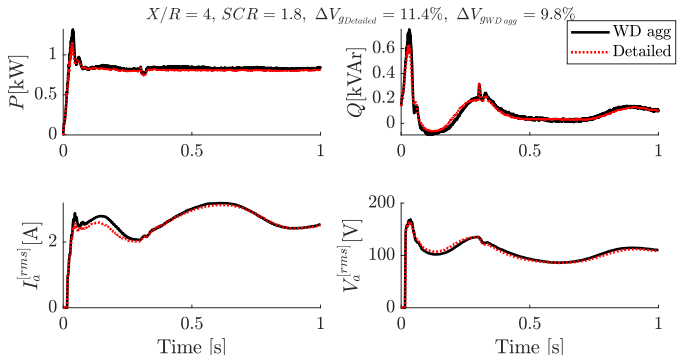

(a) Critically stable.

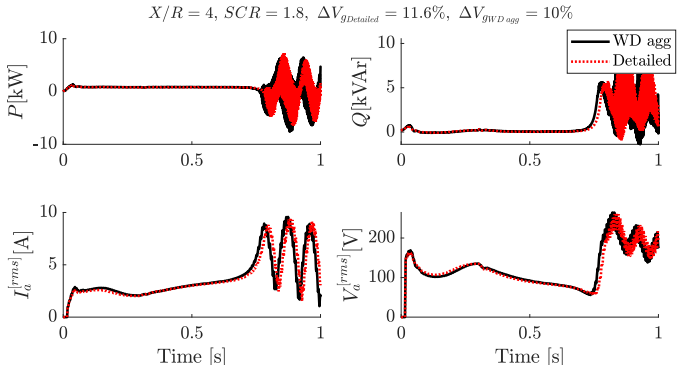

(b) Unstable.

Figure 4.21: Case 5 (Small-signal analysis): The PV farm output active power (P), reactive power (Q), phase RMS ($I_a^{[rms]}$) current, and PCC bus RMS $V_a^{[rms]}$ voltage for both detailed and the proposed aggregated models in: a) Critically stable, b) Unstable.

are longer and the dynamic performance of the system is less desirable in the weak grid. Figure 4.20a and 4.20b also validate the application of the proposed model in mimicking the overall dynamic and steady-state behavior of the system.

Stability and transient analyses:

To validate the stability and transient performance of the proposed model in systems during small-signal and large-signal events, the PV farm with control parameters of Table 4.4 is utilized in a very weak grid with $SCR = 1.8$. Small-signal analysis was conducted by studying a small grid voltage drop, while large-signal analysis was conducted by studying a symmetrical three-phase line-to-line short-circuit fault with a fault resistance of $1[m\Omega]$ and a grounding resistance of $0.01[\Omega]$. As Figure 4.21a shows the detailed system can be found critically stable with $\Delta V_{g_{Detailed}} = 11.4\%$ grid voltage drop and the WD agg model exhibits a similar condition with $\Delta V_{g_{WD\ agg}} = 9.8\%$. Moreover, Figure 4.21b illustrates that the detailed system and WD agg models can be found unstable with $\Delta V_{g_{Detailed}} = 11.6\%$ and $\Delta V_{g_{WD\ agg}} = 10\%$, respectively. Furthermore, Figure 4.22a shows the detailed system is critically stable with $\Delta t_{Detailed} = 20[ms]$

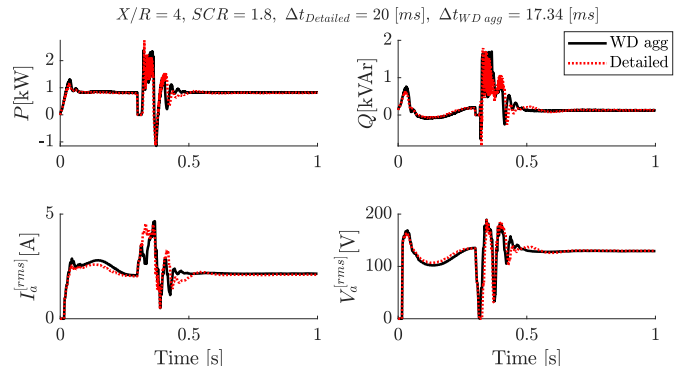

(a) Critically stable.

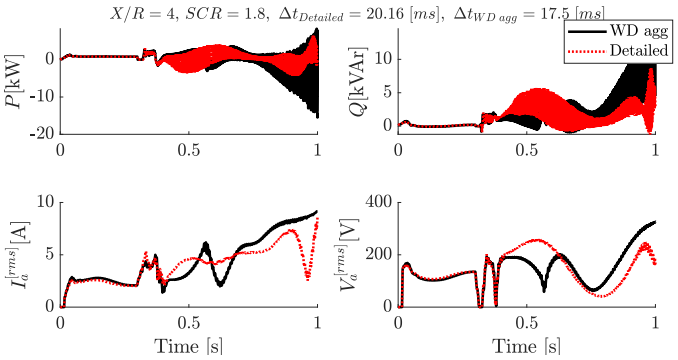

(b) Unstable.

Figure 4.22: Case 6 (Large-signal analysis): The PV farm output active power (P), reactive power (Q), phase RMS ($I_a^{[rms]}$) current, and PCC bus RMS $V_a^{[rms]}$ voltage for both detailed and the proposed aggregated models in: a) Critically stable, b) Unstable.

grid voltage drop and the WD agg model exhibits a similar condition with $\Delta t_{WD\ agg} = 17.34[ms]$. Moreover, Figure 4.22b illustrates that the detailed system and WD agg models are unstable with $\Delta t_{Detailed} = 20.16[ms]$ and $\Delta t_{WD\ agg} = 17.5[ms]$, respectively. The results obtained from both small-signal and large-signal analyses indicate that the proposed WD agg model can conservatively predict the critical stable operation points. Furthermore, as illustrated in Figure 4.21 and 4.22, the proposed model can accurately mimic the overall small-signal and large-signal transient behavior of the detailed system, thereby demonstrating its effectiveness in modeling the system's transient response.

4.6 Experimental Results

To verify the proposed modeling approach in practice a system with three paralleled PV units, shown in Figure 4.1(a) with the setup shown in Figure 4.23, Scenario C parameters of Table 4.1, and the parts number shown in Table 4.5 is implemented. The achieved experimental results are also compared with the detailed and WD agg

Table 4.3: System specifications with $V_{grid} = 120$ $[V]$, $f_{grid} = 60$ $[Hz]$.

Parameter	Inv 1	Inv 2	Inv 3	Parameter	Inv 1	Inv 2	Inv 3
$L[mH]$	2.5	2.0	2.5	$R[\Omega]$	0.44	0.64	0.44
$C[\mu F]$	2.5	2.5	2.0	$L_o[mH]$	1.0	1.0	0.5
$R_o[\Omega]$	0.38	0.38	0.28	K_p	36	36	36
K_i	8533	6400	4266	K_{pv}	0.120	0.144	0.072
K_{iv}	4.8	4	3.2	$C_{dc}[\mu F]$	390	290	540
$C_{pv}[\mu F]$	20	40	30	$V^*_{dc}[V]$	400	400	400
$L_b[mH]$	5	2	1	$R_b[m\Omega]$	1	10	5
$V_{oc}[V]$	225	195	190	$V_{mp}[V]$	220	190	185
$I_{sc}[A]$	3.2	2.2	1.1	$I_{mp}[A]$	3.1	2.1	1.0
K_{mpp}	480	500	520	$f_{sw}[kHz]$	20	20	20

Table 4.4: System control specifications for Case 5 and 6.

Parameter	Inv 1	Inv 2	Inv 3
K_p	48	48	48
K_i	64×10^3	49×10^3	32×10^3
K_{pv}	0.024	0.0288	0.0192
K_{iv}	1.92	1.6	1.28

models. Figure 4.24 shows grid phase voltage V_a, the output phase current I_a, active power P, and reactive power Q during the system start-up transient. As Figure 4.24 shows both detailed and WD agg models match with the experimental results.

To further assess the simulation models accuracy, two events are considered in the experimental system. First, a 0.2pu voltage sag is applied to the grid voltage at $t = 1.82$s and is cleared at $t = 3.705$s. Figure 4.25 compares the experimental results with both detailed and WD models. As the results show, by decreasing the grid voltage, the output currents increase due to having a constant power generation in PV units. Also, Figure 4.25 illustrates that both models have a close behavior to the experimental system. It is worth noting that the difference between experimental results and the proposed model is due to uncertainties of system parameters identifications and experimental signal measurement errors. To validate this justification, the detailed model of the system is also simulated and the results are compared with the proposed model and the experimental results. As demonstrated in Figure 4.24-4.26 the detailed and proposed models are completely matching while both have a similar difference compared with the experimental results thus it can be concluded that the error is due to uncertainties of system parameters identifications and experimental signal measurement errors.

Furthermore, to validate the proposed model accuracy for the systems with unequal parameters, an experimental setup with the parameters shown as Scenario D in Table 4.6 is implemented. To investigate the system response to reference signal variations, the dc voltage reference signal is increased at $t = 1$s to decrease the output

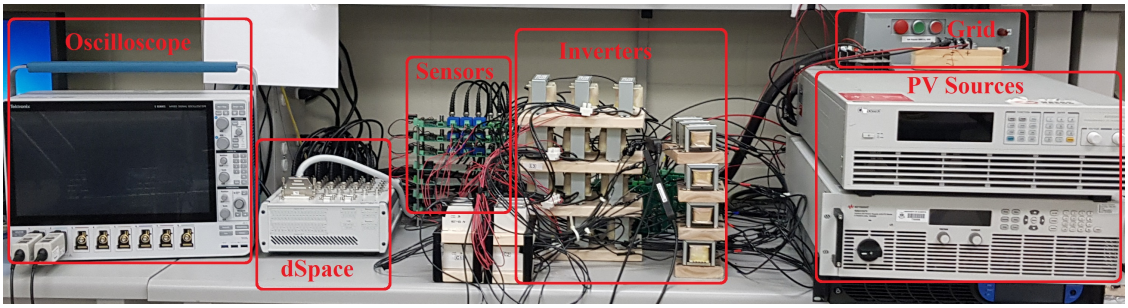

Figure 4.23: Experimental setup.

Table 4.5: Experimental part numbers.

Device	Part Number
Controller	dSpace MicroLabBox
Switches	STF23N80K5
Current Sensors	TMCS1101A1UQDRQ1
Voltage Sensors	LV 25-P
Grid Simulator	California Instruments AST 3003
PV Simulator 1	Chroma 62050H-600S
PV Simulator 2	Keysight N8937APV
PV Simulator 3	Chroma 62020H-150S

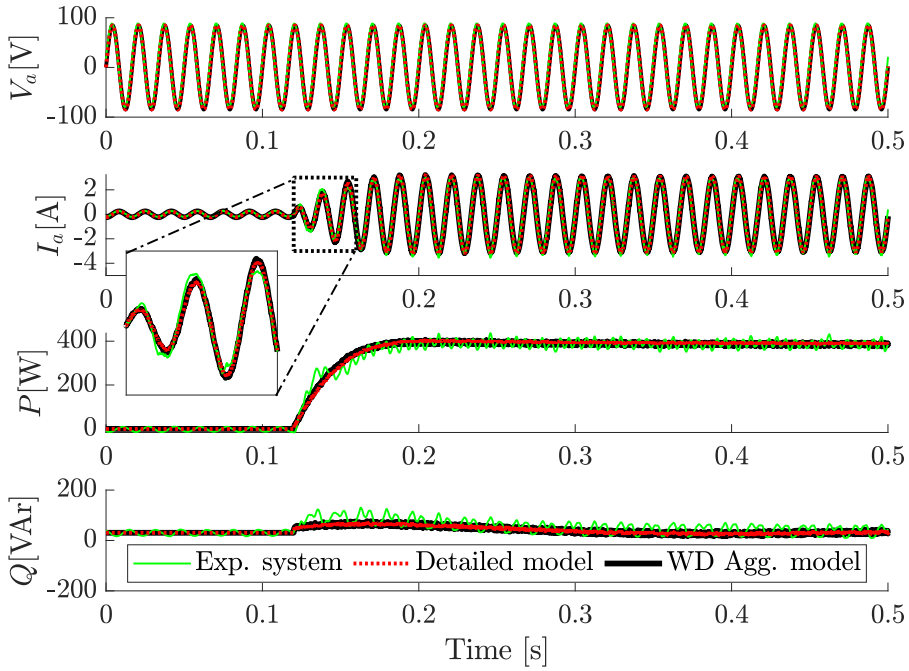

Figure 4.24: System start-up: experimental system, detailed, and WD agg models comparison.

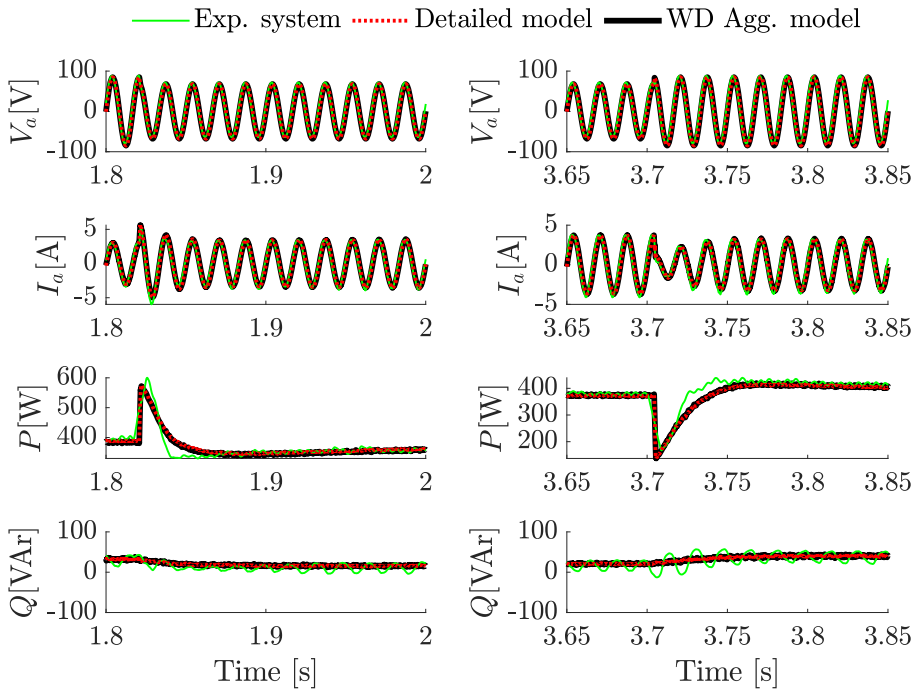

Figure 4.25: Grid voltage sag: Experimental system, detailed, and WD agg models comparison.

Table 4.6: Systems specifications used for Scenario D.

Parameter	Inv 1	Inv 2	Inv 3	Parameter	Inv 1	Inv 2	Inv 3
$L[mH]$	2.5	2.3	2.7	$R[\Omega]$	4.4	2.4	1.4
$C[\mu F]$	2.5	2.5	2.5	$R_c[\mu\Omega]$	31	31	31
$L_o[mH]$	1	1.2	0.85	$R_o[\Omega]$	3.8	1.8	0.8
K_p	12	10	8	K_i	100	80	60
K_{pv}	0.06	0.05	0.04	K_{iv}	36	30	24
$C_{DC}[\mu F]$	390	390	390	$V_{DC}[V]$	199	201	200

$$L_{grid} = 150\ [\mu H] \quad , \quad R_{grid} = 2\ [m\Omega]$$

power generation of PV units and is increased at $t = 2$s to the initial value to reach the initial power generation. Figure 4.26, 4.28, and 4.29 compare the experimental results with both detailed and WD agg models for both Scenario C and D, where Figure 4.27 shows the experimental results of Figure 4.26. As the results show, by increasing the reference signal for DC-link voltage the output power decreases, and consequently the output current decreases as well. Also, Figure 4.26, 4.28, and 4.29 illustrate both models have a close behavior to the experimental system.

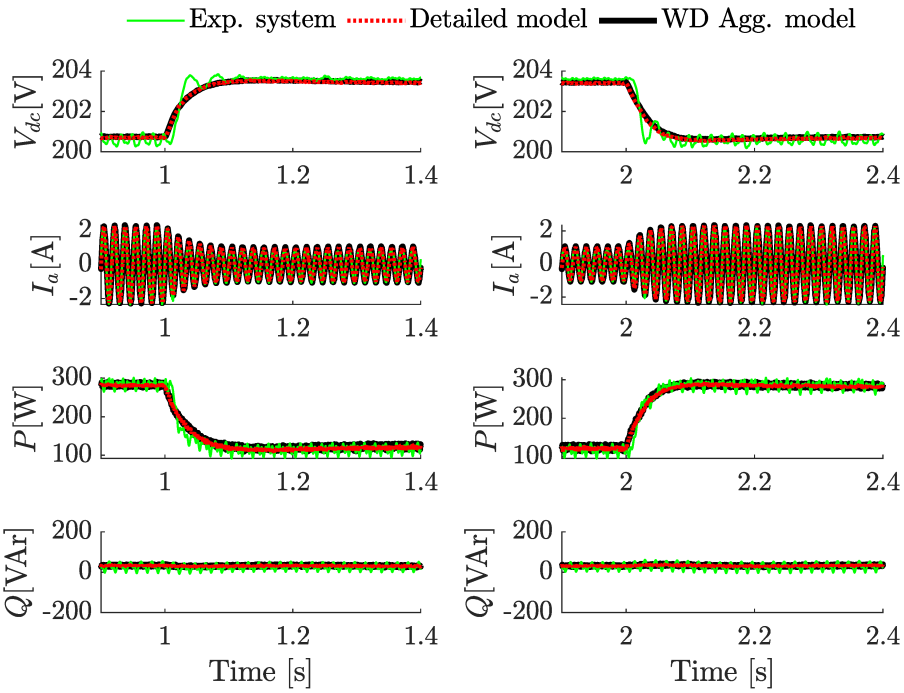

Figure 4.26: DC-link voltage reference signal changes: Experimental system, detailed, and WD agg models comparison.

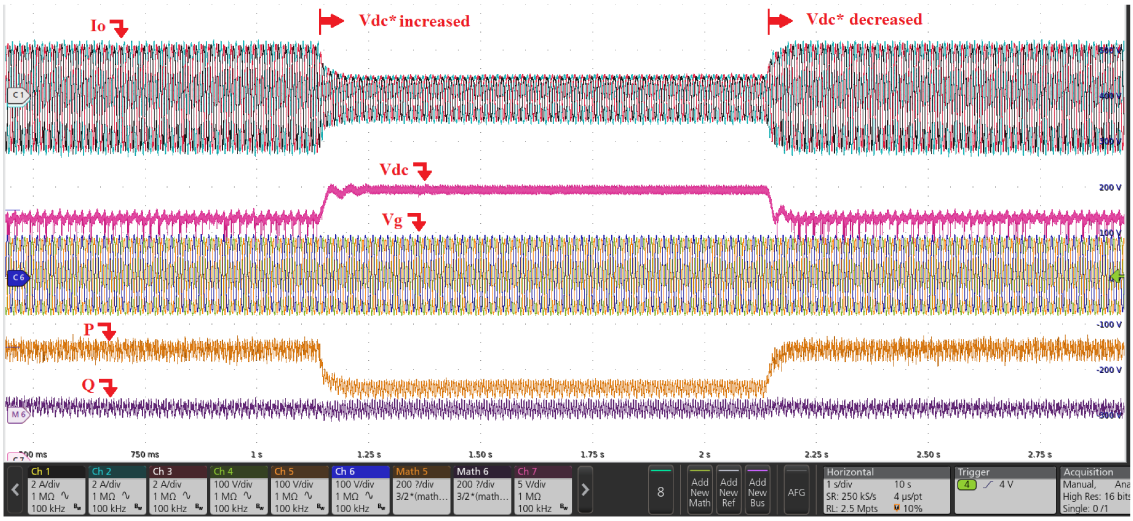

Figure 4.27: Experimental results for DC-link voltage reference signal changes.

4.7 Conclusion

This chapter introduced a novel WD aggregation (WD agg) approach to create an equivalent reduced-order model for large-scale PV farms characterized by double power conversion stages and significant parameter disparities. By applying the WD agg method, the inverter, boost converter, PV array, and control system of n paralleled PV units were combined into a single equivalent unit. The proposed model's

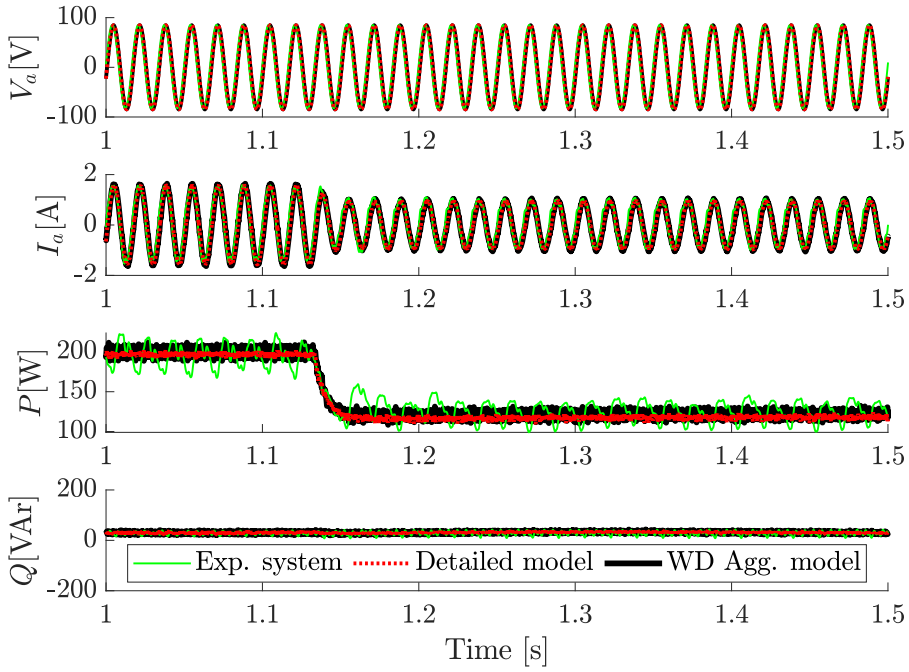

Figure 4.28: DC-link voltage reference signal increase: Experimental system, detailed, and WD agg models comparison.

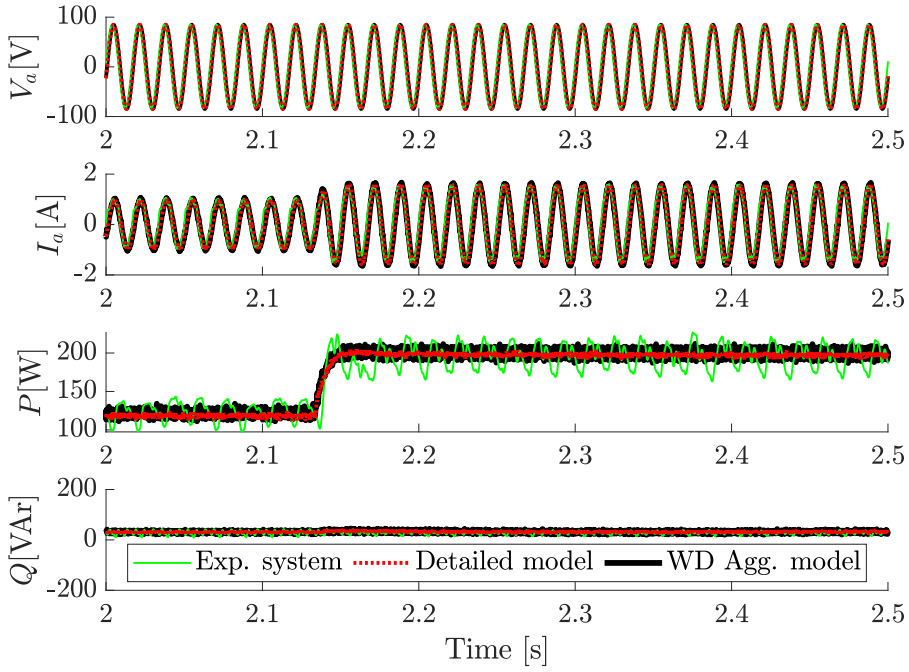

Figure 4.29: DC-link voltage reference signal decrease: Experimental system, detailed, and WD agg models comparison.

parameters were carefully determined based on the contribution of each inverter to the desired output dynamics of the system. To validate its accuracy, the model was

tested on a small-scale PV farm comprising three inverters with unequal parameters, and it successfully replicated the transient behavior during a 0.8 pu grid voltage sag. Particularly, the model accurately mimicked the dominant system oscillations in weak grid conditions. Additionally, the equivalent PV array demonstrated its capability to preserve the detailed steady-state and dynamic behavior of the system, even under partially shaded conditions. Moreover, the adoption of a single equivalent unit substantially reduced the computational burden associated with the system case studies. Furthermore, the proposed model's application was extended to larger-scale PV farms, such as the CIGRE MV/LV 14-bus benchmark for renewable energies, involving equal and unequal parameters. The achieved results exhibited a maximum error of 2.2%, demonstrating the model's ability to accurately represent the impact of up-stream buses and machine inertia on the PV farms' output dynamic behaviors, especially during harsh power system events, such as three full cycles of line-to-line faults at the PV farms' buses and 0.2 pu voltage sags at the infinite bus. Lastly, experimental results were provided, corroborating the accuracy and consistency of the proposed model with simulation and analytical findings. Overall, the WD agg approach showcased its effectiveness in creating a concise yet precise representation of large-scale PV farms, offering valuable insights into their dynamic behavior under diverse conditions while significantly reducing computational complexity.

Chapter 5

Consideration of Turbines Mechanical Dynamics in WD Aggregation for Induction Machine-Based Wind Farms

In this chapter the concept of Weighted Dynamic (WD) agg is applied to wind farms considering the mechanical and electric machine dynamics. The WD agg model a large-scale wind farm with an equivalent turbine, a generator, a back-back-to-back converter, and a collector line. The contribution of each WTG in the aggregated model is quantified and factored into the equivalent model. The equivalent turbine provides a simpler model and better insight regarding the mechanical system behavior that has not been clearly addressed in the existing literature.

The performance of the proposed method is evaluated based on the comparisons of a 4-WTGs DFIG wind farm and the obtained equivalent model. Moreover, a time-domain simulation of 20-WTGs DFIG wind farm with a variable wind speed curve is studied to verify the applicability of the proposed model in a more realistic scenario. Finally, a 4-WTGs fixed-speed wind farm is studied to demonstrate the generality of the proposed method. Simulations results conducted under identical and unequal WTGs operating conditions demonstrate a superior performance of the proposed method compared to the existing approaches.

- N. Shabanikia, A. A. Nia, A. Tabesh and S. A. Khajehoddin, "Weighted Dynamic Aggregation Modeling of Induction Machine-Based Wind Farms," in *IEEE Transactions on Sustainable Energy*, vol. 12, no. 3, pp. 1604-1614, July 2021 [95].
- S. A. Khajehoddin, A. Tabesh, and N. Shabanikia, "Aggregated model of large-scale wind farms for power system simulation software tools," Dec. 24 2020. US Patent App. 16/904,959 [96].

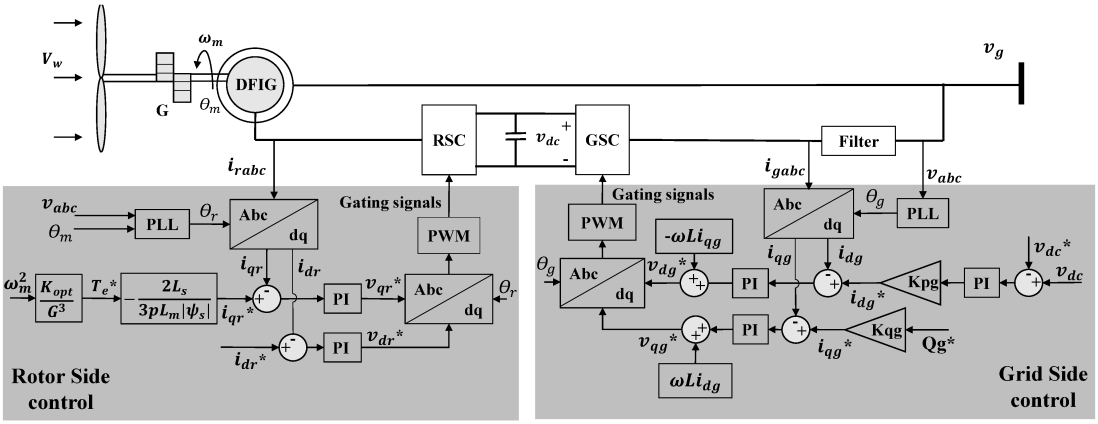

Figure 5.1: DFIG WTG Schematic.

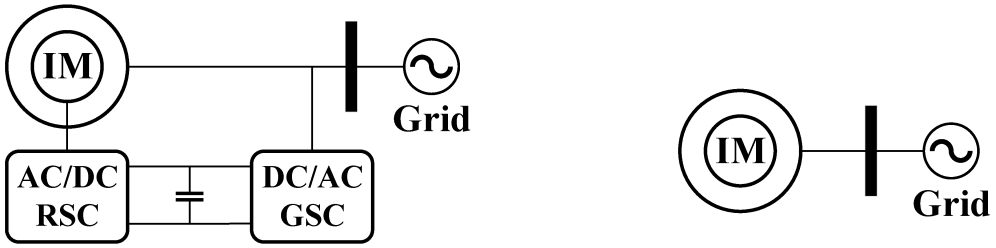

(a) (b)

Figure 5.2: a) DFIG WTG, b) Fixed-Speed WTG.

5.1 Induction Machine-based Wind Farms Structure

A large number of WTGs use induction generators with the stator directly connected to the grid. Due to the wide wind speed range, such induction machines operate at high slip away from their nominal speed. The high slip results in high rotor loss, low efficiency and heated rotor in WTGs with a squirrel cage rotor limiting the operating speed range and output power. Hence, the WTGs with a squirrel cage rotor that can efficiently operate close to the nominal speed are called fixed-speed WTGs. To expand the speed range of such induction machines, the rotor can be connected to the grid through an AC/DC/AC variable frequency converter forming a DFIG shown in Figure 5.1 and 5.2. This converter delivers a portion of the rotor energy back to the grid resulting in a rotor loss reduction and a larger wind speed operating range.

Figure 5.2 shows a diagram of a fixed-speed and a DFIG WTG. Each WTG includes a wind turbine, generating mechanical power P_m and mechanical torque τ_m according

to the following equation:

$$P_m = \tau_m \omega_m = \frac{1}{2} C_p(\lambda, \beta) \rho A V_W^3, \tag{5.1}$$

where:

$$C_p(\lambda, \beta) = \frac{C_{pmax}}{\lambda_{opt}^2} (2\lambda_{opt} - \lambda)\lambda, \tag{5.2}$$

and ω_m is the mechanical speed of generator, V_W is wind speed, ρ is air density and A is area covered by the blades. The mechanical power is related to wind power by turbine coefficient $C_p(\lambda, \beta)$. This factor depends on the structure of the wind turbine, where β is the blade angle, $\lambda = r\omega_l / V_W$ is the turbine Tip Speed Ratio (TSR), r is blades radius, ω_l is blades rotational speed, C_{pmax} is the maximum value of C_p, and λ_{opt} is the optimum TSR where $C_p = C_{pmax}$.

Although any control system can be applied, this chapter uses reference [97] DFIG control approach, as shown in Figure 5.1. In this control system, the Grid-Side Converter (GSC) controls the DC bus voltage to ensure the DC link voltage stability. A PI compensator uses the DC voltage error to generate the GSC d-axis reference current i_{dg}^*. Also, GSC can provide a desired amount of reactive power Q_g^* using the q-axis reference current i_{qg}^*. As the major reactive power consumed by an induction machine is determined by its magnetizing inductance, the Q_g^* can be estimated by $Q_g^* = v_s^2 / X_m$, where v_s is the measured stator rms line-to-line voltage and X_m is the machine magnetizing reactance. An inner current control loop generates the gating signals for the GSC by means of i_{dg}^* and i_{qg}^*. The Rotor-Side Converter (RSC) controls the induction machine operating under a large range of wind speeds. RSC measures the rotor speed ω_m and generates the torque reference T_e^* through $T_e^* = K_{opt} \omega_m^2 / G^3$, where K_{opt} is defined as:

$$K_{opt} = \frac{1}{2} \rho \pi r^5 C_{pmax} / \lambda_{opt}^3, \tag{5.3}$$

and G is the gear-box ratio. The T_e^* signal is also used to form the rotor q-axis reference current i_{qr}^* for the RSC current controllers by:

$$i_{qr}^* = -\frac{T_e^*}{\frac{3}{2} p \frac{L_m}{L_s} |\psi_s|}, \tag{5.4}$$

where p is the number of machine poles, L_m is the magnetizing inductance, L_s is the stator self-inductance and $|\psi_s|$ is stator linkage flux and estimated with $|\psi_s| = \sqrt{\frac{2}{3}} \frac{V_s}{\omega_s}$, where V_s is the rated rms value of the stator line-to-line voltage and ω_s is the synchronous speed. Also, the rotor d-axis reference current i_{dr}^* is set to zero to use all of the RSC capacity for active power delivery from the rotor windings as the required reactive power for the induction machine is provided by the GSC. It is worth mentioning that, the generality of the proposed method is not limited by the i_{dr}^* set value.

5.2 Steady-State Derivation

To find the dynamic model of the wind farm, a small-signal model of the WTG and wind farm should be derived. Small-signal model of a WTG requires the steady-state calculations at the operating condition. The steady-state electro-mechanical relationship between the mechanical side and electrical side of a WTG are expressed as:

$$\tau_m + \tau_e = D\omega_m. \tag{5.5}$$

τ_e is the electrical torque and D is the mechanical damping of the induction machine. The steady state speed, ω_{m_0}, can be found with the assumption that the control system is stable so that $T_e^* = T_e$, where T_e and T_m are the steady-state of τ_e and τ_m, respectively. Substituting (5.1) and $T_e^* = K_{opt}\omega_m^2$ into (5.5) and solve it for ω_m other DFIG steady-state parameters can be expressed as follows[97]:

$$\begin{aligned} T_e = K_{opt}\omega_{m_0}^2, \quad I_{qr} = -\frac{T_e}{\frac{3}{2}p\frac{L_m}{L_s}|\psi_s|}, \quad I_{dr} = 0, \\ T_m + T_e = D\omega_{m_0}, \quad I_{qs} = -\frac{L_m}{L_s}I_{qr}, \quad I_{ds} = \frac{|\psi_s|}{L_s}. \end{aligned} \tag{5.6}$$

A similar approach can be used for fixed-speed WTG. Referring to the [98] for a squirrel cage induction machine $T_e \cong X_m^2 R_r s_0 |v_s|/\Delta_{T_e}$ in the steady-state, where:

$$\Delta_{T_e} = [R_s R_r + s_0(X_m^2 - X_{ss}X_{rr})]^2 + [R_r X_{ss} + s_0 R_s X_{rr}]^2,$$

and, X_m, X_{ss} and X_r are the magnetizing inductance, stator and rotor self-inductances respectively. R_s and R_r are the stator and rotor resistances and s_0 is the slip. By substituting (5.1) into (5.5) and solving that for ω_m, the ω_{m_0} can also be found for a fixed-speed WTG. By applying $V_{qr} = V_{dr} = 0$ for squirrel cage rotors and ω_{m_0} in the induction machine steady-state equations, the other steady-state parameters such as I_{ds}, I_{qs}, I_{dr} and I_{qs} can be found.

5.3 The Proposed Weighted Dynamic Aggregation Method

The WD agg of GSC and inner current controller of RSC is discussed in Chapter 2. This section calculates the wind farm equivalent electrical generator, outer speed controller and mechanical part (the equivalent turbine) separately:

5.3.1 Equivalent generator

The objective is to find an equivalent WTG with the same structure of the individual WTGs whose dynamic behavior is close to the overall wind farm from the grid point of

view. Therefore, the wind farm equivalent WTG should also have a set of large-signal equations and the d-q axis circuits similar to the individual WTG where:

$$v_{ds_{eq}} = v_{ds},\ v_{qs_{eq}} = v_{qs},\ i_{ds_{eq}} = \sum_{k=1}^{n} i_{ds_k},\ i_{qs_{eq}} = \sum_{k=1}^{n} i_{qs_k}. \tag{5.7}$$

Therefore, to find the interaction of the wind farm with the grid and its equivalent model, the differential equation relating i_{dqs} and v_{dqs} should be derived. The stator equations of kth machine can be derived as:

$$\begin{aligned} v_{ds} &= (R_{s_k} + L_{s_k}\frac{d}{dt})i_{ds_k} - \omega_s L_{s_k} i_{qs_k} + L_{m_k}\frac{d}{dt}i'_{dr_k} - \omega_s L_{m_k} i'_{qr_k}, \\ v_{qs} &= \omega_s L_{s_k} i_{ds_k} + (R_{s_k} + L_{s_k}\frac{d}{dt})i_{qs_k} + \omega_s L_{m_k} i'_{dr_k} + L_{m_k}\frac{d}{dt}i'_{qr_k}, \end{aligned} \tag{5.8}$$

Now, similar to the previous chapters investigating three-phase systems in rotating reference frames, by rotating the common rotating frame to a new rotating frame, where $\sum_{k=1}^{n} i_{qs_k}^{\theta_{i_s}} = 0$, and defining the stator current weights as $\mu_{sdq} = i_{dqs_k}^{\theta_{i_s}} / \sum_{k=1}^{n} i_{dqs_k}^{\theta_{i_s}}$, unified dynamic equations for n stators can be derived as:

$$\begin{aligned} v_{ds}^{\theta_{i_s}} &= \sum_{k=1}^{n}(R_{s_k}\mu_{sd_k} + L_{s_k}\mu_{sd_k}\frac{d}{dt})i_{ds_{eq}}^{\theta_{i_s}} + \sum_{k=1}^{n}\left(L_{m_k}\frac{d}{dt}i'^{\theta_{i_s}}_{dr_k} - \omega_s L_{m_k} i'^{\theta_{i_s}}_{qr_k}\right), \\ v_{qs}^{\theta_{i_s}} &= \sum_{k=1}^{n}\omega_s\mu_{sd_k}L_{s_k} i_{ds_{eq}}^{\theta_{i_s}} + \sum_{k=1}^{n}\left(\omega_s L_{m_k} i'^{\theta_{i_s}}_{dr_k} + L_{m_k}\frac{d}{dt}i'^{\theta_{i_s}}_{qr_k}\right), \end{aligned} \tag{5.9}$$

Transforming (5.9) into the stationary reference frame dynamic equation yields:

$$v_{s_{eq}} = \sum_{k=1}^{n}(R_{s_k}\mu_{sd_k} + L_{s_k}\mu_{sd_k}\frac{d}{dt})i_{s_{eq}} + \sum_{k=1}^{n} L_{m_k}\frac{d}{dt}i'_{r_k}. \tag{5.10}$$

By comparing (5.10) with a single stator dynamic equation, the equivalent stator dynamic equation and parameters can be found as:

$$v_s = (R_{s_{eq}} + L_{s_{eq}}\frac{d}{dt})i_{s_{eq}} + L_{m_{eq}}\frac{d}{dt}i'_{r_{eq}}, \tag{5.11}$$

where:

$$\begin{aligned} v_{s_{eq}} = \sum_{k=1}^{n}\frac{v_{s_k}}{n} = v_s,\ i_{s_{eq}} = \sum_{k=1}^{n} i_{s_k},\ R_{s_{eq}} = \sum_{k=1}^{n}\frac{\mu_{sd_k}}{n}R_{s_k},\ L_{s_{eq}} = \sum_{k=1}^{n}\frac{\mu_{sd_k}}{n}L_{s_k}, \\ L_{m_{eq}}\frac{d}{dt}i'_{r_{eq}} = \sum_{k=1}^{n} L_{m_k}\frac{d}{dt}i'_{r_k}. \end{aligned} \tag{5.12}$$

It is worth noting that the stator weights μ_{sd} can be estimated with the steady-state values of stator currents as $\mu_{sd} \simeq I_{ds_k}^{\theta_{i_s}} / \sum_{k=1}^{n} I_{ds_k}^{\theta_{i_s}}$. By a similar approach the equivalent rotor equation and parameters can be derived as:

$$v'_{r_{eq}} = (R'_{r_{eq}} + L'_{r_{eq}}\frac{d}{dt})i'_{r_{eq}} + L_{m_{eq}}\frac{d}{dt}i_{s_{eq}}, \tag{5.13}$$

where:

$$v'_{r_{eq}} = \sum_{k=1}^{n} \frac{v'_{r_k}}{n},\ i'_{r_{eq}} = \sum_{k=1}^{n} i'_{r_k},\ R'_{r_{eq}} = \sum_{k=1}^{n} \frac{\mu_{rd_k}}{n} R'_{r_k},\ L'_{r_{eq}} = \sum_{k=1}^{n} \frac{\mu_{rd_k}}{n} L'_{r_k},$$
$$L_{m_{eq}} \frac{d}{dt} i_{s_{eq}} = \sum_{k=1}^{n} L_{m_k} \frac{d}{dt} i_{s_k}. \tag{5.14}$$

It is worth noting that the rotor weights μ_{rd} are found in a specific rotating frame, where $\sum_{k=1}^{n} i'^{\theta_{i_r}}_{qr_k} = 0$, and can be estimated with the steady-state values of rotor currents as $\mu_{rd} \simeq I'^{\theta_{i_r}}_{dr_k} / \sum_{k=1}^{n} I'^{\theta_{i_r}}_{dr_k}$.
To find the equivalent magnetizing inductance, the magnetizing inductance dynamic equations of (5.12) and (5.14) can be summed, which results in:

$$L_{m_{eq}} \frac{d}{dt}(i_{s_{eq}} + i'_{r_{eq}}) = \sum_{k=1}^{n} L_{m_k} \frac{d}{dt}(i_{s_k} + i'_{r_k}). \tag{5.15}$$

Deriving (5.15) in a specific reference frame, where $(i^{\theta_{L_m}}_{sq_{eq}} + i'^{\theta_{L_m}}_{rq_{eq}}) = 0$, and defining the magnetizing weights as $\mu_{md_k} = (i^{\theta_{L_m}}_{sd_k} + i'^{\theta_{L_m}}_{rd_k})/(i^{\theta_{L_m}}_{sq_{eq}} + i'^{\theta_{L_m}}_{rq_{eq}})$, the equivalent magnetizing inductance can be found as:

$$L_{m_{eq}} = \sum_{k=1}^{n} \frac{\mu_{md_k}}{n} L_{m_k}. \tag{5.16}$$

It is worth noting that the magnetizing weights μ_{md} can be estimated with the steady-state values of stator and rotor currents as:

$$\mu_{md_k} \simeq \frac{I^{\theta_{L_m}}_{ds_k} + I'^{\theta_{L_m}}_{dr_k}}{\sum_{k=1}^{n} (I^{\theta_{L_m}}_{ds_k} + I'^{\theta_{L_m}}_{dr_k})}. \tag{5.17}$$

To find the same set of equations for a fixed-speed WTG the same steps can be followed by considering $v_{dqr} = 0$ as it has a squirrel cage rotor structure.

5.3.2 Equivalent turbine

To find an equivalent turbine and the equivalent wind speed, a few facts should be considered. First, the area which is covered by the equivalent turbine should be equal to the summation of the area that is covered by all the WTGs in the wind farm combined $A_{eq} = \sum_{k=1}^{n} A_k$. Second, the amount of wind power in the area is independent of wind farm structure. Therefore:

$$P_{W_{eq}} = \sum_{k=1}^{n} P_{W_k} \Rightarrow V_{W_{eq}} = \sqrt[3]{(\sum_{k=1}^{n} A_k V^3_{W_k})/A_{eq}}. \tag{5.18}$$

Third, the equivalent mechanical power P_m generated by the equivalent turbine should also be equal to the summation of wind farm generated mechanical power:

$$P_{m_{eq}} = \sum_{k=1}^{n} P_{m_k}. \tag{5.19}$$

Fourth, $T_{e_{eq}} = \sum_{k=1}^{n} T_{e_k}$ in steady-state, thus $\omega_{m_{0_{eq}}}$ can be found by:

$$\frac{P_{m_{eq}}}{\omega_{m_{0_{eq}}}} + T_{e_{eq}} \simeq 0. \tag{5.20}$$

Therefore, $K'_{opt_{eq}} = K_{opt_{eq}}/G_{eq}^3$ can be found by $T_{e_{eq}} = \omega_{m_{0_{eq}}}^2 K'_{opt_{eq}}$. Considering (5.19), the equivalent turbine curve $C_{pmax_{eq}}$ and $\lambda'_{opt_{eq}} = \lambda_{opt_{eq}} G_{eq}$ can be found by:

$$C_{p_{eq}} P_{W_{eq}} = \sum_{k=1}^{n} C_{p_k} P_{W_k} \ , \ K'_{opt_{eq}} = \frac{1}{2}\rho\pi r_{eq}^5 C_{pmax_{eq}}/\lambda'^3_{opt_{eq}}. \tag{5.21}$$

It should be noted that any speed ratio $G_{eq}p_{eq}$ between the mechanical and electrical side can be used as long as (5.19) is satisfied and it will not limit the generality of the method. Without the loss of generality $G_{eq} = \sum_{k=1}^{n} G_k/n$ and $p_{eq} = \sum_{k=1}^{n} p_k/n$. It is worth noting that by following the same steps that led to (5.21) a $\lambda_{opt_{eq}}$ and $C_{pmax_{eq}}$ can also be found for a fixed-speed wind farm with the help of given equations:

$$C_{p_{eq}} P_{W_{eq}} = \sum_{k=1}^{n} C_{p_k} P_{W_k} \ , \ \lambda_{opt_{eq}} = \sum_{k=1}^{n} \mu_{s_k} \lambda_{opt_k}. \tag{5.22}$$

Finally, there are three possibilities to model the equivalent inertia J_{eq}:
1) By the summation of all turbines inertia similar to the existing Full and Zone agg methods:

$$J_{eq} = \sum_{k=1}^{n} J_k, \tag{5.23}$$

2) Based on the total angular momentum of all WTGs:

$$J_{eq}\omega_{m_{eq}} = \sum_{k=1}^{n} J_k \omega_{m_k}, \tag{5.24}$$

3) Based on the total rotational energy of all WTGs:

$$\frac{1}{2} J_{eq}\omega_{m_{eq}}^2 = \frac{1}{2} \sum_{k=1}^{n} J_k \omega_{m_k}^2. \tag{5.25}$$

To compare these approaches, a 4-WTG DFIG wind farm shown in Figure 5.3 is simulated in five different case scenarios of equal and unequal rated power, inertia, and operating points to highlight models accuracies. Scenario 1 to 5 specifications are listed in Table 5.1 and 5.2, respectively. The grid line-to-line voltage $v_s = 690$ $[v]$,

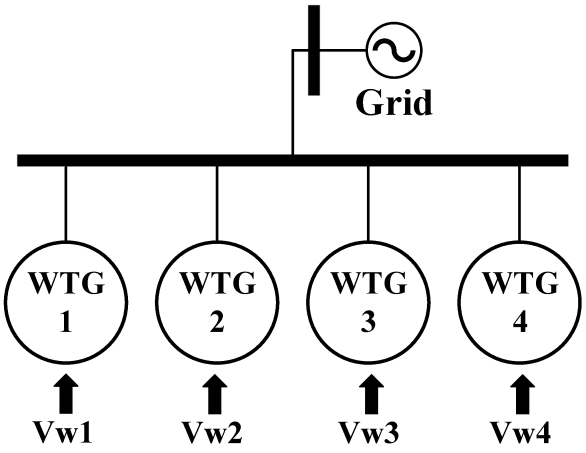

Figure 5.3: 4-WTGs wind farm, where V_W 1 to 4 and WTGs are not necessary similar.

Table 5.1: Scenario 1 and 2 specifications: A 4-WTGs DFIG wind farm with equal WTGs parameters and various wind speeds.

Parameter	WTG1	WTG2	WTG3	WTG4	Unit
V_W(Sc. 1 , 2)	9.5 , 11.5	9.5 , 11.5	9.5 , 6.5	9.5 , 6.5	$[m/s]$
S	2	2	2	2	$[MVA]$
J	127	127	127	127	$[kgm^2]$
τ_n	100	100	100	100	$[ms]$
r	48	48	48	48	$[m]$
λ_{opt}	7.9168	7.9168	7.9168	7.9168	$[-]$

grid frequency $f = 50\ [Hz]$, DC-Link voltage $V_{DC} = 1500\ [v]$ and switching frequency $f_{sw} = 4\ [kHz]$ for Scenario 1 to 5. The rest of Scenario 1 to 5 parameters can be found in Table 5.4. It is worth mentioning that Scenario 2, 4, and 5 are extreme conditions where two groups of WTGs operating speeds are different by 0.5pu. A 0.2 pu voltage drop is applied at $t = 4s$ and cleared at $t = 6s$ to study the transient behavior of the system.

Table 5.3 shows the calculated equivalent inertia J_{eq} by all approaches. As Table 5.3 shows, all approaches result in the same equivalent inertia and simulation results when WTGs operating speeds are the same. However, the equivalent inertia from different approaches can be different in scenarios 2, 4, and 5 where the operating points are different. Figure 5.4 shows that the total rotational energy approach is more accurate than the other two approaches in all scenarios combined. Therefore, this chapter uses the total rotational energy approach to model the equivalent inertia J_{eq}. Now using the equivalent generator, controllers, and turbine parameters, an equivalent WTG can be achieved for the whole wind farm.

Table 5.2: Scenario 3, 4, and 5 specifications: A 4-WTGs DFIG wind farm with unequal WTGs parameters and various wind speeds.

Parameter	WTG1	WTG2	WTG3	WTG4	Unit
V_W(Sc. 3)	9.5	9.5	9.5	9.5	$[m/s]$
V_W(Sc. 4)	11.5	11.5	6.5	6.5	$[m/s]$
V_W(Sc. 5)	6.5	6.5	11.5	11.5	$[m/s]$
S	2	2	0.5	0.5	$[MVA]$
J	127	127	31.75	31.75	$[kgm^2]$
τ_n	100	100	25	25	$[ms]$
r	48	48	24	24	$[m]$
λ_{opt}	7.91681	7.91681	3.9584	3.9584	$[-]$

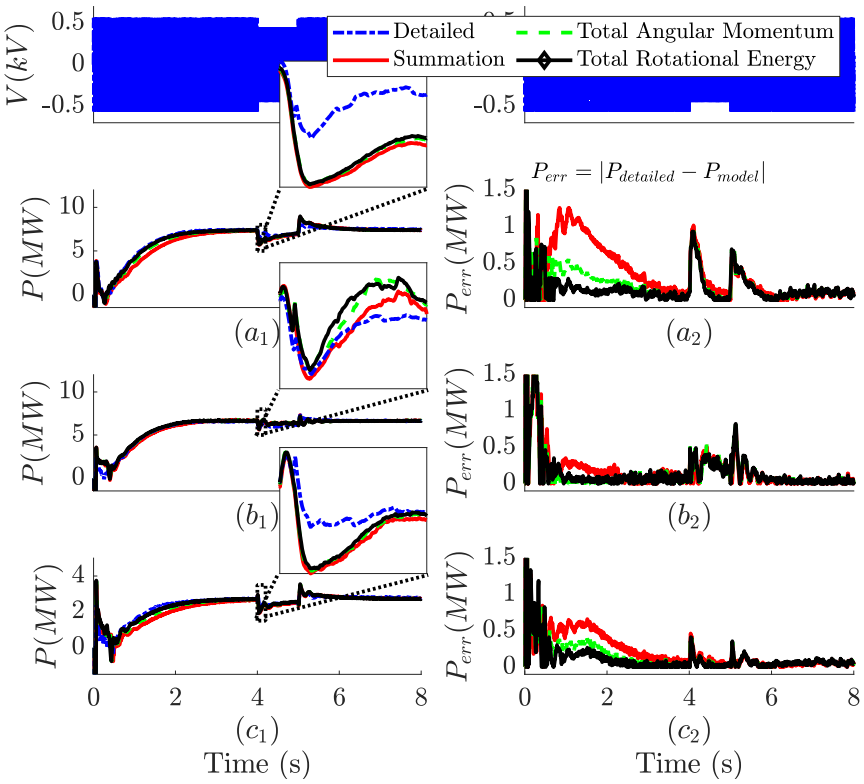

Figure 5.4: Comparison of equivalent inertia derivation with the summation, total angular momentum, and total rotational energy approaches for a detailed 4-WTGs DFIG wind farm: $a_{1,2}$) Scenario 2, $b_{1,2}$) Scenario 4, $c_{1,2}$) Scenario 5; (V PCC voltage, P active power, and P_{err} active power agg models error with respect to the detailed model).

5.4 Simulations Results

To validate the proposed WD agg model, several case studies are presented. A 4-WTGs DFIG wind farm shown in Figure 5.3 and a large-scale 20-WTGs DFIG wind

Table 5.3: Aggregated $J_{eq}[kgm^2]$ modeled by summation, total angular momentum, and total rotational energy approaches in Scenario 1 to 5.

Approach	Sc. 1	Sc. 2	Sc. 3	Sc. 4	Sc. 5
Summation	508	508	317.5	317.5	317.5
Total Angular Momentum	508	444.34	317.49	299.51	273.85
Total Rotational Energy	508	418.64	317.49	292.80	253.01

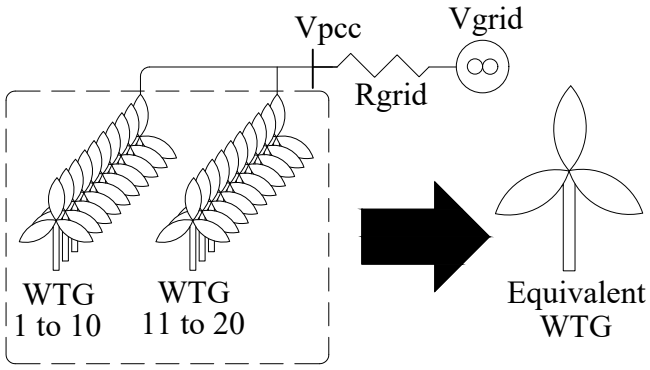

Figure 5.5: 20-WTGs wind farm, where WTGs parameters and wind speeds are not necessary similar.

farm shown in Figure 5.5 are studied under various operating scenarios. The grid parameters are similar to Scenario 1 to 5 for Scenario A, B, C and D. The rest of Scenario A, B, C, and D parameters can be found in Table 5.5, 5.7, 5.8, and 5.4, respectively. The rest of DFIG wind farm parameters are designed using [97], [99], and [100] as:

$$\begin{gathered}\sigma = 1 - L_m^2/L_sL,\ \alpha_1 = -L_m/L_s,\ \alpha_2 = L_r - L_m^2/L_s,\ \tau_i = \sigma L_r/R_r,\ \omega_{ni} = 100/\tau_i,\\ \omega_{nn} = 1/\tau_n,\ K_{p_{idq}} = 2\omega_{ni}\sigma L_r - R_r,\ K_{i_{idq}} = \omega_{ni}^2 L_r\sigma,\ K_{pg} = -K_{qg} = 1/(\sqrt{\frac{3}{2}}V_s),\\ \tau_{ig} = L_g/R_g,\ \omega_{nig} = 2\pi f,\ K_{p_{idqg}} = 2\omega_{nig}L_g - R_g,\ K_{i_{idqg}} = \omega_{nig}^2 L_g.\end{gathered} \tag{5.26}$$

To study the transients responses, Scenario A is considered where the WTGs have unequal parameters, and a 0.2 pu voltage sag is applied at t=4s and is cleared at t=6s. Similarly, for fixed-speed wind farm simulations, the voltage sag is considered to start at t=1s and end at t=2s. Also, to study the generality of the proposed method a 4-WTGs DFIG wind farm with a different power coefficient model for WTGs is presented as scenario C. To compare and verify the proposed method, all wind farms are aggregated with the Full, Zone and the proposed WD agg methods. A simple small wind farm is chosen for the first two scenarios to simplify the comparison between the proposed equivalent WTG and other existing methods. Moreover, 20-WTGs large-scale wind farm is chosen as the third scenario to verify the generality and applicability of the proposed method in real life examples.

Table 5.4: Common parameters for all DFIG WTGs in Scenario 1 to 5, A, B, C, and D.

Parameter	Value	Unit	Parameter	Value	Unit
L_{si}	87	$[\mu H]$	G	100	-
L_m	2.5	$[mH]$	C_{DC}	80	$[mF]$
R_s	2.6	$[m\Omega]$	L_g	0.4	$[mH]$
R_r	2.9	$[m\Omega]$	R_g	20	$[\mu\Omega]$
p	2	-	K_{pv}	10^3	-
D	0.001	-	K_{iv}	3×10^5	-

Table 5.5: Scenario A specifications: 4-WTGs DFIG Wind farm with unequal parameters.

Parameter	WTG 1	WTG 2	WTG 3	WTG 4	Unit
S	2	2	1	1	$[MVA]$
J	127	127	63.5	63.5	$[kgm^2]$
τ_n	12.5	12.5	12.5	12.5	$[ms]$
r	42	42	42	42	$[m]$
C_{pmax}	0.48	0.48	0.48	0.48	-
λ_{opt}	8.1	8.1	8.1	8.1	-
V_W	11	10	9	8	$[m/s]$

Scenario A: 4-WTGs DFIG wind farm with unequal parameters

Turbine shadow effect and different rated powers for WTGs are considered in this scenario. It should be noted that by different apparent power for WTGs, other parameters are also different in per unit as shown in Table 5.5. Figure 5.6 shows the PCC voltage, active and reactive power, and phase A current for all aggregation methods and their errors with respect to the detailed model. WD agg model shows better performance compared to the Full and Zone agg models. To measure the model accuracy, an error index EI can be defined as the integral of the absolute value of the difference between the model and the detailed system responses:

$$EI = \int_{t=t_0}^{t=t_1} (|F_{detailed} - F_{model}|)dt, \tag{5.27}$$

where F can be any response curves. This error index is calculated for, active, reactive power, and phase A current curves in all methods between $t_0 = 1$ to $t_1 = 10$ and normalized by the minimum error which was WD in all cases. The results are illustrated in the Table 5.6. It can be observed that WD model has at least 3 times more accurate output power in all scenarios while it has half of the complexity compared to the Zone agg model.

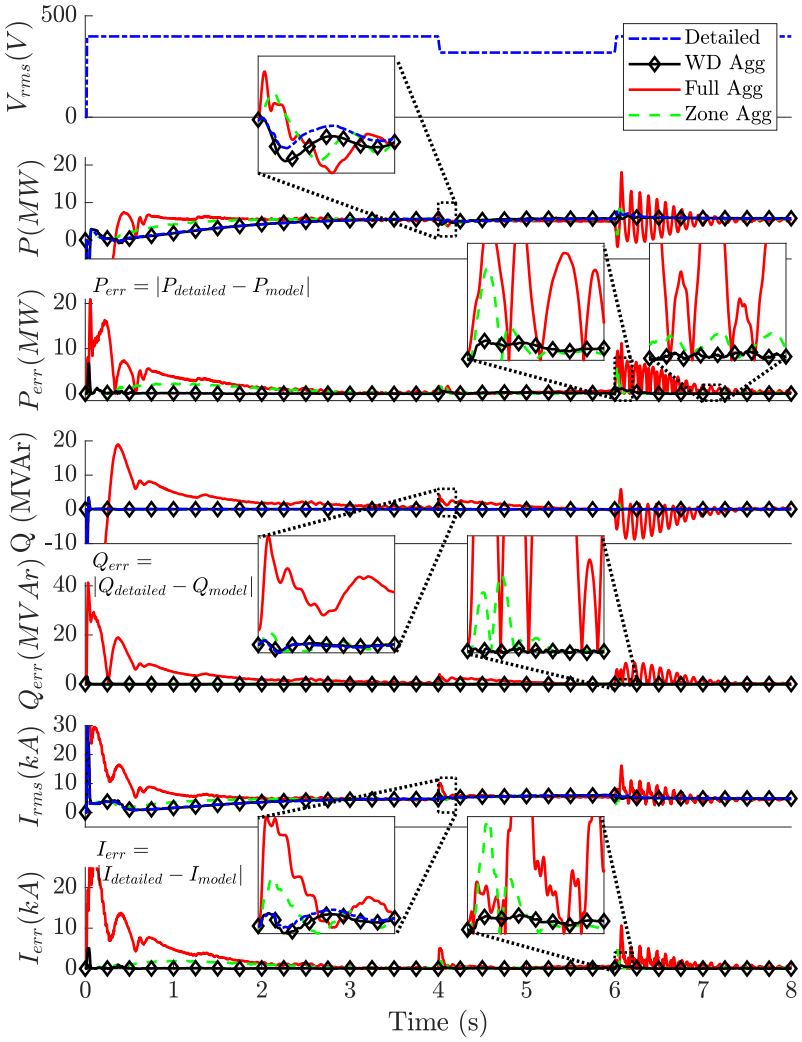

Figure 5.6: Scenario A: unequal parameters of WTGs; performance comparisons from PCC point for detailed 4-WTGs DFIG wind farm, proposed WD, Full, and Zone agg models; (V voltage rms, P & Q active and reactive powers, I phase A current rms, and subscript $_{err}$ indicates the model variable error with respect to the detailed system).

Table 5.6: Calculated error indexes for active power P, reactive power Q, and phase A current I in Scenario A.

Error Index	Active Power	Reactive power	Current
EI_{Full}/EI_{WD}	5.49	230	7.15
EI_{Zone}/EI_{WD}	3.22	2.71	1.50

Scenario B: Large-scale 20-WTGs DFIG wind farm

A large-scale wind farm including 20 DFIG WTGs with dissimilar wind speed profiles for two groups of WTGs is also studied for all aggregation methods. The system

Table 5.7: Scenario B specifications: 20-WTGs DFIG Wind farm.

Parameter	WTG 1-5 & 11-15	WTG 6-10 & 16-20	Unit
S	2	1	$[MVA]$
J	127	63.5	$[kgm^2]$
τ_n	50	50	$[ms]$
r	42	29.7	$[m]$
C_{pmax}	0.48	0.48	-
λ_{opt}	7.69	5.44	-

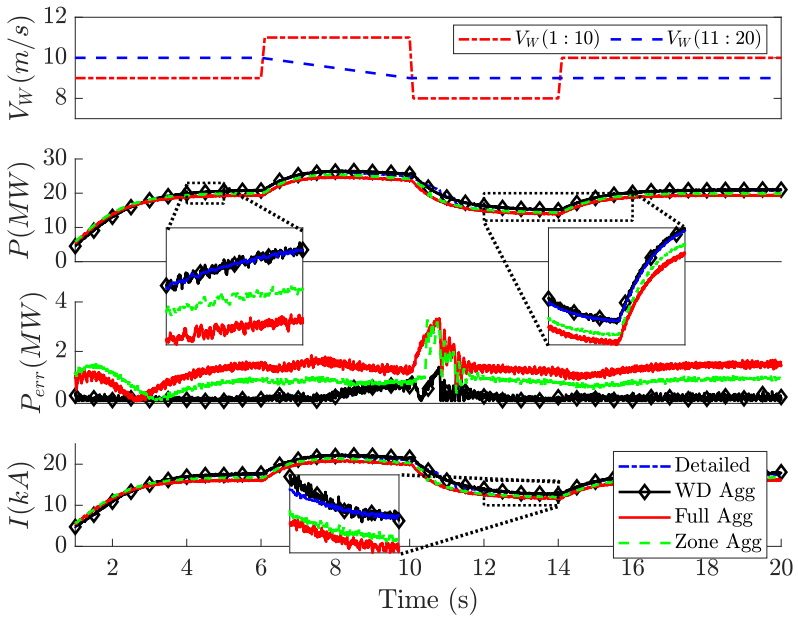

Figure 5.7: Scenario B: dissimilar wind speed profile and unequal WTGs parameters; performance comparisons from PCC point for detailed 20-WTGs DFIG wind farm, proposed WD, Full, and Zone agg models; (V_W wind speed, P active power, I phase A current rms, and subscript $_{err}$ indicates the model variable error with respect to the detailed system).

specification is shown in the Table 5.7. Figure 5.7 shows the wind speed, active power and its error with respect to the detailed system, and phase A current for all aggregation models. This figure shows a superior performance for WD agg model compared to the Full and Zone agg models especially in the transient behavior. Also, calculating the error index defined in (5.27) for all active power curves shows that the Full and Zone agg models have higher error about 7.18 and 4.51 times the WD agg model, respectively.

Table 5.8: Scenario C specifications: 4-WTGs DFIG Wind farm with (5.28) power coefficient model.

Parameter	WTG 1	WTG 2	WTG 3	WTG 4	Unit
S	2	2	1	1	$[MVA]$
J	127	127	63.5	63.5	$[kgm^2]$
τ_n	25	25	25	25	$[ms]$
r	42	42	29.69	29.69	$[m]$
C_{pmax}	0.42	0.42	0.42	0.42	-
λ_{opt}	6.92	6.92	4.89	4.89	-
V_W	10	8	10	8	$[m/s]$

Scenario C: 4-WTGs DFIG wind farm with other existing turbine power coefficient model

To show the applicability of the proposed method for WTGs with other existing power coefficient models, a 4-DFIG wind farm similar to Figure 5.3 with Table 5.8 parameters is studied with a different turbine model as[101], [102]:

$$C_p = (1.12\lambda - 2.8)e^{-0.38\lambda}, \tag{5.28}$$

where (5.28) turbine, $\lambda = 5.2r\omega_m/(\lambda_{opt}V_W G)$. Also, to study the transient behavior of proposed method a 0.2pu voltage drop is applied at $t = 10s$ and is cleared at $t = 12s$. Figure 5.8 verifies the accuracy and the applicability of the proposed method in wind farms with WTGs that have other existing power coefficient models.

Scenario D: 4-WTGs DFIG wind farm at oscillatory mode

Considering a 4-WTGs DFIG consisting of wind farm with Scenario A WTG1 and $L_m = 3.5[mH]$, $C_{DC} = 8[mF]$, $K_{iv} = 3 \times 10^6$, and $K_{opt} = 5.2242 \times 10^6$, we have conducted a special simulation as shown in Figure 5.9 to demonstrate that the method is still accurate for the eigenvalues closed to the imaginary axis. As it shows, the proposed model with good approximation matches the detailed model and predicts the dominant oscillation mode while Full and Zone Agg models show a stable behavior including only some sub-oscillation modes. The results, achieved from all scenarios, demonstrate a superior performance of the proposed WD model compared to the existing methods. As discussed before, it is worth mentioning that for pure imaginary eigenvalues, the linearization is not valid and other methods should be used to study the system behavior.

5.5 Conclusion

A systematic and simple method is proposed to model large-scale induction machine-based wind farms by a single WTG that contains an equivalent mechanical wind turbine and an equivalent electrical generator. This equivalent generator d-q model

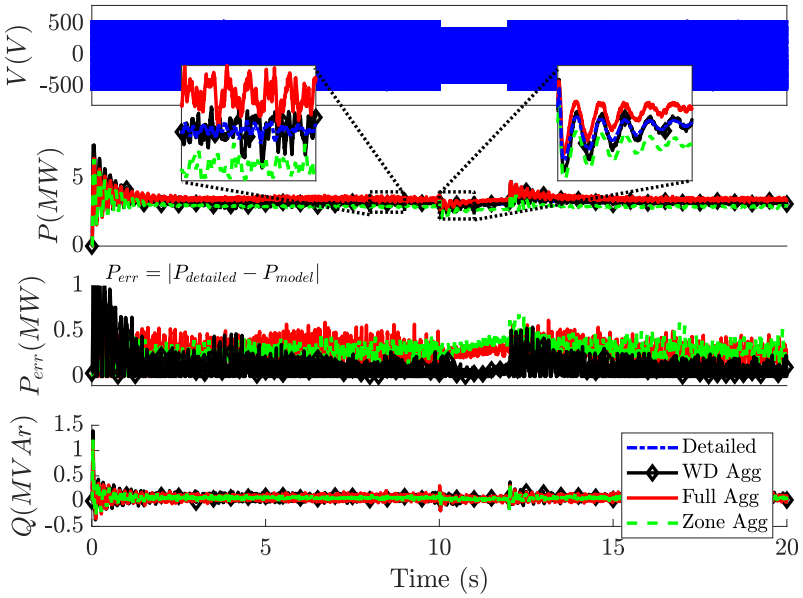

Figure 5.8: Scenario C: WTGs with power coefficient model of (5.28); performance comparisons from PCC point for detailed 4-WTGs DFIG wind farm, proposed WD, Full, and Zone agg models; (V voltage, P & Q active and reactive powers, I phase A current, and subscript $_{err}$ indicates the model variable error with respect to the detailed system).

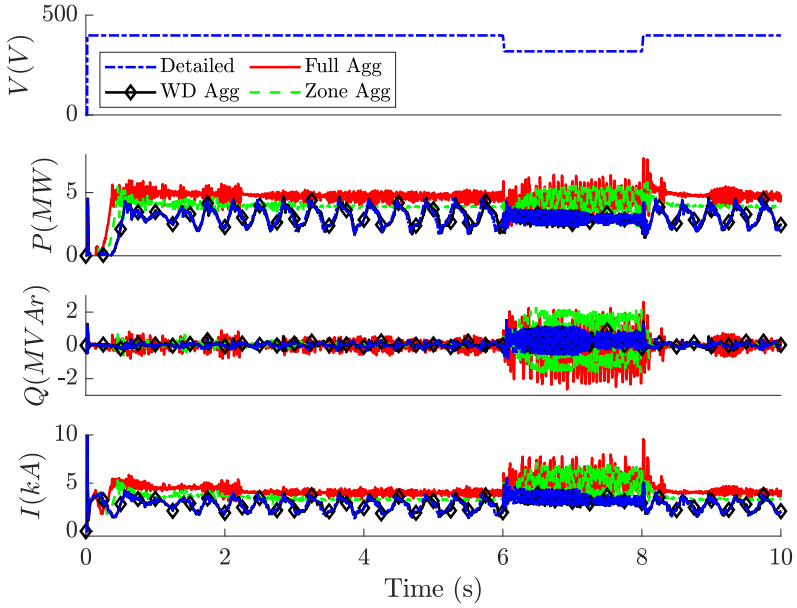

Figure 5.9: Scenario D: Oscillatory operating point for WTGs; performance comparisons from PCC point for detailed 4-WTGs DFIG wind farm, proposed WD, Full, and Zone agg models; (V voltage rms, P & Q active and reactive powers, I phase A current rms).

is obtained by quantifying the contribution of each WTG to the wind farm using Weighted Dynamics (WD). The performance of the proposed model is evaluated through simulations and investigations of a 4-WTGs and large-scale 20-WTGs wind farms in different scenarios of various wind speeds and WTGs parameters. It is shown that the error of the proposed WD agg method is at least 2 times less than Full and Zone agg models. The single equivalent WTG is derived through a one-time simple calculation, resulting in significantly less computational burden and model complexity compared to equivalent admittance, optimization methods and Semi agg models. It is shown that the proposed WD agg method is adequately accurate in both transients and steady-state responses.

Chapter 6

Summary and Future Work

6.1 Summary and Contributions

A method of aggregating modular large-scale systems with a single equivalent unit model has been presented, where the equivalent unit has a similar configuration with an individual unit in the large-scale system. The parameters of the proposed model are calculated based on the contribution of each unit to the total desired output dynamics of the large-scale system. The objective is to obtain an equivalent model of a modular large-scale system so that the model accurately mimics the behavior of the system from the PCC while preserving the important features and characteristics of the large-scale system independent of the number of units and the system parameters. The main contributions and conclusions of this report are summarized below.

(i) The application of the WD aggregation approach to model a DC-DC buck converter integrated microgrid is demonstrated, where it resulted in an equivalent single converter and control system, serving as a reduced-order model for a system comprising multiple droop-controlled DC-DC converters with different parameter values.

(ii) The WD aggregation model of the DC-DC buck converter integrated microgrid is employed to conduct sensitivity and stability analyses, showcasing its effectiveness and high accuracy. Through various case scenarios involving different converter parameters and stability conditions, the proposed model proves to be a reliable and efficient tool for analyzing the system's behavior.

(iii) By utilizing the WD aggregation model for the DC-DC buck converter integrated microgrid, an effective control strategy is devised, resulting in a desirable dynamic behavior for both the overall system and individual converters. The proposed approach optimizes the system's performance, ensuring stable and efficient transient dynamics for all converters within the microgrid

(iv) The proposed WD agg method is applied to model large-scale islanded microgrids consisting of n grid-forming parallel inverters with droop control power-sharing by a single equivalent inverter and a controller.

(v) An islanded microgrid consists of four grid-forming parallel inverters and a resistive load was modeled with the proposed WD Agg method and evaluated by simulations and experimental implementation. It was shown that for a 300% control parameters difference the proposed WD model has a 5% max error, while other conventional methods has 40% max error. It was illustrated that the proposed WD Agg method can accurately mimic the large-scale system behavior with unequal control parameters and various input changes.

(vi) The proposed model of the islanded microgrid consisting of four grid-forming parallel inverters is used in various stability analyses and it was shown that the proposed model can accurately predict the instability of the large-scale system where other existing method fail.

(vii) The proposed WD aggregation method is employed to model a system of three paralleled inverters with parameter variations exceeding 20%. This method effectively preserves the detailed system characteristics such as frequency response, root loci, and output admittance.

(viii) An equivalent single inverter, PV array, and control system is presented as the reduced-order model of n grid-following PV units with equal and unequal parameters considering the non-linearity of the PV sources.

(ix) A small-scale PV farm, consisting of three inverters with equal and unequal parameters, was modeled and it was shown that for a 50% parameter difference, a 4% max error was observed for the oscillatory condition of the detailed system connected to a weak grid. Furthermore, the small-scale system verified the ability and the accuracy of the proposed model in predicting the dynamic behavior of the detailed system with various control parameters under different stability conditions with less than 2% error in oscillation frequency predictions. Moreover, the experimental results are also provided that match simulations and analytics results.

(x) The proposed model is applied to PV farms of CIGRE HV/MV 14-bus benchmark for renewable energies with equal and unequal parameters to evaluate the application of the proposed model in large-scale systems. The results illustrated that the proposed model with the max error of 2.2% can accurately show the effect of up-stream buses and their machine inertia on the PV farms output dynamic behaviors under harsh power system events such as 3 full cycles line-to-line faults at the PV farms buses and 0.2 pu voltage sags at the infinite bus. Moreover, the proposed single equivalent unit presentation hugely reduced the computational burden of the system case studies.

(xi) A single equivalent WTG consisting of an equivalent mechanical wind turbine and an equivalent electrical generator is obtained by WD agg approach for large-scale induction machine-based wind farms.

(xii) A wind farm consists of 4 DFIG-based WTGs with different wind speeds and WTGs parameters is aggregated with the proposed WD agg method and it is shown that the error of the proposed WD agg method is at least 2 times less than Full and Zone agg models. Moreover, it has been verified that the proposed WD method is independent of the turbine power coefficient model.

(xiii) A large-scale wind farm consists of 20 DFIG-based WTGs with different wind speeds and WTGs parameters is aggregated with the proposed WD agg method and it is shown that the single equivalent WTG is derived through a one-time simple calculation, resulting in significantly less computational burden and model complexity compared to equivalent admittance, optimization methods and Semi agg models.

6.2 Suggested Future Work

There are a number of directions that this research could proceed in; three of the most promising are outlined below.

(i) WD aggregation of modular large-scale systems featuring a cascaded units configuration, such as multi-level converters, presents an intriguing research avenue. A comprehensive exploration of the series configuration system can be conducted by leveraging the duality theorem, which offers valuable insights and analytical tools to thoroughly examine the system's behavior and characteristics.

(ii) Investigation of the feasibility and effectiveness of the proposed WD approach for asymmetrical three-phase systems. Asymmetrical systems can be divided into two distinct parts, namely symmetrical and asymmetrical components. The WD aggregation approach can be employed to separately aggregate these components, offering a potential avenue to address the complexities of asymmetrical systems with enhanced efficiency and accuracy.

(iii) Identification of the dominant units within a large-scale system using the dynamic weights derived from the WD aggregation approach. These weights represent the contribution of each unit to the overall system behavior. By pinpointing the impact of dominant units, it becomes possible to strategically design the system for optimal performance, ensuring its behavior aligns with desired objectives and outcomes.

Bibliography

[1] E. Du et al., "The role of concentrating solar power toward high renewable energy penetrated power systems," *IEEE Trans. on Power Systems*, vol. 33, no. 6, pp. 6630–6641, 2018.

[2] Z. Zhuo et al., "Transmission expansion planning test system for ac/dc hybrid grid with high variable renewable energy penetration," *IEEE Trans. on Power Systems*, vol. 35, no. 4, pp. 2597–2608, 2019.

[3] D. Salomonsson, L. Soder, and A. Sannino, "An adaptive control system for a dc microgrid for data centers," in *2007 IEEE Industry Applications Annual Meeting*, pp. 2414–2421, IEEE, 2007.

[4] D. Salomonsson and L. Soder, "Comparison of different solutions for emergency and standby power systems for commercial consumers," in *INTELEC 06-Twenty-Eighth International Telecommunications Energy Conference*, pp. 1–8, IEEE, 2006.

[5] C. Collados-Rodriguez, M. Cheah-Mane, E. Prieto-Araujo, and O. Gomis-Bellmunt, "Stability analysis of systems with high vsc penetration: Where is the limit?," *IEEE Transactions on Power Delivery*, vol. 35, no. 4, pp. 2021–2031, 2020.

[6] C. Boonseng, D. Suksawat, and K. Kularbphettong, "Design and control of dc microgrids (dcmg) systems for improving reliability and stability of data centers," in *2019 5th International Conference on Engineering, Applied Sciences and Technology (ICEAST)*, pp. 1–4, IEEE, 2019.

[7] K. Palaniappan, S. Veerapeneni, R. M. Cuzner, and Y. Zhao, "Viable residential dc microgrids combined with household smart ac and dc loads for underserved communities," *Energy Efficiency*, vol. 13, no. 2, pp. 273–289, 2020.

[8] A. Ahmad et al., "Robust control of grid-tied parallel inverters using nonlinear backstepping approach," *IEEE Access*, vol. 7, pp. 111982–111992, 2018.

[9] M. Ahmed, L. Meegahapola, A. Vahidnia, and M. Datta, "Stability and control aspects of microgrid architectures–a comprehensive review," *IEEE Access*, vol. 8, pp. 144730–144766, 2020.

[10] Z. J. Meng and F. Xue, "An investigation of the equivalent wind method for the aggregation of dfig wind turbines," in *2010 Asia-Pacific Power and Energy Engineering Conference*, pp. 1–6, March 2010.

[11] L. M. Fernandez, C. A. Garcia, F. Jurado, and J. R. Saenz, "Aggregation of doubly fed induction generators wind turbines under different incoming wind speeds," in *2005 IEEE Russia Power Tech*, pp. 1–6, June 2005.

[12] X. Su et al., "On-site engineering test of active support control for the pv station and wind farm in the ac-dc hybrid power grid under extreme fault conditions," *Complexity*, vol. 2021, 2021.

[13] W. Du et al., "Harmonic oscillations in a grid-connected pv generation farm caused by increased number of parallel-connected pv generating units and damping control," *CSEE Journal of Power and Energy Systems*, 2020.

[14] M. Su, Z. Liu, Y. Sun, H. Han, and X. Hou, "Stability analysis and stabilization methods of dc microgrid with multiple parallel-connected dc–dc converters loaded by cpls," *IEEE Transactions on Smart Grid*, vol. 9, no. 1, pp. 132–142, 2016.

[15] J. Kumar, A. Agarwal, and V. Agarwal, "A review on overall control of dc microgrids," *Journal of energy storage*, vol. 21, pp. 113–138, 2019.

[16] A. Khalil, A. S. Peng, and A. Asheibi, "Stability analysis of parallel dc-dc converters controlled over communication network," *International Journal of Power Electronics*, vol. 14, no. 4, pp. 501–528, 2021.

[17] B. Wen et al., "Impedance-based analysis of grid-synchronization stability for three-phase paralleled converters," *IEEE Trans. on Power Electronics*, vol. 31, no. 1, pp. 26–38, 2016.

[18] E. Rehman et al., "Stability assessment of high penetration of inverter-based generation in the ercot grid," in *2019 IEEE Power & Energy Society General Meeting (PESGM)*, pp. 1–5, IEEE, 2019.

[19] H. Alenius et al., "Impedance-based stability analysis of multi-parallel inverters applying total source admittance," in *2019 20th Workshop on Control and Modeling for Power Electronics (COMPEL)*, pp. 1–8, 2019.

[20] S. Rahman et al., "Analysis of power grid voltage stability with high penetration of solar pv systems," *IEEE Trans. on Industry Applications*, vol. 57, no. 3, pp. 2245–2257, 2021.

[21] Z. Yang et al., "Margin balancing control design of three-phase grid-tied pv inverters for stability improvement," *IEEE Trans. on Power Electronics*, vol. 36, no. 9, pp. 10716–10728, 2021.

[22] Y. Han, X. Ning, P. Yang, and L. Xu, "Review of power sharing, voltage restoration and stabilization techniques in hierarchical controlled dc microgrids," *IEEE Access*, vol. 7, pp. 149202–149223, 2019.

[23] N. Mithulananthan et al., "Small-disturbance angle stability control with high penetration of renewable generations," *IEEE Trans. on Power Systems*, vol. 29, no. 3, pp. 1463–1472, 2013.

[24] S. Kazemlou and S. Mehraeen, "Novel decentralized control of power systems with penetration of renewable energy sources in small-scale power systems," *IEEE Trans. on Energy Conversion*, vol. 29, no. 4, pp. 851–861, 2014.

[25] N. V. Mohamed et al., "Modelling of inter-area angular dynamics and proactive defence strategy in deregulated power grids with large-scale integration of renewable energy sources," *IET Generation, Transmission & Distribution*, vol. 14, no. 15, pp. 2940–2950, 2020.

[26] M. Jyothish and E. Jasmin, "Load sharing control and circulating current minimization of parallel dc-dc converters based on droop index," in *2018 International CET Conference on Control, Communication, and Computing (IC4)*, pp. 84–88, IEEE, 2018.

[27] L. Meng, T. Dragicevic, J. M. Guerrero, and J. C. Vasquez, "Optimization with system damping restoration for droop controlled dc-dc converters," in *2013 IEEE Energy Conversion Congress and Exposition*, pp. 65–72, IEEE, 2013.

[28] Y. Gui, R. Han, J. M. Guerrero, J. C. Vasquez, B. Wei, and W. Kim, "Large-signal stability improvement of dc-dc converters in dc microgrid," *IEEE Transactions on Energy Conversion*, vol. 36, no. 3, pp. 2534–2544, 2021.

[29] F. D. Mohammadi, H. K. Vanashi, and A. Feliachi, "State-space modeling, analysis, and distributed secondary frequency control of isolated microgrids," *IEEE Transactions on Energy Conversion*, vol. 33, no. 1, pp. 155–165, 2017.

[30] S. Anand and B. G. Fernandes, "Reduced-order model and stability analysis of low-voltage dc microgrid," *IEEE Transactions on Industrial Electronics*, vol. 60, no. 11, pp. 5040–5049, 2012.

[31] Z. Yang et al., "Stability investigation of three-phase grid-tied pv inverters with impedance-based method," in *2020 22nd European Conference on Power Electronics and Applications (EPE'20 ECCE Europe)*, pp. 1–10, IEEE, 2020.

[32] M. Zhu, H. Li, and X. Li, "Improved state-space model and analysis of islanding inverter-based microgrid," in *2013 IEEE International Symposium on Industrial Electronics*, pp. 1–5, IEEE, 2013.

[33] L. P. Kunjumuhammed, B. C. Pal, C. Oates, and K. J. Dyke, "Electrical oscillations in wind farm systems: Analysis and insight based on detailed modeling," *IEEE Transactions on Sustainable Energy*, vol. 7, no. 1, pp. 51–62, 2015.

[34] C. E. Ugalde-Loo, J. B. Ekanayake, and N. Jenkins, "State-space modeling of wind turbine generators for power system studies," *IEEE Transactions on Industry Applications*, vol. 49, no. 1, pp. 223–232, 2012.

[35] Z. Liu, J. Liu, X. Hou, Q. Dou, D. Xue, and T. Liu, "Output impedance modeling and stability prediction of three-phase paralleled inverters with master–slave sharing scheme based on terminal characteristics of individual inverters," *IEEE Transactions on Power Electronics*, vol. 31, no. 7, pp. 5306–5320, 2016.

[36] M. M. S. Khan, Y. Lin, B. Johnson, V. Purba, M. Sinha, and S. Dhople, "A reduced-order aggregated model for parallel inverter systems with virtual oscillator control," in *2018 IEEE 19th Workshop on Control and Modeling for Power Electronics (COMPEL)*, pp. 1–6, 2018.

[37] X. Zhu and Z. Pan, "Impedance-model-based ssr study considering dfigs at different locations," in *2017 20th International Conference on Electrical Machines and Systems (ICEMS)*, pp. 1–5, 2017.

[38] N. Rashidirad, M. Hamzeh, K. Sheshyekani, and E. Afjei, "A simplified equivalent model for the analysis of low-frequency stability of multi-bus dc microgrids," *IEEE Transactions on Smart Grid*, vol. 9, no. 6, pp. 6170–6182, 2017.

[39] A. P. N. Tahim, D. J. Pagano, E. Lenz, and V. Stramosk, "Modeling and stability analysis of islanded dc microgrids under droop control," *IEEE Transactions on power electronics*, vol. 30, no. 8, pp. 4597–4607, 2014.

[40] M. Wu and D. D.-C. Lu, "A novel stabilization method of lc input filter with constant power loads without load performance compromise in dc microgrids," *IEEE Transactions on industrial electronics*, vol. 62, no. 7, pp. 4552–4562, 2014.

[41] J. Ma, F. Liu, L. Jiang, M. Wu, Y. Li, and W. Wang, "Multi-dfig aggregated model based ssr analysis considering wind spatial distribution," *IET Renewable Power Generation*, vol. 13, no. 4, pp. 549–554, 2019.

[42] Z. Zeng et al., "An improved impedance modeling method of grid-tied inverters with white-box property," *IEEE Trans. on Power Electronics*, vol. 37, no. 4, pp. 3980–3989, 2021.

[43] H. Wang and J. Sun, "Impedance-based stability modeling and analysis of networked converter systems," in *2019 20th Workshop on Control and Modeling for Power Electronics (COMPEL)*, pp. 1–8, 2019.

[44] D. Remon et al., "Aggregated model of a distributed pv plant using the synchronous power controller," in *2015 IEEE 24th Int. Symposium on Industrial Electronics (ISIE)*, pp. 654–659, 2015.

[45] W. Du, Z. Chen, K. P. Schneider, R. H. Lasseter, S. Pushpak Nandanoori, F. K. Tuffner, and S. Kundu, "A comparative study of two widely used grid-forming

droop controls on microgrid small-signal stability," *IEEE Journal of Emerging and Selected Topics in Power Electronics*, vol. 8, no. 2, pp. 963–975, 2020.

[46] B. Mahamedi and J. E. Fletcher, "The equivalent models of grid-forming inverters in the sequence domain for the steady-state analysis of power systems," *IEEE Transactions on Power Systems*, vol. 35, no. 4, pp. 2876–2887, 2020.

[47] Y. Zhou, L. Zhao, and W. Lee, "Robustness analysis of dynamic equivalent model of dfig wind farm for stability study," *IEEE Transactions on Industry Applications*, vol. 54, no. 6, pp. 5682–5690, 2018.

[48] Y. Zhou, L. Zhao, and W. Lee, "Robustness analysis of dynamic equivalent model of dfig wind farm for stability study," in *2018 IEEE/IAS 54th Industrial and Commercial Power Systems Technical Conference (I CPS)*, pp. 1–9, 2018.

[49] Y. Zhou, L. Zhao, I. B. M. Matsuo, and W. Lee, "A dynamic weighted aggregation equivalent modeling approach for the dfig wind farm considering the weibull distribution," in *2019 IEEE/IAS 55th Industrial and Commercial Power Systems Technical Conference (I CPS)*, pp. 1–7, 2019.

[50] R. Wang, Q. Sun, P. Tu, J. Xiao, Y. Gui, and P. Wang, "Reduced-order aggregate model for large-scale converters with inhomogeneous initial conditions in dc microgrids," *IEEE Transactions on Energy Conversion*, vol. 36, no. 3, pp. 2473–2484, 2021.

[51] M. Juneja, S. R. Mohanty, and S. K. Nagar, "Robust optimisation-based order reduction and stability analysis of autonomous dc microgrid with consideration of non-linearity," *International Transactions on Electrical Energy Systems*, vol. 30, no. 2, p. e12228, 2020.

[52] Y. Zhou, L. Zhao, I. B. M. Matsuo, and W. Lee, "A dynamic weighted aggregation equivalent modeling approach for the dfig wind farm considering the weibull distribution for fault analysis," *IEEE Transactions on Industry Applications*, vol. 55, no. 6, pp. 5514–5523, 2019.

[53] Z. Li et al., "Parameters optimization of photovoltaic power generation system based on multi-time scale reduction," in *2019 IEEE Int. Conf. on Smart Internet of Things (SmartIoT)*, pp. 205–211, 2019.

[54] M. Rasheduzzaman et al., "Reduced-order small-signal model of microgrid systems," *IEEE Trans. on Sustainable Energy*, vol. 6, no. 4, pp. 1292–1305, 2015.

[55] E. A. A. Coelho, P. C. Cortizo, and P. F. D. Garcia, "Small-signal stability for parallel-connected inverters in stand-alone ac supply systems," *IEEE Transactions on Industry Applications*, vol. 38, no. 2, pp. 533–542, 2002.

[56] L. Luo and S. V. Dhople, "Spatiotemporal model reduction of inverter-based islanded microgrids," *IEEE Transactions on Energy Conversion*, vol. 29, no. 4, pp. 823–832, 2014.

[57] X. Guo, Z. Lu, B. Wang, X. Sun, L. Wang, and J. M. Guerrero, "Dynamic phasors-based modeling and stability analysis of droop-controlled inverters for microgrid applications," *IEEE Transactions on Smart Grid*, vol. 5, no. 6, pp. 2980–2987, 2014.

[58] I. P. Nikolakakos, H. H. Zeineldin, M. S. El-Moursi, and J. L. Kirtley, "Reduced-order model for inter-inverter oscillations in islanded droop-controlled microgrids," *IEEE Transactions on Smart Grid*, vol. 9, no. 5, pp. 4953–4963, 2018.

[59] V. Mariani, F. Vasca, J. C. Vásquez, and J. M. Guerrero, "Model order reductions for stability analysis of islanded microgrids with droop control," *IEEE Transactions on Industrial Electronics*, vol. 62, no. 7, pp. 4344–4354, 2015.

[60] S. Liao et al., "Emulation of multi-inverter integrated weak grid via interaction-preserved aggregation," *IEEE Journal of Emerging and Selected Topics in Power Electronics*, pp. 1–1, 2020.

[61] S. V. Iyer, M. N. Belur, and M. C. Chandorkar, "A generalized computational method to determine stability of a multi-inverter microgrid," *IEEE Transactions on Power Electronics*, vol. 25, no. 9, pp. 2420–2432, 2010.

[62] Y. Zhou et al., "A gain scheduling wide-area damping controller for the efficient integration of photovoltaic plant," *IEEE Trans. on Power Systems*, vol. 34, no. 3, pp. 1703–1715, 2018.

[63] J. Ge et al., "Wide-area damping controller design of large-scale pv power plants in interconnected power systems," in *2016 China Int. Conf. on Electricity Distribution (CICED)*, pp. 1–5, IEEE, 2016.

[64] Z. Yang et al., "Virtual damping control design of three-phase grid-tied pv inverters for passivity enhancement," *IEEE Trans. on Power Electronics*, vol. 36, no. 6, pp. 6251–6264, 2020.

[65] Z. Yang et al., "Passivity-based virtual damping control of three-phase grid-tied pv inverters," in *2020 IEEE 21st Workshop on Control and Modeling for Power Electronics (COMPEL)*, pp. 1–8, IEEE, 2020.

[66] V. Purba et al., "Reduced-order aggregate model for parallel-connected single-phase inverters," *IEEE Trans. on Energy Conversion*, vol. 34, no. 2, pp. 824–837, 2018.

[67] J. Conroy and R. Watson, "Aggregate modelling of wind farms containing full-converter wind turbine generators with permanent magnet synchronous machines: transient stability studies," *IET Renewable Power Generation*, vol. 3, pp. 39–52, March 2009.

[68] J. Brochu, C. Larose, and R. Gagnon, "Validation of single- and multiple-machine equivalents for modeling wind power plants," *IEEE Transactions on Energy Conversion*, vol. 26, pp. 532–541, June 2011.

[69] V. Purba et al., "Reduced-order structure-preserving model for parallel-connected three-phase grid-tied inverters," in *2017 IEEE 18th Workshop on Control and Modeling for Power Electronics (COMPEL)*, pp. 1–7, 2017.

[70] V. Purba et al., "Reduced-order aggregate model for parallel-connected grid-tied three-phase photovoltaic inverters," in *2019 IEEE 46th Photovoltaic Specialists Conference (PVSC)*, pp. 0724–0729, IEEE, 2019.

[71] L. P. Kunjumuhammed, B. C. Pal, C. Oates, and K. J. Dyke, "The adequacy of the present practice in dynamic aggregated modeling of wind farm systems," *IEEE Transactions on Sustainable Energy*, vol. 8, pp. 23–32, Jan 2017.

[72] H. Liu and Z. Chen, "Aggregated modelling for wind farms for power system transient stability studies," in *2012 Asia-Pacific Power and Energy Engineering Conference*, pp. 1–6, March 2012.

[73] N. Dhlamini and S. P. Chowdhury, "The impact of wind farm aggregation techniques for analyzing power system dynamics," in *2015 50th International Universities Power Engineering Conference (UPEC)*, pp. 1–6, Sept 2015.

[74] L. M. Fernandez, F. Jurado, and J. R. Saenz, "Aggregated dynamic model for wind farms with doubly fed induction generator wind turbines," *Renewable Energy*, vol. 33, no. 1, pp. 129 – 140, 2008.

[75] M. A. Chowdhury, N. Hosseinzadeh, M. M. Billah, and S. A. Haque, "Dynamic dfig wind farm model with an aggregation technique," in *International Conference on Electrical Computer Engineering (ICECE 2010)*, pp. 330–333, Dec 2010.

[76] C. Li, J. Xu, and C. Zhao, "A coherency-based equivalence method for mmc inverters using virtual synchronous generator control," *IEEE Transactions on Power Delivery*, vol. 31, no. 3, pp. 1369–1378, 2016.

[77] C. Guo et al., "A dynamic equivalence method considering the spatial effect of wind farms," in *Innovative Techniques and Applications of Modelling, Identification and Control*, pp. 357–374, Springer, 2018.

[78] R. Fang and M. Wu, "Dynamic equivalence of wind farm considering operational condition of wind turbines," in *2016 IEEE Region 10 Conference (TENCON)*, pp. 827–830, IEEE, 2016.

[79] X. Tuo et al., "A practical equivalence method of large scale wind farm," in *2010 Int. Conf. on Power System Technology*, pp. 1–6, IEEE, 2010.

[80] V. Purba et al., "Dynamic aggregation of grid-tied three-phase inverters," *IEEE Trans. on Power Systems*, vol. 35, no. 2, pp. 1520–1530, 2019.

[81] P. J. Hart, R. H. Lasseter, and T. M. Jahns, "Coherency identification and aggregation in grid-forming droop-controlled inverter networks," *IEEE Transactions on Industry Applications*, vol. 55, no. 3, pp. 2219–2231, 2019.

[82] P. J. Hart, R. H. Lasseter, and T. M. Jahns, "Enforcing coherency in droop-controlled inverter networks through use of advanced voltage regulation and virtual impedance," in *2017 IEEE Energy Conversion Congress and Exposition (ECCE)*, pp. 3367–3374, 2017.

[83] A. A. Nia, N. Shabanikia, and S. A. Khajehoddin, "Droop-based dc microgrids analysis and control design using weighted dynamic aggregation modeling approach," *IEEE Transactions on Industrial Electronics*, 2023.

[84] A. A. Nia et al., "Weighted dynamic aggregation modeling of dc microgrid converters with droop control," in *2021 IEEE Energy Conversion Congress and Exposition (ECCE)*, pp. 700–706, IEEE, 2021.

[85] S. A. Khajehoddin, M. Karimi-Ghartemani, and M. Ebrahimi, "Optimal and systematic design of current controller for grid-connected inverters," *IEEE Journal of Emerging and Selected Topics in Power Electronics*, vol. 6, no. 2, pp. 812–824, 2017.

[86] N. Yang, B. Nahid-Mobarakeh, F. Gao, D. Paire, A. Miraoui, and W. Liu, "Modeling and stability analysis of multi-time scale dc microgrid," *Electric Power Systems Research*, vol. 140, pp. 906–916, 2016.

[87] N. Yang, F. Gao, D. Paire, A. Miraoui, and W. Liu, "Distributed control of multi-time scale dc microgrid based on adrc," *IET Power Electronics*, vol. 10, no. 3, pp. 329–337, 2017.

[88] A. M. Rahimi and A. Emadi, "Active damping in dc/dc power electronic converters: A novel method to overcome the problems of constant power loads," *IEEE Transactions on Industrial Electronics*, vol. 56, no. 5, pp. 1428–1439, 2009.

[89] S. Wang et al., "Small-signal modeling and stability prediction of parallel droop-controlled inverters based on terminal characteristics of individual inverters," *IEEE Trans. on Power Electronics*, vol. 35, no. 1, pp. 1045–1063, 2019.

[90] K. Rudion et al., "Design of benchmark of medium voltage distribution network for investigation of dg integration," in *2006 IEEE Power Engineering Society General Meeting*, pp. 6–pp, IEEE, 2006.

[91] A. M. Khalil and R. Iravani, "A dynamic coherency identification method based on frequency deviation signals," *IEEE TPWRS*, vol. 31, no. 3, pp. 1779–1787, 2015.

[92] N. Shabanikia and S. A. Khajehoddin, "Weighted dynamic aggregation modeling of grid-following inverters to analyze renewable dg integrated microgrids," *IEEE Transactions on Industrial Electronics*, 2023.

[93] Z. Yang et al., "Stability assessment of a three-phase grid-tied pv inverter with eigenvalue-based method," in *2019 IEEE 10th Int. Symposium on Power Electronics for Distributed Generation Systems (PEDG)*, pp. 722–727, IEEE, 2019.

[94] P. Suwannatrai et al., "Maximum power point tracking by incremental conductance method for photovoltaic systems with phase shifted full-bridge dc-dc converter," in *The 8th Electrical Engineering/Electronics, Computer, Telecommunications and Information Technology (ECTI) Association of Thailand-Conference 2011*, pp. 637–640, IEEE, 2011.

[95] N. Shabanikia et al., "Weighted dynamic aggregation modeling of induction machine-based wind farms," *IEEE Trans. on Sustainable Energy*, vol. 12, no. 3, pp. 1604–1614, 2021.

[96] S. A. Khajehoddin, A. Tabesh, and N. Shabanikia, "Aggregated model of large-scale wind farms for power system simulation software tools," Dec. 24 2020. US Patent App. 16/904,959.

[97] G. Abad and G. Iwanski, *Properties and Control of a Doubly Fed Induction Machine*, ch. 10. John Wiley & Sons, Ltd.

[98] P. Krause, O. Wasynczuk, S. D. Sudhoff, and S. Pekarek, *Alternative Forms of Machine Equations*. IEEE, 2013.

[99] G. Iwanski, P. Pura, T. Łuszczyk, and M. Szypulski, "Stator voltage harmonics and unbalance compensation of the sensorless standalone doubly fed induction generator," *COMPEL: The International Journal for Computation and Mathematics in Electrical and Electronic Engineering*, 2014.

[100] H. Abu-Rub, M. Malinowski, and K. Al-Haddad, *Power electronics for renewable energy systems, transportation and industrial applications*. John Wiley & Sons, 2014.

[101] Y. Xia, K. H. Ahmed, and B. W. Williams, "Wind turbine power coefficient analysis of a new maximum power point tracking technique," *IEEE Transactions on Industrial Electronics*, vol. 60, no. 3, pp. 1122–1132, 2013.

[102] R. J. Wai, C. Y. Lin, and Y. R. Chang, "Novel maximum-power-extraction algorithm for pmsg wind generation system," *IET Electric Power Applications*, vol. 1, no. 2, pp. 275–283, 2007.

Appendix A

The WD agg Stability Preservation & Controllability Requirement

Building upon the mathematical foundation of the proposed WD aggregation model introduced in Section 2.1, the subsequent two sections delve into an examination of both the proof of stability preservation and the assessment of controllability prerequisites inherent to the proposed method.

A.1 Stability Preservation

Theorem: If $\mathbf{A}_k,\ k = 1 : N$ are stable and $\mathbf{M}_k$ and $\mathbf{P}_\mathbf{x}$ are positive-definite $\Rightarrow\ \mathbf{A}_{eq}$ is stable.
Proof: $\mathbf{A}_k,\ k = 1 : N$ are stable, thus, $\mathbf{A}_k,\ k = 1 : N$ are negative definite. Therefore, $\left(\sum_{k=1}^{n} \mathbf{M}_k\mathbf{P}_\mathbf{x}\right)^{-1} \mathbf{A}_k\mathbf{M}_k\mathbf{P}_\mathbf{x},\ k = 1 : K$ are also negative-definite. Then, $\left(\sum_{k=1}^{n} \mathbf{M}_k\mathbf{P}_\mathbf{x}\right)^{-1} \sum_{k=1}^{N} \mathbf{A}_k\mathbf{M}_k\mathbf{P}_\mathbf{x}$ is also negative-definite. Therefore, $\mathbf{A}_{eq}$ is a negative definite matrix with only negative eigenvalues. Hence, $\mathbf{A}_{eq}$ is stable and the theorem is proved.

A.2 Controllability Requirement

Theorem: If $k = 1 : N$ systems are stable and all $\mathbf{M}_k$, $\mathbf{W}_k$, $\mathbf{P}_\mathbf{x}$, $\mathbf{P}_\mathbf{u}$, and $\mathbf{B}_i\mathbf{B}_j^T + \mathbf{B}_j\mathbf{B}_i^T$ matrices are positive-definite for $i,\ j,\ k = 1 : N \Rightarrow$ the pair of $(\mathbf{A}_{eq}, \mathbf{B}_{eq})$ is controllable.
Proof: If $\mathbf{B}_i\mathbf{B}_j^T + \mathbf{B}_j\mathbf{B}_i^T$ are positive-definite for $i,\ j = 1 : N$ and $\mathbf{A}_i$ is sable, therefore, pairs of $(\mathbf{A}_k, \mathbf{B}_k),\ k = 1 : N$ are controllable, i.e.:

$$\text{if } i = j \Rightarrow\ \mathbf{B}_i\mathbf{B}_j^T + \mathbf{B}_j\mathbf{B}_i^T = 2\mathbf{B}_i\mathbf{B}_i^T \text{ is positive-definite,} \tag{A.1}$$

therefore it can be shown the Controllability Gramian of $(\mathbf{A}_i, \mathbf{B}_i)$ is positive-definite. Considering $\mathbf{A}_k$ is stable, then exists the Controllability Gramian as:

$$\mathbf{Gr}_{\mathbf{c}_k} = \int_0^\infty e^{\mathbf{A}_k\tau}\mathbf{B}_k\mathbf{B}_k^T e^{\mathbf{A}_k^T\tau} d\tau, \tag{A.2}$$

where $\mathbf{Gr}_{\mathbf{c}_k}$ is a symmetric positive-definite matrix. Deriving $\mathbf{Gr}_{\mathbf{c}_{eq}}$ yields:

$$\mathbf{Gr}_{\mathbf{c}_{eq}} = \int_0^\infty e^{\mathbf{A}_{eq}\tau}\mathbf{B}_{eq}\mathbf{B}_{eq}^T e^{\mathbf{A}_{eq}^T\tau}d\tau. \tag{A.3}$$

Substituting $\mathbf{B}_{eq}$ from (2.7) in (A.3) results in:

$$\mathbf{Gr}_{\mathbf{c}_{eq}} = \int_0^\infty e^{\mathbf{A}_{eq}\tau}\mathbf{N}\sum_{i=1}^{N}\sum_{j=1}^{N}\mathbf{B}_i\mathbf{W}_i\mathbf{P}_\mathbf{u}\mathbf{P}_\mathbf{u}{}^T\mathbf{W}_j^T\mathbf{B}_j^T\mathbf{N}^T e^{\mathbf{A}_{eq}^T\tau}d\tau = \sum_{i=1}^{N}\sum_{j=1}^{N}\mathbf{Gr}_{\mathbf{c}_{ij}}, \tag{A.4}$$

where:

$$\begin{aligned}\mathbf{Gr}_{\mathbf{c}_{ij}} = \int_0^\infty e^{\mathbf{A}_{eq}\tau}\Big(&\mathbf{N}\mathbf{B}_i\mathbf{W}_i\mathbf{P}_\mathbf{u}\mathbf{P}_\mathbf{u}{}^T\mathbf{W}_j^T\mathbf{B}_j^T\mathbf{N}^T + \cdots \\ &\cdots + \mathbf{N}\mathbf{B}_j\mathbf{W}_j\mathbf{P}_\mathbf{u}\mathbf{P}_\mathbf{u}{}^T\mathbf{W}_i^T\mathbf{B}_i^T\mathbf{N}^T\Big)e^{\mathbf{A}_{eq}^T\tau}d\tau,\end{aligned} \tag{A.5}$$

$$\mathbf{N} = \left(\sum_{k=1}^{n}\mathbf{M}_k\mathbf{P}_\mathbf{x}\right)^{-1}.$$

Considering the stability preservation theorem discussed in A.1, if $\mathbf{A}_k$ are negative-definite, yields $\mathbf{A}_{eq}$, and consequently $e^{\mathbf{A}_{eq}^T}$ and $e^{\mathbf{A}_{eq}}$ to be negative-definite. Moreover, considering $\mathbf{B}_i\mathbf{B}_j^T + \mathbf{B}_j\mathbf{B}_i^T$ is positive-definite, there exists a non-zero vector as $\mathbf{q}$, where:

$$\mathbf{q}^T\left(\mathbf{B}_i\mathbf{B}_j^T + \mathbf{B}_j\mathbf{B}_i^T\right)\mathbf{q} > 0. \tag{A.6}$$

By defining $\mathbf{z}_i = \mathbf{B}_i^T\mathbf{q}$ and $\mathbf{z}_j = \mathbf{B}_j^T\mathbf{q}$, (A.6) can be rewritten as:

$$\mathbf{z}_i^T\mathbf{z}_j + \mathbf{z}_j^T\mathbf{z}_i > 0. \tag{A.7}$$

Now by defining $\mathbf{z}_j = \mathbf{H}\mathbf{z}_i$ and substituting in (A.7) yields:

$$\mathbf{z}_i^T\mathbf{H}\mathbf{z}_i + \mathbf{z}_j^T\mathbf{H}^{-1}\mathbf{z}_j > 0. \tag{A.8}$$

Therefore, if A.8 is true all time, which is one of the proof assumptions, then $\mathbf{H}$ should be a positive-definite matrix. Considering $\mathbf{W}_i\mathbf{P}_\mathbf{u}\mathbf{P}_\mathbf{u}{}^T\mathbf{W}_j^T$ is a positive-definite matrix, (A.9) can be derived as:

$$\mathbf{z}_i^T\mathbf{W}_i\mathbf{P}_\mathbf{u}\mathbf{P}_\mathbf{u}{}^T\mathbf{W}_j^T\mathbf{H}\mathbf{z}_i + \mathbf{z}_j^T\mathbf{W}_j\mathbf{P}_\mathbf{u}\mathbf{P}_\mathbf{u}{}^T\mathbf{W}_i^T\mathbf{H}^{-1}\mathbf{z}_j > 0. \tag{A.9}$$

Considering $\mathbf{z}_j = \mathbf{H}\mathbf{z}_i$, (A.9) can be rewritten as:

$$\mathbf{z}_i^T\mathbf{W}_i\mathbf{P}_\mathbf{u}\mathbf{P}_\mathbf{u}{}^T\mathbf{W}_j^T\mathbf{z}_j + \mathbf{z}_j^T\mathbf{W}_j\mathbf{P}_\mathbf{u}\mathbf{P}_\mathbf{u}{}^T\mathbf{W}_i^T\mathbf{z}_i > 0. \tag{A.10}$$

Considering $\mathbf{z}_i = \mathbf{B}_i^T\mathbf{q}$ and $\mathbf{z}_j = \mathbf{B}_j^T\mathbf{q}$, (A.10) can be rewritten as:

$$\mathbf{q}^T\mathbf{B}_i\mathbf{W}_i\mathbf{P}_\mathbf{u}\mathbf{P}_\mathbf{u}{}^T\mathbf{W}_j^T\mathbf{B}_j^T\mathbf{q} + \mathbf{q}^T\mathbf{B}_j\mathbf{W}_j\mathbf{P}_\mathbf{u}\mathbf{P}_\mathbf{u}{}^T\mathbf{W}_i^T\mathbf{B}_i^T\mathbf{q} > 0. \tag{A.11}$$

Rewriting (A.11) in the quadratic form yields:

$$\mathbf{q}^T \left(\mathbf{B}_i \mathbf{W}_i \mathbf{P_u} \mathbf{P_u}^T \mathbf{W}_j^T \mathbf{B}_j^T + \mathbf{B}_j \mathbf{W}_j \mathbf{P_u} \mathbf{P_u}^T \mathbf{W}_i^T \mathbf{B}_i^T \right) \mathbf{q} \ = \mathbf{q}^T \mathbf{L}_{ij} \mathbf{q} > 0. \tag{A.12}$$

Therefore, $\mathbf{L}_{ij}$ is positive-definite. Considering $\mathbf{N}$ is a positive-definite matrix, therefore:

$$\left\{ \begin{matrix} e^{\mathbf{A}_{eq}^T}, \ e^{\mathbf{A}_{eq}} \text{ are negative-definite,} \\ \mathbf{N}\mathbf{L}_{ij}\mathbf{N}^T \text{ is positive-definite,} \end{matrix} \right\}$$

$$\Rightarrow \mathbf{Gr}_{\mathbf{c}_{ij}} \text{ is positive-definite} \Rightarrow \mathbf{Gr}_{\mathbf{c}_{eq}} \text{ is positive-definite,} \tag{A.13}$$

hence, the pair of $(\mathbf{A}_{eq}, \mathbf{B}_{eq})$ is controllable.